



University of Kentucky  
UKnowledge

---

Theses and Dissertations--Physics and  
Astronomy

Physics and Astronomy

---

2020

## SENSITIVITY OF ELECTRON-PROTON COINCIDENCE ASYMMETRIES IN NEUTRON BETA-DECAY TO SCALAR AND TENSOR INTERACTIONS

Subash C. Nepal

*University of Kentucky*, nepalsubash@yahoo.com

Digital Object Identifier: <https://doi.org/10.13023/etd.2020.475>

[Right click to open a feedback form in a new tab to let us know how this document benefits you.](#)

### Recommended Citation

Nepal, Subash C., "SENSITIVITY OF ELECTRON-PROTON COINCIDENCE ASYMMETRIES IN NEUTRON BETA-DECAY TO SCALAR AND TENSOR INTERACTIONS" (2020). *Theses and Dissertations--Physics and Astronomy*. 77.

[https://uknowledge.uky.edu/physastron\\_etds/77](https://uknowledge.uky.edu/physastron_etds/77)

This Doctoral Dissertation is brought to you for free and open access by the Physics and Astronomy at UKnowledge. It has been accepted for inclusion in Theses and Dissertations--Physics and Astronomy by an authorized administrator of UKnowledge. For more information, please contact [UKnowledge@lsv.uky.edu](mailto:UKnowledge@lsv.uky.edu).

## **STUDENT AGREEMENT:**

I represent that my thesis or dissertation and abstract are my original work. Proper attribution has been given to all outside sources. I understand that I am solely responsible for obtaining any needed copyright permissions. I have obtained needed written permission statement(s) from the owner(s) of each third-party copyrighted matter to be included in my work, allowing electronic distribution (if such use is not permitted by the fair use doctrine) which will be submitted to UKnowledge as Additional File.

I hereby grant to The University of Kentucky and its agents the irrevocable, non-exclusive, and royalty-free license to archive and make accessible my work in whole or in part in all forms of media, now or hereafter known. I agree that the document mentioned above may be made available immediately for worldwide access unless an embargo applies.

I retain all other ownership rights to the copyright of my work. I also retain the right to use in future works (such as articles or books) all or part of my work. I understand that I am free to register the copyright to my work.

## **REVIEW, APPROVAL AND ACCEPTANCE**

The document mentioned above has been reviewed and accepted by the student's advisor, on behalf of the advisory committee, and by the Director of Graduate Studies (DGS), on behalf of the program; we verify that this is the final, approved version of the student's thesis including all changes required by the advisory committee. The undersigned agree to abide by the statements above.

Subash C. Nepal, Student

Dr. Bradley Plaster, Major Professor

Dr. Christopher Crawford, Director of Graduate Studies

SENSITIVITY OF ELECTRON-PROTON COINCIDENCE ASYMMETRIES IN  
NEUTRON  $\beta$ -DECAY TO SCALAR AND TENSOR INTERACTIONS

---

DISSERTATION

---

A dissertation submitted in partial  
fulfillment of the requirements for  
the degree of Doctor of Philosophy  
in the College of Arts and Sciences  
at the University of Kentucky

By  
Subash Chandra Nepal  
Lexington, Kentucky

Director: Dr. Bradley Plaster, Professor of Physics  
Lexington, Kentucky  
2020

Copyright© Subash Chandra Nepal 2020

## ABSTRACT OF DISSERTATION

### SENSITIVITY OF ELECTRON-PROTON COINCIDENCE ASYMMETRIES IN NEUTRON $\beta$ -DECAY TO SCALAR AND TENSOR INTERACTIONS

We study the combined sensitivity of measurements of electron-proton coincidence asymmetries in polarized neutron  $\beta$ -decay together with a measurement of the electron energy spectrum in unpolarized neutron  $\beta$ -decay to beyond Standard Model (BSM) scalar and tensor interactions, via the appearance of such BSM physics in the Fierz interference terms  $b$  and  $b_\nu$ . Whereas measurements of the electron energy spectrum directly probe  $b$ , both the proton and neutrino asymmetries for which experimental results exist are not sensitive to  $b_\nu$ , but effectively to  $b - b_\nu$ . This results in reduced sensitivity to BSM scalar and tensor physics as the dependencies of  $b_\nu$  and  $b$  on scalar and tensor physics are similar. As a remedy, we demonstrate that ratios of certain asymmetries are sensitive only to  $b_\nu$ , thus providing a new paradigm for directly accessing  $b_\nu$ . We find that with  $1 \times 10^9$  events, a combined fit to our asymmetry ratios and the spectrum yields sensitivity to  $b$  and  $b_\nu$  at the level of  $\sim 2 \times 10^{-3}$ .

KEYWORDS: Asymmetry, Sensitivity, Neutrons, Polarized, Tensor

Subash Chandra Nepal

September 2, 2020

SENSITIVITY OF ELECTRON-PROTON COINCIDENCE ASYMMETRIES IN  
NEUTRON  $\beta$ -DECAY TO SCALAR AND TENSOR INTERACTIONS

By  
Subash Chandra Nepal

Dr. Bradley Plaster

Director of Dissertation

Dr. Christopher Crawford

Director of Graduate Studies

September 2, 2020

## ACKNOWLEDGMENTS

First of all, I would like to express my sincere gratitude to my advisor Dr. Bradley Plaster, Physics and Astronomy Department at University of Kentucky, for his patience, motivation, enthusiasm and for the continuous support for the development of this work. His relentless effort during the time of research helped me to complete my thesis.

Besides my advisor, I would like to thank the rest of my thesis committee: Prof. Christopher Crawford, Prof. Michael Eides and Prof. Yang for their encouragement and valuable suggestions to complete my work.

Special thanks to IT manager Mr. Vikram Gazula of Center for Computational Sciences at University of Kentucky for his help in making optimal use of the Lipscomb HPC Cluster throughout my computational work.

Also, I would like to extend my thanks to my colleagues in my lab, Dr. Michael Brown, Lakshya Malhotra, Dr. Alina Aleksandrova, Brian Allegeier, Dr. Ryan Dadisman, Danielle Schaper, Abel Lorente Campos, Piya Amara Palamure, Jared Brewington and Rashika Gupta for many useful discussions and support.

Finally, I am thankful to my entire family for supporting up to this point. I especially want to thank my loving wife Ganga as she experienced the difficult times with two daughters Stuti and Sudipti during my research work. From the bottom of my heart, I am thankful to my octogenarian mom Devi Nepal for encouraging me to do the best. Last, but not the least, this work is dedicated in memory of my twin brother the late Sanat Nepal who left his son Swaraj with me.

# TABLE OF CONTENTS

Acknowledgments . . . . .	iii
List of Tables . . . . .	vii
List of Figures . . . . .	viii
Chapter 1 Introduction . . . . .	1
1.1 The Standard Model (SM) . . . . .	1
1.1.1 Fundamental Particles in the SM . . . . .	1
1.1.2 Neutron . . . . .	3
1.1.3 Neutron $\beta$ -decay . . . . .	3
1.2 Fermi Theory of $\beta$ -Decay . . . . .	4
1.2.1 $\beta$ - Decay Selection Rules . . . . .	6
1.2.2 Parity Violation in Weak Interaction . . . . .	7
1.2.3 First Experiment on Parity Violation . . . . .	8
1.2.4 Two-Component Neutrino Theory . . . . .	9
1.2.5 $V - A$ Interaction . . . . .	11
1.2.6 Propagator . . . . .	12
1.3 Hadronic and Leptonic Currents . . . . .	13
1.3.1 The CKM Matrix . . . . .	14
1.3.2 Hadronic Matrix . . . . .	16
1.4 Angular Correlation Coefficients . . . . .	18
1.4.1 The Measurable $\beta$ -Decay Parameters . . . . .	18
1.4.2 Recoil Order Corrections . . . . .	20
1.4.3 Beyond Standard Model (BSM) . . . . .	21
1.4.4 Neutron Lifetime . . . . .	22
1.5 Ultra Cold Neutron (UCN) . . . . .	22
1.5.1 Trapping UCN . . . . .	23
1.5.2 Fermi Potential . . . . .	23
1.5.3 Gravity . . . . .	24
1.5.4 Magnetic Field . . . . .	24
1.6 Motivation . . . . .	25
Chapter 2 Event Generator for Neutron $\beta$ -Decay . . . . .	26
2.1 Decay Probability . . . . .	26
2.1.1 Proton Momentum . . . . .	27
2.1.2 Sampling Proton Events . . . . .	29
2.2 Electron Energy Spectrum . . . . .	30
2.3 Proton Energy Spectrum . . . . .	31
2.4 Antineutrino Energy Spectrum . . . . .	32
2.5 Event Generation . . . . .	32

Chapter 3	$Q_{ij}$ Spectra for Neutron $\beta$ -Decay	34
3.1	INM Approximation	34
3.2	Differential and Integral Asymmetries	40
3.2.1	Proton Asymmetry	40
3.2.2	Electron Asymmetry	44
3.2.3	Proton-Electron Asymmetry Ratio	45
3.3	Electron-Proton Coincidence Asymmetries	45
3.3.1	Neutrino Asymmetry	45
3.3.2	Electron-Proton Tilde Asymmetry	46
3.3.3	New Coincidence Asymmetry $\alpha_X$	47
3.3.4	New Coincidence Asymmetry $\alpha_R$	48
3.4	Integral Asymmetries	49
Chapter 4	Simulation	51
4.1	UCNB Experiment	51
4.1.1	UCNB Geometry	52
4.1.2	Magnetic field	52
4.1.3	Time of Flight	54
4.1.4	Detection System	55
4.1.5	Experimental Concept	55
4.2	Overview of Simulation	57
4.2.1	Geometry	57
4.2.2	Magnetic Field	58
4.2.3	Physical Processes	59
4.2.4	Event Types	60
4.2.5	Event Sorting	62
4.2.6	Input and Output	62
Chapter 5	Results	63
5.1	Simulation of UCNA Geometry	63
5.2	Simulation of UCNB Geometry	64
5.2.1	$Q_{ij}$ spectra	64
5.2.2	Analysis of Event Generator	66
5.2.3	Backscattering	67
5.2.4	Bremsstrahlung Effect Off	70
5.2.4.1	Reconstructed $Q_{ij}$ Spectra	70
5.2.5	Bremsstrahlung Effect On	71
5.2.5.1	Reconstructed $Q_{ij}$ Spectra	72
5.2.6	Distortions of Energy Spectra	74
5.2.7	Normalization for Coincidence Asymmetries	74
5.2.8	Sensitivity of $r_{pe}$ to $b_\nu$	75
5.2.9	Sensitivity of $\alpha_x$ to $b_\nu$	76
5.2.10	Sensitivity of Combined Fit to $b$ and $b_\nu$	77
5.2.11	Summary	77



Appendix . . . . .	80
A.1 Angular correlations in terms of coupling constants . . . . .	80
A.2 Properties of Projection operator . . . . .	80
A.3 Proton momentum calculations . . . . .	82
A.4 Analysis of Errors on Asymmetries . . . . .	83
A.5 UCNA Simulation and Events Types . . . . .	89
A.5.1 Kinetic Energy Distribution . . . . .	89
A.5.2 Angular Distribution . . . . .	93
A.5.3 Angular distribution for No Endcaps (2012/2013 geometry) . .	97
A.6 Analysis of Event Generator . . . . .	97
A.6.1 Values for $A_0$ , $B_0$ and $\lambda$ . . . . .	105
A.7 $A_0$ and $B_0$ calculations with no bremsstrahlung effects . . . . .	108
A.8 $A_0$ and $B_0$ calculations with bremsstrahlung effects enabled . . . . .	115
A.9 Distortion of electron spectrum . . . . .	122
Bibliography . . . . .	123
Vita . . . . .	132

## LIST OF TABLES

1.1	Quarks and Leptons . . . . .	2
1.2	Bilinear Invariants in Dirac Theory . . . . .	5
1.3	Discrete Symmetries and $C_i, C'_i$ . . . . .	8
1.4	Fermi Potentials of Some Materials . . . . .	23
1.5	Neutrino Asymmetry Parameter $B_0$ . . . . .	25
4.1	All possible events in the four detectors system. . . . .	61
5.1	Neutrino Asymmetry (bremsstrahlung off) . . . . .	71
5.2	Neutrino Asymmetry (bremsstrahlung on) . . . . .	73
5.3	Fractional change in the neutrino asymmetry. . . . .	74

## LIST OF FIGURES

1.1	(a) $\beta$ -decay spectrum. (b) The decay of a free neutron giving three particles, proton, electron and associated antineutrino and their direction relative to the neutron spin. . . . .	4
1.2	Fermi's analogy of four-fermion interaction to the electrodynamics [1]. . . . .	5
1.3	(a) Schematic diagram of Wu's experimental set up. (b) Data from Wu et al. experiment [2] measuring the correlation between the emitted direction of the electron from the decay of polarized $^{60}\text{Co}$ . . . . .	9
1.4	(a) Neutron decay at quark level with two spectator quarks. The neutron ( $udd$ ) decays into the proton ( $udu$ ) by emitting an electron and an associated antineutrino via a $W^-$ massive vector boson. (b) Neutron decay at four fermion contact interaction level. . . . .	13
1.5	Sketch of the classification of neutrons based on energy scale along with the necessary steps taken to get ultracold neutrons (UCNs) from spallation neutrons. . . . .	23
2.1	Electron energy spectrum . . . . .	31
2.2	Proton energy spectrum . . . . .	32
2.3	Antineutrino energy spectrum . . . . .	33
3.1	The shaded area is the region of the integral for $Q_{++}$ under the constraint $r < 1$ . . . . .	36
3.2	The shaded area is the region of the integral for $Q_{++}$ under the constraint $r > 1$ . . . . .	37
3.3	The shaded areas I, II and III are the three regions of the integral for $Q_{+-}$ under the constraint $r > 1$ . . . . .	39
3.4	The shaded areas I and IV are the regions of the integral for $Q_{+-}$ under the constraint $r < 1$ . . . . .	40
4.1	The UCNB experiment modifies the UCNA superconducting spectrometer (SCS) to include biasable detection systems and an open decay trap to determine the proton and electron directions. . . . .	51
4.2	The detector mount carries the detector, preamplifier electronics, liquid nitrogen lines, and allows for high voltage bias up to 30 kV. The inner stage is in vacuum and the outer stage is in air [3]. . . . .	55
4.3	Schematic diagram for the UCNB experimental setup [4]. . . . .	56
4.4	Schematic diagram for the UCNB simulation geometry. . . . .	57
5.1	Detailed setup for the UCNA experiment [5]. . . . .	63
5.2	Schematic of event types in UCNA . . . . .	64
5.3	The theoretical $Q_{ij}$ spectra. . . . .	65
5.4	(a) Illustration of $Q_{++}$ (b) Illustration of $Q_{+-}$ [6] . . . . .	65

5.5	Magnetic field profile along $z$ -axis. . . . .	68
5.6	Backscattering fraction (electron) as a function of the detector distance (magnetic field $B(z)$ ) from the decay trap. . . . .	69
5.7	Backscattering fraction (proton) as a function of the detector distance (magnetic field $B(z)$ ) from the decay trap. . . . .	69
5.8	Comparison of the total detected energy and the initial kinetic energy of electron. . . . .	70
5.9	Reconstructed $Q_{ij}$ spectra for the simulation with $1 \times 10^9$ events in which the bremsstrahlung effects are disabled. . . . .	71
5.10	The bremsstrahlung (photon) spectrum. The inset plot shows the distribution of the total detected electron kinetic energy (Sum KE) relative to its initial kinetic energy ( $T_{e,0}$ ). . . . .	72
5.11	Reconstructed $Q_{ij}$ spectra for the simulation with $1 \times 10^9$ events in which the bremsstrahlung effects are enabled. . . . .	73
5.12	One-sigma (68.3% CL) sensitivity of the asymmetry ratio $r_{pe}$ to $b_\nu$ for $1 \times 10^9$ events as a function of the lower edge of an analysis energy window. . . . .	75
5.13	One-sigma (68.3% CL) sensitivity for an extraction of $b_\nu$ from the integral asymmetry $\langle \alpha_x \rangle$ for $1 \times 10^9$ events as a function of the lower edge of an analysis energy window. The upper edge of the window is fixed at 700 keV. We again include the 0 keV lower threshold as a statistical reference point. . . . .	76
5.14	Sensitivity of a combined fit to $b$ and $b_\nu$ . . . . .	78

## Chapter 1 Introduction

The purpose of this dissertation work is to explain in detail the methods that can be used to extract the  $\beta$ -decay parameter  $B$  (neutrino asymmetry) from a realistic UCNB experiment using the Geant4 Simulation ToolKit. The first chapter starts with a brief introduction to the standard model formalism and the fundamental particles. It gives the detailed theory of  $\beta$ -decay and its measurable parameters. The end of this chapter includes the motivation for carrying out a precision measurement of  $B$  in free neutron  $\beta$ -decay and explores the sensitivity to beyond standard model (BSM) scalar and tensor interactions.

### 1.1 The Standard Model (SM)

The Standard Model (SM) is a framework that describes the fundamental building blocks, or the particles of the universe and their interactions. Since its inception in the 1970's, the SM formalism was developed and has been subject to various experimental tests. In the SM, the particles are described by the theoretical framework based on quantum field theory (QFT). According to QFT, every particle is an excitation of a parent field, which itself is an object that has different values at every location in space-time. These fields carry energy and momentum. Every particle excitation of a particular field is identical. Consequently, SM describes the strong, weak and electromagnetic interactions in terms of fields in space-time. It is the unified theory of Electro-Weak Interaction and QCD (Quantum Chromodynamics). The unified electromagnetic and weak interaction (Electro-Weak Interaction) is described by gauge group  $SU(2)_L \times U(1)_Y$ , while QCD is a non-abelian gauge theory, with symmetry group  $SU(3)_C$ . Hence, the corresponding gauge group of the SM is  $SU(3)_C \times SU(2)_L \times U(1)_Y$  which is a fundamental symmetry group of nature [7]. Although, at present, it is the most successful theory, it is not sufficient to account for all observed phenomena in particle physics. As an example, it can not explain the matter and anti-matter asymmetry (baryon asymmetry) of the universe [8]. Another drawback of this formalism is failure to unify the gravitational interaction within its symmetry group. Also, there are open questions on the origin of CP violation and the existence of a number of free parameters.

#### 1.1.1 Fundamental Particles in the SM

In general, particles are broadly classified according to their spin states. The particles with half-integral spin are called fermions and those with integral spin are called bosons. According to quantum mechanics, the wavefunctions for systems of bosons are symmetric under interchange of any pair of bosons, while those for fermions are antisymmetric under exchange. Suppose we have two particles located at positions

$x_1$  and  $x_2$ . A wave function  $\psi(x_1, x_2)$  of the particles is symmetric if

$$\psi(x_1, x_2) = \psi(x_2, x_1)$$

and antisymmetric if

$$\psi(x_1, x_2) = -\psi(x_2, x_1)$$

The main consequence of antisymmetry is that the probability of finding two fermions with identical spin occupying the same location in space is identically zero. This is the Pauli Exclusion Principle. Unlike fermions, bosons have no such constraints and any number of bosons can occupy the same space to form a state of matter called a Bose-Einstein condensate (states of zero momentum).

As shown in the Table 1.1, fundamental fermions according to the SM are *quarks*

Table 1.1: Quarks and Leptons

Generation	1	2	3
Quarks	$u$	$c$	$t$
	$d$	$s$	$b$
Leptons	$\nu_e$	$\nu_\mu$	$\nu_\tau$
	$\nu$	$\mu$	$\tau$

( $q$ ) and *leptons* ( $l$ ). The quarks comes in six *flavors* as *up*( $u$ ), *down*( $d$ ), *charm*( $c$ ), *strange*( $s$ ), *top* ( $t$ ), and *bottom* ( $b$ ). The masses of  $u$  and  $d$  quarks are about  $2.2 \text{ MeV}/c^2$  and  $4.7 \text{ MeV}/c^2$  respectively. Similarly, other four quarks,  $c$ ,  $s$ ,  $t$  and  $b$  have their masses nearly  $1.28 \text{ GeV}/c^2$ ,  $0.096 \text{ GeV}/c^2$ ,  $173.1 \text{ GeV}/c^2$  and  $4.18 \text{ GeV}/c^2$  respectively [9]. The quarks in the top row of the table are called up-type quarks, and each has electric charge,  $Q = +\frac{2}{3}e$  ( $e$  denotes the magnitude of the electron charge,  $e = 1.6 \times 10^{-19} \text{ C}$ ). The second row are called down-type quarks and have charge,  $Q = -\frac{1}{3}e$ . Quarks do not exist independently but they exist as hadrons (particles that interact by the strong interaction). Mesons are a bound states of a quark-antiquark pair ( $q\bar{q}$ ). The heavier hadrons are called baryons and made up of three quarks ( $qqq$ ). Mesons are bosons, while the baryons are fermions. The color part of state functions of baryons ( $qqq$ ) is an  $SU(3)$  singlet, a completely antisymmetric state of three color charges. Consequently, a baryon ( $qqq$ ) has state function which is antisymmetric under the interchange of any two equal-mass quarks ( $u$  and  $d$  quarks in the limit of isospin symmetry) [9].

Similarly, there are six known lepton flavors which are either electrically charged or neutral. The charged leptons are the electron ( $e$ ), *muon* ( $\mu$ ), and *tau* ( $\tau$ ), and each has electric charge,  $Q = -e$ . These particles appear at the bottom of the table. The mass of the electron is  $\sim 0.511 \text{ MeV}/c^2$  and that of the muon is  $\sim 105.65 \text{ MeV}/c^2$ . The heaviest of all leptons is the *tau* lepton and has mass  $\sim 1776.86 \text{ MeV}/c^2$  [9]. Each charged lepton has an associated electrically neutral ( $Q = 0$ ) particle called the *neutrino*( $\nu$ ) and appears on the third row of the particle table (Table 1.1). The columns of the table are groupings, typically known as generations. Hence, there are

three generations of quarks and leptons which are ordered according to the mass hierarchy. Even though *neutrinos*( $\nu$ ) fall in the three generations but their masses are insignificant compared to other particles. Nevertheless, neutrino oscillation experiments [10] shows that they have finite mass less than an  $\sim eV$  and the mass ordering is maintained in three generations.

Apart from this, there are mediating particles that mediate the interactions among the different fermions. These are vector and scalar bosons. The vector bosons are spin-1 particles and consist of the photon ( $\gamma$ ), gluon ( $g$ ), and  $W$  ( $W^+$ ,  $W^-$  and  $Z$ ) bosons. Photons are the particles responsible for the electromagnetic force and interact with all electrically charged particles. Gluons, on the other hand, bind quarks together to make hadrons and mediate the strong force. The  $W$  and  $Z$  bosons mediate a wide variety of interactions between and among quarks and leptons and are carriers of the weak force. These bosons were discovered in 1983 by physicists at the Super Proton Synchrotron located at CERN [11]. The photon, gluon, and  $Z$  bosons are electrically neutral ( $Q = 0$ ), while the  $W$  boson has electric charge ( $Q = \pm e$ ). The photon and gluon are also massless particles, while the  $W$  and  $Z$  bosons are each quite massive, having mass around  $80.0 GeV/c^2$  and  $91.0 GeV/c^2$  respectively [12]. As a result, the  $W$  and  $Z$  bosons have relatively short lifetimes ( $\approx 3 \times 10^{-25} s$ ) and mediate interactions only over short distances. As of today's experimental limitations on particle physics, we know there exists one scalar boson called the Higgs boson, which was discovered in proton-proton collisions with the ATLAS detector at the LHC [13] in 2012. It is electrically neutral and massive, with mass about  $125 GeV/c^2$ . This boson is an excitation of the Higgs field, and plays a crucial role in imparting mass to all fermions and the  $W$  and  $Z$  bosons. Hence, there are 12 fundamental fermions and 4 fundamental bosons in the SM of elementary particles.

### 1.1.2 Neutron

After a brief description of the fundamental particles in SM, let us take a moment to give a very brief introduction of the neutron, a particle discovered by Chadwick in 1932 [14]. Since, most of my dissertation work is based on neutron  $\beta$ -decay, it is important to look at some properties of the neutron. Neutron is a baryon composed of three quarks ( one  $u$  and two  $d$ 's ) from the first generation. It is electrically neutral and has mass  $\sim 1 GeV/c^2$ . It has small electric dipole moment (EDM),  $|d_n| < 1.8 \times 10^{-26} e cm$  (90% *C.L.*) ( [15], [16], [17]). The existence of a non-zero neutron EDM would be the direct evidence of physics violating time-reversal symmetry ( [18], [19], [20], [21], [22]). The proton is also a baryon and is composed of three quarks (two  $u$ 's and one  $d$ ) with net charge,  $Q = +e$ . The proton and neutron, also called a nucleon have comparable masses.

### 1.1.3 Neutron $\beta$ -decay

This dissertation work is mostly centered around the decay of free neutrons, a semi-leptonic process (where leptons and quarks are involved) of the weak interaction,

which violates parity. The neutron is a suitable baryon for such processes, because studying neutron decay has the advantage of lacking a nuclear structure, compared to nuclear  $\beta$ -decay, where the neutron is bound to the nucleus<sup>1</sup>. A free neutron is unstable with an average life time of about  $879.4 \pm 0.6$  s [23]. Consequently, it decays to a proton ( $p$ ) and an electron ( $e$ ) with the emission of an anti-neutrino ( $\bar{\nu}_e$ ).

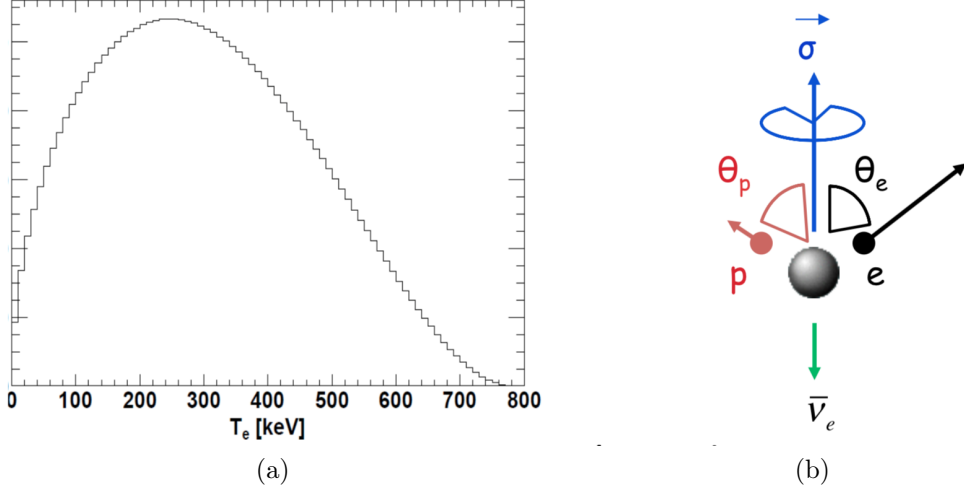


Figure 1.1: (a)  $\beta$ -decay spectrum. (b) The decay of a free neutron giving three particles, proton, electron and associated antineutrino and their direction relative to the neutron spin.

In the decay of a free polarized neutron (Figure 1.1 (b)), the spin of the neutron is correlated with the momenta of the decaying products. Therefore, a precise measurement of these correlation coefficients allows detailed tests of the Standard Model (SM) and physics beyond the Standard Model (BSM) ([24], [25], [26]). The energy spectrum is continuous from the conservation law of energy-momentum for the three-body  $\beta$ -decay. The endpoint kinetic energy of electron ( $T_e$ ) is about  $782$  keV (see Figure 1.1 (a)) and the maximum kinetic energy of proton ( $T_p$ ) is about  $751$  eV.

## 1.2 Fermi Theory of $\beta$ -Decay

In the early 1930's, there were many attempts made to explain nuclear  $\beta$ -decay which was assumed to be a two-body decay process. The  $\beta$ -spectrum for the two-body decay (parent nucleus decaying to a daughter nucleus with emission of  $\beta$ -rays) should give a discrete energy spectrum, but it is continuous. The difference in the masses of the decaying nucleus and the products did not add up to the energy averaged over the whole of the  $\beta$ -spectrum. At this point, Wolfgang Pauli (1930) took

<sup>1</sup>In a nuclear  $\beta$ -decay, it is not easy to study the correlations of momenta of various particle emitted due to many body and finite size effects.



Table 1.2: Bilinear Invariants in Dirac Theory

Operators	Parity Transformation	Number of Nonzero Elements
$\bar{\Psi}\Psi$	Scalar ( $S$ )	1
$\bar{\Psi}\gamma^\mu\Psi$	Vector ( $V$ )	4
$\bar{\Psi}\sigma^{\mu\nu}\Psi$	Tensor ( $T$ )	6
$\bar{\Psi}\gamma^\mu\gamma_5\Psi$	Axial Vector ( $A$ )	4
$\bar{\Psi}\gamma_5\Psi$	Pseudoscalar ( $P$ )	1

a bold step and suggested a three-body decay process to explain the  $\beta$ -spectrum, introducing a third particle based on the energy-momentum conservation laws. This ‘third particle’ must have negligible mass, carry an intrinsic spin momentum  $\frac{1}{2}\hbar$  and at some point be capable of carrying all of the electron energy. It must not interact electromagnetically, so it must be an electrically neutral particle. The introduction of this particle explained the continuous energy spectrum of nuclear  $\beta$ -decay. Soon after the discovery of the neutron by Chadwick in 1932 [14], this particle was named ‘neutrino’ by Fermi in reference to the neutral particle (neutron) that resides inside the nucleus of an atom. Fermi developed the theory of  $\beta$ -decay based on the Pauli

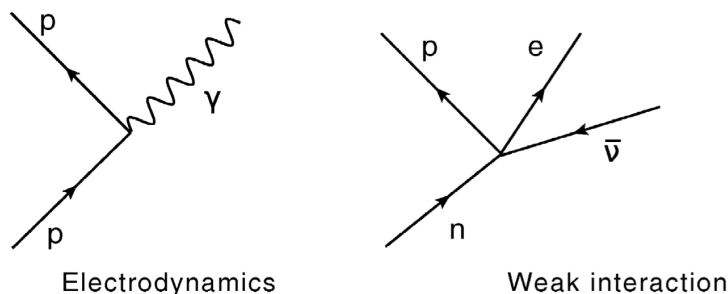


Figure 1.2: Fermi’s analogy of four-fermion interaction to the electrostatics [1].

neutrino hypothesis<sup>2</sup>. Analogous to the vector interaction in electrostatics (see Figure 1.2), Fermi considered the Hamiltonian [27] for  $\beta$ -decay as a vector-vector interaction given by

$$\mathcal{H}^\beta(x) = C_V \bar{\psi}_p(x) \gamma_\mu \psi_n(x) \bar{\psi}_e(x) \gamma^\mu \psi_{\bar{\nu}}(x), \quad (1.2)$$

where  $C_V$  is the vector coupling constant and  $\psi(x)$ ’s are the fields (Dirac fields) associated with each particle. The quantity  $\bar{\psi}_p(x) \gamma_\mu \psi_n(x)$  is a vector current and the Hamiltonian involves a current  $\times$  current interaction. In the system of units with  $\hbar = 1$  and  $c = 1$ , the charge of an electron is dimensionless and the coupling constant  $C_V$  has a dimension of  $M^{-2}$  making it an effective coupling constant (Fermi Constant

<sup>2</sup>At that time the neutrino was only a hypothetical particle introduced to explain the continuous energy spectrum in  $\beta$ -decay using the energy-momentum conservation laws. It was only in 1954 that neutrinos were "discovered" when Cowan and Reines detected the emission of antineutrinos from the nuclear reactor. Reines received the Nobel Prize in 1995 for this discovery.

$G_F$ ). The form of the Hamiltonian proposed by Fermi is not sufficient to explain the different types of nuclear  $\beta$ -decay and needs to be modified. In this Hamiltonian, four fermions interact at one vertex, and all the vector currents are calculated at the same point in space-time without consideration of force carriers. This is a four-fermion contact interaction vertex governed by one coupling constant ( $G_F$ ). The theory successfully explains the continuous  $\beta$ -spectrum of the nuclei in which there is no change in the spin angular momentum ( $\Delta S = 0$ ) and parity due to the vector  $\times$  vector nature of the Fermi interaction. The nuclear  $\beta$ -decays involving the change in spin angular momentum and parity are not allowed transitions according to this form of Hamiltonian. In 1936, Gamow and Teller [28] predicted the spins of the decay products of the  $^{233}\text{Th}$  nucleus accurately, in which they showed that the current  $\times$  current interaction is equivalent to an axial vector ( $A$ ) in the Fermi Hamiltonian. Hence, the Fermi Hamiltonian given by Eqn.1.2 required some modification to include all the possible bilinear covariants (Lorentz invariants) terms in Dirac theory. The generalized Fermi Hamiltonian becomes,

$$\mathcal{H}^\beta(x) = \sum_{i=S,V,T,A,P} C_i \bar{\psi}_p(x) O_i \psi_n(x) \bar{\psi}_e(x) O^i \psi_{\bar{\nu}}(x), \quad (1.3)$$

where,  $O^i \equiv (1, \gamma^\mu, \sigma^{\mu\nu}, \gamma^\mu \gamma^5, \gamma^5)$ . The coefficients,  $C_i \equiv (C_S, C_V, C_T, C_A, C_P)$  are the coupling constants corresponding to each current in the Hamiltonian. More explicitly, the Hamiltonian can be written as,

$$\begin{aligned} \mathcal{H}^\beta(x) = & C_S \bar{\psi}_p(x) \psi_n(x) \bar{\psi}_e(x) \psi_{\bar{\nu}}(x) + C_V \bar{\psi}_p(x) \gamma_\mu \psi_n(x) \bar{\psi}_e(x) \gamma^\mu \psi_{\bar{\nu}}(x) \\ & + C_T \bar{\psi}_p(x) \sigma_{\mu\nu} \psi_n(x) \bar{\psi}_e(x) \sigma^{\mu\nu} \psi_{\bar{\nu}}(x) + C_A \bar{\psi}_p(x) \gamma_\mu \gamma^5 \psi_n(x) \bar{\psi}_e(x) \gamma^\mu \gamma^5 \psi_{\bar{\nu}}(x) \\ & + C_P \bar{\psi}_p(x) \gamma^5 \psi_n(x) \bar{\psi}_e(x) \gamma^5 \psi_{\bar{\nu}}(x) \end{aligned} \quad (1.4)$$

This is a typical Hamiltonian which includes the currents of the forms  $S \times S$ ,  $V \times V$ ,  $T \times T$ ,  $A \times A$  and  $P \times P$  and there is no mixing of different currents. This is still a current  $\times$  current theory similar to Eqn. 1.2 except with all bilinear invariants taken into account.

### 1.2.1 $\beta$ - Decay Selection Rules

When the nuclei undergo  $\beta$ -decay, most contributions come from transitions in which electron and antineutrino are produced in  $S$ -states with orbital momenta equal to zero. It follows from the vector nature of the Fermi Hamiltonian that the spins and parities of the initial and final nuclei must be equal for allowed transitions. This is called the Fermi selection rule, i.e

$$\begin{aligned} \Delta J &= J_f - J_i = 0, \\ \Delta \pi &= \pi_f - \pi_i = 0, \end{aligned}$$

where  $(J_i, \pi_i)$  and  $(J_f, \pi_f)$  are the spin-parity of the initial and final nucleus. Thus, under the Fermi selection rule, the electron and antineutrino are produced in a singlet state with the net spin,  $\Delta S = 0$  which corresponds to scalar ( $S$ ) and vector ( $V$ )

interactions.

If the electron and antineutrino are produced in the triplet state ( $S = 1$ ) in this case for the allowed transition the total angular momentum of the final state is equal to  $J_f = J_i \pm 1$  or  $J_f = J_i$  (for  $J_i = 0$  the total final angular momentum is equal to 1). This is called the Gamow-Teller selection rule [28], i.e,

$$\begin{aligned}\Delta J &= J_f - J_i = \pm 1, 0, \\ \Delta \pi &= \pi_f - \pi_i = 0,\end{aligned}$$

and the transition ( $0^+ \rightarrow 0^+$ ) is forbidden. This transition corresponds to the axial vector ( $A$ ) and tensor ( $T$ ) interactions. Experimentally, all the nuclear  $\beta$ -decays were found to satisfy the Fermi and Gamow-Teller (GT) transition rules. Hence, the Fermi Hamiltonian for the  $\beta$ -decay given by Eqn. 1.4 must be modified to account for the observed interactions.

### 1.2.2 Parity Violation in Weak Interaction

The fundamental discrete symmetries in the Standard Model are parity (P), charge conjugation (C) and time-reversal (T). In the early 1950's, these symmetries were assumed to be separately conserved in all the interactions. Consequently, the two particles  $\theta^+$  and  $\tau^+$  were considered as distinct particles as they decay to give products (two and three pions respectively), with opposite parities.

$$\begin{aligned}\theta^+ &= \pi^+ + \pi^0 \\ \tau^+ &= \pi^+ + \pi^+ + \pi^-\end{aligned}$$

If parity is strictly conserved, then the two particles must be different. But, several experiments showed that they have same mass and same lifetimes. It was only in 1956, Lee and Yang [29] proposed that there is no evidence of parity being conserved in weak interactions. As a result, the ( $\tau - \theta$ ) puzzle was solved by allowing parity violation in the two decay modes of the same particle,  $K^+$  meson. In the general Fermi theory (see Eqn. 1.4), all the couplings are of types vector  $\times$  vector and there are not any admixture terms. This means that, each term in this Hamiltonian transforms as a scalar under the parity operation. As an example, if we consider a term with pseudoscalar ( $\psi\gamma^\mu\gamma^5\psi$ ) current, the parity operation gives,  $-\psi\gamma^\mu\gamma^5\psi$  and the product of these two terms transforms as a scalar. Overall, the Hamiltonian is strictly parity conserving and not useful as it does not take into account parity violation in the weak interaction. Hence, Lee and Yang [29] modified the Fermi Hamiltonian by writing down the five usual types of currents and in addition to these they introduced the five types of currents that conserved angular momentum but not parity. If parity is not conserved in  $\beta$ -decay, the most general form of the Hamiltonian according to them

can be written as,

$$\begin{aligned}
\mathcal{H}^\beta(x) = & \bar{\psi}_p(x)\psi_n(x)\left(C_S\bar{\psi}_e(x)\psi_{\bar{\nu}}(x) + C'_S\bar{\psi}_e(x)\gamma^5\psi_{\bar{\nu}}(x)\right) \\
& + \bar{\psi}_p(x)\gamma_\mu\psi_n(x)\left(C_V\bar{\psi}_e(x)\gamma^\mu\psi_{\bar{\nu}}(x) + C'_V\bar{\psi}_e(x)\gamma^\mu\gamma^5\psi_{\bar{\nu}}(x)\right) \\
& + \bar{\psi}_p(x)\sigma_{\mu\nu}\psi_n(x)\left(C_T\bar{\psi}_e(x)\sigma^{\mu\nu}\psi_{\bar{\nu}}(x) + C'_T\bar{\psi}_e(x)\sigma^{\mu\nu}\gamma^5\psi_{\bar{\nu}}(x)\right) \\
& + \bar{\psi}_p(x)\gamma_\mu\gamma^5\psi_n(x)\left(C_A\bar{\psi}_e(x)\gamma^\mu\gamma^5\psi_{\bar{\nu}}(x) + C'_A\bar{\psi}_e(x)\gamma^\mu\psi_{\bar{\nu}}(x)\right) \\
& + \bar{\psi}_p(x)\gamma_\mu\gamma^5\psi_n(x)\left(C_P\bar{\psi}_e(x)\gamma^5\psi_{\bar{\nu}}(x) + C'_P\bar{\psi}_e(x)\psi_{\bar{\nu}}(x)\right) + h.c. \quad (1.5)
\end{aligned}$$

All of the coefficients  $C_i$  and  $C'_i$  are real if time-reversal symmetry is preserved in  $\beta$ -decay (see Table 1.3). This form of Hamiltonian still obeys the selection rules

Table 1.3: Discrete Symmetries and  $C_i, C'_i$

Symmetry	Conditions for Violation
$C$	$(Re(C_i) \neq 0 \text{ and } Re(C'_i) \neq 0) \text{ or } (Im(C_i) \neq 0 \text{ and } Im(C'_i) \neq 0)$
$P$	$C_i \neq 0 \text{ and } C'_i \neq 0$
$T$	$Im(C_i/C_j) \neq 0 \text{ or } Im(C'_i/C'_j) \neq 0$

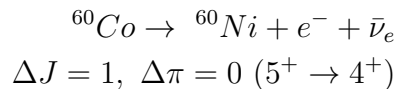
(both Fermi and Gamow-Teller) because all the observables are proportional to  $|C_i|^2$  and  $|C'_i|^2$  (there is no interference between parity-conserving and parity-violating parts). The interference term  $C_i C'_i$  occurs only when a pseudoscalar is formed from the experimentally measured quantities such as momentum and the spin ( $C_i C'_i \vec{p} \cdot \vec{\sigma}$ ). The presence of such a pseudoscalar term in the Hamiltonian is responsible for parity violation. Lee and Yang worked out the number of possible ways to quantify parity violation in the weak interactions. They also suggested polarized neutron  $\beta$ -decay as a possible candidate to directly observe parity violation. The angular distribution of emitted  $\beta$ -particles in such a decay is given by

$$I(\theta)d\theta \propto (1 + \alpha \cos(\theta))d\theta, \quad (1.6)$$

They showed that the asymmetry  $\alpha$  is proportional to pseudoscalar ( $C_i C'_i$ ) and if  $\alpha \neq 0$ , then it would prove parity violation in the weak interaction. Hence, one should design an experiment that would give the intensity distribution as a function of angle ( $\theta$ ) between the polarized decaying nucleus and the outgoing  $\beta$ -particle.

### 1.2.3 First Experiment on Parity Violation

Soon after the proposed experiments on parity violation in  $\beta$ -decay and other weak interactions by Lee and Yang [29], Wu et al. worked out a setup to test it. They considered the  $\beta$ -decay of polarized  $^{60}\text{Co}$  nucleus (a decay allowed by the Gamow-Teller selection rule) for their experiment to study the potential asymmetry in the  $\beta$ -ray emission.



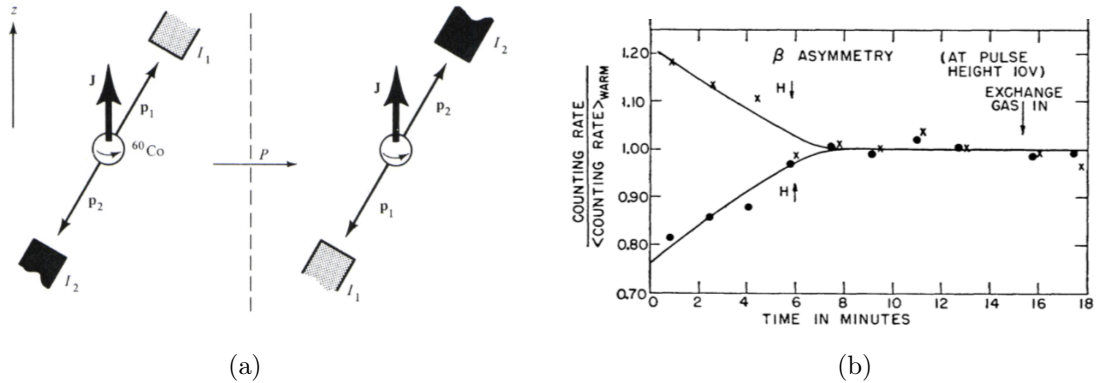
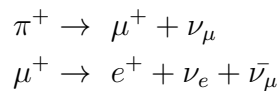


Figure 1.3: (a) Schematic diagram of Wu's experimental set up. (b) Data from Wu et al. experiment [2] measuring the correlation between the emitted direction of the electron from the decay of polarized  $^{60}\text{Co}$ .

The experiment was designed so that  $^{60}\text{Co}$  nuclei initially polarized in either  $\pm z$  directions are allowed to decay in a cryostat and the intensities of the electron beam emitted at angles  $\theta$  and  $(\pi - \theta)$  were measured (see Figure 1.3 (a)). In Figure 1.3 (b), the results of Wu et al.'s actual experiment [2] is shown. The plot shows, two curves of normalized counting rates when the spin of the  $^{60}\text{Co}$  nuclei were oriented anti-parallel with respect to the detector. The two curves indicate the parity violation because the electrons are emitted preferentially in the direction opposite to the spin of the nucleus. The spin relaxation time of  $^{60}\text{Co}$  nuclei exactly coincides with the disappearance of the splitting of the two curves. These results prove unequivocally, the violation of parity in  $\beta$ -decay which have pseudoscalar ( $\vec{p}\cdot\vec{\sigma}$ ), tensor ( $T$ ) and axial vector ( $A$ ) terms in the Hamiltonian. After this pioneering experiment by Wu et al. in the same year, Richard, Lederman and Weinrich [30] confirmed the violation of parity from the experiment proposed by Lee and Yang. In this experiment, they studied the successive decay of  $\pi^+$  mesons,



and measured the possibility of a non-zero correlation between polarization of the subsequent decay products,  $\mu^+$  and the electron momentum. The asymmetry between the decay of polarized muons and electrons was determined in the similar way as Cobalt  $\beta$ -decay. They found a non-zero asymmetry value which is the absolute proof of the parity violation in weak interactions. These were the most important experiments which triggered the rapid progress in understanding of the underlying nature of the weak interactions.

#### 1.2.4 Two-Component Neutrino Theory

Soon after the discovery of parity violation in the  $\beta$ -decay process, Landau [31], Salem [32], Lee and Yang [33] and Marshak [34] made enormous progress in un-

derstanding the theory of weak interactions. They proposed the theory of the two-component neutrino. This theory is based on the assumption that the neutrino is a massless particle and only left handed neutrinos appear in the Hamiltonian. As we now know that neutrinos have negligibly small mass (from neutrino oscillation experiments) different from zero and the theory is still incomplete. They came to an idea of a possible connection of the violation of parity observed in  $\beta$ -decay and other weak processes involving neutrinos. The neutrino field  $\psi_\nu(x)$  satisfies the Dirac equation,

$$(i\gamma^\mu\partial_\mu - m_\nu)\psi_\nu(x) = 0 \quad (1.7)$$

where,  $m_\nu$  is the mass of the neutrino. The neutrino field can be expressed as a sum of the two helicity states as

$$\psi_\nu(x) = \psi_\nu^L(x) + \psi_\nu^R(x), \quad (1.8)$$

where,  $\psi_\nu^L(x) = \frac{1}{2}(1 - \gamma_5)\psi_\nu(x)$  and  $\psi_\nu^R(x) = \frac{1}{2}(1 + \gamma_5)\psi_\nu(x)$ . Substituting these helicity states into the Dirac equation and letting the mass of the neutrino be zero ( $m_\nu = 0$ ), the coupled equation becomes decoupled in the two states as  $\psi_\nu^L(x)$  or  $\psi_\nu^R(x)$  given by

$$i\gamma^\mu\partial_\mu\psi_\nu^{L,R}(x) = 0 \quad (1.9)$$

Hence, for  $m_\nu = 0$ , the neutrino field can either be left-handed ( $\psi_\nu^L(x)$ ) or right-handed ( $\psi_\nu^R(x)$ ). Also under parity,  $\psi_\nu(x)$  transforms as

$$P\psi_\nu(t, \vec{x})P = \eta_a\gamma^0\psi_\nu(t, -\vec{x}) \quad (1.10)$$

where  $\eta_a$  is some phase factor which is restricted by the condition that two successive applications of the parity operator should retrieve observables to their original values. This requires that the phase factor must satisfy  $\eta_a^2 = \pm 1$ . Finally, under the parity operation, the two neutrino states transform as

$$P\psi_\nu^{L,R}(x)P = \eta_a\gamma^0\psi_\nu^{R,L}(x) \quad (1.11)$$

Thus, parity is maximally violated in the process in which neutrinos are present and only helicity states (left or right-handed neutrinos) take part in the weak interactions. In 1958, Goldhaber and his collaborators [35], confirmed the two-component neutrino theory and also measured the helicity of the emitted neutrino<sup>3</sup>. They found that, only the left handed neutrinos take part in the weak interaction. This led to the formulation of the universal  $V - A$  interaction in weak processes involving only left-handed fermions.

---

<sup>3</sup>The neutrino helicity was obtained from the measurement of the circular polarization of  $\gamma$ 's produced in the chain of reactions

$$e^- + {}^{152}\text{Eu} \rightarrow \nu + {}^{152}\text{Sm}^* \rightarrow {}^{152}\text{Sm} + \gamma$$

The circular polarization of  $\gamma$ 's emitted in the direction of the  ${}^{152}\text{Sm}^*$  momentum is equal to the helicity of the neutrino ( [35], [36]).

### 1.2.5 $V - A$ Interaction

After the discovery of parity violation by T.D Lee , Yang and Wu et al. [29], it was found that these involve only the left-handed components of all fermion fields including the massless neutrino field in the Hamiltonian of the weak interaction. These left-handed fermions can be expressed as

$$\psi^L(x) = \frac{1}{2} (1 - \gamma_5) \psi(x) = a\psi(x) \quad (1.12)$$

where  $a = \frac{1}{2} (1 - \gamma_5)$  is a projection operator and  $\gamma_5$  is a Dirac matrix. Soon after the left-handedness of the fermion fields was proposed [29], Feynmann and Gell-Mann developed a theory of weak interactions. They modified the weak interaction Hamiltonian developed by Fermi [27] to a parity non-conserving one. The most general Hamiltonian according to Fermi [25] for  $\beta$ -decay (Ref. Eqn. 1.2) is given by

$$\mathcal{H}_T^\beta(x) = \sum_i G_i \bar{\psi}_p^L(x) O_i \psi_n^L(x) \bar{\psi}_e^L(x) O_i^i \psi_{\bar{\nu}}^L(x) + h.c. \quad (1.13)$$

where the  $G_i$ 's are coupling constants to be discussed, the operators  $O_i$ 's are some Lorentz invariant quantities and  $\psi_p(x)$ ,  $\psi_n(x)$ ,  $\psi_e(x)$  and  $\psi_{\bar{\nu}}(x)$  are proton, neutron, electron and antineutrino fields respectively. It is clear that the Hamiltonian contains only chiral fermionic fields. In this Hamiltonian, each bilinear term can be expressed as

$$\bar{\psi}_p^L(x) O_i \psi_n^L(x) = [\bar{\psi}_p(x) a] O_i [a \psi_n(x)] = \bar{\psi}_p(x) [a O_i a] \bar{\psi}_n(x) = \bar{\psi}_p(x) [O_i'] \psi_n(x)$$

where  $O_i' = \bar{a} O_i a$  is the chirality projected operator. In the case of  $QED$ , the operator  $O_i'$  is simply given by a vector  $\gamma^\mu$ , whereas in the weak interaction, the matrix elements are restricted by left-handed fermions and the effective currents are to be evaluated for all the possible bilinear covariants listed in the Table 1.2. Using the properties of the projection operators and replacing  $O_i$  by  $S$ ,  $V$ ,  $A$ ,  $P$  and  $T$  operators, the effective coupling  $O_i'$  can be calculated (Ref. Appendix A.2). For vector ( $V$ ) and axial vector ( $A$ ) respectively, we get

$$O_i' = \bar{a} O_i a = \gamma^\mu a \quad (1.14)$$

and

$$O_i' = \bar{a} O_i a = -\gamma^\mu a \quad (1.15)$$

We see that for operators  $S$ ,  $P$  and  $T$ , the contributions to the Hamiltonian are zero. The effective current is nonzero only for  $V$  and  $A$  operators. The effective interaction Hamiltonian of the  $\beta$ -decay becomes

$$\begin{aligned} \mathcal{H}_T^\beta(x) &= \frac{G_F}{\sqrt{2}} 4 \bar{\psi}_p^L(x) \gamma_\mu \psi_n^L(x) \bar{\psi}_e^L(x) \gamma^\mu \psi_{\bar{\nu}}^L(x) + h.c.. \\ &= \frac{G_F}{\sqrt{2}} \bar{\psi}_p(x) \gamma_\mu (1 - \gamma_5) \psi_n(x) \bar{\psi}_e(x) \gamma^\mu (1 - \gamma_5) \psi_{\bar{\nu}}(x) + h.c.. \end{aligned} \quad (1.16)$$

where  $G_F$  is the Fermi constant. The numerical factors in the Hamiltonian are chosen to make the expression analogous to the four-fermion contact interaction so that it has only one universal coupling constant  $G_F$  [37]. Thus, the charge-changing ( $CC$ ) weak interaction involves only ( $V - A$ ) currents. The fact that only chiral fermions take part in the weak interaction insists that only  $V - A$  currents exist and the Hamiltonian does not conserve parity. The Eqn. 1.16 can be written as

$$\mathcal{H}_I^\beta(x) = \frac{G_F}{\sqrt{2}} J_\mu L^\mu + h.c.. \quad (1.17)$$

where,  $J_\mu = \bar{\psi}_p(x)\gamma_\mu(1 - \gamma_5)\psi_n(x)$  and  $L^\mu = \bar{\psi}_e(x)\gamma^\mu(1 - \gamma_5)\psi_{\bar{\nu}}(x)$  are called hadronic and leptonic currents respectively.

### 1.2.6 Propagator

In 1935, Yukawa made his first attempt to explain the nature of nuclear forces based on meson exchange between the nucleons <sup>4</sup> [38]. On the basis of his theory, the weak interaction is mediated by an exchange of a massive boson between the two involved currents at different points in space-time. When a free neutron decays at the quark level, only one down ( $d$ ) quark changes flavor to up quark ( $u$ ) while the other two quarks (spectator quarks) do not change flavor ( see Figure 1.4 (a) for Feynman diagram). The interaction from quark vertex to the lepton vertex is mediated by the vector boson ( $W^-$ ). From the view point of QFT, the propagator is given by

$$D_{\mu\nu}(q^2) = \frac{-i}{q^2 - M_W^2} \left[ g_{\mu\nu} - \frac{q_\mu q_\nu}{M_W^2} \right] \quad (1.18)$$

where,  $g_{\mu\nu}$  is a metric tensor,  $M_W$  is the mass of the virtual  $W^-$  boson and  $q$  is the momentum transfer. According to this formalism, in the first step, one of the  $d$  quarks of the neutron emits a virtual  $W^-$  boson and itself transforms to a  $u$  quark. Next, the virtual boson propagates from the vertex formed by an up quark ( $u$ ) and a down quark ( $d$ ) to the weak vertex and subsequently decays to an electron and an antineutrino.

The currents are calculated at two different points in space-time. The currents are still a  $V - A$  type, but vector and axial components in the hadronic current have different coupling constants than the corresponding leptonic current at the lepton vertex. The mass of the  $W^-$  boson is about  $80 \text{ GeV}$  and the momentum transfer  $q$  is of the order  $1 \text{ MeV}$  so in the limit of low momentum transfer ( $q^2 \rightarrow 0$ ), the propagator reduces to,

$$D_{\mu\nu} = \frac{ig_{\mu\nu}}{M_W^2} \quad (1.19)$$

Thus, in the limit of large boson mass and low momentum transfer, the interaction reduces to an effective four-fermion interaction (( see Figure 1.4 (b)). From this point of view, Fermi theory is valid at low energy and is only an approximation. So, by

---

<sup>4</sup>At that time, neutrons and proton were considered as fundamental particles.



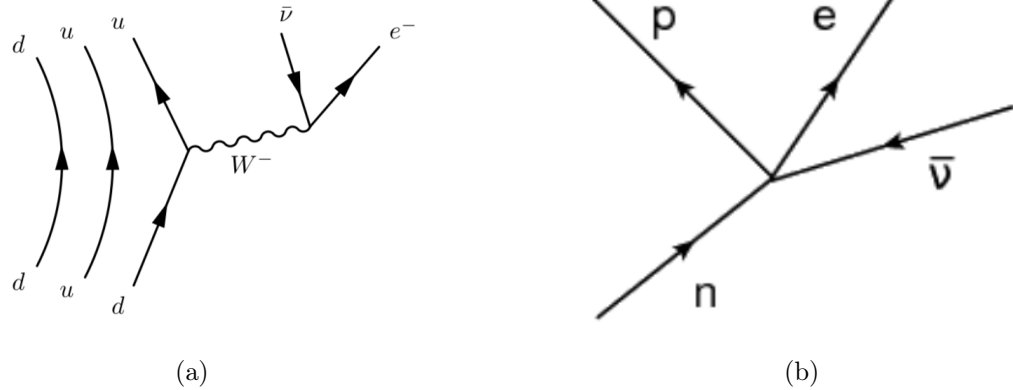


Figure 1.4: (a) Neutron decay at quark level with two spectator quarks. The neutron ( $udd$ ) decays into the proton ( $udu$ ) by emitting an electron and an associated antineutrino via a  $W^-$  massive vector boson. (b) Neutron decay at four fermion contact interaction level.

comparing the coupling strengths in the Hamiltonian given by Fermi theory, one can make a connection between Fermi constant  $G_F$  and weak coupling constant  $g_w$  by,

$$\frac{G_F}{\sqrt{2}} = \left[ \frac{g_w}{2\sqrt{2}M_W} \right]^2 (\hbar c)^3 \quad (1.20)$$

The experimental value of the Fermi constant measured from the decay of muons is  $G_F = 1.16637 \times 10^{-5} \text{ GeV}^{-2}$  in natural units [9]. The actual processes involved in the decay are quite complex and will be discussed in the next section.

### 1.3 Hadronic and Leptonic Currents

The interaction Hamiltonian for  $\beta$ -decay ( see Eqn. 1.17) , involves two currents at two vertices. The current  $J_\mu$  is the current evaluated at the quark vertex and the current  $L^\mu$  is evaluated at the lepton vertex in the decay process. These currents are of the type  $V - A$  and have the same vector and axial vector coupling constants. The only difference between them is, one corresponds to the hadron and other belongs to the lepton. In the case of the leptonic current, equal relative strengths of the vector and axial vector couplings allow parity to be violated maximally in the weak interaction. This is not exactly the case with the hadronic current as the neutron and proton are not fundamental particles. In the decay process of the neutron, only one quark changes flavor in the background of the other two quarks (spectator quarks, which do not take part in the interaction). Obviously, the relative strength of the couplings between the vector and axial vector are completely different.

$$\mathcal{H}_I^\beta(x) = \frac{G_F}{\sqrt{2}} \bar{\psi}_p(x) (g_V \gamma_\mu + g_A \gamma_\mu \gamma_5) \psi_n(x) \bar{\psi}_e(x) \gamma^\mu (1 - \gamma_5) \psi_{\bar{\nu}}(x) + h.c. \quad (1.21)$$

where, the new coupling constants  $g_V$  and  $g_A$  are called the vector and axial coupling constants. For the leptonic case,  $g_V = 1$  and  $g_A = -1$ , whereas in the case of hadronic interaction, these values are different from 1 and  $-1$  respectively. The presence of these couplings  $\lambda \equiv \frac{g_A}{g_V} \neq -1$  makes the hadronic part more complex. The complexity gets even more severe due to the nature of the weak interaction among the quarks through mixing matrix [39] which will be discussed later.

### 1.3.1 The CKM Matrix

The weak couplings between the three generations of quarks is not one to one, rather they interact as an admixture of quark mass states through a unitary rotation matrix. This idea of a mixing matrix was proposed by Kobayashi and Maskawa in order to take into account of the weak interactions in the quarks sector. It was an extension to the  $2 \times 2$  matrix proposed by Cabibbo in 1974. Cabibbo was able to explain the mixing of just two quarks responsible for modification of hadronic currents<sup>5</sup> in terms of the Cabibbo angle ( [40], [41] [39] ). The Cabibbo-Kobayashi-Maskawa (CKM) mixing matrix is defined as the transformation matrix from the weak to the mass eigenstates of three generation of quarks [42].

$$\begin{pmatrix} d' \\ s' \\ b' \end{pmatrix} = \begin{pmatrix} V_{ud} & V_{us} & V_{ub} \\ V_{cd} & V_{cs} & V_{cb} \\ V_{td} & V_{ts} & V_{tb} \end{pmatrix} \begin{pmatrix} d \\ s \\ b \end{pmatrix} = V_{CKM} \begin{pmatrix} d \\ s \\ b \end{pmatrix} \quad (1.22)$$

where the  $d$ ,  $s$ , and  $b$  denote the mass eigenstates and the primed are the weak eigenstates of the down, strange and bottom quarks respectively. The weak eigenstates of quarks exist as pairs given by,

$$\begin{pmatrix} u \\ d' \end{pmatrix}, \begin{pmatrix} c \\ s' \end{pmatrix}, \begin{pmatrix} t \\ b' \end{pmatrix}$$

The elements in the CKM matrix are in general complex numbers and are the fundamental parameters of the SM. The element of the CKM matrix,  $V_{ij}$ , determines the coupling of quark  $i$  to quark  $j$  and is responsible for modifying the hadronic currents. The unitarity condition of the CKM-matrix requires that the matrix elements satisfy the normalization condition

$$\begin{aligned} \sum_i V_{ij} V_{ik}^\dagger &= \delta_{jk} \\ \sum_j V_{ij} V_{kj}^\dagger &= \delta_{ik} \end{aligned} \quad (1.23)$$

and the orthogonality condition

$$\sum_k V_{ik} V_{kj}^\dagger = \sum_k V_{ik}^\dagger V_{kj} = 0 \quad (1.24)$$

---

<sup>5</sup>The Cabibbo-hadronic current is  $J^\mu = \cos \theta_C J^\mu(\Delta S = 0) + \sin \theta_C J^\mu(\Delta S = 1)$ ,  $\Delta S$  is the change in the strangeness of the quarks involved and  $\sin \theta_C \sim 0.225$ . At the quark level, this is equivalent to replacing the  $d$ -quark field by the linear combination of  $d$  and  $s$ -quark fields:  $d(x) \rightarrow d'(x) = \cos \theta_C d(x) + \sin \theta_C s(x)$ .

The Standard Model insists that the mixing matrix is strictly unitary but it itself does not provide any values of its elements [43]. These are to be determined experimentally. Hence, precise measurements of these parameters is important and has been done by studying the decay products of mesons and baryons that take into account the quarks from all three generations. As an example, the most accurate determination of  $V_{ud}$  comes from superallowed ( $0^+ \rightarrow 0^+$ ) nuclear  $\beta$ -decays, which are pure vector transitions [44]. It can also be obtained from the measurement of the neutron lifetime and from the measurement of the  $\beta$ -decay asymmetry of the free neutron ([45], [46]). William J. Marciano and Alberto Sirlin [47] used higher order perturbative QCD results to obtain the value of  $V_{ud} \sim 0.97377$ . Similarly, the other CKM-matrix elements are determined from the semileptonic decays of respective mesons. If we consider the first row of the mixing matrix, the unitary condition becomes

$$|V_{ud}|^2 + |V_{us}|^2 + |V_{ub}|^2 = 1 \quad (1.25)$$

Using the experimental values <sup>6</sup> of these matrix elements, the top-row unitarity condition gives

$$|V_{ud}|^2 + |V_{us}|^2 + |V_{ub}|^2 = 0.9994 \pm 0.0005. \quad (1.26)$$

So far, SM prediction on the properties of CKM matrix is not violated as the deviation from unity is quite small ( $<0.07\%$ ). Any deviation from unitarity would be an indication of physics beyond the Standard Model. It is clear that, most of the contributions to the unitarity come from  $V_{ud}$ . It has to be measured as precisely as possible compared to the other terms in the top-row of the mixing matrix.

The unitary matrix can be specified by four parameters<sup>7</sup>: three rotation angles  $\theta_{12}$ ,  $\theta_{13}$ ,  $\theta_{23}$  and one phase  $\delta$  as ([48], [49])

$$V_{CKM} = \begin{pmatrix} 1 & 0 & 0 \\ 0 & c_{23} & V_{23} \\ 0 & -s_{23} & c_{23} \end{pmatrix} \begin{pmatrix} c_{13} & 0 & s_{13}e^{-i\delta} \\ 0 & 1 & 0 \\ -s_{13}e^{-i\delta} & 0 & c_{13} \end{pmatrix} \begin{pmatrix} c_{12} & s_{12} & 0 \\ -s_{12} & c_{12} & 0 \\ 0 & 0 & 1 \end{pmatrix} \quad (1.27)$$

where  $c_{ij} = \cos(\theta_{ij})$  and  $s_{ij} = \sin(\theta_{ij})$ . The presence of phase  $\delta$  introduces  $CP$  violation with three quark generations. For  $CP$  invariance, the matrix  $V_{CKM}$  must be real ( $\delta = 0$ ). The  $CP$  violating phase can also be expressed in terms of the *Jarlskog* invariant  $J$  [50] defined by

$$J = s_1^2 s_2 s_3 c_1 c_2 c_3 \sin(\delta) \quad (1.28)$$

where,  $s_i = \sin(\theta_i)$  and  $c_i = \cos(\theta_i)$ . It is clear that  $CP$  ( $J = 0$ ) is conserved if any of the conditions:  $\theta_i = 0$ ,  $\theta_i = \pi/2$ ,  $\delta = 0$  and  $\delta = \pi$  is satisfied. With two generations

---

<sup>6</sup> $|V_{ud}| = 0.97420 \pm 0.00021$ ,  $|V_{us}| = 0.2243 \pm 0.0005$  and  $|V_{ub}| = (3.94 \pm 0.36) \times 10^{-3}$

<sup>7</sup>The matrix  $V_{CKM}$  can be specified by  $n^2$  parameters, one phase can be absorbed into the definition of each of the  $2n$  quarks minus the overall phase. So  $V_{CKM}$  has  $n^2 - (2n - 1) = (n - 1)^2$  parameters to be determined [43].

of quarks, the mixing matrix becomes,

$$V_{Cabibbo} = \begin{pmatrix} \cos(\theta_C) & \sin(\theta_C) \\ -\sin(\theta_C) & \cos(\theta_C) \end{pmatrix} \quad (1.29)$$

in which case there is only one parameter, the Cabibbo angle  $\theta_C$  and the  $2 \times 2$  matrix is always real and there is no  $CP$  violation [40]. The CKM matrix has another representation in terms of  $\lambda = \sin(\theta_C) \sim 0.225$  and the other three parameters, maintaining the unitarity condition up to third order in  $\lambda$  known as the Wolfenstein parameterization [51]. One of the major objectives of the present work is to obtain the value of the first element  $|V_{ud}|$  of the mixing matrix from precision measurements of the  $\beta$ -decay parameters of free neutrons.

### 1.3.2 Hadronic Matrix

The matrix element for  $\beta$ -decay is given by

$$\mathcal{M}_\beta = \frac{G_F V_{ud}}{\sqrt{2}} \langle \psi_p(p) | J^\mu | \psi_n(p) \rangle L_\mu \quad (1.30)$$

where,  $V_{ud}$  is the first element of the CKM matrix. The leptonic current  $L_\mu$  is given by

$$L_\mu = \bar{\psi}_e(p_e) \gamma_\mu (1 - \gamma_5) \psi_{\bar{\nu}}(p_\nu) \quad (1.31)$$

and the hadronic current can be expressed as

$$\langle \psi_p(p) | J^\mu | \psi_n(p) \rangle = V^\mu - A^\mu \quad (1.32)$$

where

$$V^\mu = \langle \psi_p(p) | \gamma^\mu | \psi_n(p) \rangle \quad (1.33)$$

and

$$A^\mu = \langle \psi_p(p) | \gamma^\mu \gamma_5 | \psi_n(p) \rangle \quad (1.34)$$

In general,  $V$  and  $A$  are complicated functions due to strong interaction effects. However, since  $V$  is one of the bilinear invariants in the Dirac theory, it must be constructed from all the possible vectors available. With the same argument,  $A$  must be constructed from all the axial vectors which are bilinear invariants. Since, all currents in  $J_\mu$  are constructed out of vectors and axial vectors, the matrix element for the  $\beta$ -decay is either scalar or pseudoscalar. According to S. Gardner and Zhang [52], applying the Lorentz and translational invariance, the nucleon weak current  $\langle \bar{\psi}_p(p) | J^\mu | \psi_n(p) \rangle$  has six non-vanishing terms given by

$$\begin{aligned} \langle \psi_p(p') | J^\mu | \psi_n(p) \rangle = & \bar{\psi}_p(p') \left[ f_1(q^2) \gamma^\mu - i \frac{f_2(q^2)}{M} \sigma^{\mu\nu} q_\nu + \frac{f_3(q^2)}{M} q^\mu \right. \\ & \left. + g_1(q^2) \gamma^\mu \gamma_5 - i \frac{g_2(q^2)}{M} \sigma^{\mu\nu} \gamma_5 q_\nu + \frac{g_3(q^2)}{M} \gamma_5 q^\mu \right] \psi_n(p) \end{aligned} \quad (1.35)$$

where  $q = p - p'$  is the momentum transfer from the neutron to the proton and  $M$  is the mass of the neutron. The form factors  $f_1, f_2, f_3, g_1, g_2$  and  $g_3$  are arbitrary

functions of  $q^2$ . The form factors  $f_1$  and  $g_1$  correspond to the vector ( $g_V$ ) and axial ( $g_A$ ) coupling constants in the limit,  $q^2 \rightarrow 0$  (see Eqn. 1.21) that constitute the current due to the weak interaction. The other form factors give the hadronic modification to the weak interaction due to the presence of strong interaction. The form factors  $f_1$  and  $g_1$  are the leading order terms associated with Fermi and GT transitions in the  $\beta$ -decay.

The vector ( $V$ ) part of the weak interaction has close resemblance to the current in the electromagnetic interaction (a vector interaction with conserved electric charge). The electric charge which is same as the coupling constant in the electromagnetic interaction which is strictly conserved even in the strong interaction. In the same way, it is assumed that the vector part of the weak interaction has a strictly conserved coupling constant. This is known as the Conserved Vector Current (CVC) hypothesis [53]. This means that the vector form factor  $g_V$  can be taken to be unity. The stronger form of the CVC hypothesis can be formulated in terms of isospin in which the neutron and proton are two components of the same nucleon spinor,  $\Psi = (u_p, u_n)^T$ ,  $\bar{\Psi} = (\bar{u}_p, \bar{u}_n)$  and using the Pauli's matrices,  $\vec{\tau} = (\tau_1, \tau_2, \tau_3)$ , we can write the electromagnetic and weak vector currents as

$$J_{em}^\mu = \frac{1}{2}\bar{\Psi}\gamma^\mu(I + \tau_3)\Psi, \quad V^\mu = \frac{1}{2}\bar{\Psi}\gamma^\mu(\tau_1 + i\tau_2)\Psi \quad (1.36)$$

where  $J_{em}^\mu = \langle \bar{u}_p | \gamma^\mu | u_p \rangle$  and  $V^\mu = \langle \bar{u}_p | \gamma^\mu | u_n \rangle$  are the hadronic current of the electromagnetic interaction and the vector current of the weak interaction respectively. The isoscalar part of the electromagnetic current is conserved i.e,  $\partial_\mu(\bar{\Psi}\gamma^\mu\Psi) = 0$  and the rest of the isovector currents are assumed to be the different components of the isospin current,

$$I_i^\mu = \frac{1}{2}\bar{\Psi}\gamma^\mu\tau_i\Psi \quad (1.37)$$

and is conserved ( $\partial_\mu I_i^\mu = 0$ ). But in QCD, the Hamiltonian has the term proportional to  $(m_u - m_d)(\bar{u}u - \bar{d}d)$  due to the presence of quarks and calculations [54] show that  $\partial_\mu I_i^\mu \propto (m_u - m_d)^2 \neq 0$ . Thus, the CVC hypothesis (isotriplet hypothesis) is true only if the masses of the two quarks are comparable.

The form factor  $f_2$  is a weak magnetism contribution to the current. Assuming the CVC hypothesis and in the limit  $q^2 \rightarrow 0$ ,  $f_2(0) = (\kappa_p - \kappa_n)/2$ , where  $\kappa_p$  and  $\kappa_n$  are the magnetic moments of the proton and neutron respectively. The form factor  $g_3$  is the induced pseudoscalar term and its effect is that it produces a distortion on the energy spectrum which is of the order  $m_e^2/ME_e \sim 10^{-4}$ . The induced scalar form factor  $f_3$  and induced tensor form factor  $g_2$  are called second-class currents (SCC) [55]. These form factors appear due to the violation of G-parity [56] in weak interactions. G-parity is defined as the rotation by  $\pi$  around the 2-axis of isospin (I) space followed by a charge conjugation (C).

$$G = C e^{i\pi I_2} \quad (1.38)$$

The G-parity is always conserved in the strong interaction, so if one assumes that G-parity is also conserved in the weak interactions, the form factors  $f_3$  and  $g_2$  must vanish in the hadronic current of the  $\beta$ -decay matrix element.

## 1.4 Angular Correlation Coefficients

The couplings  $C_i$  and  $C'_i$  in the general expression of the interaction Hamiltonian given by Lee and Yang (see Eqn. 1.5) are to be evaluated in terms of measurable parameters in  $\beta$ -decay. The expression for the differential decay rate for oriented nuclei as a function of the emitted electron momentum, the neutrino momentum, and the nuclear spin of the decaying nucleus was initially derived by Jackson, Treiman, and Wyld ( [57] [58], [59] ) using the Hamiltonian suggested by Lee and Yang. They obtained an expression for the decay rate of the oriented nucleus (allowed transition  $\Delta J = 0, \pm 1$ ), assuming that the momentum but not the spin of the outgoing electron is observable, given by

$$\begin{aligned} \frac{d^3\Gamma}{dE_e d\Omega_e d\Omega_\nu} &= \frac{F(\pm Z, E_e)}{2(2\pi)^5} p_e (E_0 - E_e)^2 \\ &\times \xi \left\{ 1 + a \frac{\vec{p}_e \cdot \vec{p}_\nu}{E_e E_\nu} + b \frac{m_e}{E_e} + \frac{\langle \vec{J} \rangle}{J} \cdot \left[ A \frac{\vec{p}_e}{E_e} + B \frac{\vec{p}_\nu}{E_\nu} + D \frac{\vec{p}_e \times \vec{p}_\nu}{E_e E_\nu} \right] \right. \\ &\left. + c \left[ \frac{1}{3} \frac{\vec{p}_e \cdot \vec{p}_\nu}{E_e E_\nu} - \frac{(\vec{p}_e \cdot \hat{j})(\vec{p}_\nu \cdot \hat{j})}{E_e E_\nu} \right] \left[ \frac{J(J+1) - 3\langle (\vec{J} \cdot \hat{j})^2 \rangle}{J(2J-1)} \right] \right\} \end{aligned} \quad (1.39)$$

where  $F(\pm Z, E_e)$  is the Fermi function that takes into account of Coulomb correction to the spectrum.  $E$  's and  $\vec{p}$  's are the energies and momenta of the respective particles.  $E_0$  is the endpoint energy of the electron.  $\vec{J}$  is the spin of the decaying nucleus and  $\hat{j}$  is the unit vector in the direction of  $\vec{J}$ . The coefficients  $\xi$ ,  $a$ ,  $b$ ,  $c$ ,  $A$ ,  $B$  and  $D$  depend on eight of the complex coupling constants  $C_i$  and  $C'_i$  in the interaction Hamiltonian. The constants ( $\xi$ ,  $a$ ,  $b$ ,  $c$ ,  $A$ ,  $B$  and  $D$ ) are functions of the coupling constants and the matrix elements for both Fermi ( $M_F$ ) and Gamow-Teller ( $M_{GT}$ ) transitions. The explicit expressions are given in the appendix A.1. In the decay of free polarized neutrons, a spin- $\frac{1}{2}$  system,  $\langle (\vec{J} \cdot \hat{j})^2 \rangle = J(J+1)$  and the decay rate does not have the expression containing  $c$ . Also,  $D$  contains crossed terms of the imaginary part of the scalar and tensor coupling constants and vanishes if the time reversal symmetry is not violated (see Table 1.3). The decay rate formula for  $\beta$ -decay becomes simple in terms of angular correlations, given by

$$\begin{aligned} \frac{d^3\Gamma}{dE_e d\Omega_e d\Omega_\nu} &= \frac{F(\pm Z, E_e)}{2(2\pi)^5} p_e (E_0 - E_e)^2 \\ &\times \xi \left\{ 1 + a \frac{\vec{p}_e \cdot \vec{p}_\nu}{E_e E_\nu} + b \frac{m_e}{E_e} + \frac{\langle \vec{J} \rangle}{J} \cdot \left[ A \frac{\vec{p}_e}{E_e} + B \frac{\vec{p}_\nu}{E_\nu} + D \frac{\vec{p}_e \times \vec{p}_\nu}{E_e E_\nu} \right] \right\} \end{aligned} \quad (1.40)$$

### 1.4.1 The Measurable $\beta$ -Decay Parameters

The Fierz interference term ( $b$ ) is one of the neutron  $\beta$ -decay parameters. A non-zero value causes a distortion in the electron energy spectrum. In the standard model, since the interaction is of the type  $(V - A)$ , the scalar and tensor coupling constants are absent,  $C_S = 0 = C'_S$  and  $C_T = 0 = C'_T$  giving  $b = 0$  (see Eqn.17).

Its nonzero value serves as a probe for possibility of beyond Standard Model physics (BSM) in scalar and tensor interactions. It requires precision measurement of the  $\beta$ -decay spectrum and so far its value is close to that predicted by the standard model.

The other important parameter is the correlation between the electron momentum and the spin of the neutron which is called the electron asymmetry  $A$ . The value of  $A$  can be obtained from  $A\xi$  and  $\xi$  for the neutron  $\beta$ -decay assuming a  $V - A$  interaction so that ( $C_V$ ) and axial ( $C_A$ ) coupling constants are real. In such simplification, the Fermi matrix ( $M_F$ ) and Gamow-Teller matrix ( $M_{GT}$ ) elements are given by [57]

$$|M_F|^2 = 1, |M_{GT}|^2 = 3, \Delta J = 0, \left(\frac{1}{2}^+ \rightarrow \frac{1}{2}^+\right) \quad (1.41)$$

From Eqn.17, we get

$$\xi = 2|M_F|^2 C_V^2 + 2|M_{GT}|^2 C_A^2 = 2(C_V^2 + 3C_A^2) \quad (1.42)$$

and

$$\begin{aligned} A\xi &= 2 \left[ -\frac{2}{3}|M_{GT}|^2 C_A^2 - 2\frac{1}{\sqrt{3}}|M_{GT}||M_F|C_V C_A \right] \\ &= -4 \left( \frac{1}{3}|M_{GT}|^2 C_A^2 + \frac{1}{\sqrt{3}}|M_{GT}||M_F|C_V C_A \right) \\ &= -4(C_A^2 + C_V C_A) \end{aligned} \quad (1.43)$$

Thus, the electron asymmetry  $A$ , neglecting the recoil order terms becomes

$$A_0 = \frac{A\xi}{\xi} = \frac{-4(C_A^2 + C_V C_A)}{2(C_V^2 + 3C_A^2)} = -2\frac{\lambda(\lambda + 1)}{1 + 3\lambda^2} \quad (1.44)$$

where  $\lambda = \frac{C_A}{C_V}$  denotes the ratio of the axial to the vector coupling constants.

The term  $B$  is the angular correlation between the momentum of the neutron and the emitted antineutrino and in the lowest order,  $B_0$  is given by

$$B_0 = -2\frac{\lambda(1 - \lambda)}{1 + 3\lambda^2} \quad (1.45)$$

The term  $a$  is the angular correlation between the momentum of the emitted electron and the antineutrino and is called the electron-antineutrino correlation. The lowest order expression for  $a_0$  is given by

$$a_0 = \frac{1 - \lambda^2}{1 + 3\lambda^2} \quad (1.46)$$

The Fierz interference term ( $b$ ) is given by

$$b = \pm \frac{\sqrt{1 - \alpha^2}}{1 + 3\lambda^2} \left[ \text{Re} \left( \frac{C_S + C'_S}{C_V} \right) + 3\lambda^2 \text{Re} \left( \frac{C_T + C'_T}{C_A} \right) \right] \quad (1.47)$$

where  $\alpha$  is the fine structure constant and the correlation coefficient  $D$  is given by

$$D = 2 \frac{\text{Im}(\lambda)}{1 + 3\lambda^2} \quad (1.48)$$

The angular correlation coefficients  $A$ ,  $B$  and  $a$  are collectively known as asymmetry parameters of neutron  $\beta$ -decay and are related by

$$1 + A_0 - B_0 - a_0 = 0, \quad a_0 B_0 - A_0 - A_0^2 = 0, \quad a_0^2 + A_0^2 + B_0^2 = 1 \quad (1.49)$$

The pseudo-T-odd coefficient  $D$  is small and can be neglected. The decay rate expression (see Eqn.1.40) does not contain the proton term explicitly. But, as it is kinematically coupled to the electron and neutrino energies and momenta through the conservation laws, one can write a relation between the correlation coefficients  $A_0$  and  $B_0$  and the proton asymmetry  $C$  given by

$$C = x_C(A + B) = x_C \frac{4\text{Re}(\lambda)}{1 + 3\lambda^2}$$

where,  $x_C = 0.2484$  is a kinematical factor [60].

#### 1.4.2 Recoil Order Corrections

In unpolarized neutron  $\beta$ -decay, the differential distribution, neglecting terms beyond next-to-leading order in the recoil expansion but accounting for all six possible form factors:  $f_1, f_2, f_3, g_1, g_2$  and  $g_3$ , Gardner and Plaster [61] have shown the dependence of asymmetries on the coupling constants. If the quantities are defined in terms of dimensionless parameters:

$$\epsilon = \left( \frac{m_e}{M_n} \right)^2, \quad R = \frac{E_0}{M_n}, \quad x = \frac{E_e}{E_0}, \quad \lambda = \frac{g_A}{g_V} > 0,$$

the expression for  $A$  can be written as

$$\begin{aligned} A(x) = & A_0 + \frac{1}{(1 + 3\lambda^2)^2} \left\{ \frac{\epsilon}{Rx} \left[ 4\lambda^2(1 - \lambda)(1 + \lambda + 2f_2) + 4\lambda(1 - \lambda)(\lambda g_2 - f_3) \right] \right. \\ & + R \left[ \frac{2}{3} [1 + \lambda + 2(f_2 + g_2)](3\lambda^2 + 2\lambda - 1) \right] \\ & + Rx \left[ \frac{2}{3} (1 + \lambda + 2f_2)(1 - 5\lambda - 9\lambda^2 - 3\lambda^3) \right. \\ & \left. \left. + \frac{4}{3} g_2(1 + \lambda + 3\lambda^2 + 3\lambda^3) \right] \right\} \quad (1.50) \end{aligned}$$

In the absence of second class currents,  $f_3 = g_2 = 0$ , and  $A(x)$  returns to the SM value  $A_0$ . Similarly, the other parameter  $a$  has the energy dependence through the second class currents.



### 1.4.3 Beyond Standard Model (BSM)

Possible Beyond Standard Model (BSM) interactions include scalar (S) and tensor (T) interactions. In the presence of S and T interactions, the Fierz interference term ( $b$ ) is nonzero. The connection between quark-level effective theory [62] and nucleon-level effective theory proposed by Lee and Yang (coupling coefficients,  $C_i, C'_i \in (V, A, S, T)$ ) is given by

$$C_i = \frac{G_F}{\sqrt{2}} V_{ud} \tilde{C}_i$$

$$\tilde{C}_V = g_V(1 + \epsilon_L + \epsilon_R), \quad (1.51)$$

$$\tilde{C}_A = -g_A(1 + \epsilon_L - \epsilon_R), \quad (1.52)$$

$$\tilde{C}_S = g_S \epsilon_S,$$

$$\tilde{C}_T = 4g_T \epsilon_T \quad (1.53)$$

where the  $\epsilon$  coefficients are the low-energy scalar and tensor coupling constants of the quark-level effective theory and  $C_i = C'_i$ , since only left-chiral neutrinos are present in the low energy regime. As there is no interference between left and right-handed neutrinos, so the right-handed currents contribute at second order to all observables.

In terms of the coupling constants of BSM parameters, the correlations at the lowest order approximation are given by

$$A_0 = \frac{2\lambda(1 - \lambda) + 2(4g_T \epsilon_T)^2 + 2(g_S \epsilon_S)(4g_T \epsilon_T)}{1 + 3\lambda^2 + (g_S \epsilon_S)^2 + 3(4g_T \epsilon_T)^2} \quad (1.54)$$

$$a_0 = \frac{(1 - \lambda^2) - (g_S \epsilon_S)^2 + (4g_T \epsilon_T)^2}{1 + 3\lambda^2 + (g_S \epsilon_S)^2 + 3(4g_T \epsilon_T)^2} \quad (1.55)$$

The expressions defined above return to the SM model prediction in the absence of new physics. The effective Fierz interference term  $b$  and the effective energy-dependent correlation coefficient  $B(E_e)$  according to Bhattacharya et al. [62] are given by

$$b^{BSM} = \frac{2(g_S \epsilon_S) - 6\lambda(4g_T \epsilon_T)}{1 + 3\lambda^2 + (g_S \epsilon_S)^2 + 3(4g_T \epsilon_T)^2} \quad (1.56)$$

$$b_\nu^{BSM} = \frac{2g_S \epsilon_S \lambda - 8g_T \epsilon_T (1 + 2\lambda)}{1 + 3\lambda^2 + (g_S \epsilon_S)^2 + 3(4g_T \epsilon_T)^2} \quad (1.57)$$

$$b = b^{SM} + b^{BSM}$$

$$B(E_e) = B_0 + c_0 + c_1 \frac{E_e}{M_N} + \frac{m_e}{E_e} (b_\nu^{SM} + b_\nu^{BSM}) \quad (1.58)$$

where,

$$c_0 = -\frac{2\lambda(\lambda + \mu_V)}{1 + 3\lambda^2} \frac{E_0}{M_N} \quad (1.59)$$

$$c_1 = \frac{\mu_V(1 + 3\lambda) + \lambda(5 + 7\lambda)}{1 + 3\lambda^2} \quad (1.60)$$

In the above expression  $\mu_V$  is difference between the magnetic moments of the proton and neutron.  $M_N$  is the mass of the nucleon. The term  $b_\nu$  is the coefficient of  $\frac{m_e}{E_e}$  that appears in the energy dependent expression of  $B(E_e)$ . The present work mainly focuses on the study of the sensitivities of asymmetries (discussed in details in the next chapter) towards  $b_\nu$  through the calculations of  $B(E_e)$ .

#### 1.4.4 Neutron Lifetime

An important observable in neutron  $\beta$ -decay is the lifetime of the neutron. The lifetime of the neutron can be obtained using the matrix element given by Eqn. 1.30 after integrating over the entire allowable phase space for the decay.

$$\frac{1}{\tau_n} = \frac{G_F^2 m_e^5}{2\pi^3} V_{ud}^2 (1 + 3\lambda^2) f (1 + RC) \quad (1.61)$$

where  $f$  is the phase factor and  $(1 + RC)$  accounts for the radiative corrections. When  $G_F$ ,  $f$  and  $(1 + RC)$  values are combined the lifetime expression reduces to

$$\tau_n = \frac{4908.7(1.9)s}{|V_{ud}|^2(1 + 3\lambda^2)} \quad (1.62)$$

A number of independent experiments are done with neutrons (cold or ultracold neutrons) to determine the lifetime ([63], [64], [65], [66], [67], [68], [69], [70], [71]). As an example, Serebrov et al. obtained the lifetime of neutron to be  $878.5 \pm 0.7(stat) \pm 0.3(sys)$  s from the decay of gravitationally trapped ultracold neutrons ([72], [73]). The other methods involve the neutron beam method to determine the lifetime by simply studying the decay of given population of neutrons as a function of time [74]. This is considered to be the most accurate value for the lifetime of neutron. The neutron lifetime is very important because by knowing  $\tau_n$  and  $\lambda$ , the first matrix element of CKM mixing matrix  $V_{ud}$  can be calculated which can be used for testing the SM predictions that constrain the elements.

### 1.5 Ultra Cold Neutron (UCN)

When a spallation neutron from the source with kinetic energy of  $keV$  order is moderated and down scattered to the kinetic energy less than  $350 neV$  (speed  $\sim 7 m/s$ ), it is called an ultracold neutron (UCN) ([75], [76]). In most experiments, neutrons are produced by hitting a tungsten spallation target with  $800 MeV$  protons. The neutrons are reflected by beryllium ( $V_F = 252 neV$ ) held at near liquid nitrogen temperature, then moderated by a polyethylene layer to produce cold neutrons. The cold neutrons then interact with solid deuterium (SD2) where downscattering occurs to obtain UCN ([77], [78]). These ultracold neutrons can be affected by gravity and the magnetic field and can be stored in a container made up of suitable material.

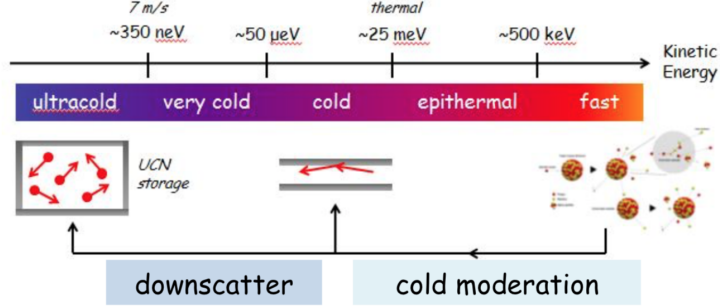


Figure 1.5: Sketch of the classification of neutrons based on energy scale along with the necessary steps taken to get ultracold neutrons (UCNs) from spallation neutrons.

Table 1.4: Fermi Potentials of Some Materials

Elements	$V_F(\text{neV})$
$^{58}\text{Ni}$	335
Ni	252
Steel	189
Be	252
Fe	210
Cu	168
Al	64
H	< 0
D	> 0

### 1.5.1 Trapping UCN

Ultracold neutrons (UCNs) with kinetic energies less than the neutron optical potential of well-chosen materials can be confined in a material “bottle” via total internal reflections [79]. These neutrons can also be trapped using magnetic (Stern-Gerlach force) and gravitational traps as they are affected by both of these fields. The ability to manipulate UCN with material guides and bottles, magnetic fields, and gravity can be useful for precision experiments with lower systematic errors than in experiments performed with cold neutron beams [77].

### 1.5.2 Fermi Potential

One of the most important properties of a UCN is that it can be trapped in a container made up of special materials determined by their Fermi potential. The Fermi potential is defined by the sum of delta functions seen by the neutron wave packet when the wavelength is much larger than the atomic spacing of a material,

$$V_F = \frac{2\pi\hbar^2}{m_n} \sum_k b_k(\vec{x} - \vec{x}_k) \quad (1.63)$$

where,  $b_k$  are the coherent neutron scattering lengths of the constituent nuclei and  $m_n$  is the mass of the nuclei. The sum over delta functions gives the mean scattering length ( $b$ ) for a material,

$$V_F = \frac{2\pi^2}{m_n}nb \quad (1.64)$$

Here,  $n$  is the number density of these nuclei in the material. The Fermi potentials,  $V_F$ , of some common materials used for trapping UCNs in the experiments are shown in Table 1.4. In the case H and D the Fermi potentials are of opposite sign but the magnitude is highly dependent on their densities [80]. This means that when the energy of the incoming neutron wave packet is less than  $V_F$ , the neutron will be totally reflected from the walls of the material, although quantum mechanical tunneling effects comes in play and penetrates the material to a finite distance [81]. The trapping of the UCN is not perfect and there is a loss of UCN through either neutron capture or upscattering via interactions of the neutron with the nuclei in the material [82]. Therefore, it is important to make a neutron-trap out of the material with very high Fermi potential so that it can be guided to the experimental volume before it decays. There are elements like hydrogen, which have negative Fermi potential and cannot be used for trapping UCN as they are absorbed. Efficient transport of ultracold neutrons requires guides with a high Fermi potential, low absorption and a low diffuse reflection (non-specular reflection) probability. This allows backscattering of the UCN and hence decreases the loss probability [79].

### 1.5.3 Gravity

The neutron is a particle with the mass of  $m_n = 939.5654 \text{ MeV}$  and in the gravitational field of earth, the potential energy as a function of height ( $h$ ) from the earth is given by

$$V_G = m_ngh \approx [102 \text{ (neV)}m^{-1}]h \quad (1.65)$$

As the neutron obtained from the fission of heavy nuclei has the energy of the order of  $\text{MeV}$ , the gravitational energy is insignificant for such neutron. However, UCN which have the energy nearly  $300 \text{ neV}$  greatly affected by gravity. A slight change in the height of the UCN from the bottom of the storage chamber makes a huge energy difference of the UCN. Thus, a change in the height of UCN in the container can be used for guiding and selecting the UCN of desired energy.

### 1.5.4 Magnetic Field

The neutron has the intrinsic magnetic moment of  $\mu_N = -1.91304272 \text{ [9]}$  which is aligned opposite to its spin ( $\hat{\sigma}_n$ ) as indicated by the negative sign. The potential energy of the neutron interacting with the magnetic field ( $\vec{B}$ ) is given by

$$V_B = -\mu_N \cdot \vec{B} = \mu_N \hat{\sigma}_n \cdot \vec{B} \approx \pm[60 \text{ (neV)}T^{-1}] \hat{\sigma}_n \cdot \vec{B} \quad (1.66)$$

It is clear from this expression that if the spin of the neutron is parallel to the field, it experiences a repulsive force from the potential whereas the neutron with an opposite spin will feel an attractive force from the potential. The strength of the potential shows that application of a magnetic field can be used as a spin filter for the UCN.

## 1.6 Motivation

The focus of this dissertation work is to explore ways to obtain the neutrino asymmetry parameter  $B_0$  from several possible electron-proton coincidence asymmetries that can be constructed in free neutron  $\beta$ -decay via the simulation of a realistic experiment. The advancement in the technology to manipulate cold neutrons, triggered a number of electron-proton coincidence experiments ( [6], [83], [84], [85], [86], [87], [88] ) to determine  $B_0$ . Table 1.5 shows the values of  $B_0$  so far measured [89] using cold neutrons.

Table 1.5: Neutrino Asymmetry Parameter  $B_0$

$B_0$	Group	Year
0.9802(34)(36)	Schumann et al. [6]	2007
0.967(6)	Kreuz et al. [90]	2005
0.9876(4)	Mostovoi et al. [88]	2001
0.9894(83)	Kuznetsov et al. [91]	1998
1.00(5)	Christensen et al. [84]	1970
0.995(34)	Erozolimsky et al. [83]	1970

In all of the previous experiments, only  $B_0$  was extracted, without any attempts thus far to extract the energy-dependent term  $b_\nu$ . Furthermore, the results in the 70's have large uncertainties which were not taken into account. The values of  $B_0$  reported after 1990 are more or less in agreement with the SM predictions.

The measurement of the neutrino asymmetry  $B$  in free neutron  $\beta$ -decay is very important because it has the term  $b_\nu$  as the coefficient in the energy dependence. Hence, by measuring  $B$  precisely, one can extract  $b_\nu$ , the nonzero value of which would indicate the possibility of the existence of scalar and tensor interactions in the semi-leptonic decay of the neutron [92]. In this work, we investigate a number of different experimental strategies for accessing  $b_\nu$  in electron-proton coincidence experiments, and then assess the combined sensitivity of these asymmetries together with a measurement of the electron energy spectrum to  $b$  and  $b_\nu$ . We show how the construction of ratios of asymmetries permits a separation of  $b_\nu$  from  $b$ , thereby increasing the sensitivity of an experiment with a fixed number of statistics to  $b_\nu$ .

## Chapter 2 Event Generator for Neutron $\beta$ -Decay

### 2.1 Decay Probability

In the determination of both  $a$  and  $B$ , the electron and proton momentum must be measured simultaneously [93]. This makes it more difficult to design an experiment to detect them, because the maximum proton energy is only 751 eV. But in the case of the  $\beta$ -decay asymmetry parameter  $A$ , it requires a high degree of polarization and precise determination of the electron momentum. The detection design for an electron, as in UCNA experiment, is quite simple since its maximum kinetic energy is about 782 keV. In order to correctly model the systematic effects in the study of the  $\beta$ -decay parameters of interest, it is important to have an accurate neutron event generator that could give the correct energy and angular distributions of all the decay products. We consider the decay probability of the free neutron as

$$\frac{d^6\Gamma(\vec{p}_e, \vec{p}_\nu)}{d^3p_e d^3p_\nu} = CF(Z, E_e) \left[ 1 + a \frac{\vec{p}_e \cdot \vec{p}_\nu}{E_e E_\nu} + b \frac{m_e}{E_e} + \vec{\sigma}_n \cdot \left( A \frac{\vec{p}_e}{E_e} + B \frac{\vec{p}_\nu}{E_\nu} \right) \right] \delta^{(4)}(p_n - p_e - p_\nu) \quad (2.1)$$

where  $C$  is a constant,  $F(Z, E_e)$  is the Fermi function and  $a$ ,  $b$ ,  $A$  and  $B$  are correlation coefficients. The time-odd term  $D$  is dropped in the above expression as its value is zero in the SM and is not an observable parameter in the scope of the current UCNB experiment. Also,  $\vec{p}_i$  ( $i = e, \nu$ ) are the momenta of the electron and the associated antineutrino. The Fierz interference term  $b$  depends on the existence of tensor or scalar contributions to the weak interaction and is therefore zero in the SM. The Fermi function  $F(Z, E_e)$  distorts the electron energy spectrum due to Coulomb effects on the final state wave function of the electron. The Coulomb effects for a point nucleus ([94], [95]), can be represented as

$$F(Z, E_e) = \left| \frac{\psi_e(r)}{\psi_0(r)} \right|^2 = 2(1 + \gamma)(2p_e R)^{2(\gamma-1)} e^{\pi\eta} \frac{|\Gamma(\gamma + i\eta)|^2}{|\Gamma(2\gamma + 1)|^2} \quad (2.2)$$

where,  $\psi_e(r)$  and  $\psi_0(r)$  represent the perturbed and unperturbed wave functions of the electron, respectively.  $\Gamma(x)$  is a gamma function,  $\eta = \pm \frac{\alpha Z}{\beta_e}$  ( $\pm$  denotes the cases of  $\beta^\pm$ -decay),  $\gamma = \sqrt{1 - \alpha^2 Z^2}$ ,  $R$  is the radius of the nucleus in the units of  $\hbar^2/(m_e c^2)$  and  $\alpha$  is the fine structure constant. In the case of electron with kinetic energy  $T_e = E_e - m_e > 5$  keV, the following expression for the Coulomb correction is a good approximation with relative error less than 0.01% [96].

$$F(Z, E_e) = \sum_n^{\infty} a_n (\alpha Z)^n \quad (2.3)$$

where,

$$\begin{aligned}
a_0 &= 1 \\
a_1 &= \frac{\pi}{\beta_e} \\
a_2 &= \frac{11}{4} - \gamma_E - \ln(2\beta_e E_e R) + \frac{\pi^2}{3\beta_e^2} \\
a_3 &= \frac{\pi}{\beta_e} \left[ \frac{11}{4} - \gamma_E - \ln(2\beta_e E_e R) \right]
\end{aligned} \tag{2.4}$$

Here,  $\beta_e$ , the radius  $R$  of the nucleus and Euler's constant  $\gamma_E$  are defined as

$$\beta_e = \frac{|\vec{p}_e|}{E_e}, \quad R \approx 1 \approx \frac{0.01}{4m_e}, \quad \gamma_E = 0.57722. \tag{2.5}$$

But, for an electron with kinetic energy  $T_e = E_e - m_e < 1 \text{ keV}$ , we can use the non-relativistic expression for the Fermi function [94] at low energy given by

$$F_{NR}(Z, E_e) = y (1 - e^{-y})^{-1} \tag{2.6}$$

where  $y = \frac{2\pi\alpha Z}{\beta_e}$  for the  $\beta^-$  decay. In the present analysis of the energy spectra for the emitted particles in the  $\beta$ -decay where the energies of the particles ranges from zero to maximum (about  $782 \text{ keV}$ ), the expansion of of Fermi function given by Eqn.2.3 up to order  $\alpha^3$  was chosen in the event generator.

### 2.1.1 Proton Momentum

Since, in the experiment neutrinos are unobservable, the neutrino variables in Eqn.2.1 must be replaced by the proton variables so that the decay expression can be integrated with respect to the electron and proton momenta. Considering the mass of the antineutrino to be zero, the momentum-energy conservation gives

$$\begin{aligned}
\vec{p}_\nu &= -(\vec{p}_e + \vec{p}_p) \\
\vec{p}_\nu \cdot \vec{p}_e &= -\vec{p}_e \cdot (\vec{p}_e + \vec{p}_p) = -(p_e^2 + p_e p_p \cos \theta_{ep})
\end{aligned} \tag{2.7}$$

and the energy of the massless antineutrino is given by

$$E_\nu = |\vec{p}_\nu| = |\vec{p}_e + \vec{p}_p| = \sqrt{p_e^2 + 2p_e p_p \cos \theta_{ep} + p_p^2} \tag{2.8}$$

where  $\theta_{ep}$  is the angle between the direction of the outgoing electron and proton. In order to calculate  $\theta_{ep}$ , consider the unit vectors in  $(\theta_e, \phi_e)$  and  $(\theta_p, \phi_p)$  direction. Then, the cosine of the angle between these unit vectors is given by

$$\cos \theta_{ep} = \sin \theta_e \sin \theta_p \cos(\phi_e - \phi_p) + \cos \theta_e \cos \theta_p \tag{2.9}$$

Now, by substituting the antineutrino variables in Eqn.2.1 by the proton variables, we obtain

$$\begin{aligned} \frac{d^6\Gamma(\vec{p}_e, \vec{p}_p)}{d^3p_e d^3p_p} &= CF(Z, E_e) \left[ 1 - a \frac{p_e^2 + p_e p_p \cos \theta_{ep}}{E_e(m_n - E_e - E_p)} + b \frac{m_e}{E_e} \right. \\ &\quad \left. + \vec{\sigma}_n \cdot \left( A \frac{\vec{p}_e}{E_e} - B \frac{\vec{p}_e + \vec{p}_p}{m_n - E_e - E_p} \right) \right] \times \delta^{(0)}(m_n - E_e - E_p - |\vec{p}_e + \vec{p}_p|) \end{aligned} \quad (2.10)$$

The integral over the proton's momentum can be easily evaluated using the properties of the delta function and we get an equation for the magnitude of the proton momentum as

$$\begin{aligned} m_n - E_e - E_p - |\vec{p}_e + \vec{p}_p| &= 0 \\ m_n - E_e - \sqrt{p_p^2 + m_p^2} - |\vec{p}_e + \vec{p}_p| &= 0 \end{aligned} \quad (2.11)$$

Solving this quadratic equation ( see appendix A.3 for detailed derivation), we get the magnitude of the proton momentum as

$$p_p^\pm(p_e, E_e, \theta_{ep}) = \frac{-U \pm S}{2W} \quad (2.12)$$

Using notation,  $c_f = |\cos \theta_{ep}|$  and  $d = m_n - E_e$ , the other variables  $U$ ,  $S$  and  $W$  are defined by

$$\begin{aligned} U &= 4|\vec{p}_e|c_f(d^2 + m_p^2 - p_e^2), \\ S &= (U^2 - 4Wh)^{1/2}, \\ W &= 4(d^2 - p_e^2c_f^2), \\ h &= 4(m_n^2 - m_p^2)(E_e - E_{crit})(H - E_e) \end{aligned} \quad (2.13)$$

where  $E_{crit}$  and  $H$  are given by

$$\begin{aligned} E_{crit} &= \frac{1}{2} \left( m_n - m_p + \frac{m_e^2}{m_n - m_p} \right) \\ H &= \frac{1}{2} \left( m_n + m_p + \frac{m_e^2}{m_n + m_p} \right) \end{aligned} \quad (2.14)$$

The Dalitz region of the  $(E_e, c_f = \cos \theta_{ep})$  distribution is constraint by [96]

$$\begin{aligned} -1 &\leq c_f \leq (c_f)_{Max}(E_e) \\ (c_f)_{Max}(E_e) &= +1 \quad \text{if } E_e < E_{crit}, \\ (c_f)_{Max}(E_e) &= -\sqrt{1 - s_{fm}^2(E_e)} \quad \text{if } E_e > E_{crit} \end{aligned} \quad (2.15)$$



where,

$$s_{fm}(E_e) = \frac{m_n}{m_p} \frac{E_0 - E_e}{|\vec{p}_e|} \quad (2.16)$$

Here,  $E_0$  is the endpoint energy for the electron and is given by

$$E_0 = \Delta - \frac{\Delta^2 - m_e^2}{2m_n} \quad (2.17)$$

where,  $\Delta = m_n - m_p$

### 2.1.2 Sampling Proton Events

Consider a function  $f(x)$  defined by [87]

$$\begin{aligned} f(p_p) &= m_n - E_e - \sqrt{p_p^2 + m_p^2} - |\vec{p}_e + \vec{p}_p| \\ f'(p_p) &= \frac{p_p}{E_p} - \frac{p_p + p_e \cos \theta_{ep}}{m_n - E_e - \sqrt{p_p^2 + m_p^2}} \end{aligned} \quad (2.18)$$

If  $p_p^+$  and  $p_p^-$  are the values of  $p_p$  for the equations  $f(p_p) = 0$ , then from the property of the delta function, we can write

$$\delta(f(p_p)) = \frac{\delta(p_p - p_p^+)}{|f'(p_p^+)|} + \frac{\delta(p_p - p_p^-)}{|f'(p_p^-)|} \quad (2.19)$$

Making the substitution for the proton energy and using  $d^3\vec{p}_p = p_p^2 dp_p d\Omega_p$ , the distribution function in terms of the proton and electron energy-momentum is given by

$$W(\vec{p}_e, \vec{p}_p) = f_b - a \frac{p_e^2 + p_e p_p^\pm \cos \theta_{ep}}{E_e(m_n - E_e - E_p^\pm)} + A \frac{p_e \cos \theta_e}{E_e} - B \frac{p_e \cos \theta_e + p_p^\pm \cos \theta_p}{m_n - E_e - E_p^\pm} \quad (2.20)$$

where  $f_b = 1 + b \frac{m_e}{E_e}$ . The decay probability as a function of electron energy and the angular distribution of the proton and electron becomes

$$\begin{aligned} \frac{d^5\Gamma(E_e, \Omega_e, \Omega_p)}{dE_e d\Omega_e d\Omega_p} &= CF(Z, E_e) \left[ W(\vec{p}_e, \vec{p}_p)(p_p^+)^2 \frac{\delta^{(0)}(p_p - f(p_p^+))}{|f'(p_p^+)|} \right. \\ &\quad \left. + W(\vec{p}_e, \vec{p}_p)(p_p^-)^2 \frac{\delta^{(0)}(p_p - f(p_p^-))}{|f'(p_p^-)|} \right] E_e \sqrt{E_e^2 - m_e^2} \end{aligned} \quad (2.21)$$

where

$$\begin{aligned} d\Omega_e &= \sin \theta_e d\theta_e d\phi_e \\ d\Omega_p &= \sin \theta_p d\theta_p d\phi_p \end{aligned}$$

Looking at this decay rate, both the solutions for the proton momentum contribute to the distribution function through the delta functions. Hence, we must be careful

to consider the solutions because either of them are equally valid and choice depends on the energy cut for the electron determined by  $E_{crit} \sim 236 \text{ keV}$ . The following two cases arises in the selection of the proton events.

**(I)**  $E_e < E_{crit}$

When  $E_e < E_{crit}$  then  $h < 0$  which gives one of the roots  $p_p < 0$ . This negative root falls outside the ranges of the integration (not a valid solution) and can be neglected. For such energy scale, only one of the roots gives the momentum and energy of the proton event. In this case, only one term contributes in the distribution function (see Eqn. 2.21) corresponding to the positive solution ( $p_p > 0$ ).

**(II)**  $E_e > E_{crit}$

In this case,  $h > 0$  and for the given value of  $\theta_{ep}$ , both the roots ( $p_p^- > 0$ ,  $p_p^+ > 0$ ) give the valid momentum for the proton and will contribute to the distribution function. In the distribution function, what matters is the relative weights for the two valid proton momenta. The relative weights for proton momenta  $p_p^+$  and  $p_p^-$  are defined as

$$W^+ = \frac{W(p_e, p_p^+)}{W(p_e, p_p^+) + W(p_e, p_p^-)}$$

$$W^- = \frac{W(p_e, p_p^-)}{W(p_e, p_p^+) + W(p_e, p_p^-)}$$

where,  $W^- + W^+ = 1$ . Using the random number generator that generates numbers in the range  $[0, 1]$  which corresponds to  $[W^-, W^+]$ , will allow us to pick up either of the two proton momenta ( $p_p^+$  or  $p_p^-$ ) and determine the energy ( $E_p^+$  or  $E_p^-$ ) for the proton event. We use Monte Carlo acceptance/rejection method to accept these values or reject them and move on to the new values for  $(E_e, \theta_e, \phi_e)$  and  $(\theta_p, \phi_p)$ .

## 2.2 Electron Energy Spectrum

The energy spectrum for the electron in the  $\beta$ -decay is given by

$$w_e(E_e) = F(Z, E_e)p_e E_e (\Delta - E_e)^2 \quad (2.22)$$

$$\frac{d\Gamma}{dE_e} = w_e(E_e) \left( 1 + b \frac{m_e}{E_e} \right) \quad (2.23)$$

The shape of the electron spectrum is modified by the Fierz interference term  $b$  and the presence of the Fermi function. Figure 2.1 shows an electron spectrum in the absence of Fierz term for the free neutron  $\beta$ -decay.

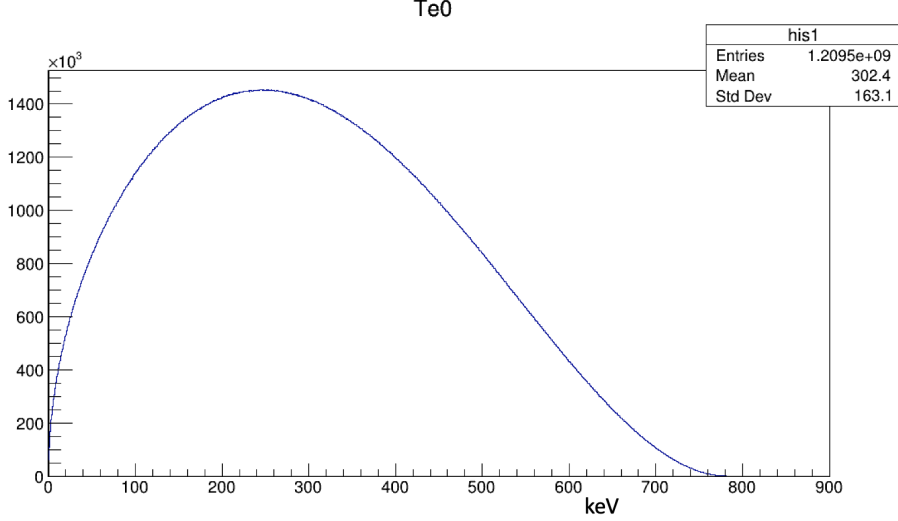


Figure 2.1: Electron energy spectrum

### 2.3 Proton Energy Spectrum

The proton energy spectrum according to Gluck ([60], [97]) is given by

$$w_p(E_p) = m_n \frac{G_F^2 \xi}{4\pi^3} \left[ W_p(E_{emax}, E_p) - W_p(E_{emin}, E_p) \right] \quad (2.24)$$

$$W_P(E_e, E_p) = \frac{1}{2}(1+a)(\Delta - \frac{2}{3}E_e)E_e^2 + am_n E_e(E_p - E_{pmax}) + bm_e E_e(\Delta - \frac{1}{2}E_e) \quad (2.25)$$

where  $\xi$  is defined in appendix A.1. Unlike the electron energy spectrum, the proton spectrum is modified by the presence of both Fierz interference term  $b$  and the electron-antineutrino asymmetry parameter  $a$ . Figure 2.2 shows a proton spectrum for the free neutron  $\beta$ -decay. The maximum energy of the proton is given by

$$E_{pmax} = m_p + \frac{\Delta^2 - m_e^2}{2m_n} \sim 751.0 \text{ eV} \quad (2.26)$$

and for the given proton momentum (kinetic energy), the minimum and maximum energies for the electron are given by

$$E_{emin} = \frac{1}{2} \left( \Delta - p_p + \frac{m_e^2}{\Delta - p_p} \right) \quad (2.27)$$

$$E_{emax} = \frac{1}{2} \left( \Delta + p_p + \frac{m_e^2}{\Delta + p_p} \right) \quad (2.28)$$

The proton energy distribution is modified by Fermi function  $F(Z = 1, E_p)$  that takes into account the Coulomb corrections of the proton recoil. For this,  $\beta_e$  has to be replaced by

$$\beta_r = |\beta - (1 - \beta^2)v_f c_f| \quad (2.29)$$

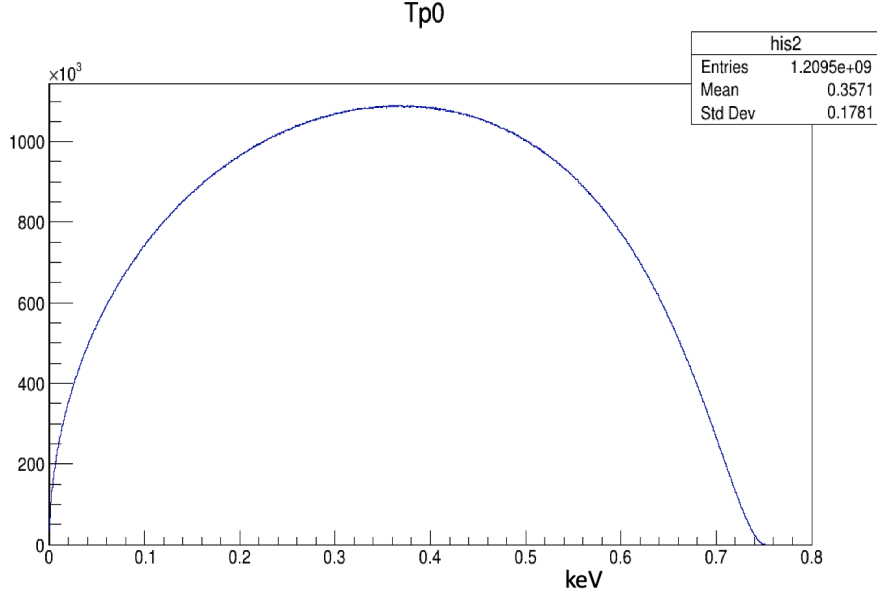


Figure 2.2: Proton energy spectrum

where

$$\beta_r = |\vec{p}_p|/E_p, \quad c_f = \frac{\vec{p}_e \cdot \vec{p}_p}{|\vec{p}_e||\vec{p}_p|} = \cos \theta_{ep} \quad (2.30)$$

## 2.4 Antineutrino Energy Spectrum

The energy spectrum for the antineutrino is not an observable unlike the electron and proton spectra and must be calculated from the distribution functions for the electron and proton. The spectral shape is determined by the shapes of proton and electron spectra. The maximum energy of the electron antineutrino is the same that of the electron end point energy (assuming massless antineutrino) of electron. Due to the fact that the energy scale of proton ( $T_{pmax} \sim 751.0 \text{ eV}$ ) is three orders of magnitude smaller than the electron, the energy spectrum of antineutrino has maximum kinetic energy equal to the endpoint energy of the electron. Figure 2.3 shows an antineutrino spectrum for the free neutron  $\beta$ -decay.

## 2.5 Event Generation

In the generation of an event, we used Monte Carlo (MC) acceptance and rejection to sample the electron energy. The sampled electron energy is next used to sample the proton energy.

- Randomize  $\theta_e$  in the interval  $[0, \pi]$  and  $\phi_e$  in the interval  $[0, 2\pi]$  and apply the MC acceptance/rejection method to the electron distribution function in order to select the electron momentum and the energy for that event.

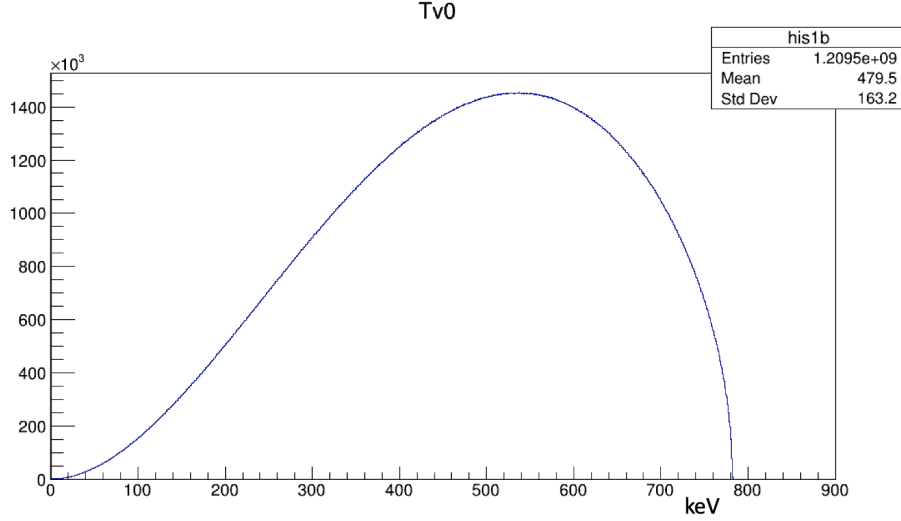


Figure 2.3: Antineutrino energy spectrum

- Randomize  $\theta_p$  in the interval  $[0, \pi]$  and  $\phi_p$  in the interval  $[0, 2\pi]$  for the proton with all the constraints discussed earlier.
- If the electron energy is greater than or equal to the critical energy, accept an angle for which  $\theta_{ep}$  is less than the maximum angle constrained by the energy and momentum of an electron, else check again.
- If the electron energy is less than the critical energy, the positive momentum of the proton is accepted.
- If the electron energy is greater than the critical energy, the MC method is used to select the momentum of the proton for that event.
- Finally, use the MC method for the proton distribution function to sample the proton energy.

After sampling the energy/ momentum of the electron and proton, we use conservation laws to obtain the energy/momentum of the antineutrino. These energy and momentum of the particles serve as the input to the simulation described in the present work.

## Chapter 3 $Q_{ij}$ Spectra for Neutron $\beta$ -Decay

The  $Q_{ij}$  are the angular part of the decay rate integrated over the angular variables in the polarized neutron  $\beta$ -decay. The index  $i$  and  $j$  refer to the polarization of the electron and proton relative to the neutron. Each indices can either have value  $+$  or  $-$  depending on whether the particle is emitted parallel or anti-parallel to the polarization of the neutron. Hence, we have four  $Q_{ij}$ s and their explicit expressions are derived in the section to follow in the infinite nucleon mass (INM) approximation.

### 3.1 INM Approximation

The decay of free the neutron is a three body decay given by

$$n \rightarrow p + e^- + \bar{\nu}_e$$

In the infinite nucleon mass (INM) approximation ( $m_n \rightarrow \infty$  and  $m_p \rightarrow \infty$ ), the energy balance condition gives [60]

$$\begin{aligned} m_n &\cong m_p + (T_e + m_e) + E_\nu \\ E_\nu &= (m_n - m_p) - E_e = \Delta - E_e \end{aligned}$$

In the INM limit, the total neutron  $\beta$ -decay rate can be written as

$$\rho = \frac{1}{(4\pi)^2} \int_{m_e}^{\Delta} dE_e w_s(E_e) \int_{-1}^{+1} d(\cos \theta_e) \int_0^{2\pi} d\phi_e \int_{-1}^{+1} d(\cos \theta_\nu) \int_0^{2\pi} d\phi_\nu \mathcal{D}. \quad (3.1)$$

where  $w_s(E_e)$  and  $\mathcal{D}$  are given by

$$w_s(E_e) = \frac{G_F^2 V_{ud}^2 \xi}{2\pi^3} \beta_e E_e^2 E_\nu^2 = \frac{G_F^2 V_{ud}^2 \xi}{2\pi^3} \frac{p_e}{E_e} E_e^2 (\Delta - E_e)^2 \quad (3.2)$$

where

$$\xi = 1 + 3g_A^2$$

and

$$\mathcal{D} = 1 + b \frac{m_e}{E_e} + a\beta_e \cos \theta_{e\nu} + PA\beta_e \cos \theta_e + PB \cos \theta_\nu + PD\beta_e \cos \theta_\perp \quad (3.3)$$

In the expression of  $w_s(E_e)$ ,  $G_F$  is the Fermi constant,  $V_{ud}$  is the first element of the Cabibbo-Kobayashi-Masakawa (CKM) mixing matrix ( see Eqn.1.22) and  $g_A$  is the axial coupling constant. Inside the expression  $\mathcal{D}$  are various correlation coefficients  $a$ ,  $b$ ,  $A$ ,  $B$  and  $D$  known as asymmetry parameters of neutron  $\beta$ -decay and are measured experimentally to various degrees of accuracy.  $P$  is the polarization and  $\beta_e$  is the velocity  $v_e/c$  for an electron [98].

$$\cos \theta_\perp = \frac{\vec{s} \cdot (\vec{p}_e \times \vec{p}_\nu)}{|\vec{p}_e| |\vec{p}_\nu|} \quad (3.4)$$

Taking the neutron spin  $\vec{s}$  along  $\hat{z}$ , we have

$$\begin{aligned} \cos \theta_{\perp} \propto s \hat{z} \cdot & \left[ (p_e \sin \theta_e \cos \phi_e \hat{x} + p_e \sin \theta_e \sin \phi_e \hat{y} + p_e \cos \theta_e \hat{z}) \right. \\ & \left. \times (p_{\nu} \sin \theta_{\nu} \cos \phi_{\nu} \hat{x} + p_{\nu} \sin \theta_{\nu} \sin \phi_{\nu} \hat{y} + p_{\nu} \cos \theta_{\nu} \hat{z}) \right] \end{aligned}$$

Also, we have

$$\begin{aligned} \cos \theta_{e\nu} &= \hat{p}_e \cdot \hat{p}_{\nu} \\ &= (\sin \theta_e \cos \phi_e \hat{x} + \sin \theta_e \sin \phi_e \hat{y} + \cos \theta_e \hat{z}) \cdot (\sin \theta_{\nu} \cos \phi_{\nu} \hat{x} + \sin \theta_{\nu} \sin \phi_{\nu} \hat{y} + \cos \theta_{\nu} \hat{z}) \end{aligned}$$

And, under the azimuthal symmetry

$$\langle \cos \theta_{\perp} \rangle = \int_0^{2\pi} d\phi_e \int_0^{2\pi} d\phi_{\nu} \cos \theta_{\perp} = 0 \quad (3.5)$$

Also, in the  $\int_0^{2\pi} d\phi_e$  and  $\int_0^{2\pi} d\phi_{\nu}$  integrals of  $\cos \theta_{e\nu}$ , only the  $\cos \theta_e \cos \theta_{\nu}$  term survives! Hence, we have

$$\begin{aligned} \rho &= \frac{(2\pi)^2}{(4\pi)^2} \int_{m_e}^{\Delta} dE_e w_s(E_e) \int_{-1}^{+1} d(\cos \theta_e) \int_{-1}^{+1} d(\cos \theta_{\nu}) \\ &\times \left[ 1 + b \frac{m_e}{E_e} + a\beta_e \cos \theta_e \cos \theta_{\nu} + PA\beta_e \cos \theta_e + PB \cos \theta_{\nu} \right] \end{aligned} \quad (3.6)$$

The integrals over  $d(\cos \theta_e)$  and  $d(\cos \theta_{\nu})$  are constrained by momentum conservation:

$$\vec{p}_p + \vec{p}_e + \vec{p}_{\nu} = 0 \quad (3.7)$$

This implies

$$\vec{p}_p \cdot \vec{s} = -\vec{s} \cdot (\vec{p}_e + \vec{p}_{\nu}) = -(\beta_e E_e \hat{p}_e + E_{\nu} \hat{p}_{\nu}) \cdot s \hat{z} = -\beta_e E_e \cos \theta_e - E_{\nu} \cos \theta_{\nu}$$

Now, the integrals in Eqn. 3.6 can be evaluated over the allowed regions of  $(\cos \theta_e, \cos \theta_{\nu})$  phase space.

Consider the case in which both an electron and a proton are emitted parallel to the neutron polarization, the decay rate ( $\rho_{++}$ ) can be calculated in the allowed region of phase space. For this, we have  $\vec{p}_e \cdot \vec{s} > 0$  and  $\vec{p}_p \cdot \vec{s} > 0$

$$\begin{aligned} \vec{p}_p \cdot \vec{s} = -\beta_e E_e \cos \theta_e - E_{\nu} \cos \theta_{\nu} > 0 &\implies -\beta_e E_e \cos \theta_e > E_{\nu} \cos \theta_{\nu} \\ \implies \cos \theta_{\nu} < \frac{-\beta_e E_e}{E_{\nu}} \cos \theta_e < 0 &\implies \cos \theta_{\nu} < -r \cos \theta_e < 0 \end{aligned}$$

where,  $r \equiv \frac{\beta_e E_e}{E_{\nu}} \geq 0$ . Hence,

$$\begin{aligned} \rho_{++} &= \frac{1}{4} \int_{m_e}^{\Delta} dE_e w_s(E_e) \int_0^{+1} d(\cos \theta_e) \int_{-1}^{\max(-1, -r \cos \theta_e)} d(\cos \theta_{\nu}) \\ &\times \left[ 1 + b \frac{m_e}{E_e} + a\beta_e \cos \theta_e \cos \theta_{\nu} + PA\beta_e \cos \theta_e + PB \cos \theta_{\nu} \right] \end{aligned} \quad (3.8)$$

$$\equiv \int_{m_e}^{\Delta} dE_e w_{++}(E_e) \quad (3.9)$$

where,

$$w_{++}(E_e) = \frac{1}{4} w_s(E_e) Q_{++} \quad (3.10)$$

$$Q_{++} = \int_0^{+1} d(\cos \theta_e) \int_{-1}^{\max(-1, -r \cos \theta_e)} d(\cos \theta_\nu) \quad (3.11)$$

$$\times \left[ 1 + b \frac{m_e}{E_e} + a \beta_e \cos \theta_e \cos \theta_\nu + PA \beta_e \cos \theta_e + PB \cos \theta_\nu \right]$$

The region of integrals are constrained by  $r$ . There are two expressions for  $Q_{++}$

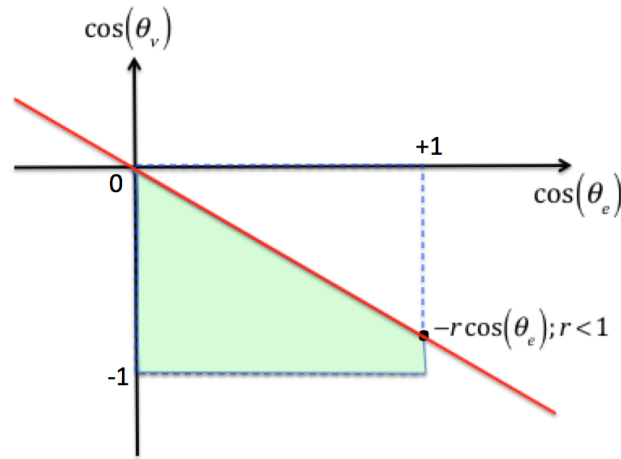


Figure 3.1: The shaded area is the region of the integral for  $Q_{++}$  under the constraint  $r < 1$ .

depending on the energy scale  $r < 1$  and  $r > 1$ . If  $r < 1$  then  $-r \cos \theta_e > -1$ , we get (refer to Figure 3.1),

$$Q_{++}^{r < 1} = \int_0^1 d(\cos \theta_e) \int_{-1}^{-r \cos \theta_e} d(\cos \theta_\nu) \quad (3.11)$$

$$\times \left[ 1 + b \frac{m_e}{E_e} + a \beta_e \cos \theta_e \cos \theta_\nu + PA \beta_e \cos \theta_e + PB \cos \theta_\nu \right]$$

$$Q_{++}^{r < 1} = (1 + b \frac{m_e}{E_e})(1 - \frac{r}{2}) + \frac{1}{4} a \beta_e (\frac{r^2}{2} - 1) + \frac{1}{2} PA \beta_e (1 - \frac{2r}{3}) + \frac{1}{2} PB (\frac{r^2}{3} - 1) \quad (3.12)$$

If  $r > 1$ , then  $-r \cos \theta_e > -1$  which gives  $\cos \theta_e < \frac{1}{r}$  (refer Figure 3.2), we can write,



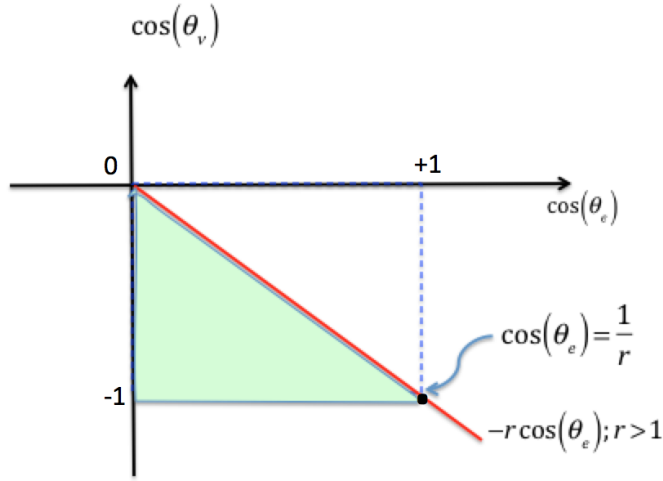


Figure 3.2: The shaded area is the region of the integral for  $Q_{++}$  under the constraint  $r > 1$ .

$$\begin{aligned}
Q_{++}^{r>1} &= \int_0^{1/r} d(\cos \theta_e) \int_{-1}^{-r \cos \theta_e} d(\cos \theta_\nu) \\
&\times \left[ 1 + b \frac{m_e}{E_e} + a\beta_e \cos \theta_e \cos \theta_\nu + PA\beta_e \cos \theta_e + PB \cos \theta_\nu \right] \\
Q_{++}^{r>1} &= \frac{1}{2r} \left[ \left(1 + b \frac{m_e}{E_e}\right) - \frac{1}{4r} a\beta_e + \frac{1}{3r} PA\beta_e - \frac{2}{3} PB \right] \quad (3.13)
\end{aligned}$$

Since the polarization of  $Q_{++}$  is  $P$ , the polarization of  $Q_{--}$  is  $-P$ . Thus,  $Q_{++}$  and  $Q_{--}$  are related to each other as  $Q_{--} = Q_{++}(P \rightarrow -P)$ . Hence, for the two regions, we get

$$Q_{--}^{r\leq 1} = \left(1 + b \frac{m_e}{E_e}\right) \left(1 - \frac{r}{2}\right) + \frac{1}{4} a\beta_e \left(\frac{r^2}{2} - 1\right) - \frac{1}{2} PA\beta_e \left(1 - \frac{2r}{3}\right) - \frac{1}{2} PB \left(\frac{r^2}{3} - 1\right) \quad (3.14)$$

$$Q_{--}^{r>1} = \frac{1}{2r} \left[ \left(1 + b \frac{m_e}{E_e}\right) - \frac{1}{4r} a\beta_e - \frac{1}{3r} PA\beta_e + \frac{2}{3} PB \right] \quad (3.15)$$

Next, we consider  $\rho_{+-}$  in which  $\vec{p} \cdot \vec{s} > 0$  and  $\vec{p}_p \cdot \vec{s} < 0$ . Also, we assume only protons with the longitudinal kinetic energies  $T_z = \frac{(p_{pz})^2}{2m_p} \geq u$  can be detected where,  $p_{pz}$  is the proton longitudinal momentum. So now we need to calculate

$$Q_{+-} = \int_u d(\cos \theta_e) d(\cos \theta_\nu) \left[ 1 + b \frac{m_e}{E_e} + a\beta_e \cos \theta_e \cos \theta_\nu + PA\beta_e \cos \theta_e + PB \cos \theta_\nu \right] \quad (3.16)$$

The region of the integration is defined by  $\cos \theta_e > 0$  and

$$\begin{aligned}
\vec{p}_p \cdot \vec{s} = p_{pz} = -\beta_e E_e \cos \theta_e - E_\nu \cos \theta_\nu &\leq -\sqrt{2m_p u} \\
\implies E_\nu \cos \theta_\nu &\leq -\sqrt{2m_p u} + \beta_e E_e \cos \theta_e \\
\implies \cos \theta_\nu &\geq \frac{\sqrt{2m_p u}}{E_\nu} - \frac{\beta_e E_e}{E_\nu} \cos \theta_e \\
\implies \cos \theta_\nu &\geq \frac{\sqrt{2m_p u}}{E_\nu} - r \cos \theta_e
\end{aligned}$$

So  $\cos \theta_\nu \in [\frac{\sqrt{2m_p u}}{E_\nu} - r \cos \theta_e, +1]$  and also we have  $\cos \theta_e > 0$  for this case. Again, we have two case for  $u > 0$ :

- a. if  $\frac{\sqrt{2m_p u}}{E_\nu} - r \cos \theta_e > -1$ , the limit on the  $d(\cos \theta_\nu)$  integral is from  $(\frac{\sqrt{2m_p u}}{E_\nu} - r \cos \theta_e)$  to  $+1$ .
- b. if  $\frac{\sqrt{2m_p u}}{E_\nu} - r \cos \theta_e < -1$ , the limit on the  $d(\cos \theta_\nu)$  integral is from  $-1$  to  $+1$ .

If  $u = 0$ , we have the constraint on  $d(\cos \theta_\nu)$  but for  $\cos \theta_e > 0$ , there is no constraint on  $\cos \theta_\nu$ , hence

$$\begin{aligned}
\vec{p}_p \cdot \vec{s} = p_{pz} = -\beta_e E_e \cos \theta_e - E_\nu \cos \theta_\nu &< 0 \\
\implies E_\nu \cos \theta_\nu < \beta_e E_e \cos \theta_e &\implies \cos \theta_\nu > -\frac{\beta_e E_e}{E_\nu} \cos \theta_e \\
\implies \cos \theta_\nu > -r \cos \theta_e &> -r
\end{aligned}$$

So  $\cos \theta_e \in [0, 1]$  and  $r > 1$  or  $r < 1$ . Suppose  $r > 1$ , then  $\cos \theta_\nu > -r \cos \theta_e$  will always be satisfied, but  $\cos \theta_\nu \in [-1, +1]$ . Thus, for  $r > 1$  the integral over  $d(\cos \theta_e)$  and  $d(\cos \theta_\nu)$  in the three regions of the phase space (see Figure 3.3) gives  $Q_{+-}^{r>1}$  as

$$Q_{+-}^{r>1} = I + II + III \quad (3.17)$$

where,

$$I = \int_0^1 d(\cos \theta_e) \int_0^1 d(\cos \theta_\nu) \left[ 1 + b \frac{m_e}{E_e} + a \beta_e \cos \theta_e \cos \theta_\nu + PA \beta_e \cos \theta_e + PB \cos \theta_\nu \right] \quad (3.18)$$

$$II = \int_0^{1/r} d(\cos \theta_e) \int_{-r \cos \theta_e}^0 d(\cos \theta_\nu) \left[ 1 + b \frac{m_e}{E_e} + a \beta_e \cos \theta_e \cos \theta_\nu + PA \beta_e \cos \theta_e + PB \cos \theta_\nu \right] \quad (3.19)$$

and

$$III = \int_{1/r}^0 d(\cos \theta_e) \int_{-1}^0 d(\cos \theta_\nu) \left[ 1 + b \frac{m_e}{E_e} + a \beta_e \cos \theta_e \cos \theta_\nu + PA \beta_e \cos \theta_e + PB \cos \theta_\nu \right] \quad (3.20)$$

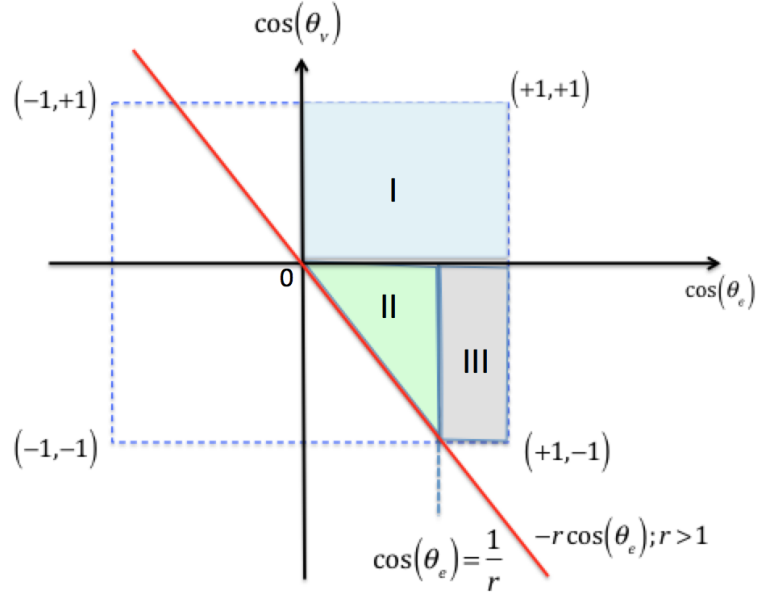


Figure 3.3: The shaded areas I, II and III are the three regions of the integral for  $Q_{+-}$  under the constraint  $r > 1$ .

If  $r < 1$ , the integral over  $d(\cos \theta_e)$  and  $d(\cos \theta_\nu)$  in the two regions of the phase space (see Figure 3.4) gives  $Q_{+-}^{r < 1}$  as

$$Q_{+-}^{r < 1} = I + IV \quad (3.21)$$

where,

$$IV = \int_0^1 d(\cos \theta_e) \int_{-r \cos \theta_e}^0 d(\cos \theta_\nu) \left[ 1 + b \frac{m_e}{E_e} + a \beta_e \cos \theta_e \cos \theta_\nu + PA \beta_e \cos \theta_e + PB \cos \theta_\nu \right] \quad (3.22)$$

The calculation of the integrals gives

$$\begin{aligned} I &= \left(1 + b \frac{m_e}{E_e}\right) + \frac{1}{4} a \beta_e + \frac{1}{2} PA \beta_e + \frac{1}{2} PB \\ II &= \frac{1}{2r} \left(1 + b \frac{m_e}{E_e}\right) - \frac{1}{8r^2} a \beta_e + \frac{1}{3r^2} PA \beta_e - \frac{1}{6r} PB \\ III &= \left(1 + b \frac{m_e}{E_e}\right) \left(1 - \frac{1}{r}\right) - \frac{1}{4} a \beta_e \left(1 - \frac{1}{r^2}\right) + \frac{1}{2} PA \beta_e \left(1 - \frac{1}{r^2}\right) - \frac{1}{2} PB \left(1 - \frac{1}{r}\right) \\ IV &= \left(1 + b \frac{m_e}{E_e}\right) \frac{r}{2} - \frac{1}{8} a \beta_e r^2 + \frac{1}{3} PA \beta_e r - \frac{1}{3} PB r^2 \end{aligned} \quad (3.23)$$

Putting these together from Eqn.3.23, we get

$$Q_{+-}^{r > 1} = \left(1 + b \frac{m_e}{E_e}\right) \left(2 - \frac{1}{2r}\right) + \frac{1}{8r^2} a \beta_e + \frac{1}{2} PA \beta_e \left(2 - \frac{1}{3r^2}\right) + \frac{1}{3r} PB \quad (3.24)$$

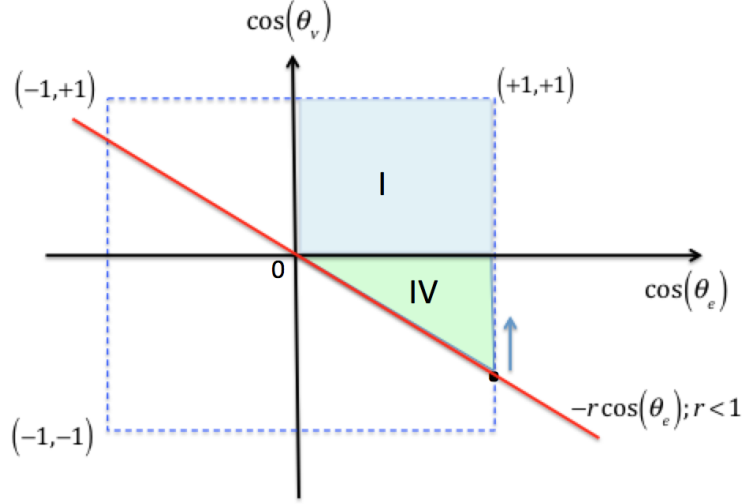


Figure 3.4: The shaded areas I and IV are the regions of the integral for  $Q_{+-}$  under the constraint  $r < 1$ .

and

$$Q_{+-}^{r < 1} = \left(1 + b \frac{m_e}{E_e}\right) \left(1 + \frac{r}{2}\right) + \frac{1}{4} a \beta_e \left(1 - \frac{r^2}{2}\right) + \frac{1}{2} P A \beta_e \left(1 + \frac{2r}{3}\right) + \frac{1}{2} P B \left(1 - \frac{r^2}{3}\right) \quad (3.25)$$

Introducing  $f_b = 1 + b \frac{m_e}{E_e}$ , the relationship among the  $Q_{ij}$ 's can be simply be expressed as

$$Q_{-+} = 2f_b - P A \beta_e - Q_{--} \quad (3.26)$$

and

$$Q_{+-} = 2f_b + P A \beta_e - Q_{++} \quad (3.27)$$

irrespective of whether  $r < 1$  or  $r > 1$ .

## 3.2 Differential and Integral Asymmetries

### 3.2.1 Proton Asymmetry

The proton asymmetry  $\alpha_p$  is defined by the following expression

$$\alpha_p = \frac{\rho_-^p - \rho_+^p}{\rho_-^p + \rho_+^p} \quad (3.28)$$

where  $\rho_+^p$  and  $\rho_-^p$  are the decay rates of the proton events for  $\vec{p}_p \cdot \vec{s} > 0$  and  $\vec{p}_p \cdot \vec{s} < 0$  respectively. These  $\rho$ 's are calculated by integrating over the electron energy  $E_e$  and

are different from the  $Q$ 's which are integrals only over the angular variables [60]. The decay rates for the proton are given by

$$\begin{aligned}\rho_+^p &= \rho_{++} - \rho_{--} + \rho_-^e \\ \rho_-^p &= \rho_{--} - \rho_{++} + \rho_+^e\end{aligned}\quad (3.29)$$

where

$$\rho_{\pm}^e = \frac{1}{4} \int_{m_e}^{\Delta} dE_e w_s(E_e) [2f_b \pm PA\beta_e] \quad (3.30)$$

$$\begin{aligned}\rho_{++} &= \frac{1}{4} \int_{m_e}^{\Delta} dE_e w_s(E_e) \int_0^{+1} d(\cos \theta_e) \int_{-1}^{\max(-1, -r \cos \theta_e)} d(\cos \theta_\nu) \\ &\quad \times [f_b + a\beta_e \cos \theta_e \cos \theta_\nu + PA\beta_e \cos \theta_e + PB \cos \theta_\nu]\end{aligned}\quad (3.31)$$

and using  $\rho_{--} = \rho_{++}[P \rightarrow -P]$ , we get

$$\begin{aligned}\rho_{--} &= \frac{1}{4} \int_{m_e}^{\Delta} dE_e w_s(E_e) \int_0^1 d(\cos \theta_e) \int_{-1}^{\max(-1, -r \cos \theta_e)} d(\cos \theta_\nu) \\ &\quad \times [f_b + a\beta_e \cos \theta_e \cos \theta_\nu - PA\beta_e \cos \theta_e - PB \cos \theta_\nu]\end{aligned}\quad (3.32)$$

Hence

$$\begin{aligned}\rho_+^p &= \frac{1}{4} \int_{m_e}^{\Delta} dE_e w_s(E_e) \int_0^1 d(\cos \theta_e) \int_{-1}^{\max(-1, -r \cos \theta_e)} d(\cos \theta_\nu) \\ &\quad \times [2PA\beta_e \cos \theta_e + 2PB \cos \theta_\nu] + \frac{1}{4} \int_{m_e}^{\Delta} dE_e w_s(E_e) [2f_b - PA\beta_e] \\ &= \frac{1}{4} \int_{m_e}^{\Delta} dE_e w_s(E_e) \left[ 2f_b - PA\beta_e + 2PA\beta_e \underbrace{\int_0^1 d(\cos \theta_e) \int_{-1}^{\max(-1, -r \cos \theta_e)} d(\cos \theta_\nu) \cos \theta_\nu}_I \right] \\ &\quad + \frac{1}{4} \int_{m_e}^{\Delta} dE_e w_s(E_e) \left[ 2PB \underbrace{\int_0^1 d(\cos \theta_e) \int_{-1}^{\max(-1, -r \cos \theta_e)} d(\cos \theta_\nu) \cos \theta_\nu}_{II} \right]\end{aligned}\quad (3.33)$$

Consider the case when  $r < 1 \implies r \cos \theta_e > -1$  and for  $r < 1$  (see Figure 3.1), we have

$$\begin{aligned}\rho_+^p &= \frac{1}{4} \int_{m_e}^{\Delta} dE_e w_s(E_e) \left[ 2f_b - PA\beta_e + 2PA\beta_e \int_0^1 d(\cos \theta_e) \int_{-1}^{-r \cos \theta_e} d(\cos \theta_\nu) \cos \theta_e \right] \\ &\quad + \frac{1}{4} \int_{m_e}^{\Delta} dE_e w_s(E_e) \left[ 2PB \int_0^1 d(\cos \theta_e) \int_{-1}^{-r \cos \theta_e} d(\cos \theta_\nu) \cos \theta_\nu \right]\end{aligned}\quad (3.34)$$

$$= \frac{1}{4} \int_{m_e}^{\Delta} dE_e w_s(E_e) \left[ 2f_b - PA\beta_e + PA\beta_e \left(1 - \frac{2r}{3}\right) + PB \left(\frac{r^2}{3} - 1\right) \right] \quad (3.35)$$

Referring to the same Figure 3.1, and integrating over the shaded region, we get

$$\begin{aligned} \rho_-^p &= \frac{1}{4} \int_{m_e}^{\Delta} dE_e w_s(E_e) \int_0^1 d(\cos \theta_e) \int_{-1}^{-r \cos \theta_e} d(\cos \theta_\nu) \\ &\quad \times \left[ -2PA\beta_e \cos \theta_e - 2PB \cos \theta_\nu \right] + \frac{1}{4} \int_{m_e}^{\Delta} dE_e w_s(E_e) \left[ 2f_b + PA\beta_e \right] \end{aligned} \quad (3.36)$$

$$= \frac{1}{4} \int_{m_e}^{\Delta} dE_e w_s(E_e) \left[ 2f_b + PA\beta_e - PA\beta_e \left(1 - \frac{2r}{3}\right) - PB \left(\frac{r^2}{3} - 1\right) \right] \quad (3.37)$$

For the other case of  $r > 1$ , which requires that  $-r \cos \theta_e > -1$  (see Figure 3.1), we have

$$\begin{aligned} \rho_+^p &= \frac{1}{4} \int_{m_e}^{\Delta} dE_e w_s(E_e) \left[ 2f_b - PA\beta_e + 2PA\beta_e \int_0^{1/r} d(\cos \theta_e) \int_{-1}^{-r \cos \theta_e} d(\cos \theta_\nu) \cos \theta_e \right] \\ &\quad + \frac{1}{4} \int_{m_e}^{\Delta} dE_e w_s(E_e) \left[ 2PB \int_0^{1/r} d(\cos \theta_e) \int_{-1}^{-r \cos \theta_e} d(\cos \theta_\nu) \cos \theta_\nu \right] \end{aligned} \quad (3.38)$$

$$= \frac{1}{4} \int_{m_e}^{\Delta} dE_e w_s(E_e) \left[ 2f_b - PA\beta_e + 2PA\beta_e \left(\frac{1}{6r^2}\right) + PB \left(\frac{-2}{3r}\right) \right] \quad (3.39)$$

Similarly, we get

$$\rho_-^p = \frac{1}{4} \int_{m_e}^{\Delta} dE_e w_s(E_e) \left[ 2f_b + PA\beta_e - 2PA\beta_e \left(\frac{1}{6r^2}\right) + PB \left(\frac{2}{3r}\right) \right] \quad (3.40)$$

Hence, the proton asymmetry  $\alpha_p$  for  $r < 1$  is given by (see Eqn.3.28)

$$\begin{aligned} \alpha_p^{r < 1} &= \frac{\frac{1}{4} \int_{m_e}^{\Delta} dE_e w_s(E_e) \left[ \frac{2r}{3} PA\beta_e + PB \left(1 - \frac{r^2}{3}\right) \right]}{\frac{1}{4} \int_{m_e}^{\Delta} dE_e w_s(E_e) [2f_b]} \\ &= \frac{\int_{m_e}^{\Delta} dE_e w_s(E_e) \left[ \frac{2r}{3} PA\beta_e + PB \left(1 - \frac{r^2}{3}\right) \right]}{\int_{m_e}^{\Delta} dE_e w_s(E_e) [2f_b]} \end{aligned} \quad (3.41)$$

And the proton asymmetry  $\alpha_p$  for  $r > 1$  is given by

$$\begin{aligned}\alpha_p^{r \geq 1} &= \frac{\frac{1}{4} \int_{m_e}^{\Delta} dE_e w_s(E_e) \left[ \left(1 - \frac{1}{3r^2}\right) PA\beta_e + \frac{2}{3r} PB \right]}{\frac{1}{4} \int_{m_e}^{\Delta} dE_e w_s(E_e) [2f_b]} \\ &= \frac{\int_{m_e}^{\Delta} dE_e w_s(E_e) \left[ \left(1 - \frac{1}{3r^2}\right) PA\beta_e + \frac{2}{3r} PB \right]}{\int_{m_e}^{\Delta} dE_e w_s(E_e) [2f_b]}\end{aligned}\quad (3.42)$$

This is the integral (integrated over the electron energy  $E_e$ ) expression for the proton asymmetry. The first single-particle proton asymmetry denoted by  $C_{exp}$ , differential in electron energy is defined as [6]

$$\begin{aligned}C_{exp} &= \frac{(Q_{+-} + Q_{--}) - (Q_{++} + Q_{-+})}{(Q_{+-} + Q_{--}) + (Q_{++} + Q_{-+})} \\ &= \frac{(2f_b + PA\beta_e - Q_{++} + Q_{--}) - (Q_{++} + 2f_b - PA\beta_e - Q_{--})}{(2f_b + PA\beta_e - Q_{++} + Q_{--}) + (Q_{++} + 2f_b - PA\beta_e - Q_{--})} \\ &= \frac{1}{2f_b} [(Q_{--} - Q_{++}) + PA\beta_e]\end{aligned}$$

Using the expressions of  $(Q_{--} - Q_{++})$  for the two cases with  $r < 1$  and  $r > 1$ , we get

$$C_{exp}^{r < 1} = \frac{1}{2f_b} \left[ \frac{2r}{3} PA\beta_e + PB \left(1 - \frac{r^2}{3}\right) \right] \quad (3.43)$$

And

$$C_{exp}^{r \geq 1} = \frac{1}{2f_b} \left[ \left(1 - \frac{1}{3r^2}\right) PA\beta_e + \frac{2}{3r} PB \right] \quad (3.44)$$

These are the differential form of the proton asymmetries which are the integrand of the integral asymmetries  $\alpha_p$ . Thus, we can write the proton asymmetry as a function of electron energy as

$$\alpha_p(E_e) = \frac{Q_-^p - Q_+^p}{Q_-^p + Q_+^p}, \quad (3.45)$$

where  $Q_-^p = Q_{+-} + Q_{--}$  and  $Q_+^p = Q_{++} + Q_{-+}$ . From this, it follows that

$$\alpha_p(E_e) = \begin{cases} P \frac{\frac{2r}{3} A\beta_e + B \left(1 - \frac{r^2}{3}\right)}{2f_b}, & r < 1, \\ P \frac{A\beta_e \left(1 - \frac{1}{3r^2}\right) + \frac{2}{3r} B}{2f_b}, & r \geq 1. \end{cases} \quad (3.46)$$

This represents the asymmetry in the number of protons emitted parallel and anti-parallel to the neutron spin as a function of the electron energy. It is also clear that

all dependence on  $b_\nu$  (via  $B$ ) is restricted to the numerator, whereas all dependence on  $b$  (via  $f_b = 1 + b\frac{m_e}{E_e}$ ) is restricted to the denominator only. If  $b = 0$ , then we can determine the value of  $b_\nu$  from the value of  $B$  using the proton asymmetry  $\alpha_p$  setting the polarization of the neutron to be  $P = \pm 1$ . The sign of the proton asymmetry  $\alpha_p$  is given by the corresponding sign of  $P$ . The correlation coefficients  $A$  and  $B$  can be taken to be constant for the lowest order approximation whereas  $\beta_e$  and  $r$  depend on electron energy given by

$$\begin{aligned}\beta_e(E_e) &= \frac{p_e}{E_e} = \frac{\sqrt{E_e^2 - m_e^2}}{E_e} = \frac{\sqrt{T_e^2 + 2T_em_e}}{T_e + m_e} \\ r(E_e) &= \frac{\beta_e E_e}{\Delta - E_e} = \frac{\beta_e(T_e + m_e)}{\Delta - (T_e + m_e)} = \frac{\sqrt{T_e^2 + 2T_em_e}}{\Delta - (T_e + m_e)}\end{aligned}\quad (3.47)$$

where  $T_e = E_e - m_e$  is the kinetic energy of the electron. With endpoint kinetic energy of  $\beta^-$  decay spectrum ( $T_{emax} = 782 \text{ keV}$ ), the  $Q_{ij}$ 's are separated into two regions ( $r < 1$ ,  $r \geq 1$ ) by  $r(E_e)$  such that  $r = 1$  corresponds to  $T_e = 236 \text{ keV}$ .

With  $f_b = 1$  and  $P = 1$  and from the electron energy dependent  $Q_{ij}$ -spectra, one can obtain the number of protons emitted in the hemisphere parallel ( $N_+^p \propto Q_+^p$ ) or anti parallel ( $N_-^p \propto Q_-^p$ ) to the neutron spin direction and use the Eqn.3.46 to obtain  $B$  through  $\alpha_p(E_e)$  given by

$$B(E_e) = \begin{cases} \frac{6\alpha_p - 2rA\beta_e}{3 - r^2}, & r < 1, \\ \frac{6r^2\alpha_p - A\beta_e(3r^2 - 1)}{2r}, & r \geq 1. \end{cases}\quad (3.48)$$

In the zeroth order approximation  $A = A_0$ , hence one can determine the value of  $B(E_e)$  as a function of the electron energy. A differential fit to  $B(E_e)$  can be used to obtain the lowest order Standard Model (SM) value of  $B_0$ .

### 3.2.2 Electron Asymmetry

The differential electron asymmetry  $\alpha_e$  as a function of electron energy is defined as

$$\alpha_e(E_e) = \frac{Q_-^e - Q_+^e}{Q_-^e + Q_+^e}\quad (3.49)$$

where  $Q_-^e = Q_{-+}^e + Q_{--}^e$  and  $Q_+^e = Q_{++}^e + Q_{+-}^e$ . Substituting the expressions from Eqn.3.26 and Eqn.3.27, we get

$$\alpha_e(E_e) = -\frac{1}{2f_b}PA\beta_e\quad (3.50)$$

From this, it follows that all of the dependence on  $b$  (via  $f_b$ ) is restricted to the denominator. Again, when  $b = 0$ , direct determination of the value of the correlation



coefficient  $A$  can be performed by a differential analysis of the electron energy ( $E_e$ ) dependent electron asymmetry  $\alpha_e$  from the  $\beta$ -decay spectrum using

$$A(E_e) = -2 \frac{\alpha_e(E_e)}{\beta_e(E_e)} \quad (3.51)$$

where  $P = 1$ . Thus, from the electron energy dependent  $Q_{ij}$ -spectra, one can obtain the number of electrons emitted in the hemisphere in parallel ( $N_+^e \propto Q_+^e$ ) or against ( $N_-^e \propto Q_-^e$ ) the neutron spin direction and use the Eqn.3.51 to obtain  $A$  through  $\alpha_e(E_e)$ .

### 3.2.3 Proton-Electron Asymmetry Ratio

Dividing each of the expressions in Eqn.3.46 by that given by Eqn.3.50, we immediately obtain the *ratio*  $r_{pe}$  of the proton and electron asymmetries as

$$r_{pe}(E_e) = \frac{\alpha_p(E_e)}{\alpha_e(E_e)} = \begin{cases} -\frac{2}{3}r - \frac{1}{\beta_e} \left(1 - \frac{r^2}{3}\right) \frac{B}{A}, & r < 1, \\ -\left(1 - \frac{1}{3r^2}\right) - \frac{2}{3r} \frac{1}{\beta_e} \frac{B}{A}, & r \geq 1 \end{cases} \quad (3.52)$$

This *ratio*  $r_{pe}$  is sensitive only to  $b_\nu$  (via  $B$ ) because all dependence on the Fierz term  $b$  (via  $f_b$ ) cancels in the ratio. Also, the polarization term automatically goes away. This opens up an avenue to measure  $B$  irrespective of the neutron polarization. Therefore, a simultaneous measurement of  $\alpha_p(E_e)$  and  $\alpha_e(E_e)$  in the same apparatus will permit an extraction of  $b_\nu$  via their ratio  $r_{pe}$ . The expression for  $B$  in terms of ratio then becomes

$$B(E_e) = \begin{cases} \frac{A\beta_e}{r^2 - 3} (3r_{pe} + 2r), & r < 1, \\ \frac{1}{2}A\beta_e r \left(\frac{1}{r^2} - 3r_{pe} - 3\right), & r \geq 1 \end{cases} \quad (3.53)$$

Hence, a determination of the value of  $B$  can be performed by a differential analysis of the electron energy ( $E_e$ ) dependent proton-electron asymmetry ratio  $r_{pe}$  from the  $Q_{ij}$ -spectra.

## 3.3 Electron-Proton Coincidence Asymmetries

### 3.3.1 Neutrino Asymmetry

The differential neutrino asymmetry  $\alpha_{ep}(E_e)$ , is defined as [60]

$$\alpha_{ep}(E_e) = \frac{Q_{--} - Q_{++}}{Q_{--} + Q_{++}} \quad (3.54)$$

Substituting the expressions for  $Q_{--}$  and  $Q_{++}$  from the earlier derivation, we get

$$\alpha_{ep}(E_e) = \begin{cases} -\frac{4P}{3} \frac{[A\beta_e(3-2r) + B(r^2-3)]}{[4f_b(2-r) + a\beta_e(r^2-2)]}, & r < 1, \\ \frac{4P}{3} \frac{(-A\beta_e + 2rB)}{(4rf_b - a\beta_e)}, & r \geq 1, \end{cases} \quad (3.55)$$

Although this asymmetry is quite sensitive to  $B$ , it offers less sensitivity to  $b_\nu$  or  $b$ . The reason for this can be seen explicitly in Eqn. 3.55, where one sees  $b_\nu$  ( $b$ ) appears in the numerator (denominator), leading to significantly reduced sensitivity due to their similar dependence on scalar and tensor physics. The expression for  $B$  with  $P = 1$  and  $f_b = 1$  in terms of the neutrino asymmetry becomes

$$B(E_e) = \begin{cases} \frac{\frac{3}{4}\alpha_{ep} [(8-4r) + a\beta_e(r^2-2)] - A\beta_e(2r-3)}{3-r^2}, & r < 1, \\ \frac{\frac{3}{4}\alpha_{ep}(4r - a\beta_e) + A\beta_e}{2r}, & r \geq 1, \end{cases} \quad (3.56)$$

Hence, with the given values of the correlation coefficients ( $a$  and  $A$ ), direct determination of the value of  $B$  can be performed by a differential analysis of the electron energy ( $E_e$ ) dependent neutrino asymmetry  $\alpha_{ep}$  from the  $Q_{ij}$ -spectra.

### 3.3.2 Electron-Proton Tilde Asymmetry

Another differential asymmetry proposed in Ref. [60] is the electron-proton tilde asymmetry ( $\tilde{\alpha}_{ep}$ ) and is defined as

$$\tilde{\alpha}_{ep}(E_e) = \frac{Q_{+-} - Q_{-+}}{Q_{+-} + Q_{-+}} \quad (3.57)$$

Substituting the expressions for  $Q_{+-}$  and  $Q_{-+}$  and following some simplification, we get

$$\tilde{\alpha}_{ep}(E_e) = \begin{cases} P \frac{A\beta_e \left(1 + \frac{2r}{3}\right) - B \left(\frac{r^2}{3} - 1\right)}{f_b(2+r) - \frac{1}{2} \left(\frac{r^2}{2} - 1\right) a\beta_e}, & r < 1, \\ P \frac{\left(2 - \frac{1}{3r^2}\right) A\beta_e + \frac{2}{3r} B}{\left(4 - \frac{1}{r}\right) f_b + \frac{1}{4r^2} a\beta_e}, & r \geq 1, \end{cases} \quad (3.58)$$

As noted in Ref. [60], this asymmetry offers sensitivity to  $B$  (and, hence,  $b_\nu$ ) at low energies (note the  $2/3r$  suppression factor on  $B$  for  $r > 1$  higher energies), and is useful

for extracting a value of  $\lambda$ . Compared to  $\alpha_{ep}$ ,  $\tilde{\alpha}_{ep}(E_e)$  offers improved sensitivity to BSM physics. The expression for  $B$  with  $P = 1$  and  $f_b = 1$  in terms of electron-proton tilde asymmetry becomes

$$B(E_e) = \begin{cases} \frac{1}{(r^2-3)} \left[ A\beta_e (3 + 2r) - \frac{3}{4}\tilde{\alpha}_{ep} (8 + 4r - (r^2 - 2)a\beta_e) \right], & r < 1, \\ \frac{3r}{2} \left[ \tilde{\alpha}_{ep} \left( 4 - \frac{1}{r} + \frac{1}{4r^2}a\beta_e \right) - \left( 2 - \frac{1}{3r^2} \right) A\beta_e \right], & r \geq 1, \end{cases} \quad (3.59)$$

Thus, direct determination of the value of  $B$  can be done with the given values of the correlation coefficients ( $a$  and  $A$ ), by a differential analysis of the electron energy ( $E_e$ ) dependent tilde asymmetry  $\tilde{\alpha}_{ep}$  from the  $Q_{ij}$ -spectra.

### 3.3.3 New Coincidence Asymmetry $\alpha_x$

The first of the new coincidence differential asymmetry  $\alpha_x(E_e)$  is defined as

$$\alpha_x(E_e) = \frac{Q_{--} - Q_{++}}{Q_{+-} - Q_{-+}} \quad (3.60)$$

Substituting the expressions for  $Q_{ij}$  in terms of angular correlation coefficients, we get

$$\alpha_x(E_e) = \begin{cases} \frac{-A\beta_e \left( 1 - \frac{2r}{3} \right) + B \left( 1 - \frac{r^2}{3} \right)}{A\beta_e \left( 1 + \frac{2r}{3} \right) + B \left( 1 - \frac{r^2}{3} \right)}, & r < 1 \\ \frac{-A\beta_e \frac{2}{3r} + \frac{4}{3}B}{4r\beta_e \left( 1 - \frac{1}{6r^2} \right) + \frac{4}{3}B}, & r \geq 1 \end{cases} \quad (3.61)$$

It is clear that  $\alpha_x(E_e)$  does not depend on  $b$  and can be exploited to extract the value of  $B$  given the value of the correlation  $A$ . More explicitly,  $B$  as a function of  $\alpha_x(E_e)$  can be written as

$$B(E_e) = \begin{cases} \frac{A\beta_e}{(1 - \frac{r^2}{3})} \left[ \frac{1 + \alpha_x}{1 - \alpha_x} - \frac{2r}{3} \right], & r < 1, \\ \frac{A\beta_e}{(1 - \alpha_x)} \left[ 3 \left( r - \frac{1}{6r} \right) \alpha_x + \frac{1}{2r} \right], & r \geq 1, \end{cases} \quad (3.62)$$

Hence, given the value of the correlation coefficient ( $A$ ), direct determination of the value of  $B$  can be performed by a differential analysis of the electron energy ( $E_e$ )

dependent coincidence asymmetry  $\alpha_x(E_e)$  from the  $Q_{ij}$ -spectra.

Note: We can also construct a new coincidence differential asymmetry  $\alpha_y(E_e)$  defined by

$$\alpha_y(E_e) = \frac{Q_{--} - Q_{++}}{Q_{+-} + Q_{-+}} \quad (3.63)$$

Putting the expressions for  $Q_{ij}$  in terms of angular correlation coefficients, we get

$$\alpha_y(E_e) = \begin{cases} P \frac{-\left(1 - \frac{2r}{3}\right) A\beta_e + B \left(1 - \frac{r^2}{3}\right)}{2 \left(1 + \frac{r}{2}\right) f_b + \frac{1}{2} a\beta_e \left(1 - \frac{r^2}{2}\right)}, & r < 1 \\ P \frac{-\frac{2}{3r} A\beta_e + \frac{4}{3} B}{\left(4 - \frac{1}{r}\right) f_b + \frac{1}{4r^2} a\beta_e}, & r \geq 1 \end{cases} \quad (3.64)$$

It is clear that  $\alpha_y(E_e)$  depend on  $b$  via  $f_b$  and  $b_\nu$  via  $B$  along with the dependence on  $A$  and  $a$ . In principle, we can use this asymmetry to obtain the  $B$  but it is not possible to separate out  $b$  from  $b_\nu$ . Hence, this is the least sensitive asymmetry among others to the BSM physics.

### 3.3.4 New Coincidence Asymmetry $\alpha_R$

The differential asymmetry  $\alpha_R(E_e)$ , is constructed such that it is independent of  $b$  and depends on  $b_\nu$  via  $B$  and is defined as

$$\alpha_R(E_e) = \begin{cases} \frac{\left[\left(1 + \frac{r}{2}\right) Q_{++} - \left(1 - \frac{r}{2}\right) Q_{+-}\right] - \left[\left(1 + \frac{r}{2}\right) Q_{--} - \left(1 - \frac{r}{2}\right) Q_{-+}\right]}{\left[\left(1 + \frac{r}{2}\right) Q_{++} - \left(1 - \frac{r}{2}\right) Q_{+-}\right] + \left[\left(1 + \frac{r}{2}\right) Q_{--} - \left(1 - \frac{r}{2}\right) Q_{-+}\right]}, & r < 1, \\ \frac{\left[\left(2 - \frac{1}{2r}\right) Q_{++} - \frac{1}{2r} Q_{+-}\right] - \left[\left(2 - \frac{1}{2r}\right) Q_{--} - \frac{1}{2r} Q_{-+}\right]}{\left[\left(2 - \frac{1}{2r}\right) Q_{++} - \frac{1}{2r} Q_{+-}\right] + \left[\left(2 - \frac{1}{2r}\right) Q_{--} - \frac{1}{2r} Q_{-+}\right]}, & r \geq 1, \end{cases} \quad (3.65)$$

Substituting the expressions for  $Q_{ij}$ 's in terms of angular correlation coefficients, we get

$$\alpha_R(E_e) = \begin{cases} P \frac{-\frac{r}{3}A\beta_e + 2\left(\frac{r^2}{3} - 1\right)B}{\frac{1}{2}a\beta_e(r^2 - 2)}, & r < 1 \\ P \frac{\left(r - \frac{2}{3}\right)A\beta_e + \frac{4r}{3}B}{\frac{1}{2}a\beta_e} & r \geq 1 \end{cases} \quad (3.66)$$

It is clear that  $\alpha_R(E_e)$  also does not depend on  $b$  and can be used to obtain the value of  $B$  given the value of the angular correlations  $A$  and  $a$ . More explicitly,  $B$  as a function of  $\alpha_R(E_e)$  with  $P = 1$  can be written as

$$B(E_e) = \begin{cases} \frac{\beta_e}{2(r^2 - 3)} \left[ \frac{3}{2}a(r^2 - 2)\alpha_R + Ar \right], & r < 1, \\ \frac{3\beta_e}{4r} \left[ \frac{1}{2}a\alpha_R - \left(r - \frac{2}{3}\right)A \right], & r \geq 1, \end{cases} \quad (3.67)$$

Hence, given the value of angular correlation coefficients ( $A$  and  $a$ ), direct determination of the value of  $B$  can be determined by a differential analysis of the electron energy ( $E_e$ ) dependent coincidence asymmetry  $\alpha_R(E_e)$  from the  $Q_{ij}$ -spectra.

### 3.4 Integral Asymmetries

The integral asymmetries, corresponding to the proton asymmetry  $\alpha_p$  and electron asymmetry  $\alpha_e$  are defined by

$$\langle \alpha_p \rangle = \frac{\int dE_e w_s(E_e) (Q_-^p) - \int dE_e w_s(E_e) (Q_+^p)}{\int dE_e w_s(E_e) (Q_-^p) + \int dE_e w_s(E_e) (Q_+^p)}, \quad (3.68)$$

$$\langle \alpha_e \rangle = \frac{\int dE_e w_s(E_e) (Q_-^e) - \int dE_e w_s(E_e) (Q_+^e)}{\int dE_e w_s(E_e) (Q_-^e) + \int dE_e w_s(E_e) (Q_+^e)}. \quad (3.69)$$

where the integrals are over some prescribed energy range. Under the integral technique, one would extract the asymmetries from the numbers of counts within some energy range, and then compare the resulting ratio of integral asymmetries,  $r_{pe} = \langle \alpha_p \rangle / \langle \alpha_e \rangle$ , to the value the ratio would assume under the Standard Model (i.e.,  $b_\nu = 0$ ). In contrast to the differential fitting technique, one would not perform a direct fit for any evidence of BSM physics, but would instead, under a global analysis

of other neutron  $\beta$ -decay observables, search for a pull on the observed value from that expected under the Standard Model.

The integral asymmetry corresponding to  $\alpha_{ep}$  is given by

$$\langle \alpha_{ep} \rangle = \frac{\int dE_e w_s(E_e) (Q_{--}) - \int dE_e w_s(E_e) (Q_{++})}{\int dE_e w_s(E_e) (Q_{--}) + \int dE_e w_s(E_e) (Q_{++})}. \quad (3.70)$$

where the integrals are over some prescribed energy range. Using the integral expression, we can determine asymmetry the  $\langle \alpha_{ep} \rangle$  from the numbers of counts within some energy range of the  $Q_{ij}$ -spectra.

Similarly, the integral asymmetry corresponding to  $\tilde{\alpha}_{ep}$  is given by

$$\langle \tilde{\alpha}_{ep} \rangle = \frac{\int dE_e w_s(E_e) (Q_{+-}) - \int dE_e w_s(E_e) (Q_{-+})}{\int dE_e w_s(E_e) (Q_{+-}) + \int dE_e w_s(E_e) (Q_{-+})}. \quad (3.71)$$

as usual, the integrals are over some specified energy range. Again using this integral technique, we can extract the asymmetry  $\langle \tilde{\alpha}_{ep} \rangle$  from the numbers of counts within some energy range of the  $Q_{ij}$ -spectra.

Another integral asymmetry corresponding to the asymmetry  $\alpha_x$  can be constructed as usual and is given by

$$\langle \alpha_x \rangle = \frac{\int dE_e w_s(E_e) (Q_{--}) - \int dE_e w_s(E_e) (Q_{++})}{\int dE_e w_s(E_e) (Q_{+-}) - \int dE_e w_s(E_e) (Q_{-+})}. \quad (3.72)$$

where the integrals are over some specified energy interval. We can extract the new coincidence asymmetry  $\langle \alpha_x \rangle$  from the numbers of counts within some specified energy range of the  $Q$ -spectra.

The integral approach is the usual way to extract the asymmetries and by doing the global analysis of the other neutron  $\beta$ -decay observable one can obtain the observed value as demanded by the Standard Model. Also, it should be noted that while implementing the integral techniques for analysis of  $\beta$ -decay parameters, one must take into account of the change in the functional form of the  $Q_{ij}$ 's at  $r = 1$ .

## Chapter 4 Simulation

### 4.1 UCNB Experiment

UCNB aims to measure the antineutrino asymmetry  $B$  between the neutron spin and the emitted antineutrino momentum with better than 0.1 % precision using ultracold neutrons. The experiment is designed to utilize polarized ultracold neutrons (UCN) at the Los Alamos Neutron Science Center (LANSCE) UCN facility ([3], [77]). UCNB will be carried out with ultracold neutrons at the Ultracold Neutron Source at Los Alamos National Laboratory. The UCNB collaboration has developed a significantly advanced detection system over earlier approaches. The most important challenges in this experiment is the coincident detection of electrons and recoil protons by the detector system. In general, the requirements for detection of protons include very low noise and a thin entrance window in addition to the accelerating potential. Also in order to determine the electron energy, the detector must have sufficient thickness to fully stop the electron and a very thin dead layer to limit the corrections needed for energy loss and backscattering. The antineutrinos emitted in

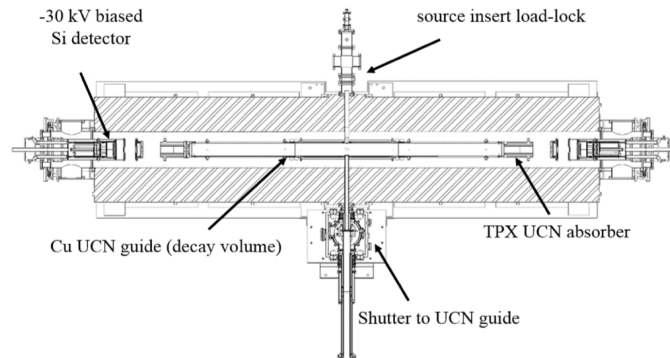


Figure 4.1: The UCNB experiment modifies the UCNA superconducting spectrometer (SCS) to include biasable detection systems and an open decay trap to determine the proton and electron directions.

the decay process of UCN are not directly detected as they do not interact with the detector due their infinite penetrating power. Hence, in the experiment, the information about the neutrino direction/momentum is determined from the proton and electron directions/momenta. The UCNB experiment is performed using a modified version of the UCNA apparatus (Fig. 4.1) [99]. In both the experiments, silicon is used as the detector material and uses magnetic field to guide the electrically charged particles.

### 4.1.1 UCNB Geometry

The experimental concept and design according to the UCNB and Nab collaborators [3], is the modification of the Ultracold Neutron Asymmetry (UCNA) experiment. The UCNB experimental geometry consist of a hollow cylindrical copper decay trap of length  $\sim 3.0$  m. The radius of the decay trap is about 12.7 cm and this diamond-like carbon-coated copper guide is located inside the 1 T superconducting spectrometer (SCS) magnet, with identical detectors at either end. In the case of UCNA, thin Beryllium coated Mylar foils are used at the ends of the guide to completely trap UCN but allowing electrons to pass through. But in the UCNB experiment, copper end caps with 3.8 cm diameter central holes are used to allow the protons of energy  $< 800$  eV within the viewing area of the detector to escape, while still partially trapping UCN. A TPX Polymethylpentene 1 tube is installed between the decay trap and the detection system. The purpose of TPX tube is to absorb UCN and reduce decays in the magnetic field expansion region. The detectors are located in the homogeneous 0.6 T region in the magnetic field expansion region.

The main idea is that the decay of the polarized UCN gives two charged particles which are guided by the magnetic field to one of the two detectors located at  $\pm Z$  directions. The detectors are biased to  $-30$  kV to accelerate the protons with enough energy to be detected. The number of coincident events  $N^{ep} = (N^{++}, N^{--})$  permits an extraction of the asymmetry according to

$$B_{(Exp)}(E_e) = \frac{N^{--}(E_e) - N^{++}(E_e)}{N^{--}(E_e) + N^{++}(E_e)} \quad (4.1)$$

This experimental asymmetry is a function of neutrino asymmetry parameter,  $B$ , electron asymmetry,  $A$  electron-neutrino asymmetry,  $a$  and the electron energy,  $E_e$ . Using the other experimentally determined values, the magnitude of  $B$  can be extracted to the level of 0.1 % [100] from the current experimental set up.

### 4.1.2 Magnetic field

The general requirements for the magnetic field within the decay trap is that it must be aligned with the axis of the decay trap to define the axis of polarization. The field also needs to be strong enough to confine the cyclotron radius of the decay products (electrons and protons) as they spiral toward the detectors without interacting with the walls of the decay trap. The field has to be uniform so that decaying particles will not be reflected during their motion toward the detectors. The cyclotron (Larmor) radius ( $r_i$ ) of a relativistic charged ( $q_i$ ) particle of mass ( $m_i$ ) gyrating in a uniform magnetic field,  $B$  is given by

$$r_i = \frac{p_{i\perp}}{|q_i|B} = \gamma_i \frac{m_i v_{i\perp}}{|q_i|B} \quad (4.2)$$

where,  $i = (e, p)$  corresponds to electron and proton respectively and

$$\gamma_i = \frac{1}{\sqrt{1 - \frac{v_i^2}{c^2}}}$$



Here,  $p_{i\perp}$  is the component of the momentum perpendicular to the direction of the magnetic field. In general, from Eqn. 4.2, the Larmor radius for proton seems to be larger than that for an electron due to the large difference in the masses. But, it is the perpendicular component of the momentum that determines the radius. Since, in the decay of free neutrons, the momentum of the two particles are comparable so their Larmor radii for a given magnetic field are similar. Hence, the strength of magnetic field which will be able to confine an electron will confine a proton, too. The strength of the magnetic field in the region of the decay trap is 1 T and from the end of the decay trap to the detector is the field expansion from 1 T to 0.6 T. Also, we know from J. D. Jackson [101], the flux through the spiral of the particles around the uniform magnetic field is an adiabatic invariant, that is

$$Br_i^2 \sim \frac{p_{i\perp}^2}{B}$$

The momentum of the particle can be written as

$$p_i = \sqrt{p_{i\parallel}^2 + p_{i\perp}^2}$$

A charged particle emitted with momentum  $p_{i,0} = (p_{i\parallel,0}^2 + p_{i\perp,0}^2)^{1/2}$  where  $p_{i\parallel,0}$  ( $p_{i\perp,0}$ ) is the initial transverse (longitudinal) momentum component, in some field  $B_0$  will be reflected from the field regions  $B$  if

$$B > B_{crit} \equiv \frac{p_{i,0}^2}{p_{i\perp,0}^2} B_0 \quad (4.3)$$

The pitch angle of the gyrating particle in the field is given by

$$\theta_i = \cos^{-1} \left( \frac{p_{i\parallel}}{p_i} \right) \quad (4.4)$$

The particle emitted with the large pitch angle near the local field minimum will be trapped. Hence, the magnetic field inside the decay trap must be extremely uniform to minimize particle localization instead of spiralling toward the detectors. So by decreasing the pitch angle, we can decrease the probability of backscattering of the particles drastically. Under the adiabatic condition, the pitch angle depends on the local field value  $B(z)$  and the starting angle  $\theta_1$  at field  $B_1$  (at  $z = z_0$ ) is given by

$$\sin \theta(z) = \sqrt{\frac{B(z)}{B_1}} \sin \theta_0 \quad (4.5)$$

But, under the adiabatic transport condition, the Larmor radius of the particle (both electron and proton) about the magnetic field along the  $z$ -direction increases in going from a uniform field ( $B_1$ ) to the field expansion region of the detectors which is given by

$$r(z) = \sqrt{\frac{B_1}{B(z)}} r_0 \quad (4.6)$$

In the case of the UCNB spectrometer, the fields are  $B_1 = 1 T$  and  $B(z) = 0.6 T$  so the pitch angle and Larmor radius at the location of the two silicon detectors are given by

$$\sin \theta(z) = \sqrt{0.6} \sin \theta_0, \quad r(z) = \frac{1}{\sqrt{0.6}} r_0 \quad (4.7)$$

It is for this reason that the silicon detector disks have larger radii as compared to the exit radii of the two ends of the decay trap.

### 4.1.3 Time of Flight

The time of flight ( $t_i$ ) of a relativistic charged particle (electron or proton) in a uniform magnetic field  $B$  depends on the energy  $E_i$ , and its polar emission angle  $\theta_i$  relative to the axis  $z$  of the magnetic field and is given by [102]

$$t_i = \frac{z_0}{v_i \cos \theta_i} = \frac{z_0}{\beta_i \cos \theta_i} \quad (4.8)$$

where, as usual  $i = (e, p)$  and  $z_0$  is the distance of the detector from the point origin of an electron or proton event. With  $c = 1$ ,  $\beta_i = v_i$  and is given by

$$\beta_i = \frac{p_i}{E_i} = \frac{\sqrt{E_i^2 - m_i^2}}{E_i} \quad (4.9)$$

Solving for  $E_i$ , we get

$$E_i = m_i \frac{t_i \cos \theta_i}{\sqrt{t_i^2 \cos^2 \theta_i - z_0^2}} \quad (4.10)$$

and the kinetic energy ( $T_i$ ) of the particle as a function of time of flight  $t_i$  and emission angle  $\theta_i$  is given by

$$T_i = m_i \left( \frac{t_i \cos \theta_i}{\sqrt{t_i^2 \cos^2 \theta_i - z_0^2}} - 1 \right) \quad (4.11)$$

However, for the the non-uniform field as in the case of the UCNB experiment, the time of flight of the particle is given by

$$t_i = \int_{z_1}^{z_2} \frac{dz}{\beta_i \cos \theta_i} = \frac{1}{\beta_i} \int_{z_1}^{z_2} \frac{dz}{\sqrt{1 - \frac{B^2(z)}{B_1^2} \sin^2 \theta_0}} \quad (4.12)$$

Hence, the difference in the time of flight for the electron and proton comes from the difference in the  $\beta_i$  and can be used to distinguish between the electron and proton events [103].

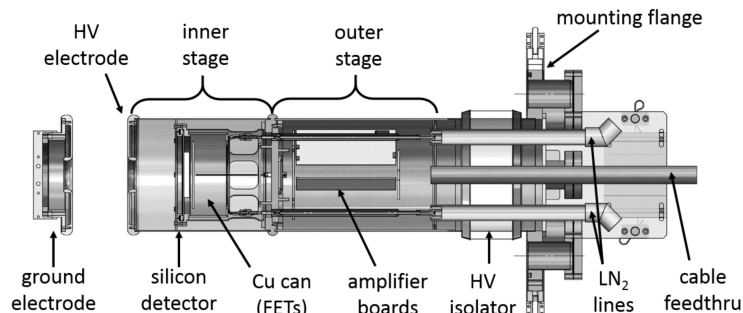


Figure 4.2: The detector mount carries the detector, preamplifier electronics, liquid nitrogen lines, and allows for high voltage bias up to 30 kV. The inner stage is in vacuum and the outer stage is in air [3].

#### 4.1.4 Detection System

The detector system is shown in Fig. 4.2. The detection system consists of highly segmented silicon detectors about 2 mm thick. The active area has a diameter of about 11.5 cm and a thin front dead layer of about 100 nm thick. A dead layer is a silicon layer created by the rectifying junction through which charged particles must pass to be detected [3]. The front junction for the active area is created by a shallow boron implant to give a reduced dead layer, while the periphery has a deep implant to ensure good contact [3]. The junction face is metallized with a 300 nm thick, square aluminum grid to improve charge collection. The detector system carries the detector, preamplifier electronics, liquid nitrogen lines, and allows for high voltage bias up to 30 kV for the detection of proton. The main problem in the experiment is the detection of protons due to their low energies as compared to the electron detection. The efficiency of detecting protons is further made worse due to the presence of the dead layer which has to be penetrated in order to be detected. Since most of the proton events are lost in the dead layer, it becomes harder to perform electron-proton coincidence experiment. A particle interacting with this layer will lose its energy without detection and therefore it is important to minimize the thickness of the dead layer [104]. This is one of the main issues in detector development for the this experiment where the dead layer must be thin enough to detect low energy protons ( [104], [105]). Nevertheless, using suitable biasing of the detector to accelerate proton helps enormously to overcome the dead layer enough to be detected by the silicon detectors. The main principle involved in the identification of proton and electron events is their time of flight measurements from the energy vs. timing spectra of the coincidence events [106].

#### 4.1.5 Experimental Concept

The UCNB experimental concept according to W. S. Wilburn et al. is shown in the Fig.4.3 [4]. UCNs produced by the LANSCE source pass through a polarizing magnet and spin flipper and then enter the decay volume located inside a spectrometer

magnet. Similar to the UCNA experiment [107], the neutrons are initially polarized using the  $\pm 60$  neV/T potential. The UCN pass through the 6 T prepolarizing magnet and then through the 7 T primary AFP (Adiabatic Fast Passage) polarizing magnet. Neutrons with spin aligned to the field (the magnetic moment of the neutron is negative and so is anti-parallel to the spin) see a repulsive potential of 420 neV from the 7 T magnet, so all the UCNs in this spin states get reflected. The opposite spin states sees an attractive potential and is transmitted, thus producing completely polarized UCNs beyond the AFP magnet. At this point, the neutrons pass through the AFP spin flipper. If the spin flipper is on, the spins undergo a  $\pi$  spin-flip before entering into the decay volume, and when off, the spins remain in the same state that was selected by the AFP magnet. The polarizer produces a neutron polarization

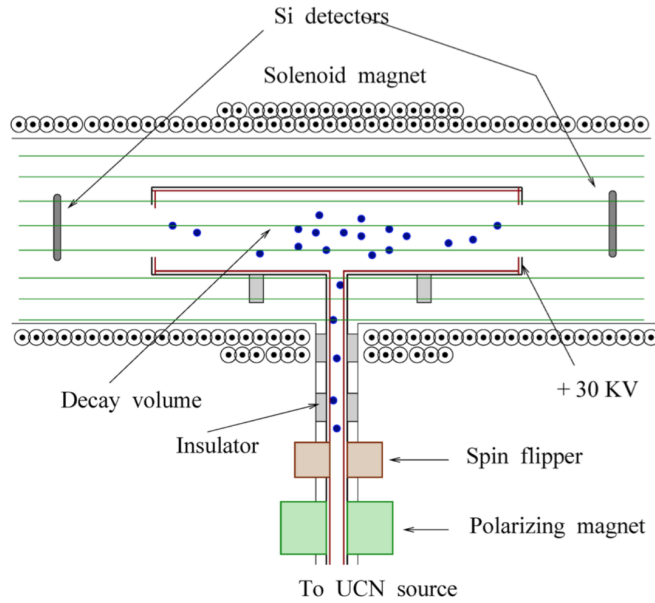


Figure 4.3: Schematic diagram for the UCNB experimental setup [4].

about  $\sim 0.99$ , and the spin flipper can reverse the neutrons polarization direction with an efficiency  $\geq 0.997$ . This will allow to cancel the systematic effects related to differences in the detector efficiencies. The electrons and protons obtained from the decay of the UCNs are confined to spiral about the magnetic field of 1 T until they reach the silicon detectors. In order to avoid back scattering the magnetic field as in the UCNA spectrometer can be implemented here. Since the end point energy of the proton is very small  $\sim 0.751$  keV, it is not possible to detect, so an electric potential of 30 keV is applied outside the decay trap to accelerate the proton to be detected by the silicon detectors. The proton and electron events are detected at different times in the detectors from which coincidence events are determined. The experimental proton asymmetry as a function of the electron energy can be determined using Eqn. 4.1 and  $B$  can be extracted [90].

## 4.2 Overview of Simulation

The present work is the simulation of the UCNB experiment to determine the value of the neutrino-asymmetry  $B$  very precisely. The energy scale for electron,  $0-800.0 \text{ MeV}$  is about thousand times higher than for the proton which is  $0-751.0 \text{ eV}$  [108]. Furthermore, applying energy-momentum conservation laws to the three body decay process, the energy and the momentum of the emitted antineutrinos can be reconstructed. In general, all the physics process are accounted and are tractable within simulation. GEANT4 (**GE**ometry **ANd** **T**racking **4**) is an object-oriented Monte Carlo simulation toolkit that has been developed by a worldwide collaboration of scientists [109]. It simulates the passage of particles through matter. The GEANT4 simulation [98] for the realistic UCNB geometry gives the detailed analysis of the decay process through particle tracking irrespective of the energy scale of the involved particles.

### 4.2.1 Geometry

The geometry of the simulation consists of a decay trap and a detector system. The decay trap is a 3.0 m long copper cylinder with inner and outer radius 6.5 cm and 7.0 cm respectively so that the thickness of the copper tube is 5.0 mm. The origin of the coordinate system coincides with the center of the copper cylinder with the  $z$ -axis along the cylindrical axis such that the ends of the tube lie at coordinates  $(0, 0, \pm 1.5) \text{ m}$ . Two silicon disks each of radii 8.0 cm and thickness 2.0 mm are placed

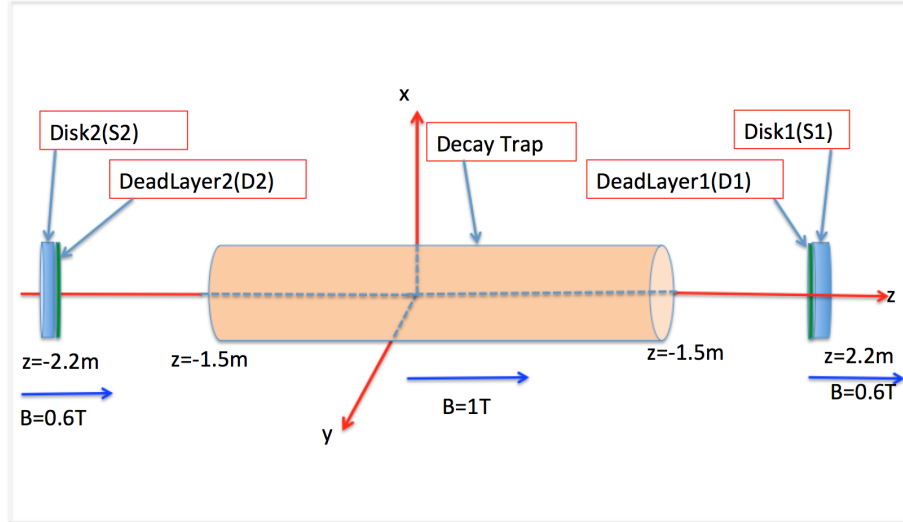


Figure 4.4: Schematic diagram for the UCNB simulation geometry.

on either sides of the cylindrical axis at  $(0, 0, \pm 2.2) \text{ m}$ . Each of these disks has dead layers of thickness 80.0 nm and the axis of these disks coincides with the axis of the cylinder. The decay trap is placed in a uniform magnetic field of 1.0 T along the axis. This field extends from  $z = -1.5 \text{ m}$  to  $z = 1.5 \text{ m}$ . The magnetic field drops to 0.6 T at the detector location such that the field gradient between the end of the decay

trap to the detector is  $\frac{\partial B}{\partial z} = -\frac{4}{7}$  T/m. The detectors in this geometry are labelled as Silicon Disk1 ( $S_1$ ), Dead Layer1 ( $D_1$ ), Silicon Disk2 ( $S_2$ ) and Dead Layer2 ( $D_2$ ) as shown in the figure 4.4. The medium inside the decay trap and outside the detector system is a vacuum. This makes the geometry simple as there are only five places (four detectors and a decay trap) for the particles to deposit energy. The events are generated uniformly within the cylindrical volume of radius 6.5 cm and length,  $l = 3$  m.

#### 4.2.2 Magnetic Field

The input geometry into the Geant4 simulation is taken directly from UCNA with a slight modification to meet the requirement for UCNB experiment as stated in the earlier sections of this chapter. Also, in the simulation any other differences in the geometry is also incorporated in the detector construction. The magnetic field is assumed to be perfectly uniform along the axis of the decay trap. This is done to save the computational time. In the real experiment, the magnetic field profile inside the spectrometer is not flat [5]. The magnitude of the field is 1 T in the decay trap with the field expansion to 0.6 T at the detector locations on either sides of the decay trap.

The magnetic field is passed to the simulation as a set of discrete  $B_z$  values along the  $z$ -axis of the spectrometer. The continuous field profile on the  $z$ -axis is then interpolated between consecutive  $z_i$  locations using the respective  $B_z(z_i)$  values by a half-wave of a cosine function [110] given by

$$B_z(z) = \frac{B_z(z_i) + B_z(z_{i+1})}{2} + \frac{B_z(z_i) - B_z(z_{i+1})}{2} \cos\left(\frac{z - z_i}{z_{i+1} - z_i}\pi\right) \quad (4.13)$$

where  $z_i < z_{i+1}$ . Now the magnetic field is taken to be azimuthally symmetric ( $B_\phi = 0$ ) so that, we have

$$\vec{B}(r, z) = B_r(r, z)\hat{r} + B_z(r, z)\hat{z} \quad (4.14)$$

From Maxwell's equations, the radial component of the magnetic field can be calculated as

$$\nabla \cdot \vec{B}(r, z) = \frac{1}{r} \frac{\partial(rB_r)}{\partial r} + \frac{\partial(B_z)}{\partial z} = 0 \quad (4.15)$$

$$B_r = -\frac{1}{r} \int \left(\frac{\partial(B_z)}{\partial z}\right) r dr \quad (4.16)$$

This leads to the expression for the radial field as

$$B_r(r, z) = \frac{\pi r}{4} \frac{B_z(z_i) - B_z(z_{i+1})}{z_{i+1} - z_i} \sin\left(\frac{z - z_i}{z_{i+1} - z_i}\pi\right) \quad (4.17)$$

The field in the Geant4 simulation is implemented using a six component electromagnetic field ( $\vec{B}, \vec{E}$ ) in which the first three components correspond to the magnetic

field and the remaining three components represent the electric field.

$$\begin{aligned}\vec{B}(r, z) &= B_x \hat{x} + B_y \hat{y} + B_z \hat{z} \\ \vec{E}(r, z) &= E_x \hat{x} + E_y \hat{y} + E_z \hat{z}\end{aligned}$$

These fields are implemented in the simulation through the G4ElectroMagneticField class available in the package.

### 4.2.3 Physical Processes

The physical processes involved in the Geant4 simulation depend on the particle types. The most common particles are photons, electrons, positrons, muons and hadrons. The particles undergo only certain physical processes. For example, physical processes related to photon are [98]:

1. Pair production
2. Compton collision
3. Photo-electric effect
4. Photo-fission of heavy elements
5. Rayleigh effect

For the electron/positron pair, the physical processes involved that account for energy losses in the medium are:

1. Multiple scattering
2. Ionization and delta ray production
3. Bremsstrahlung
4. Annihilation of positron
5. Generation of cherenkov radiation and scintillation light
6. Synchrotron radiation
7. Transition radiation

Similarly, for the muon and hadron, the physical processes involved which account for various energy losses in the medium are:

1. Decay
2. Multiple scattering
3. Ionization and delta ray production

4. Ionization by heavy ions
5. Bremsstrahlung
6. Direct electron/positron pair production
7. Nuclear interaction
8. Generation of cherenkov radiation and scintillation light
9. Elastic and inelastic scattering
10. Particle induced X-ray emission
11. Atomic relaxation

The physics (processes) are implemented through the Geant4 Physics List. Physics List is an object that specifies all the particles that will be used in the simulation application [98]. It provides a very flexible way to set up the physics environment including the specification of the particle used in the simulation and the physics associated with each particle. Failure to use relevant particles and physics interactions could lead to poor simulation results. Geant4 does not provide the physics by default because there are many different approximations and models to describe the same interaction. Also, computational time is a real issue. Some users may want a less accurate but significantly faster model for a given interaction while others need the most accurate description. Furthermore, there is probably not any simulation application that would require all the particles and all their possible interactions that Geant4 can provide. The physics provided by Geant4 are:

1. Electromagnetic (EM) physics
2. Weak interaction physics
3. Hadronic physics
4. Parameterized or "fast simulation" physics

Hence, one must have a good understanding of the physics required to properly describe the given problem. Also, depending upon the energy scale, the physics must be implemented carefully. As an example, in the decay of the free neutron, the simulation uses all of the relevant physics such as EM, Weak interaction and Hadronic physics.

#### 4.2.4 Event Types

The sensitive detectors in the GEANT4 simulation are Silicon Disk1 ( $S_1$ ), Dead Layer1 ( $D_1$ ), Silicon Disk2 ( $S_2$ ) and Dead Layer2 ( $D_2$ ). The proton and electron after spiralling in the magnetic field deposit their energies in these detectors. Some of the events which fail to deposit energy in these detectors might deposit energy in



the decay trap. These events are considered lost events and do not contribute to the detected energy spectrum. The only useful events for analysis are the events which encounter any of the detectors including dead layers. In the present simulation, the low energy scale is much lower than 1 eV which allows the proton to be propagated in the magnetic field and to be detected by the detectors. This condition was imposed in the simulation by setting the low energy cuts.

The number of sensitive detectors is four, hence there are  $2^4 = 16$  ( $C(n, r)$  with  $r = 0, 1, 2, 3, 4$  and  $n = 4$ ) possible types of events for each proton and electron to deposit their energy completely. In order to do that, we make use of Boolean variables in which a "0" state represents the situation that the particle does not deposit sufficient energy on a particular detector and "1" state stands for the situation when the particle deposits sufficient energy to be detected in a particular detector. Table 4.1 show all the possibilities of the four detectors events that register a hit or no hit. Direct events are those events which are detected only on one side. This

Table 4.1: All possible events in the four detectors system.

Number	Detectors at $+z$		Detectors at $-z$		Energy Deposition in
	$S_1$	$D_1$	$D_2$	$S_2$	
1	0	0	0	0	Decay Trap
2	1	1	1	1	All
3	1	0	0	0	$S_1$
4	0	1	0	0	$D_1$
5	0	0	1	0	$D_2$
6	0	0	0	1	$S_2$
7	1	1	0	0	$S_1, D_1$
8	1	0	1	0	$S_1, D_2$
9	1	0	0	1	$S_1, S_2$
10	0	1	1	0	$D_1, D_2$
11	0	0	1	1	$D_2, S_2$
12	0	1	0	1	$D_1, S_2$
13	1	1	1	0	$S_1, D_1, D_2$
14	1	1	0	1	$S_1, D_1, S_2$
15	0	1	1	1	$D_1, D_2, S_2$
16	1	0	1	1	$S_1, D_2, S_2$

means that if the events generated with momenta in the  $+z$  direction are detected in the detectors at  $+z$  or vice versa, we called the direct events. For example, the events which deposit energy only in the detectors  $S_1$  or  $D_1$  located at  $+z$  direction are the direct events. There are six possible types of direct events as shown in the Table 4.1. All the events except the direct events which are detected on both sides (detectors at  $\pm z$ ) are called the backscattering events. The backscattering events (see Table 4.1) include four two-detector events (8, 9, 10, 12), four three-detector events (13, 14, 15, 16) and one four-detector event (2). In total, there are nine possible types of backscattering events with the four detector system.

### 4.2.5 Event Sorting

The charged particles (electron or proton) spiral about the magnetic field and hit the detectors. If the particle loses all of its energy, it will not be backscattered. However, if it fails to deposit all the energy, then it spirals back and forth multiple times until all of its energy is exhausted. In the simulation, we are interested in isolating the events on the basis of the experimentally measurable variables. In the experiment, electron and proton events are observed at different times due to the difference in the time of flight. The electron events are detected earlier than the slowly gyrating proton. For this reason, the times for all the hits for both the particles in the detectors are recorded. The time of flight for the particle is defined as the time taken by the particle to be detected in the detector, starting from the origin of the event. The first nonzero time of flight of the particle gives the actual direction of the motion relative to the axis of neutron polarization. This is useful for sorting out the electron and proton events detected on either detectors placed on  $\pm z$  direction.

### 4.2.6 Input and Output

The input needed for the Geant4 simulation has been mostly discussed in the earlier section. The geometry is build and implemented in the G4DetectorConstruction class available in the package. In particular, the most important input to the simulation is the event generator itself which samples the proton and electron momenta/energies based on the physics involved in the decay of free neutron. An event is specified by its origin vertex  $(x_0, y_0, z_0)$ , its kinetic energy  $(T_0)$  and the direction of the momentum  $(\hat{p}_x, \hat{p}_y, \hat{p}_z)$  vector. In the case of the two particle event generator, each of the particles are described by the vertex, kinetic energy and momentum direction before being incorporated into the Geant4 simulation [98]. The following are the output of the simulation:

- The initial kinetic energies for all the decay products.
- The event vertices  $(x_0, y_0, z_0)$ .
- The energy depositions in the detectors,  $S_1, D_1, D_2$  and  $S_2$ .
- The angles relative to the direction of magnetic field.
- The time of flights to each detectors.
- The  $(x, y, z)$  positions of hits on each detectors.
- The energy and momentum of bremsstrahlung photons.

The output listed above represents the minimal variables required for the analysis of the  $Q_{ij}$  spectra.

## Chapter 5 Results

### 5.1 Simulation of UCNA Geometry

In the beginning of my research on neutron  $\beta$ -decay, GEANT4 simulation of UCNA experiments for the 2011/2012 and 2012/2013 geometries were carried out. The two geometries were different on the basis of the material used for the caps (thin foil) at two ends of the UCNA spectrometer (see Figure 5.1). The end caps are used to prevent the loss of UCNs and also to control the backscattering ([111], [112]).

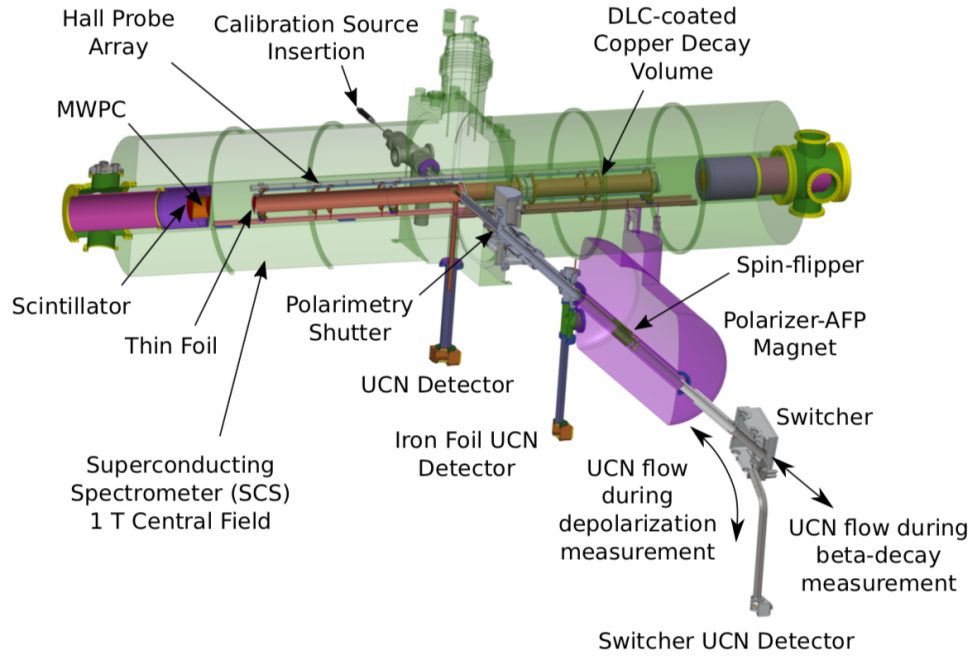


Figure 5.1: Detailed setup for the UCNA experiment [5].

The results obtained from the simulations were first analyzed based on the types of the events. The events in UCNA are classified as Type 0, Type 1, Type 2/3 and Type 4 [56]. On the basis of which detector components trigger, we classify events into those that do not backscatter (Type 0) and those that are backscatter (Types 1, 2, and 3). A schematic of the different types of UCNA events is shown in Figure 5.2. Type 0 events are a combination of the “no backscattering” and “missed” events. They trigger one scintillator and one Multi Wire Proportional Chamber (MWPC) on the same side. Type 1 events are backscattering events that trigger both scintillators and both MWPCs. Type 2/3 events consist of events that backscatter and trigger both MWPCs, but only trigger a single scintillator. The remaining events are called Type 4 which are missed or the lost events.

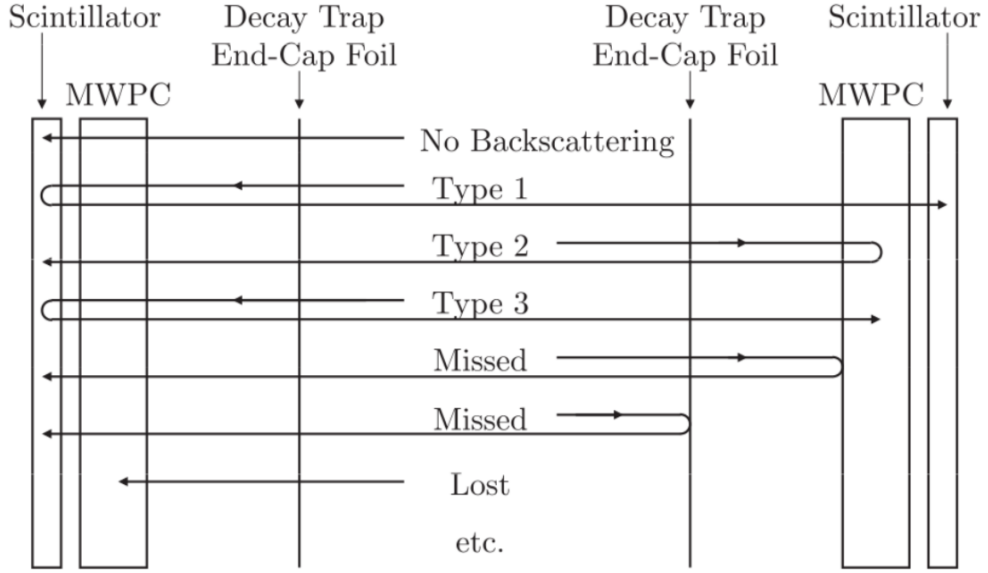


Figure 5.2: Schematic of event types in UCNA

Given the geometry in hand, three parallel simulations were done: with endcaps, without endcaps and annular endcaps. The results of the simulations were then analyzed. We have studied the kinetic energy distributions (see appendix A.5.1) and the angular distributions (see appendix A.5.2) of the direct events and the backscatter events. The analysis show that the backscattering decreases in the case of with: endcaps as compared to that of without-endcaps case. Also, Type 0 events dominate over all other event types. We also analyzed the event types for the UCNA geometry 2012/2013 with no endcaps [113]. The angular distribution of the events under different radius cuts are shown in the appendix A.5.3. In the plots shown, the smallest event radius of 0.5 cm was taken and incremented by 0.5 cm. These plots show the fractions of the different events types in each regions of the radial distribution of the events. Since the distribution is proportional to the area of the cylindrical cross-section, the fraction of Type 0 events gets larger as the event radius becomes larger.

## 5.2 Simulation of UCNB Geometry

### 5.2.1 $Q_{ij}$ spectra

The  $Q_{ij}$  spectra as discussed in Chapter 5 are shown in the Figure 5.3. These energy spectra and the probabilities of the events with different  $Q_{ij}$  are different. As an example, the probability that both an electron and a proton with spins aligned with neutron be emitted is the least compared to all other cases. The analytical expressions corresponding to these spectra are related to the  $\beta$ -decay parameters. Hence, by constructing various asymmetries, we can extract different correlation coefficients in neutron  $\beta$ -decay. The main task of the present simulation is to reconstruct the  $Q_{ij}$

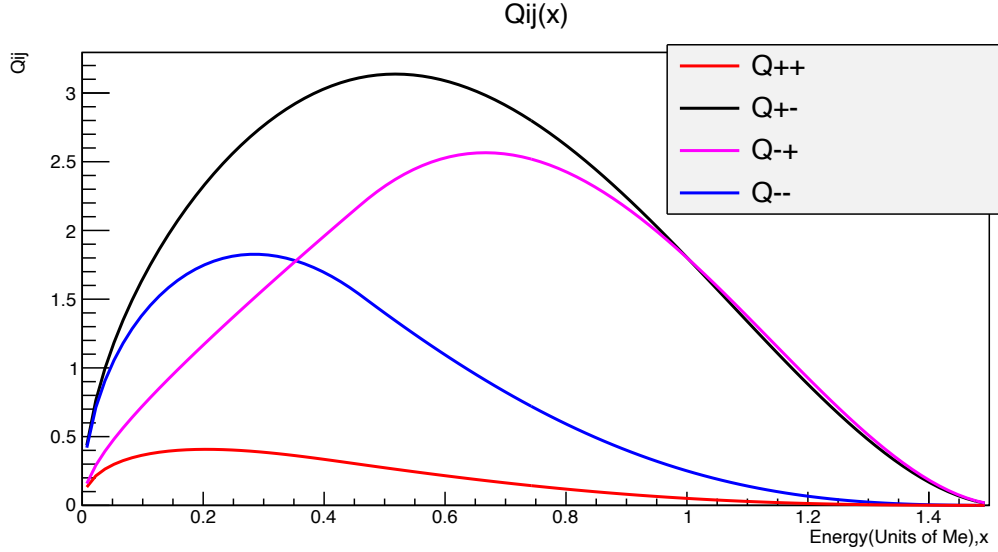


Figure 5.3: The theoretical  $Q_{ij}$  spectra.

from the experimentally observed variables. In the UCNB experiment, the observables are the time of flight and the energy deposition in the respective detectors for the electron and proton events. Using these variables, we were able to reconstruct the  $Q_{ij}$ . We can visualize  $Q_{++}$  and  $Q_{+-}$  geometrically in which the spin of neutron divides the space into two hemisphere (see Figure 5.4 ) [6]. Figure 5.4 (a) shows a scenario when electron and proton are emitted in the same hemisphere (momenta of electron and proton are oriented into the hemisphere parallel to the neutron spin). The antineutrino is restricted to the opposite hemisphere due to momentum conservation. Similarly, Figure 5.4 (b) [6] shows another scenario when an electron and proton

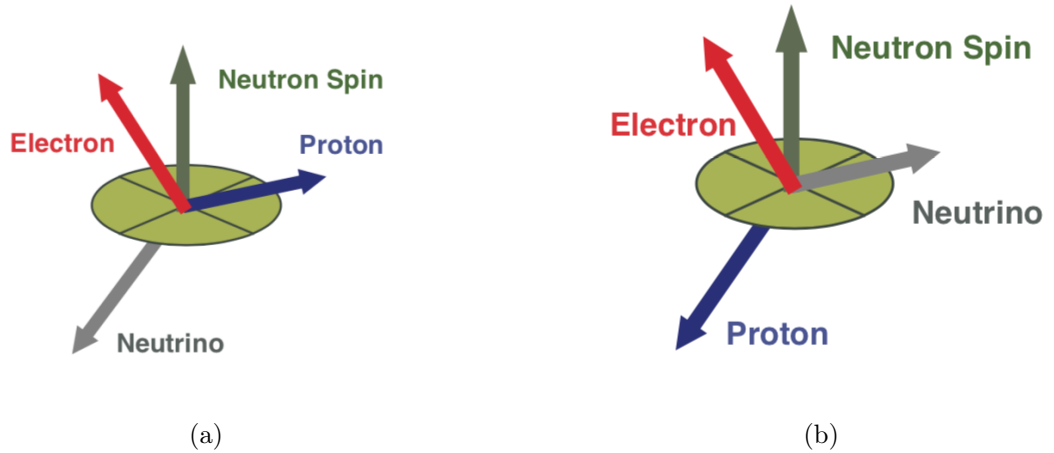


Figure 5.4: (a) Illustration of  $Q_{++}$  (b) Illustration of  $Q_{+-}$  [6]

are emitted in opposite hemispheres (momenta of electron and proton are oriented into the hemisphere parallel to the neutron spin). This provides more possibilities for the direction of emitted antineutrino. As the antineutrino cannot be detected easily, we have to deduce its emission direction from a coincident measurement of the electron and proton momenta emitted into the two hemispheres defined by the neutron spin.

### 5.2.2 Analysis of Event Generator

Prior to the implementation of the event generator (see Chapter 2) into the Geant4 simulation, it was made a standalone code. The input values of the  $\beta$ -decay asymmetry parameters were taken from the Standard Model expression in terms of  $\lambda = -1.2701$  [97] such that

$$A_0 = -2 \frac{\lambda(\lambda + 1)}{1 + 3\lambda^2} = -0.1174,$$

$$B_0 = -2 \frac{\lambda(1 - \lambda)}{1 + 3\lambda^2} = 0.9875,$$

$$a_0 = \frac{1 - \lambda^2}{1 + 3\lambda^2} = -0.1051.$$

and  $b = 0$ . The results of the event generator were analyzed. We were able to construct the  $Q_{ij}$  spectra based on the initial angular distribution of the electron and proton events. Thereafter, using the various asymmetries described in the Chapter 3, we were able to reproduce all the input  $\beta$ -decay parameters ( $A_0$  and  $B_0$ ) within one sigma. The statistical errors in  $A_0$ ,  $B_0$  and  $\lambda$  were in perfect agreement with Glück's results [60]. The variation of  $\lambda$  with respect to  $A$  and  $B$  were also in agreement with those stated in this paper.

$$\frac{d\lambda}{dA} = 2.6,$$

and

$$\frac{d\lambda}{dB} = 13.4$$

The electron asymmetry  $A_0$  is obtained by fitting an energy dependent electron asymmetry  $A(E_e)$  (see Eqn.3.51) using the fit function given by

$$A(E) = A_0 \left[ 1 + A_{\mu m} \left( A_1 W_0 + A_2 \frac{E_e}{m_e} + A_3 \frac{m_e}{E_e} \right) \right], \quad (5.1)$$

where  $A_{\mu m}$ ,  $A_1$ ,  $A_2$  and  $A_3$  are constants defined in terms of  $\lambda$  as

$$\begin{aligned} A_{\mu m} &= \frac{\lambda + \mu}{M_n \lambda (1 - \lambda) (1 + 3\lambda^2)}, \\ A_1 &= \lambda^2 + \frac{2}{3}\lambda - \frac{1}{3}, \\ A_2 &= -\lambda^3 - 3\lambda^2 - \frac{5}{2}\lambda + \frac{1}{3}, \\ A_3 &= 2\lambda^2(1 - \lambda). \end{aligned}$$

In the fit function,  $W_0 = m_n - m_p$  and  $\mu = \mu_p - \mu_n$  is the difference between the magnetic moments of proton and neutron. With  $A_0$  as a fit parameter [114], we were able to extract  $A_0$ . However, in order to extract  $B_0$ , a single parameter function (see Eqn. 1.58) was fitted to the values of  $B$  obtained from different asymmetries defined in Chapter 3. The results of the simulation with the event generator are shown in Appendix A.6 (see Figure A.41 and Figure A.42). Also, we performed 10 independent simulations each with  $1 \times 10^8$  events. We constructed  $Q_{ij}$ s for each of these 10 independent results and extracted the value of  $A_0$ . According to Glück [60], one-sigma deviation error in  $A_0$  and  $\lambda$  are given respectively by

$$\begin{aligned} \sigma_A &= \frac{2.7}{\sqrt{N}} \\ \sigma_\lambda &= \frac{7}{\sqrt{N}} \end{aligned} \tag{5.2}$$

For each of the 10 independent simulations with 0.1 billion events, the error in  $A_0$  is found to be  $2.7 \times 10^{-4}$  and the corresponding error in  $\lambda$  is found to be  $7 \times 10^{-4}$ . Furthermore, we have also used the proton asymmetry ( $\alpha_p$ ) (see Eqn. 3.48) to extract the value of the neutrino asymmetry correlation coefficient ( $B_0$ ). With the same analysis of the  $Q_{ij}$  spectra, we have used the asymmetry  $\alpha_{ep}$  (see Eqn. 3.56) and  $\tilde{\alpha}_{ep}$  (see Eqn. 3.59) to extract the values of  $B_0$ . The values of  $A_0$ ,  $B_0$  and  $\lambda$  for the 10 independent simulations each with  $1 \times 10^8$  events are tabulated in Appendix A.6.1. Also, the plots to extract the values of  $A_0$  and  $B_0$  are shown in Appendix A.6. The results show that the calculated values are in agreement with the corresponding input values within one sigma deviation.

### 5.2.3 Backscattering

The electron-proton event generator was incorporated into the Geant4 to simulate the UCNB experiment and the outputs were analyzed. The backscatter (BS) events are defined as the events which deposit energy on both the detectors (Disk1 and Disk2). In the simulation, the total events directed towards each detectors were obtained making cuts on the direction of the initial electron and proton events.

The total of five independent simulations with the detectors placed at five different positions from the center of the spectrometer (decay trap) were carried out. The magnetic field between the decay trap and the detector was given by the sinusoidal

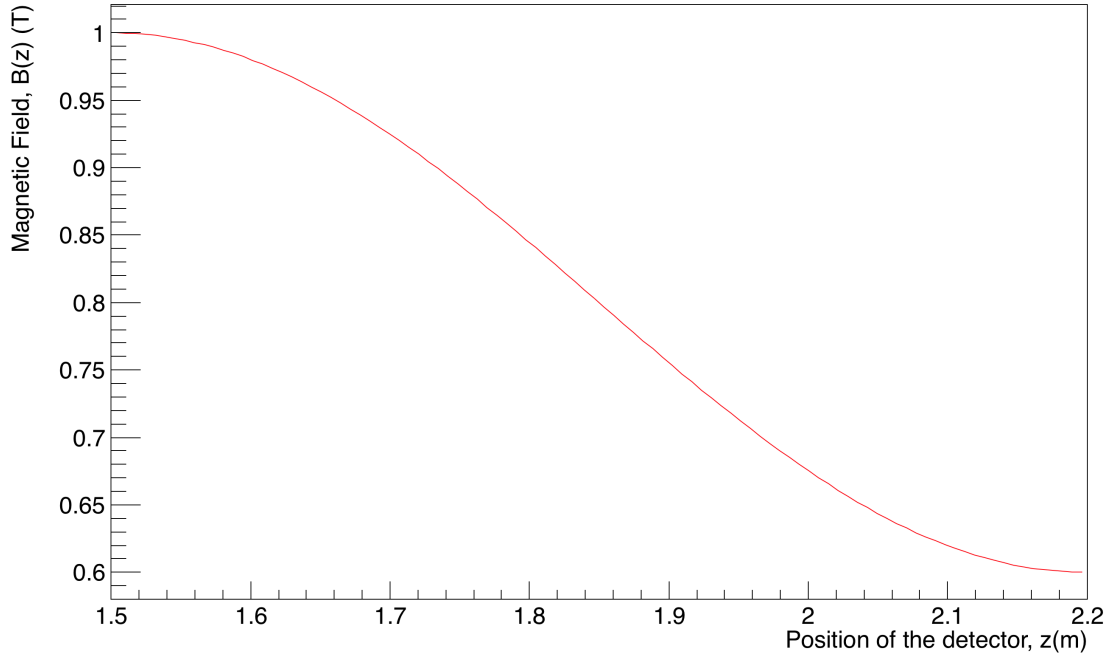


Figure 5.5: Magnetic field profile along  $z$ -axis.

interpolation of the field from 1.5 m to 2.2 m. Hence, changing the detector positions changes the magnetic field such that field decreases as the distance increases. The magnetic field  $B(z)$  at the detector position  $z$  can be calculated using

$$B(z) = 0.8 + 0.2 \cos\left(\frac{(z - 1.5)\pi}{0.7}\right) \quad (5.3)$$

where values of  $B(z)$  at 1.5 m and 2.2 m are 1.0 T and 0.6 T respectively. Figure 5.5 shows the magnetic field profile along  $z$ -axis between  $z = 1.5$  m and  $z = 2.2$  m, the center of the decay trap being at  $z = 0.0$  m.

The fraction of the backscatter events decreases as the magnetic field at the detector position decreases (see Figure 5.5). In other words, the backscattering depends on the magnetic field at the detector location (see Eqn.5.3). As the magnetic field decreases, the fraction of the backscattering events increases. This is quite obvious because the scattering probability depends on the pitch angle. The pitch angle for an electron or a proton travelling from the region of the higher magnetic field to the lower field becomes larger and hence the probability of scattering decreases.

Figure 5.6 shows that the backscattering decreases as the detector is moved away from the center of the decay trap for electron events. Also, the fraction of the backscattering events from either of the Disk1 or Disk2 at the given positions show the same trend. Figure 5.12 shows that the backscattering decreases as the detector is moved away from the center of the decay trap for proton events. It is clear that the backscattering from either of the Disk1 or Disk2 are not symmetrical. Also, at the given position of the detector, the probability of backscattering for the proton events is higher than the corresponding probability for the electron events.



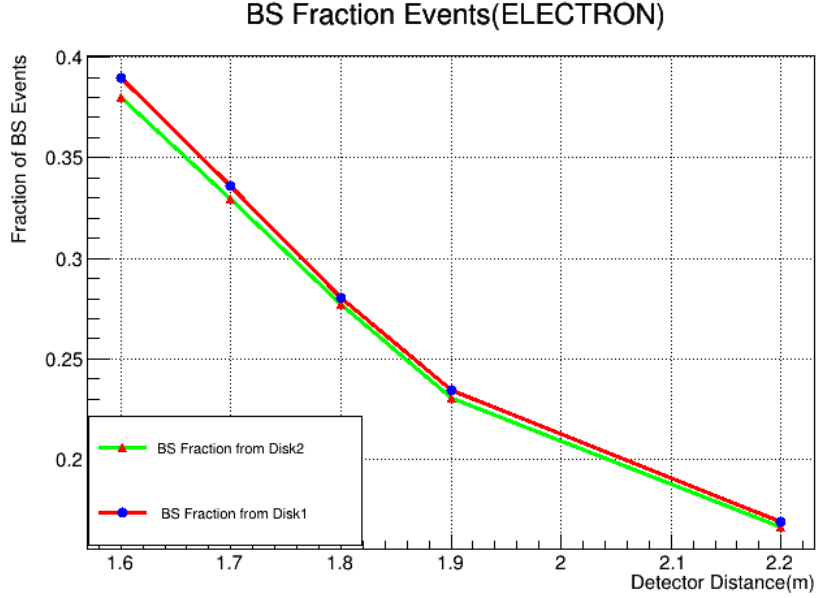


Figure 5.6: Backscattering fraction (electron) as a function of the detector distance (magnetic field  $B(z)$ ) from the decay trap.

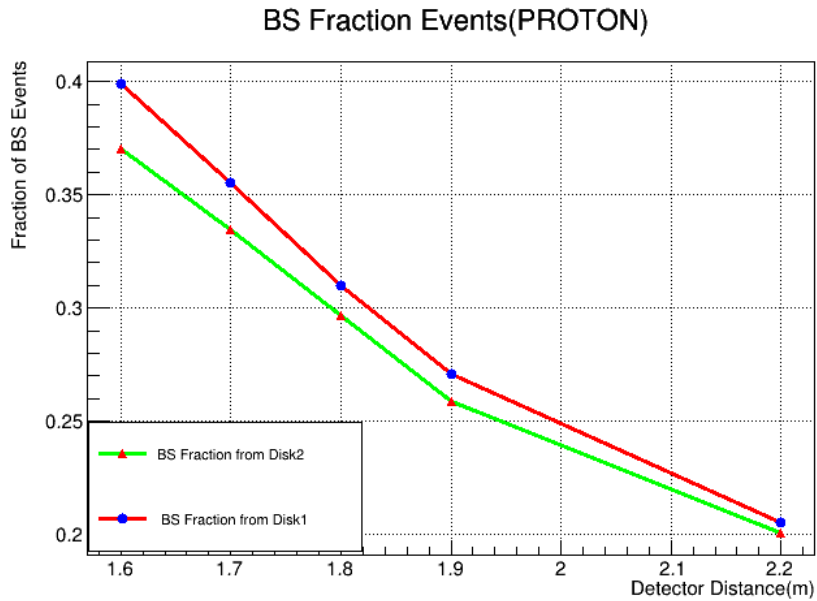


Figure 5.7: Backscattering fraction (proton) as a function of the detector distance (magnetic field  $B(z)$ ) from the decay trap.

## 5.2.4 Bremsstrahlung Effect Off

We carried out the Geant4 simulation with the bremsstrahlung effect disabled so that no photons are emitted during the interactions of the electron with materials. This was implemented by inactivating the electron bremsstrahlung. Hence, the sum of the energies deposited in all the detectors should be equal to the total initial kinetic energies of the electrons. Figure 5.8 shows the two dimensional distribution of the

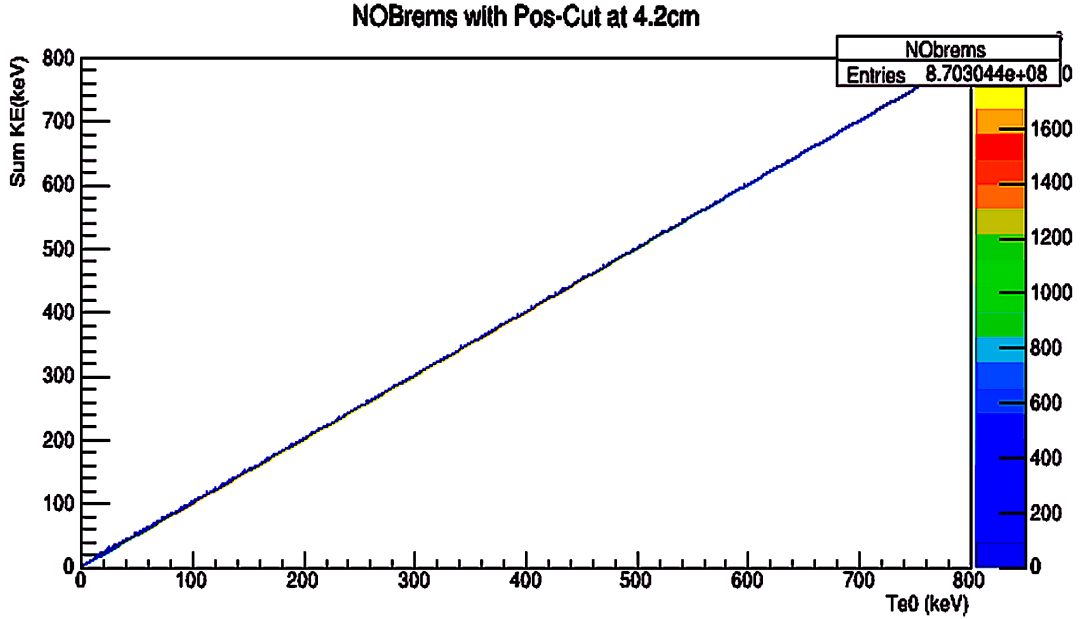


Figure 5.8: Comparison of the total detected energy and the initial kinetic energy of electron.

total detected energy to the initial kinetic energy of the electron. Within the event radius of 4.2 cm, there is no bremsstrahlung effect. All the electron events lie on the straight line with the gradient equal to one, showing that the detected total energies for each of the events is equal to the corresponding initial energies for those events.

### 5.2.4.1 Reconstructed $Q_{ij}$ Spectra

The reconstructed  $Q_{ij}$  spectra are the distributions as a function of the detected electron energy. If both the electron and the proton are detected in the  $+z$ -direction, we assign the event to  $Q_{++}$ . Similarly, all the other distributions are obtained based on which side the particles are first detected based on the time of flights. Figure 5.8 shows the reconstructed  $Q_{ij}$  spectra used for the analysis of the asymmetry parameters. On the  $x$ -axis is the sum of the electron energies detected in the Silicon Disk1, Silicon Disk2, Dead Layer1 and Dead Layer2.

These spectra were used to calculate all the asymmetries defined in Chapter 3. Using these asymmetries, the neutrino asymmetry  $B_0$  was calculated in the two distinct regions of the spectra ( $r < 1$  and  $r > 1$ ). Table 5.1 summarizes the results of the calculations. The statistical errors on  $B_0$  were calculated using the expressions

derived in Appendix A.4. The values of  $B_0$  obtained with the given asymmetry agree with the input value within one sigma. Appendix A.7 shows the neutrino asymmetry  $B$  as a function of the detected electron energy. The value of the electron asymmetry was obtained to be  $-0.1172(3)$  which agrees with the input value within 1.0 sigma. The number of sigma deviations for  $B_0$  is calculated using

$$\sigma = \frac{B_{input} - B_{calculated}}{\delta B}$$

where,  $\delta B$  is the statistical error in the calculated value of  $B_0$ .

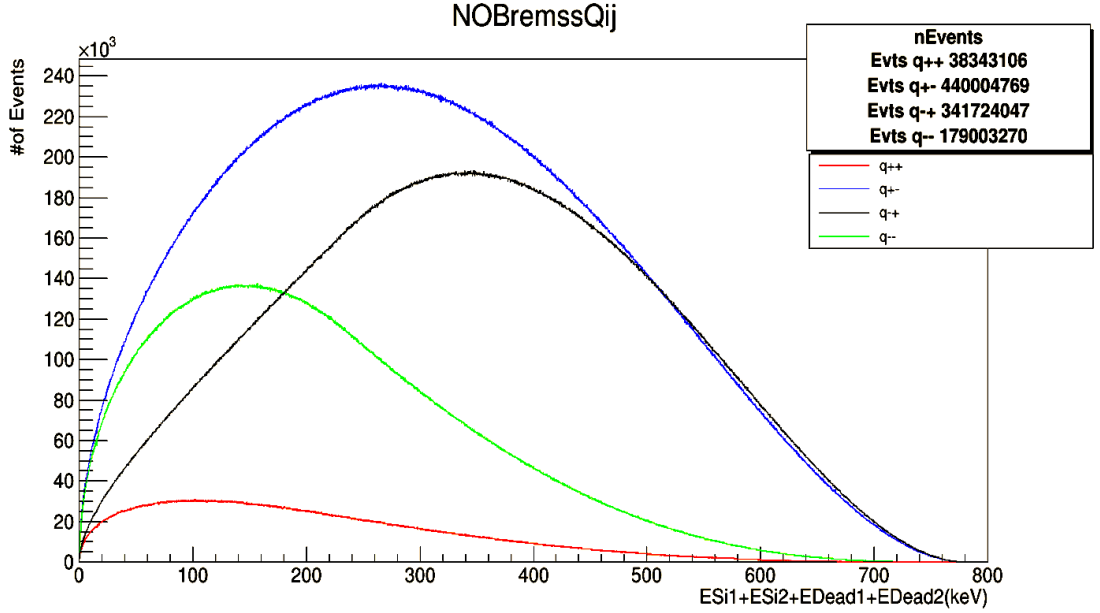


Figure 5.9: Reconstructed  $Q_{ij}$  spectra for the simulation with  $1 \times 10^9$  events in which the bremsstrahlung effects are disabled.

Table 5.1: Neutrino Asymmetry (bremsstrahlung off)

Asymmetry	$r < 1$	$\sigma$	$r > 1$	$\sigma$
$\alpha_p$	0.98808(34)	1.67109	0.98699(63)	0.82366
$\alpha_{ep}$	0.98750(17)	0.04	0.98740(48)	0.222
$\tilde{\alpha}_{ep}$	0.98704(34)	-1.35742	0.98814(63)	1.00299
$r_{pe}$	0.98743(40)	-0.180991	0.98747(39)	0.09689
$\alpha_x$	0.98743(12)	-0.658075	0.98748(12)	-0.22496
$\alpha_R$	0.98803(40)	1.31471	0.98777(39)	0.686367

### 5.2.5 Bremsstrahlung Effect On

Next, we carried out the Geant4 simulation with the bremsstrahlung effects enabled so that an electron can also lose energy via emission of a photon. This effect

was implemented by activating the electron bremsstrahlung in the simulation. Hence, the difference between the total initial kinetic energy of the electron and the energies deposited in all the detectors must be equal to the energy carried away by the bremsstrahlung photons. Figure 5.10 shows the bremsstrahlung (photon) spectrum from the simulation with  $1 \times 10^9$  events. The inset plot shows the distribution of the total detected electron kinetic energy (Sum KE) relative to its initial kinetic energy ( $T_{e,0}$ ). The bremsstrahlung effect is shown by the events below the 45° line. This effect from the proton was not important in our simulation (at least under the energy scale of the proton emitted from the decay of the free neutron). Also, as the proton is about 2000 times more massive than an electron, bremsstrahlung effects are highly suppressed.

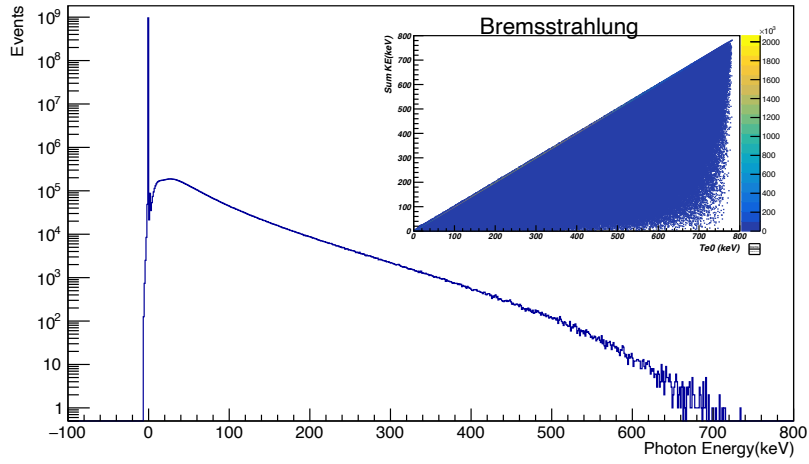


Figure 5.10: The bremsstrahlung (photon) spectrum. The inset plot shows the distribution of the total detected electron kinetic energy (Sum KE) relative to its initial kinetic energy ( $T_{e,0}$ ).

### 5.2.5.1 Reconstructed $Q_{ij}$ Spectra

We used the total detected energy of the electron and time of flights of the electron and proton for sorting out the events and reconstructing the  $Q_{ij}$  spectra. Figure 5.11 shows these spectra as a function of the detected electron energy. These are the  $Q_{ij}$ 's with the bremsstrahlung effects turned on. Comparison of these spectra with those with the bremsstrahlung effects tuned off, reveals a slight distortion.

For this case also, the spectra were analyzed to obtain all the asymmetries defined in Chapter 3. Using these asymmetries, neutrino asymmetry  $B_0$  were calculated in the two distinct regions of the spectra ( $r < 1$  and  $r > 1$ ). Appendix A.8 shows the neutrino asymmetry  $B$  as a function of the detected electron energy and Table 5.2 summarizes the results of the calculations. The statistical errors on  $B_0$  were calculated using the expressions derived in Appendix A.4. The values of  $B_0$  obtained with the given asymmetry agree with the input value within one sigma deviation.

The value of the electron asymmetry was obtained to be  $-0.11740(8)$  which agrees with the input value within 1.1 sigma (see Appendix A.8 for the fitted plot).

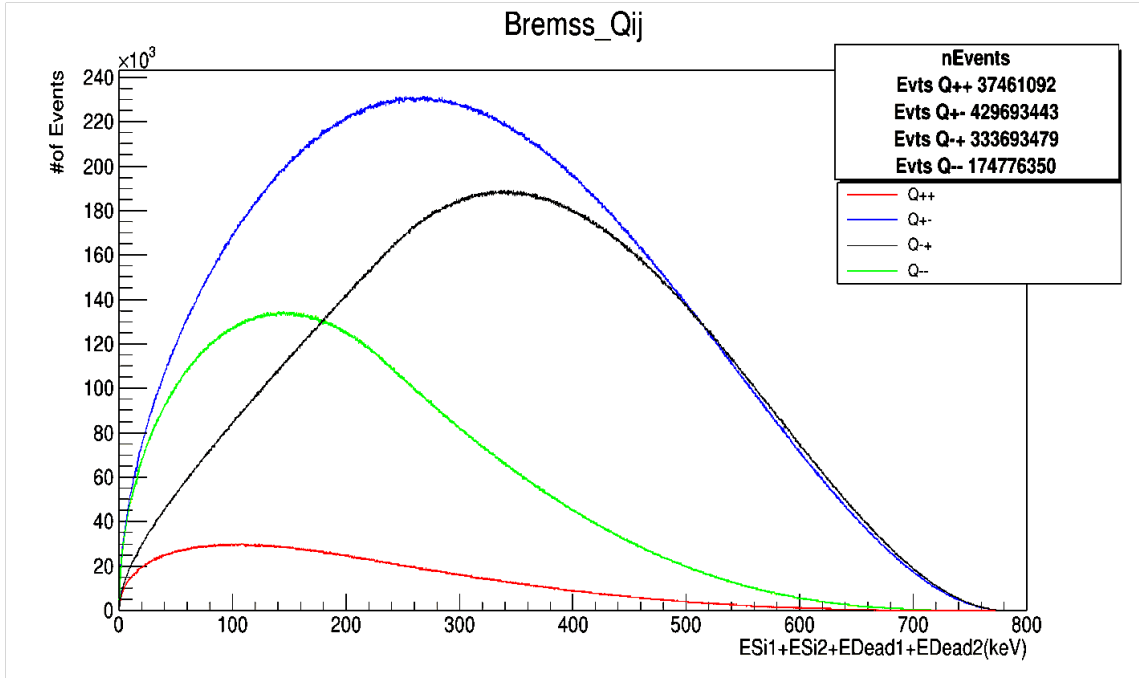


Figure 5.11: Reconstructed  $Q_{ij}$  spectra for the simulation with  $1 \times 10^9$  events in which the bremsstrahlung effects are enabled.

Table 5.2: Neutrino Asymmetry (bremsstrahlung on)

Asymmetry	$r < 1$	$\sigma$	$r > 1$	$\sigma$
$\alpha_p$	0.98750(18)	0.03	0.98760(52)	-0.10
$\alpha_{ep}$	0.98780(18)	1.6	0.98760(53)	-0.17
$\tilde{\alpha}_{ep}$	0.98762(10)	1.08602	0.98759(19)	0.437602
$r_{pe}$	0.98804(34)	1.55074	0.98791(63)	0.641134
$\alpha_x$	0.9876(14)	0.06	0.98750(81)	0.01
$\alpha_R$	0.98740(34)	-0.271818	0.98790(73)	1.02411

### 5.2.6 Distortions of Energy Spectra

The energy depositions by the electron in all the detectors were analyzed for the case with the bremsstrahlung effects enabled and the other with the effect disabled (see Appendix A.9 for the figure). Using the asymmetries described in Chapter 3, values of  $B$  were calculated. Table 5.3 shows that the fractional change in the computed values of the neutrino asymmetry  $B$  for the two cases in the two regions of the spectrum with  $r < 1$  and  $r > 1$ . It is clear that the bremsstrahlung effects are not significant in the determination of the  $\beta$ -decay parameters.

Table 5.3: Fractional change in the neutrino asymmetry.

	$ B_{NoBrem} - B_{Brem} /(B_{NoBrem})$	
Asymmetry	$r < 1$	$r > 1$
$\alpha_p$	0.00059(39)	0.00062(83)
$\alpha_{ep}$	0.00030(25)	0.00020(72)
$\tilde{\alpha}_{ep}$	0.00059(36)	0.00056(67)
$r_{pe}$	0.00061(53)	0.00045(74)
$\alpha_x$	0.00018(14)	0.00002(81)
$\alpha_R$	0.00064(53)	0.00013(83)

### 5.2.7 Normalization for Coincidence Asymmetries

For measurements of single-particle asymmetries, such as the proton and electron asymmetries  $\alpha_p$  and  $\alpha_e$ , these single-particle asymmetries can be constructed from a super ratio,  $r_{p,e}$ , of the (proton or electron) spectral counts  $Q_{\pm}^{1p,2p,1e,2e}$  in the two detectors (1 or 2) for the two neutron spin states (+ or -), under which differences in the two detectors' efficiencies and the neutron flux or density for the two spin states largely cancel to first order. Here, it does not matter if the detection efficiencies for electrons vs. protons are different.

On the other hand, electron-proton coincidence asymmetries are sensitive to any such differences in the detection efficiencies for electrons vs. protons. However, these issues can be mitigated in the following manner, which we illustrate using the example of the differential neutrino asymmetry,  $\alpha_{ep}(E_e)$ , defined previously in Eq. 3.54 to be  $\alpha_{ep}(E_e) = (Q_{--} - Q_{++})/(Q_{--} + Q_{++})$ . If we assume that the proton detection efficiency is nominally 100%, any sensitivity to the electron detector efficiency cancels if the  $Q_{--}$  and  $Q_{++}$  are extracted from the same detector (detector 1 or 2), meaning  $\alpha_{ep}$  is extracted only from  $(Q_{--}^1, Q_{++}^1)$  or  $(Q_{--}^2, Q_{++}^2)$ . (This assumes the experiment has the ability to toggle the neutron spin state.) However, there remains the problem of the normalization for the two spin states. This can be accomplished by using the total number of protons detected in the two detectors for the particular spin state,  $N_{\pm}^{\text{tot},p} = N_{\pm}^{1,p} + N_{\pm}^{2,p}$ , as an absolute measure of the total number of neutron decays in the experimental apparatus for the two spin states, such that the asymmetry is then

calculated as

$$\alpha_{ep}(E_e) = \frac{\frac{Q_{--}^1}{N_{-}^{\text{tot},p}} - \frac{Q_{++}^1}{N_{+}^{\text{tot},p}}}{\frac{Q_{--}^1}{N_{-}^{\text{tot},p}} + \frac{Q_{++}^1}{N_{+}^{\text{tot},p}}}. \quad (5.4)$$

### 5.2.8 Sensitivity of $r_{pe}$ to $b_\nu$

In order to study the the sensitivity of asymmetry ratio  $r_{pe}$  to  $b_\nu$ , first the neutrino asymmetry  $B$  and the corresponding statistical error were calculated from the asymmetry ratio  $r_{pe}$ . The asymmetry ratio itself was obtained from the reconstructed  $Q_{ij}$ 's. The values of  $B$  were then fitted with the function

$$B(E_e) = B_0 + c_0 + c_1 \frac{E_e}{M_N} + \frac{m_e}{E_e} b_\nu \quad (5.5)$$

with  $b_\nu$  as a free parameter. The constant  $B_0$ ,  $C_0$  and  $c_1$  are known constants in terms of  $\lambda$  and  $\mu$  [62] (see Eqns. 1.58, Eqn. 1.59 and Eqn. 1.60). Using the TMinuit minimization routine, we obtained the error in  $b_\nu$  at 68.3% CL.

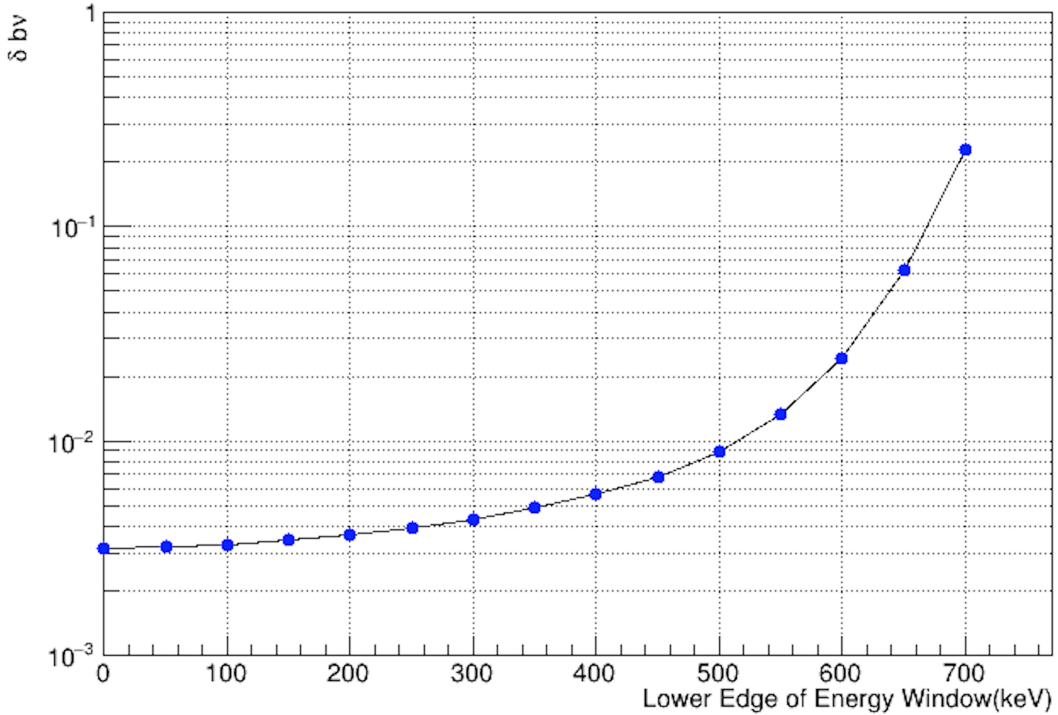


Figure 5.12: One-sigma (68.3% CL) sensitivity of the asymmetry ratio  $r_{pe}$  to  $b_\nu$  for  $1 \times 10^9$  events as a function of the lower edge of an analysis energy window.

We assessed the sensitivity of this asymmetry ratio,  $r_{pe}(E_e) \equiv \alpha_p(E_e)/\alpha_e(E_e)$ , to  $b_\nu$  by performing a differential fit, with one free parameter  $b_\nu$ , to our Monte Carlo data set consisting of  $1 \times 10^9$  events. These results are summarized in Figure 5.12,

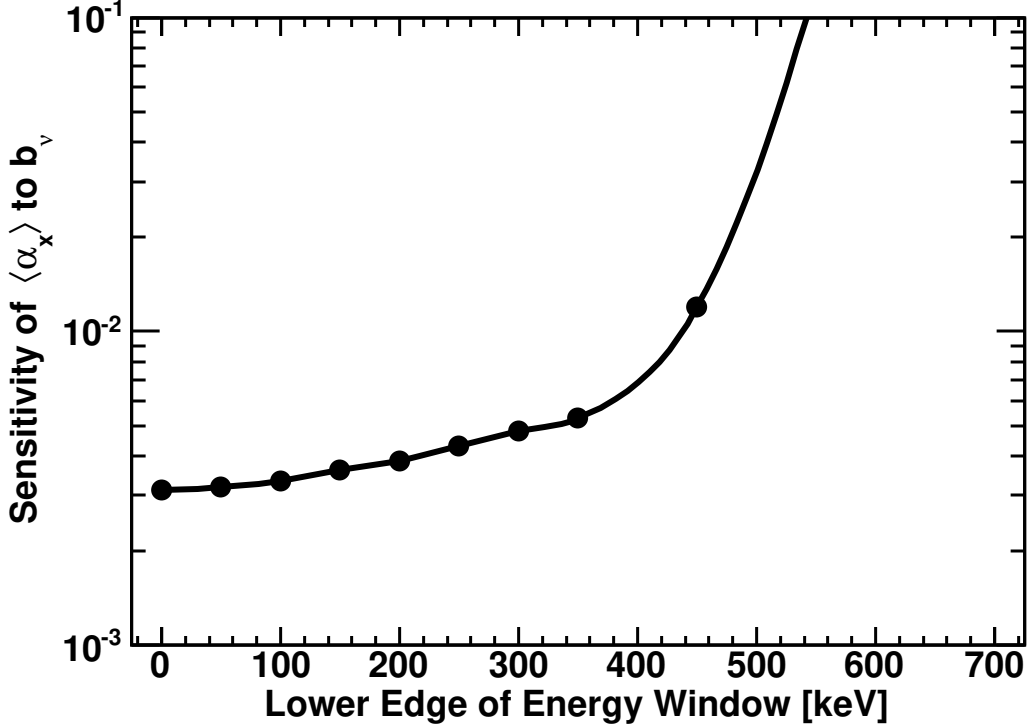


Figure 5.13: One-sigma (68.3% CL) sensitivity for an extraction of  $b_\nu$  from the integral asymmetry  $\langle \alpha_x \rangle$  for  $1 \times 10^9$  events as a function of the lower edge of an analysis energy window. The upper edge of the window is fixed at 700 keV. We again include the 0 keV lower threshold as a statistical reference point.

where we have plotted the one-sigma (i.e., 68.3% CL) sensitivity of  $r_{pe}$  to  $b_\nu$  as a function of the lower edge of the energy window. As can be seen there, at this level of statistics our asymmetry ratio technique offers the potential to probe  $b_\nu$  to the level of  $3.3 \times 10^{-3}$  over our baseline 100–750 keV energy window. In this plot, the upper edge of the window is fixed at 750 keV. Although achieving a lower threshold of 0 keV will not be possible, we include this as a reference point for the statistical error.

### 5.2.9 Sensitivity of $\alpha_x$ to $b_\nu$

We see that  $\alpha_x(E_e)$  also does not depend on  $b$ ; however, in contrast to  $\alpha_R$ ,  $\langle \alpha_x \rangle$  offers greater sensitivity to  $b_\nu$ . As shown in Fig. 5.13,  $\langle \alpha_x \rangle$  would provide sensitivity to  $b_\nu$  at the level of  $3.3 \times 10^{-3}$  over our baseline 100–700 keV energy window. This sensitivity is very similar to that of our  $r_{pe} = \alpha_p/\alpha_e$  asymmetry ratio method; however, the sensitivity of  $\langle \alpha_x \rangle$  degrades significantly above  $\sim 500$  keV for the same reason as for  $\alpha_R$ . However, if the lower edge of the energy window is 200 keV, we see that  $\alpha_x$  offers another promising avenue for accessing  $b_\nu$ . Note also because  $\alpha_x(E_e)$  is independent of the polarization  $P$ , the ratio  $A/B$  can be determined in a manner that is independent of the polarization.



### 5.2.10 Sensitivity of Combined Fit to $b$ and $b_\nu$ .

Finally, we study the sensitivity of a combined fit to the electron energy spectrum (in unpolarized  $\beta$ -decay) (see Eqn.3.2), the energy dependence of  $\alpha_e(E_e)$  (see Eqn. 3.50), and the energy dependence of the asymmetry ratio  $r_{pe}$  (see Eqn. 3.52). Here, the observables are the four independent  $Q_{\pm\pm}$  spectra, and if  $\lambda$ ,  $b$ ,  $b_\nu$ , and a normalization for the spectrum are treated as (unbounded) fit parameters, with  $10^9$  events such a fit over the 100–700 keV baseline energy window would determine  $\lambda$  to 0.13% (equivalent to, e.g., a  $\sim 0.5\%$  stand-alone measurement of  $A$ ),  $b$  to the level of  $2.2 \times 10^{-3}$ , and  $b_\nu$  to  $1.2 \times 10^{-2}$ . The sensitivity to  $b$  and  $b_\nu$  as a function of the lower edge of the energy window is summarized in the top panel of Fig. 5.14. However, as previously noted, we can exploit the  $b$  and  $b_\nu$  “degeneracy” and parametrize  $b$  as  $b = b_\nu + x$ , where  $x$  is constrained to the range of  $[-0.0005, 0.0003]$  (at 68.3% CL). If we then carry out a fit in which  $\lambda$ ,  $b$ , and the normalization for the spectrum are treated as (unbounded) fit parameter, but  $x$  is treated as a bounded fit parameter, the resulting sensitivity to  $b_\nu$  increases significantly. Such a constrained fit over the 100–700 keV baseline energy window would then determine  $\lambda$  to 0.09%, and both  $b$  and  $b_\nu$  to  $2.2 \times 10^{-3}$ . The resulting sensitivity to  $b$  and  $b_\nu$  for other energy windows is shown in the bottom panel of Figure 5.14. The top panel of Figure 5.14(a) shows one-sigma (68.3% CL) sensitivity for  $1 \times 10^9$  events to  $b$  and  $b_\nu$  from a combined fit to the electron energy spectrum,  $\alpha_e(E_e)$ , and the asymmetry ratio  $r_{pe}(E_e)$  with  $\lambda$ ,  $b$ ,  $b_\nu$ , and a normalization for the spectrum as free parameters. Bottom panel Figure 5.14(b) shows one-sigma (68.3% CL) sensitivity for  $1 \times 10^9$  events from a combined fit to the same observables, but with  $b$  parametrized as  $b = b_\nu + x$ , with  $x$  bounded by current constraints on scalar and tensor physics. Note that only one curve is shown here, as the sensitivities to  $b$  and  $b_\nu$  are similar. We again include the 0 keV lower threshold in both plots as a statistical reference point.

### 5.2.11 Summary

Correlation coefficients ( $A$ ,  $B$  and  $a$ ) in the decay of polarized neutrons relate the neutron spin and momenta of the decay products. Their determination with high precision is important to check the Standard Model of Particle Physics and to search for the possibility of physics beyond the SM. Within the framework of this thesis, we have calculated the neutrino asymmetry  $B$ , the correlation between the neutron spin and the neutrino momentum, using the electron-proton coincidence asymmetries described in Chapter 3. We also compared the  $Q_{ij}$  spectra and the resulting asymmetries for the bremsstrahlung enabled vs. disabled cases, and found that asymmetries for these two cases generally agreed to better than one sigma.

Furthermore, we have studied the sensitivity of a number of different experimental asymmetries which can be constructed from measurements of electron-proton coincidences in polarized neutron  $\beta$ -decay to the Fierz interference terms  $b$  and  $b_\nu$ . We have also identified several methods by which  $b_\nu$  can be isolated, notably via the construction of asymmetry ratios. We have shown that with  $1 \times 10^9$   $\beta$ -decay events, it will be possible to simultaneously determine  $\lambda$  to 0.09 % and the Fierz terms to the level of

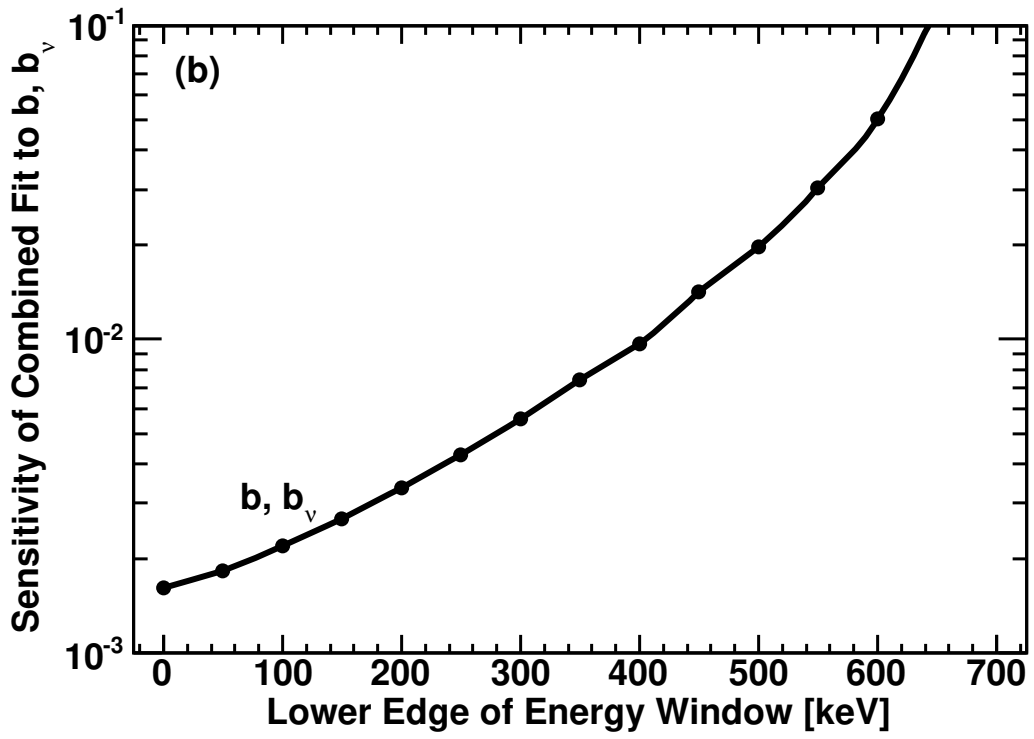
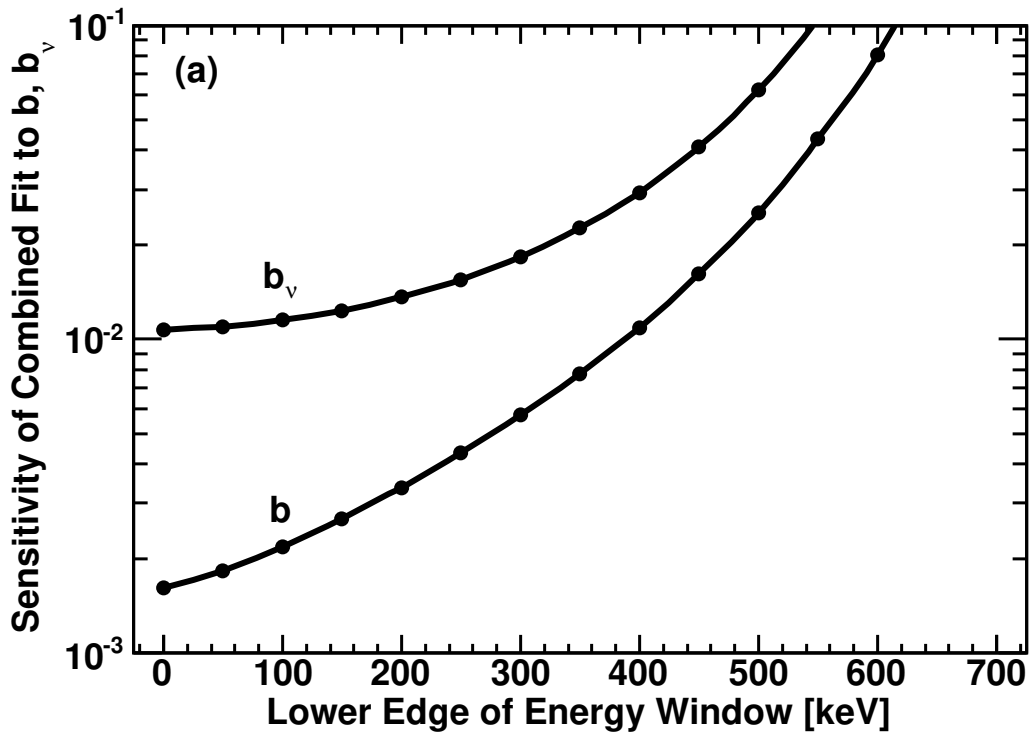


Figure 5.14: Sensitivity of a combined fit to  $b$  and  $b_\nu$

$\sim 2 \times 10^{-3}$ ; this sensitivity goal is certainly within the statistical reach of ongoing and future experiments. With the strategies we have proposed for constructing experimental observables and addressing experimental systematic issues, the next round of neutron  $\beta$ -decay experiments (such as the UCNB experiment) holds the potential to probe BSM scalar and tensor interactions at energy scales competitive with the reach of the Large Hadron Collider.

## Appendix

### A.1 Angular correlations in terms of coupling constants

With  $\delta_{JJ'}$  and  $\lambda_{JJ'}$  defined as [57]

$$\delta_{JJ'} = \begin{cases} 1, & J \rightarrow J' = J - 1 \\ \frac{1}{J+1}, & J \rightarrow J' = J \\ \frac{-1}{J+1}, & J \rightarrow J' = J + 1 \end{cases}$$

and

$$\lambda_{JJ'} = \begin{cases} 1, & J \rightarrow J' = J - 1 \\ -\frac{(2J-1)}{J+1}, & J \rightarrow J' = J \\ \frac{J(2J-1)}{(J+1)(2J+3)}, & J \rightarrow J' = J + 1, \end{cases}$$

we get the following relations for the correlation coefficients in the  $\beta$ -decay [57]:

$$\xi = |M_F|^2 \left( |C_S|^2 + |C_V|^2 + |C'_S|^2 + |C'_V|^2 \right) \quad (6)$$

$$+ |M_{GT}|^2 \left( |C_T|^2 + |C_A|^2 + |C'_T|^2 + |C'_A|^2 \right) \quad (7)$$

$$a\xi = |M_F|^2 \left( -|C_S|^2 + |C_V|^2 - |C'_S|^2 + |C'_V|^2 \right) \quad (8)$$

$$+ \frac{1}{3} |M_{GT}|^2 \left( |C_T|^2 - |C_A|^2 + |C'_T|^2 - |C'_A|^2 \right) \quad (9)$$

$$b\xi = \pm 2Re \left[ |M_F|^2 (C_S C_V^* + C'_S C'_V^*) + |M_{GT}|^2 (C_T C_A^* + C'_T C'_A^*) \right] \quad (10)$$

$$c\xi = |M_{GT}|^2 \lambda_{JJ'} \left( |C_T|^2 - |C_A|^2 + |C'_T|^2 - |C'_A|^2 \right) \quad (11)$$

$$A\xi = 2Re \left[ \pm |M_{GT}|^2 \lambda_{JJ'} (C_T C_T^* - C'_A C'_A^*) \right] \quad (12)$$

$$+ \delta_{JJ'} |M_F| |M_{GT}|^2 \left( \frac{J}{J+1} \right)^{1/2} (C_S C_T^* + C'_S C'_T^* - C_V C_A^* - C'_V C'_A^*) \quad (13)$$

$$B\xi = 2Re \left\{ |M_{GT}|^2 \lambda_{JJ'} \left[ \frac{m_e}{E_e} (C_T C_T^* - C'_A C'_A^*) \pm (C_T C_T^* - C'_A C'_A^*) \right] \right\} \quad (14)$$

$$- \delta_{JJ'} |M_F| |M_{GT}|^2 \left( \frac{J}{J+1} \right)^{1/2} \left[ (C_S C_T^* + C'_S C'_T^* + C_V C_A^* + C'_V C'_A^*) \right] \quad (15)$$

$$\pm \frac{m_e}{E_e} (C_S C_A^* + C'_S C'_A^* + C_V C_T^* + C'_V C'_T^*) \left. \right\} \quad (16)$$

$$D\xi = 2Im \left\{ \delta_{JJ'} |M_F| |M_{GT}|^2 \left( \frac{J}{J+1} \right)^{1/2} \left[ (C_S C_T^* - C_V C_A^* + C'_S C'_T^* - C'_V C'_A^*) \right] \right\} \quad (17)$$

### A.2 Properties of Projection operator

The Dirac matrices  $\gamma^\mu$  ( $\mu = 0, 1, 2, 3$ ) satisfy the relations:

$$\gamma^\mu \gamma^\nu + \gamma^\nu \gamma^\mu = 2g^{\mu\nu}, \quad (18)$$

where  $g^{00} = 1$ ,  $g^{ii} = -1$  and for  $\mu \neq \nu$ , we have  $g^{\mu\nu} = 0$ . The matrix  $\gamma_5$  is defined through (Weyl Representation)

$$\gamma_5 = i\gamma^0\gamma^1\gamma^2\gamma^3. \quad (19)$$

$$\gamma^0 = \begin{pmatrix} 0 & -1 \\ -1 & 0 \end{pmatrix}, \quad \gamma^k = \begin{pmatrix} 0 & \sigma^k \\ -\sigma^k & 0 \end{pmatrix} \quad (20)$$

$$(21)$$

It satisfies the relations

$$\gamma^\mu\gamma_5 + \gamma_5\gamma^\mu = 0 \quad (22)$$

$$\gamma_5\gamma_5 = 1. \quad (23)$$

Sixteen matrices  $1$ ,  $\gamma^\mu$ ,  $\sigma^{\mu\nu} = \frac{i}{2}(\gamma^\mu\gamma^\nu - \gamma^\nu\gamma^\mu)$ ,  $\gamma^\mu\gamma_5$  and  $\gamma_5$  form a complete system of  $4 \times 4$  matrices. The projection operator has the following useful properties:

$$a = \frac{1}{2}(1 - \gamma_5) \quad (24)$$

$$\bar{a} = \frac{1}{2}(1 + \gamma_5) \quad (25)$$

$$aa = \frac{1}{4}(1 + (\gamma_5)^2 - 2\gamma_5) = \frac{1}{2}(1 - \gamma_5) = a \quad (26)$$

$$\bar{a}a = \frac{1}{4}(1 + \gamma_5)(1 - \gamma_5) = \frac{1}{4}(1 - (\gamma_5)^2) = 0 \quad (27)$$

$$\bar{a}\gamma_5 = \frac{1}{2}(\gamma_5 + (\gamma_5)^2) = \frac{1}{2}(1 + \gamma_5) = \bar{a} \quad (28)$$

$$a\gamma_5 = \frac{1}{2}(\gamma_5 - (\gamma_5)^2) = -\frac{1}{2}(1 - \gamma_5) = -a \quad (29)$$

$$\bar{a}\gamma^\mu = \frac{1}{2}(1 + \gamma_5)\gamma^\mu = \gamma^\mu\frac{1}{2}(1 - \gamma_5) = \gamma^\mu a \quad (30)$$

Scalar:

$$O'_i = \bar{a}O_i a = 0 \quad (31)$$

Vector:

$$O'_i = \bar{a}O_i a = \bar{a}\gamma^\mu a = \gamma^\mu aa = \gamma^\mu a \quad (32)$$

Axial Vector:

$$O'_i = \bar{a}O_i a = \bar{a}\gamma^\mu\gamma_5 a = \gamma^\mu a\gamma_5 a = -\gamma^\mu aa = -\gamma^\mu a \quad (33)$$

PseudoScalar:

$$O'_i = \bar{a}O_i a = \bar{a}\gamma_5 a = \bar{a}a = 0 \quad (34)$$

Tensor:

$$O'_i = \bar{a}O_i a = \bar{a}\sigma^{\mu\nu} a = \frac{i}{2}\bar{a}(\gamma^\mu\gamma^\nu - \gamma^\nu\gamma^\mu)a = \frac{i}{2}(\gamma^\mu\gamma^\nu\bar{a}a - \gamma^\nu\gamma^\mu\bar{a}a) = 0 \quad (35)$$

### A.3 Proton momentum calculations

With usual notations, the momentum of the proton is given by the solution of the following equation

$$\begin{aligned} m_n - E_e - \sqrt{p_p^2 + m_p^2} - |\vec{p}_e + \vec{p}_p| &= 0 \\ m_n - E_e - \sqrt{p_p^2 + m_p^2} - \sqrt{p_e^2 + 2p_e p_p \cos \theta_{ep} + p_p^2} &= 0 \end{aligned} \quad (36)$$

Writing  $c_f = \cos \theta_{ep}$  and  $d = m_n - E_e$ , the above equation can be written as

$$\begin{aligned} d - \sqrt{p_p^2 + m_p^2} - \sqrt{p_e^2 + 2p_e p_p c_f + p_p^2} &= 0 \\ d^2 + p_p^2 + m_p^2 - 2d\sqrt{p_p^2 + m_p^2} &= p_e^2 + 2p_e p_p c_f + p_p^2 \\ d^2 + m_p^2 - p_e^2 - 2p_e p_p c_f &= 2d\sqrt{p_p^2 + m_p^2} \\ a - 2p_e p_p c_f &= 2d\sqrt{p_p^2 + m_p^2} \end{aligned} \quad (37)$$

where  $a = d^2 + m_p^2 - p_e^2$ . After squaring both sides and rearranging, we get

$$\begin{aligned} a^2 + (2p_e p_p c_f)^2 - 4ap_e p_p c_f &= 4d^2(p_p^2 + m_p^2) \\ 4(d^2 - p_e^2 c_f^2)p_p^2 + (4ap_e c_f)p_p + (4d^2 m_p^2 - a^2) &= 0 \end{aligned} \quad (38)$$

Consider,

$$\begin{aligned} 4d^2 m_p^2 - a^2 &\equiv h \\ 4ap_e c_f &= 4p_e c_f (d^2 + m_p^2 - p_e^2) \equiv U \\ 4(d^2 - p_e^2 c_f^2) &\equiv W \end{aligned} \quad (39)$$

Hence, the two roots of the equation can be expressed as

$$p_p^\pm = \frac{-U \pm S}{2W} \quad (40)$$

with  $S$  defined by

$$S = \sqrt{U^2 - 4Wh} \quad (41)$$

where,

$$\begin{aligned} h &= 4d^2 m_p^2 - a^2 \\ &= 4d^2 m_p^2 - (d^2 + m_p^2 - p_e^2)^2 \\ &= 4d^2 m_p^2 - (d^2 + m_p^2 - E_e^2 + m_e^2)^2 \\ &= 4d^2 m_p^2 - (d^2 + m_p^2 - (m_n - d)^2 + m_e^2)^2 \\ &= 4d^2 m_p^2 - (m_p^2 - m_n^2 + m_e^2 + 2m_n d)^2 \\ &= -m_n^4 - m_p^4 - m_e^4 + 2m_n^2 m_e^2 + 2m_n^2 m_p^2 - 2m_p^2 m_e^2 \\ &\quad - 4m_n(m_n^2 - m_p^2 - m_e^2)d - 4(m_n^2 - m_p^2)d^2 \end{aligned} \quad (42)$$

Also,  $E_{crit}$  and  $H$  are defined as

$$\begin{aligned} E_{crit} &= \frac{1}{2} \left( m_n - m_p + \frac{m_e^2}{m_n - m_p} \right) \\ H &= \frac{1}{2} \left( m_n + m_p + \frac{m_e^2}{m_n + m_p} \right) \end{aligned} \quad (43)$$

The expression for  $h$  can be expressed in terms of two other expression that depends on the masses of the three particles involved in the decay process. Consider an expression of the form

$$\begin{aligned} h' &= 4(m_n^2 - m_p^2)(E_e - E_{crit})(H - E_e) \\ &= 4(m_n^2 - m_p^2) \left( E_e - \frac{(m_n - m_p)^2 + m_e^2}{2(m_n - m_p)} \right) \left( \frac{(m_n + m_p)^2 + m_e^2}{2(m_n + m_p)} - E_e \right) \\ &= \left[ 2(m_n - m_p)E_e - (m_n - m_p)^2 - m_e^2 \right] \left[ (m_n + m_p)^2 + m_e^2 - 2(m_n + m_p)E_e \right] \\ &= \left[ m_n^2 - m_e^2 - m_p^2 - 2(m_n - m_p)d \right] \left[ -m_n^2 + m_e^2 + m_p^2 + 2(m_n + m_p)d \right] \\ &= -m_n^4 - m_p^4 - m_e^4 + 2m_n^2 m_e^2 + 2m_n^2 m_p^2 - 2m_p^2 m_e^2 \\ &\quad - 4m_n(m_n^2 - m_e^2 - m_p^2)d - 4(m_n^2 - m_p^2)d^2 \end{aligned} \quad (44)$$

Since  $h' = h$ , we can write the expression for  $h$  as

$$h = 4(m_n^2 - m_p^2)(E_e - E_{crit})(H - E_e) \quad (45)$$

The critical energy  $E_{crit} \sim 236 \text{ KeV}$  and for  $E_e < E_{crit}$ , we get  $h < 0$ .

#### A.4 Analysis of Errors on Asymmetries

In terms of  $Q_{ij}$ 's, the proton asymmetry is given by

$$\alpha_p = \frac{(Q_{+-} + Q_{--}) - (Q_{++} + Q_{-+})}{(Q_{+-} + Q_{--}) + (Q_{++} + Q_{-+})} = \frac{Q_-^p - Q_+^p}{Q_-^p + Q_+^p} \quad (46)$$

The error in  $\alpha_p$  is given by

$$\delta(\alpha_p) = \sqrt{\left( \frac{\partial \alpha_p}{\partial Q_-^p} \right)^2 (\delta Q_-^p)^2 + \left( \frac{\partial \alpha_p}{\partial Q_+^p} \right)^2 (\delta Q_+^p)^2} \quad (47)$$

where,

$$\frac{\partial \alpha_p}{\partial Q_-^p} = \frac{2Q_+^p}{(Q_-^p + Q_+^p)^2} \quad (48)$$

$$\frac{\partial \alpha_p}{\partial Q_+^p} = \frac{-2Q_-^p}{(Q_-^p + Q_+^p)^2} \quad (49)$$

and

$$\delta Q_-^p = \sqrt{Q_-^p}, \quad \delta Q_+^p = \sqrt{Q_+^p}$$

Again, from the expression for  $B$  calculated from the proton asymmetry  $\alpha_p$  (Ref. Eqn. 3.48 ), we get

$$\left( \frac{\partial B}{\partial \alpha_p} \right)_A = \begin{cases} \frac{6}{3-r^2}, & r < 1, \\ 3r, & r \geq 1 \end{cases} \quad (50)$$

Hence, the error in  $B$  calculated from the proton asymmetry  $\alpha_p$  is given by

$$\delta(B) = \left| \left( \frac{\partial B}{\partial \alpha_p} \right)_A \right| \delta(\alpha_p) \quad (51)$$

where, correlation coefficients  $A$  is replaced by the lowest order value  $A_0$  set by Standard Model.

For the error in the electron asymmetry, we have

$$\alpha_e = \frac{(Q_{-+} + Q_{--}) - (Q_{++} + Q_{+-})}{(Q_{-+} + Q_{--}) + (Q_{++} + Q_{+-})} = \frac{Q_-^e - Q_+^e}{Q_-^e + Q_+^e} \quad (52)$$

The error in the electron asymmetry can be obtained using the same technique as used for  $\alpha_p$  as

$$\delta(\alpha_e) = \sqrt{\left( \frac{\partial \alpha_e}{\partial Q_-^e} \right)^2 (\delta Q_-^e)^2 + \left( \frac{\partial \alpha_e}{\partial Q_+^e} \right)^2 (\delta Q_+^e)^2} \quad (53)$$

where,

$$\frac{\partial \alpha_e}{\partial Q_-^e} = \frac{2Q_+^e}{(Q_-^e + Q_+^e)^2} \quad (54)$$

$$\frac{\partial \alpha_e}{\partial Q_+^e} = \frac{-2Q_-^e}{(Q_-^e + Q_+^e)^2} \quad (55)$$

and

$$\delta Q_-^e = \sqrt{Q_-^e}, \quad \delta Q_+^e = \sqrt{Q_+^e}$$

The corresponding error in  $A$  can be calculated from (Ref. Eqn. 3.51 )

$$\delta(A) = \left| \left( \frac{\partial A}{\partial \alpha_e} \right) \right| \delta(\alpha_e) = \left| -\frac{2}{\beta_e} \right| \delta(\alpha_e) \quad (56)$$

The ratio of the two asymmetries is given by

$$r_{pe} = \frac{\alpha_p}{\alpha_e} \quad (57)$$



The corresponding statistical error is given by

$$\delta(r_{pe}) = r_{pe} \sqrt{\left(\frac{\delta\alpha_e}{\alpha_e}\right)^2 + \left(\frac{\delta\alpha_p}{\alpha_p}\right)^2} \quad (58)$$

Also, from the expression for  $B$  calculated from the asymmetry ratio  $r_{pe}$  (Ref. Eqn. 3.53), we get

$$\left(\frac{\partial B}{\partial r_{pe}}\right)_A = \begin{cases} \frac{3A\beta_e}{(r^2 - 3)} & r < 1, \\ -\frac{3}{2}A\beta_e r & r \geq 1 \end{cases} \quad (59)$$

Hence, the error in  $B$  calculated from the asymmetry ratio  $r_{pe}$  is given by

$$\delta(B) = \left| \left(\frac{\partial B}{\partial r_{pe}}\right)_A \right| \delta(r_{pe}) \quad (60)$$

Here, the correlation coefficients  $A$  is replaced by the lowest order value  $A_0$  set by Standard Model.

The error in the neutrino asymmetry  $\alpha_{ep}$ , defined as

$$\alpha_{ep}(E_e) = \frac{Q_{--} - Q_{++}}{Q_{--} + Q_{++}} \quad (61)$$

is given by

$$\delta(\alpha_{ep}) = \sqrt{\left(\frac{\partial\alpha_{ep}}{\partial Q_{--}}\right)^2 (\delta Q_{--})^2 + \left(\frac{\partial\alpha_{ep}}{\partial Q_{++}}\right)^2 (\delta Q_{++})^2} \quad (62)$$

where,

$$\frac{\partial\alpha_{ep}}{\partial Q_{--}} = \frac{2Q_{++}}{(Q_{--} + Q_{++})^2} \quad (63)$$

$$\frac{\partial\alpha_{ep}}{\partial Q_{++}} = \frac{-2Q_{--}}{(Q_{--} + Q_{++})^2} \quad (64)$$

and

$$\delta Q_{--} = \sqrt{Q_{--}}, \quad \delta Q_{++} = \sqrt{Q_{++}}$$

Also, from the expression of  $B$  in terms of  $\alpha_{ep}$  (Ref. Eqn.3.56), we get

$$\left(\frac{\partial B}{\partial\alpha_{ep}}\right)_{a,A} = \begin{cases} \frac{3[(8 - 4r) + a\beta_e(r^2 - 2)]}{4(3 - r^2)}, & r < 1, \\ \frac{3(4r - a\beta_e)}{8r}, & r \geq 1, \end{cases} \quad (65)$$

The statistical error in the calculated value of  $B$  is given by

$$\delta(B) = \left| \left( \frac{\partial B}{\partial \alpha_{ep}} \right)_{a,A} \right| \delta(\alpha_{ep}) \quad (66)$$

where, the correlation coefficients  $a$  and  $A$  are replaced by the lowest order value  $a_0$  and  $A_0$  respectively.

The error in electron-proton tilde asymmetry  $\tilde{\alpha}_{ep}$  which is defined as

$$\tilde{\alpha}_{ep}(E_e) = \frac{Q_{+-} - Q_{-+}}{Q_{+-} + Q_{-+}} \quad (67)$$

is given by

$$\delta(\tilde{\alpha}_{ep}) = \sqrt{\left( \frac{\partial \tilde{\alpha}_{ep}}{\partial Q_{+-}} \right)^2 (\delta Q_{+-})^2 + \left( \frac{\partial \tilde{\alpha}_{ep}}{\partial Q_{-+}} \right)^2 (\delta Q_{-+})^2} \quad (68)$$

where,

$$\frac{\partial \tilde{\alpha}_{ep}}{\partial Q_{+-}} = \frac{2Q_{-+}}{(Q_{+-} + Q_{-+})^2} \quad (69)$$

$$\frac{\partial \tilde{\alpha}_{ep}}{\partial Q_{-+}} = \frac{-2Q_{+-}}{(Q_{+-} + Q_{-+})^2} \quad (70)$$

and

$$\delta Q_{+-} = \sqrt{Q_{+-}}, \quad \delta Q_{-+} = \sqrt{Q_{-+}}$$

Again, from the expression of  $B$  obtained from asymmetry  $\tilde{\alpha}_{ep}$  (Ref. Eqn.3.59 ), we get

$$\left( \frac{\partial B}{\partial \tilde{\alpha}_{ep}} \right)_{a,A} = \begin{cases} -\frac{3}{4(r^2-3)} [8 + 4r - (r^2 - 2)a\beta_e], & r < 1, \\ \frac{3}{2}r \left( 4 - \frac{1}{r} + \frac{1}{4r^2}a\beta_e \right), & r \geq 1, \end{cases} \quad (71)$$

Hence, the error in the calculated value of  $B$  is given by

$$\delta(B) = \left| \left( \frac{\partial B}{\partial \tilde{\alpha}_{ep}} \right)_{a,A} \right| \delta(\tilde{\alpha}_{ep}) \quad (72)$$

Here also, the correlation coefficients  $a$  and  $A$  are replaced by the lowest order value  $a_0$  and  $A_0$  respectively.

The error in the first new coincidence differential asymmetry  $\alpha_x(E_e)$  defined as

$$\alpha_x(E_e) = \frac{Q_{--} - Q_{++}}{Q_{+-} - Q_{-+}} \quad (73)$$

is given by

$$\delta(\alpha_x) = \sqrt{\sum_{(i,j)=(\pm,\pm)} \left(\frac{\partial\alpha_x}{\partial Q_{ij}}\right)^2 (\delta Q_{ij})^2} \quad (74)$$

where,

$$\frac{\partial\alpha_x}{\partial Q_{--}} = \frac{-1}{(Q_{+-} - Q_{-+})^2}, \quad \frac{\partial\alpha_x}{\partial Q_{++}} = \frac{1}{(Q_{+-} - Q_{-+})^2} \quad (75)$$

$$\frac{\partial\alpha_x}{\partial Q_{+-}} = -\frac{(Q_{--} - Q_{++})}{(Q_{+-} - Q_{-+})^2}, \quad \frac{\partial\alpha_x}{\partial Q_{-+}} = \frac{(Q_{--} - Q_{++})}{(Q_{+-} - Q_{-+})^2} \quad (76)$$

and

$$\begin{aligned} \delta Q_{--} &= \sqrt{Q_{--}}, & \delta Q_{++} &= \sqrt{Q_{++}} \\ \delta Q_{+-} &= \sqrt{Q_{+-}}, & \delta Q_{-+} &= \sqrt{Q_{-+}} \end{aligned}$$

Again, from the functional form of  $B$  in terms of  $\alpha_x$  (Ref. Eqn.3.61 ), we get

$$\left(\frac{\partial B}{\partial\alpha_x}\right)_{a,A} = \begin{cases} \frac{2A\beta_e}{(1 - \frac{r^2}{3})(1 - \alpha_x)^2}, & r < 1, \\ \frac{3A\beta_e r}{(1 - \alpha_x)^2}, & r \geq 1, \end{cases} \quad (77)$$

The statistical error in the calculated value of  $B$  is then given by

$$\delta(B) = \left| \left(\frac{\partial B}{\partial\alpha_x}\right)_{a,A} \right| \delta(\alpha_x) \quad (78)$$

Here also, the correlation coefficient  $A$  are replaced by the lowest order value  $A_0$ .

The asymmetry  $\alpha_R$  for  $r < 1$  and  $r \geq 1$  are defined by

$$\alpha_R = \frac{\left[ \left(1 + \frac{r}{2}\right) Q_{++} - \left(1 - \frac{r}{2}\right) Q_{+-} \right] - \left[ \left(1 + \frac{r}{2}\right) Q_{--} - \left(1 - \frac{r}{2}\right) Q_{-+} \right]}{\left[ \left(1 + \frac{r}{2}\right) Q_{++} - \left(1 - \frac{r}{2}\right) Q_{+-} \right] + \left[ \left(1 + \frac{r}{2}\right) Q_{--} - \left(1 - \frac{r}{2}\right) Q_{-+} \right]}, \quad r < 1 \quad (79)$$

and

$$\alpha_R = \frac{\left[ \left(2 - \frac{1}{2r}\right) Q_{++} - \frac{1}{2r} Q_{+-} \right] - \left[ \left(2 - \frac{1}{2r}\right) Q_{--} - \frac{1}{2r} Q_{-+} \right]}{\left[ \left(2 - \frac{1}{2r}\right) Q_{++} - \frac{1}{2r} Q_{+-} \right] + \left[ \left(2 - \frac{1}{2r}\right) Q_{--} - \frac{1}{2r} Q_{-+} \right]}, \quad r \geq 1 \quad (80)$$

The error in  $\alpha_R$  is given by

$$\delta(\alpha_R) = \sqrt{\sum_{(i,j)=(\pm,\pm)} \left(\frac{\partial\alpha_R}{\partial Q_{ij}}\right)^2 (\delta Q_{ij})^2} \quad (81)$$

with

$$\begin{aligned}\delta Q_{--} &= \sqrt{Q_{--}}, & \delta Q_{++} &= \sqrt{Q_{++}} \\ \delta Q_{+-} &= \sqrt{Q_{+-}}, & \delta Q_{-+} &= \sqrt{Q_{-+}}\end{aligned}$$

For simplicity, the two expressions for  $\alpha_R$  can be rewritten as

$$\alpha_R = \frac{f_1(Q_{++} - Q_{--}) - f_2(Q_{+-} - Q_{-+})}{f_1(Q_{++} + Q_{--}) - f_2(Q_{+-} + Q_{-+})} \equiv \frac{N}{D} \quad (82)$$

where, for  $r < 1$ ,  $f_1$  and  $f_2$  are given by

$$f_1 = \left(1 + \frac{r}{2}\right), \quad f_2 = \left(1 - \frac{r}{2}\right)$$

and for  $r \geq 1$ ,  $f_1$  and  $f_2$  are given by

$$f_1 = \left(2 - \frac{1}{2r}\right), \quad f_2 = \frac{1}{2r}$$

The derivatives  $\frac{\partial \alpha_R}{\partial Q_{ij}}$  are given by

$$\frac{\partial \alpha_R}{\partial Q_{++}} = f_1 \left(\frac{D - N}{D^2}\right), \quad \frac{\partial \alpha_R}{\partial Q_{--}} = -f_1 \left(\frac{D + N}{D^2}\right) \quad (83)$$

$$\frac{\partial \alpha_R}{\partial Q_{+-}} = -f_2 \left(\frac{D - N}{D^2}\right), \quad \frac{\partial \alpha_R}{\partial Q_{-+}} = f_2 \left(\frac{D + N}{D^2}\right) \quad (84)$$

The statistical error in the asymmetry  $\alpha_R$  for both the cases can be obtained by substituting the corresponding expressions of  $f_1$ ,  $f_2$ ,  $N$  and  $D$  in the above formula. Also, from the expression for  $B$  (Ref. Eqn.3.67), we get

$$\left(\frac{\partial B}{\partial \alpha_R}\right)_{a,A} = \begin{cases} \frac{3a\beta_e(r^2 - 2)}{4(r^2 - 3)}, & r < 1, \\ \frac{3a\beta_e}{8r}, & r \geq 1, \end{cases} \quad (85)$$

The statistical error in the calculated value of  $B$  is given by

$$\delta(B) = \left| \left(\frac{\partial B}{\partial \alpha_R}\right)_{a,A} \right| \delta(\alpha_R) \quad (86)$$

In the above error analysis, the correlation coefficient  $a$  is replaced by the lowest order value  $a_0$ .

It should be noted that in general, the correlation coefficient  $B$  depends explicitly on the values of  $\alpha$ ,  $A$  and  $a$  apart from the implicit dependence on the electron energy  $E_e$  of  $r(E_e)$  and  $\beta_e(E_e)$ . In order to calculate the lowest order value of  $B$  and its statistical error, we strictly assume that  $A$  and  $a$  are replaced by lowest order Standard Model values given in terms of  $\lambda = -1.2701$  [97], [115] defined by

$$A_0 = -\frac{2\lambda(1 + \lambda)}{1 + 3\lambda^2}, \quad a_0 = \frac{1 - \lambda^2}{1 + 3\lambda^2} \quad (87)$$

If these were not the cases, we must take into account of the statistical errors on both  $A$  and  $a$  in the analysis of the errors in  $B$ .

## A.5 UCNA Simulation and Events Types

In UCNA geometry, the events are generated uniformly in the cylindrical volume such that any event is specified by  $(R_0, \phi_0, z_0)$ . This is also called the initial vertex in which  $\phi_0$  takes the values from 0 to  $2\pi$  and  $z$  is constrained by the length of the cylinder.  $R_0$  is the radius of the cylinder where the events are uniformly distributed. In the case of the geometry with the Annular Endcaps,  $R_0$  is given by

$$R_0 = \frac{R_{max}}{\sqrt{2}}$$

where,  $R_{max} = 6.2$  cm is the maximum radius of the event distribution inside a cylindrical decay trap.

### A.5.1 Kinetic Energy Distribution

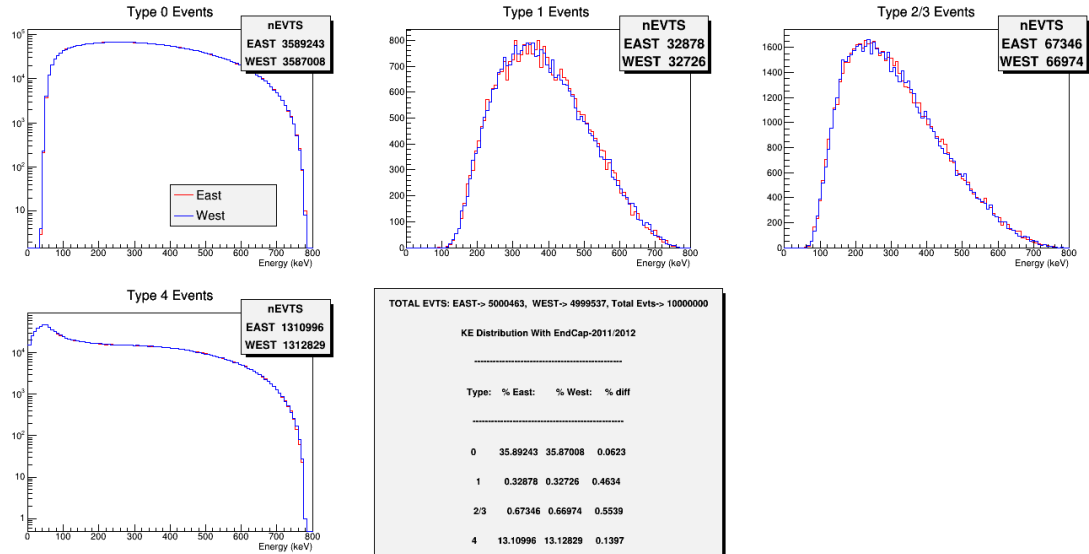


Figure A.15: Kinetic energy distribution with Endcaps 2011/2012

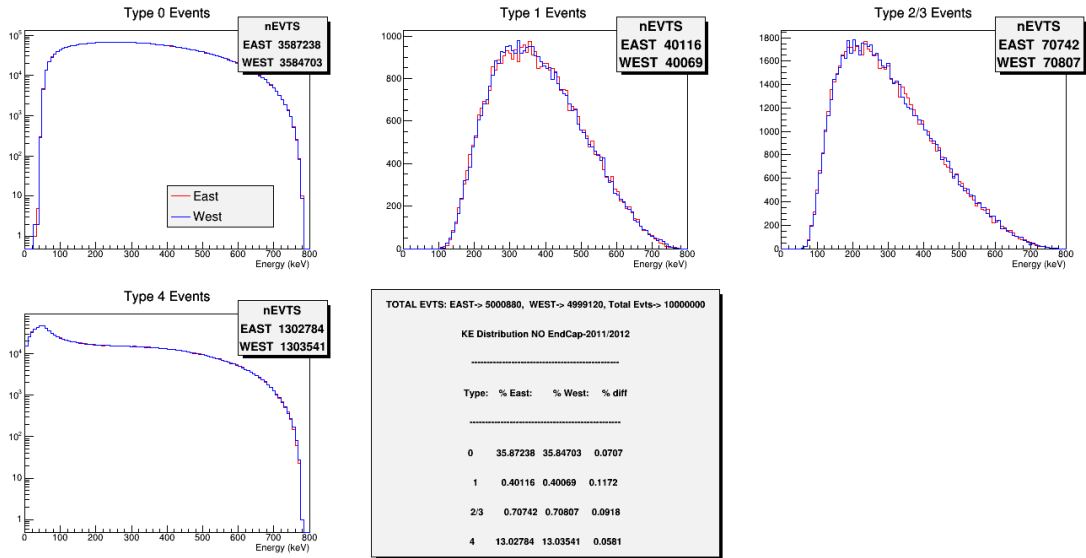


Figure A.16: Kinetic energy distribution with No Endcaps 2011/2012

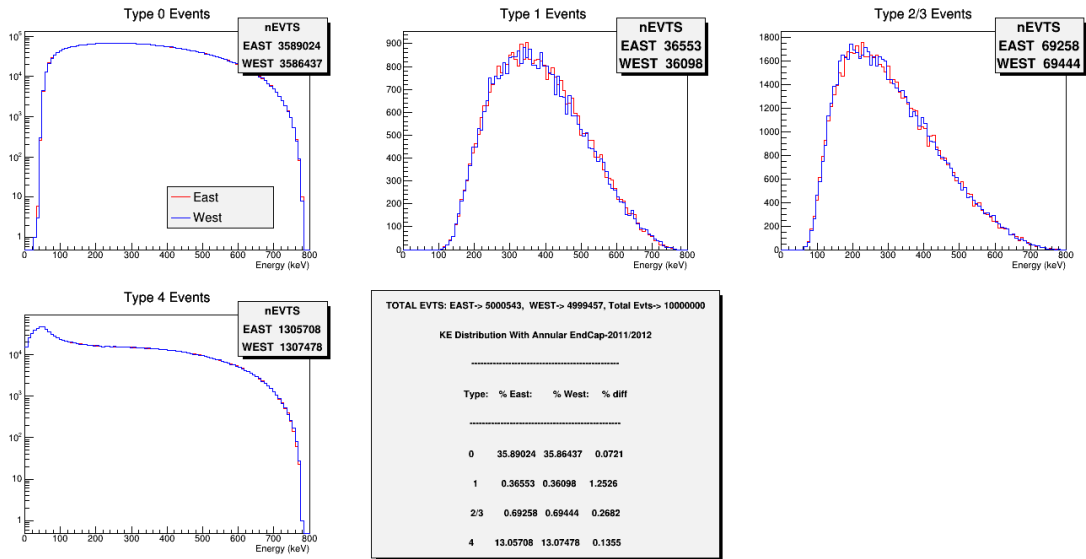


Figure A.17: Kinetic energy distribution with Annular Endcaps 2011/2012

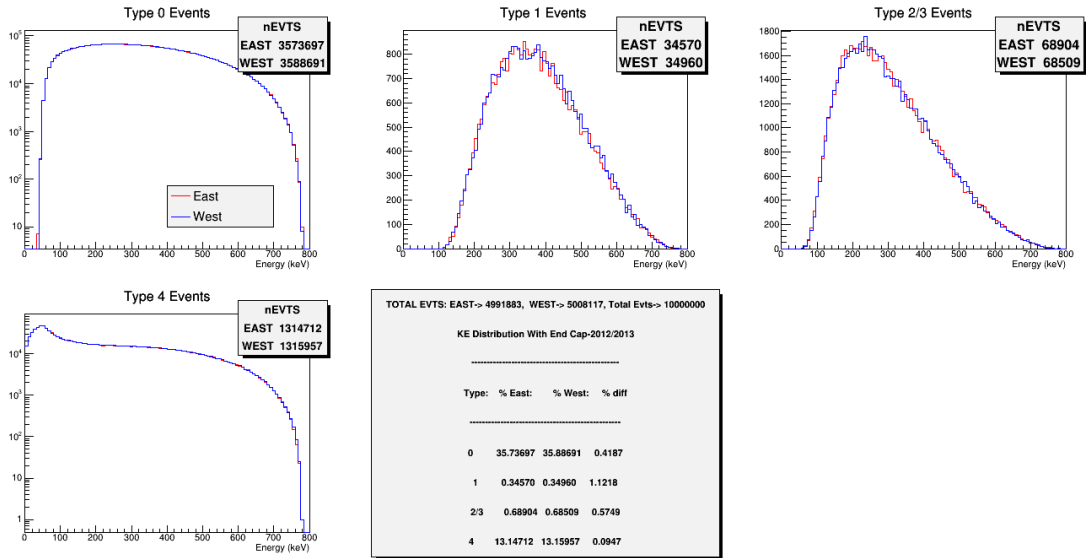


Figure A.18: Kinetic energy distribution with Endcaps 2012/2013

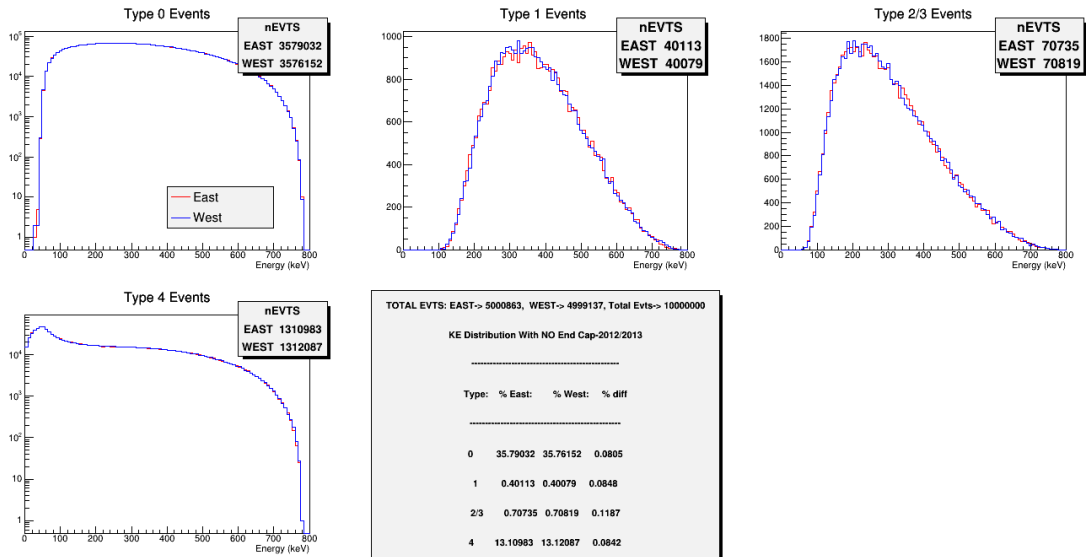


Figure A.19: Kinetic energy distribution with No Endcaps 2012/2013

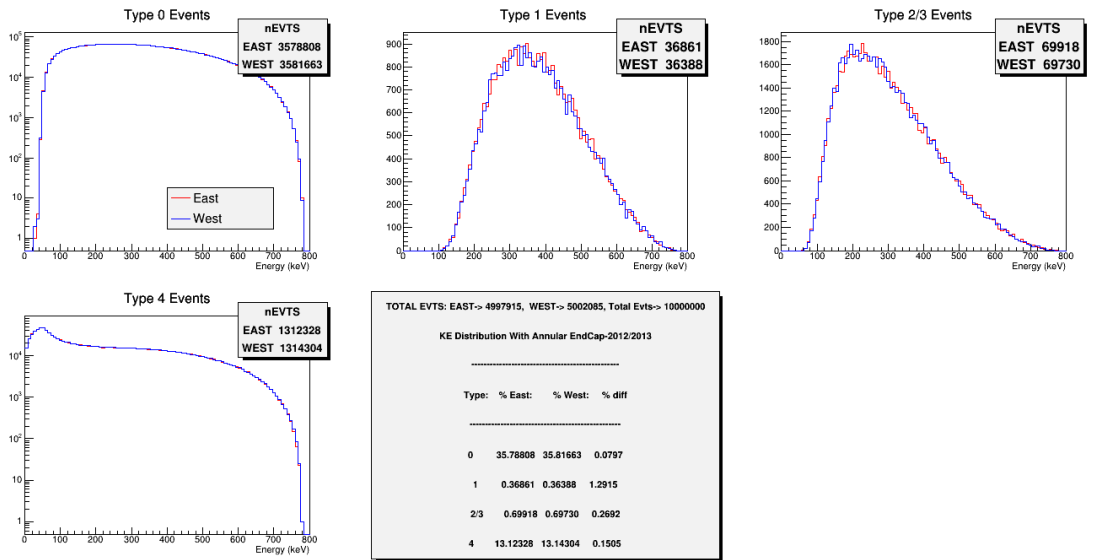


Figure A.20: Kinetic energy distribution with Annular Endcaps 2012/2013



## A.5.2 Angular Distribution

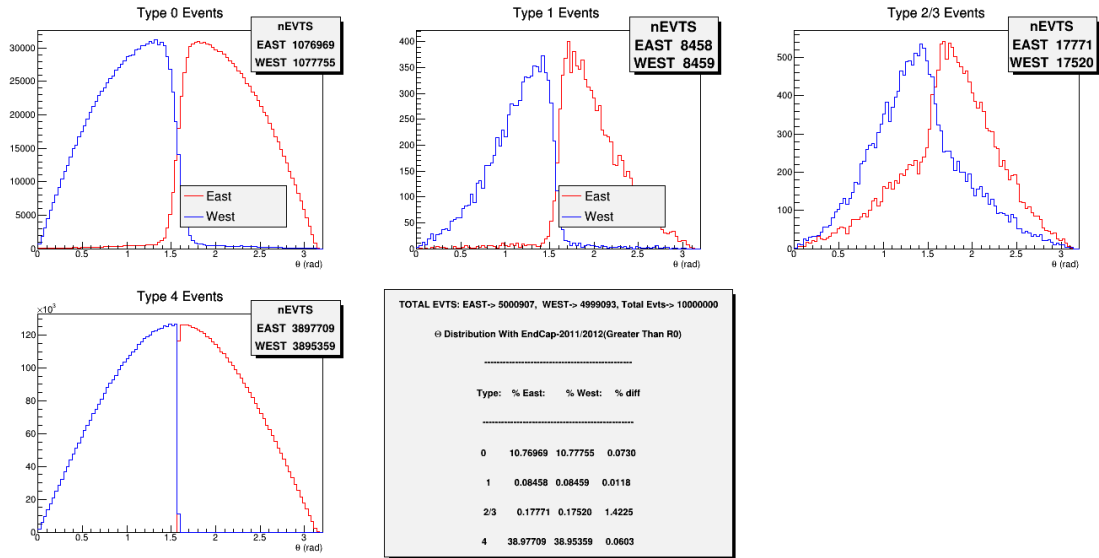


Figure A.21: Angular distribution for the events with Endcaps 2011/12

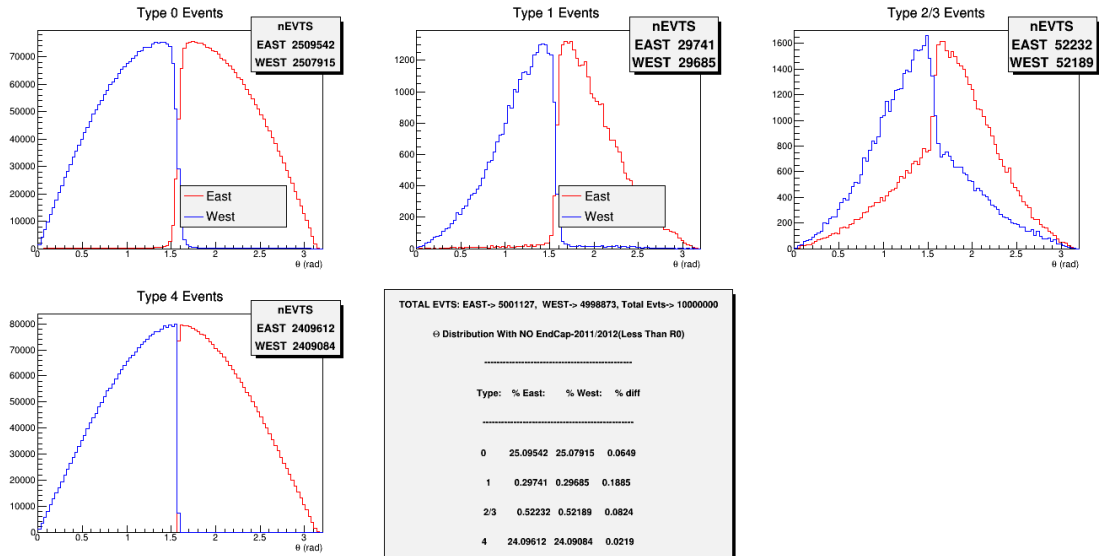


Figure A.22: Angular distribution for the events with No Endcaps 2011/12

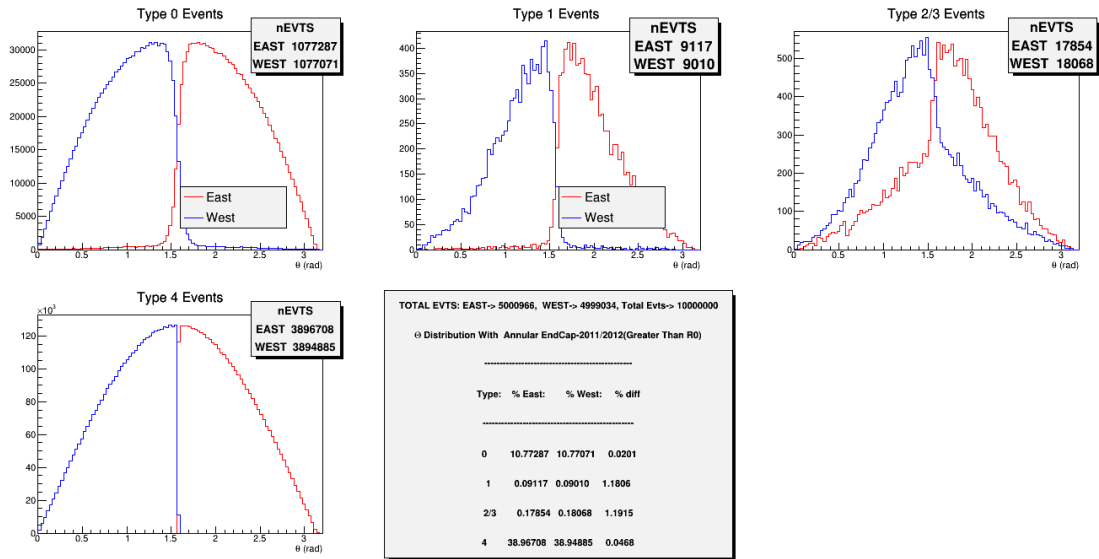


Figure A.23: Angular distribution for the events with Annular Endcaps 2011/12

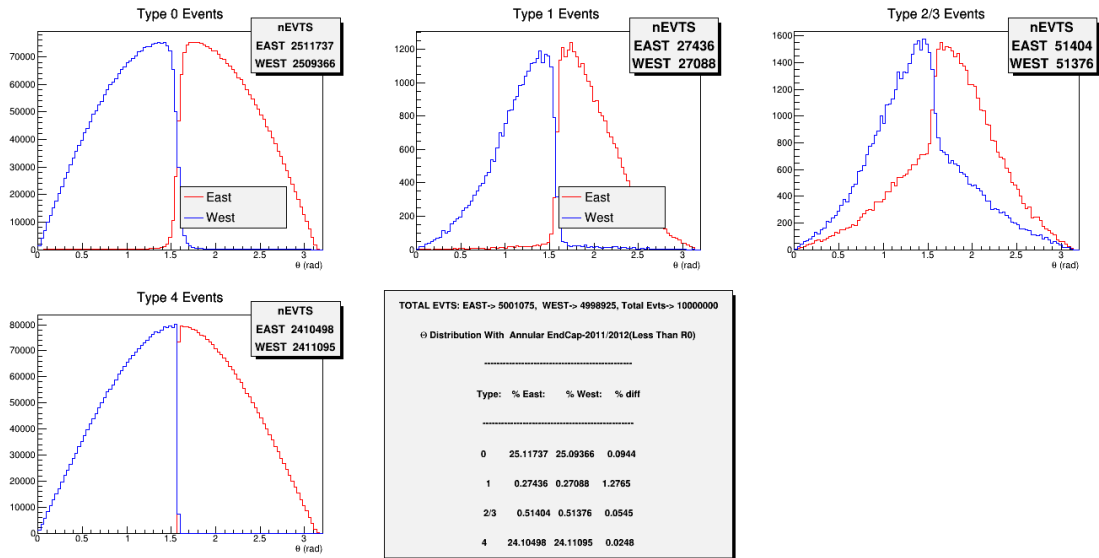


Figure A.24: Angular distribution for the events with Annular Endcaps (less than  $R_0$ ) 2011/12

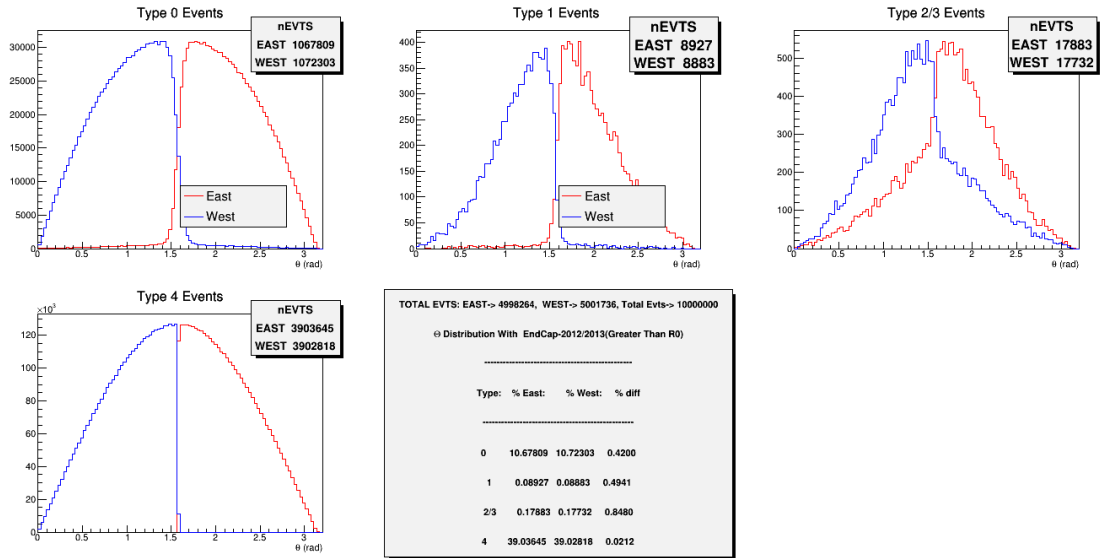


Figure A.25: Angular distribution for the events with Endcaps 2012/13

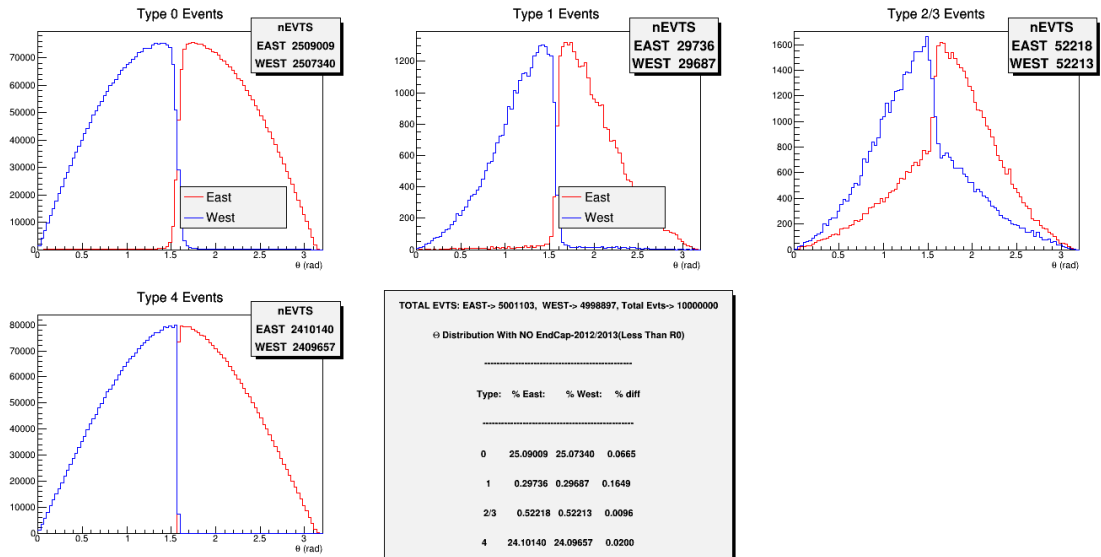


Figure A.26: Angular distribution for the events with No Endcaps 2012/13

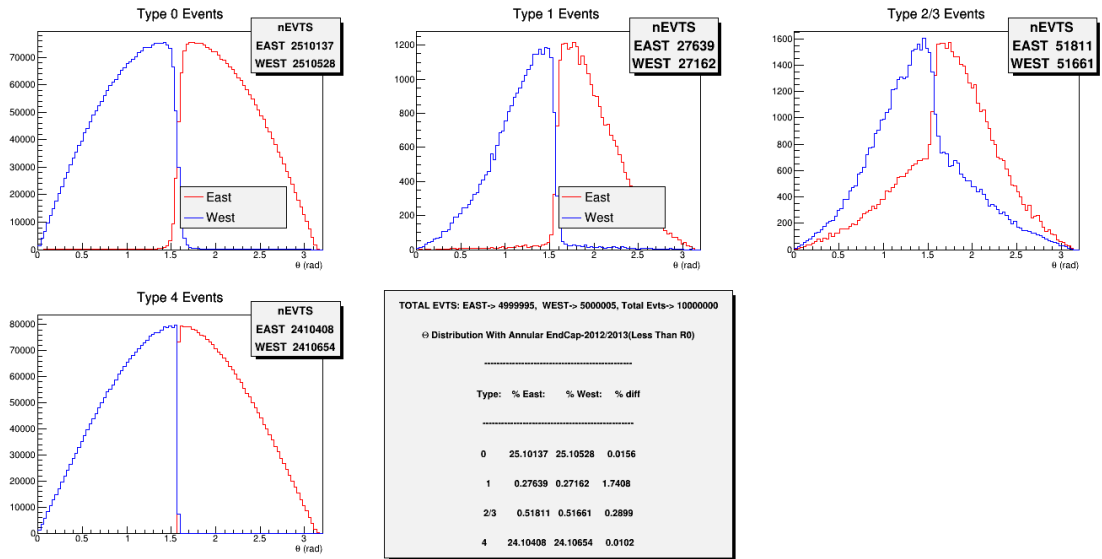


Figure A.27: Angular distribution for the events with Annular Endcaps 2012/13

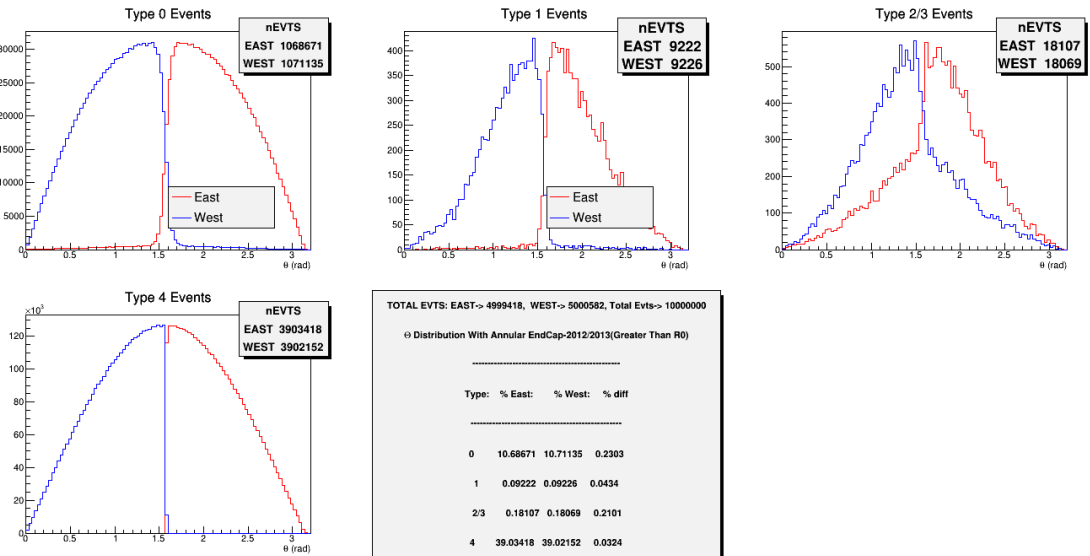


Figure A.28: Angular distribution for the events with Annular Endcaps (greater than  $R_0$ ) 2012/13

### A.5.3 Angular distribution for No Endcaps (2012/2013 geometry)

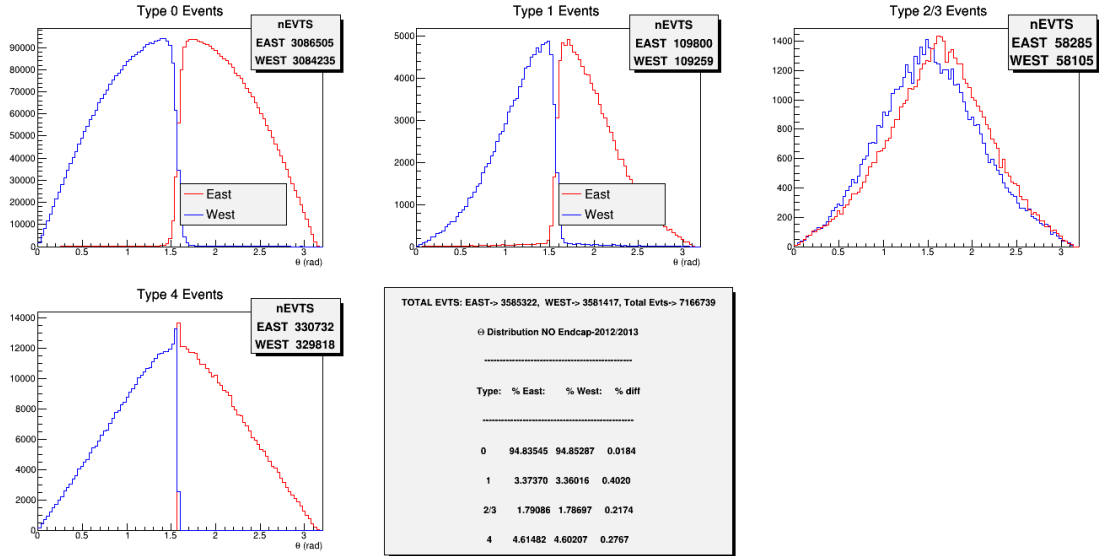


Figure A.29: Angular distribution for the events within the radius cut,  $0.0 < R_0 < 0.5$  cm

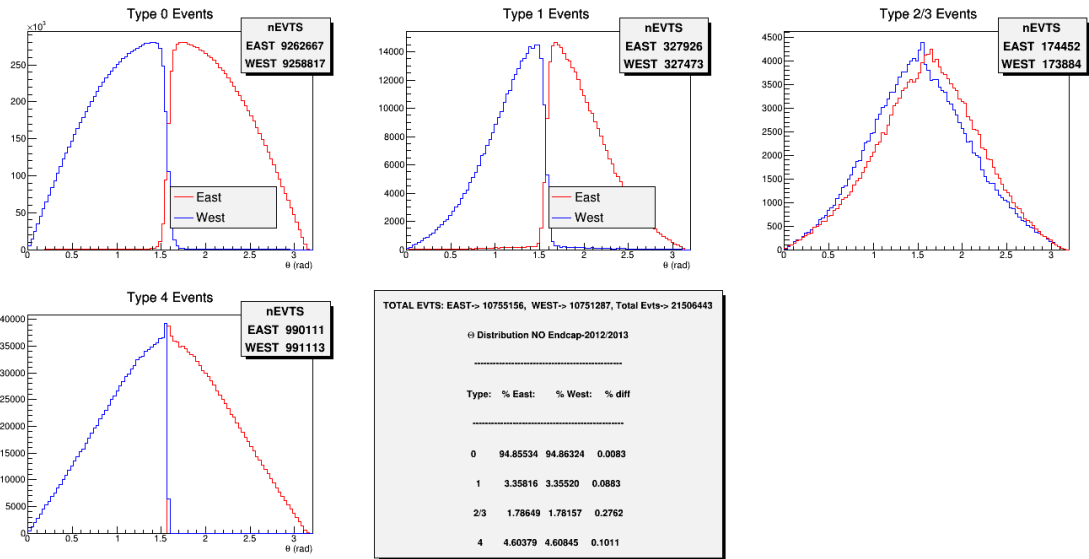


Figure A.30: Angular distribution for the events within the radius cut,  $0.5 < R_0 < 1.0$  cm

## A.6 Analysis of Event Generator

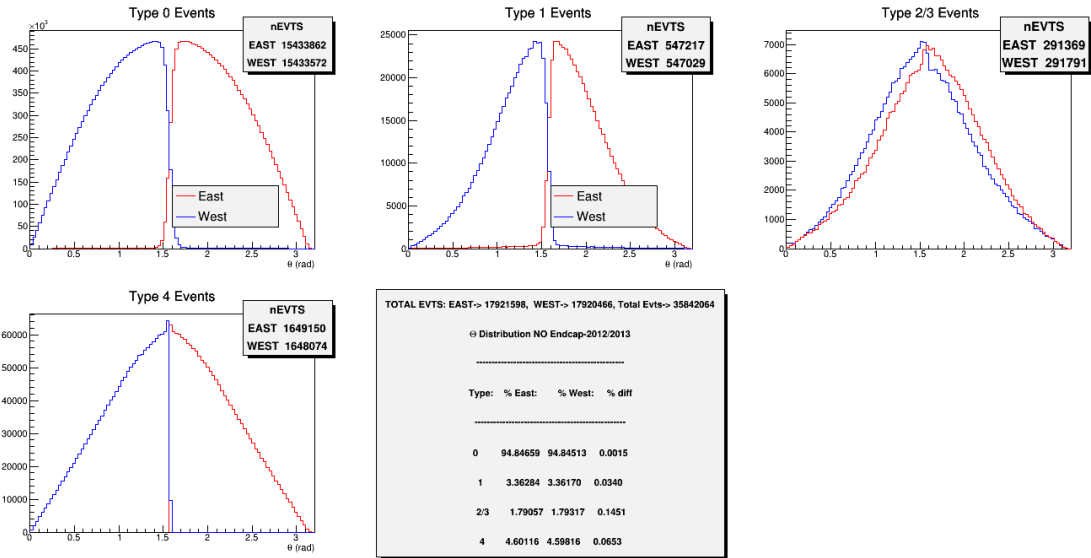


Figure A.31: Angular distribution for the events within the radius cut,  $1.0 < R_0 < 1.5$  cm

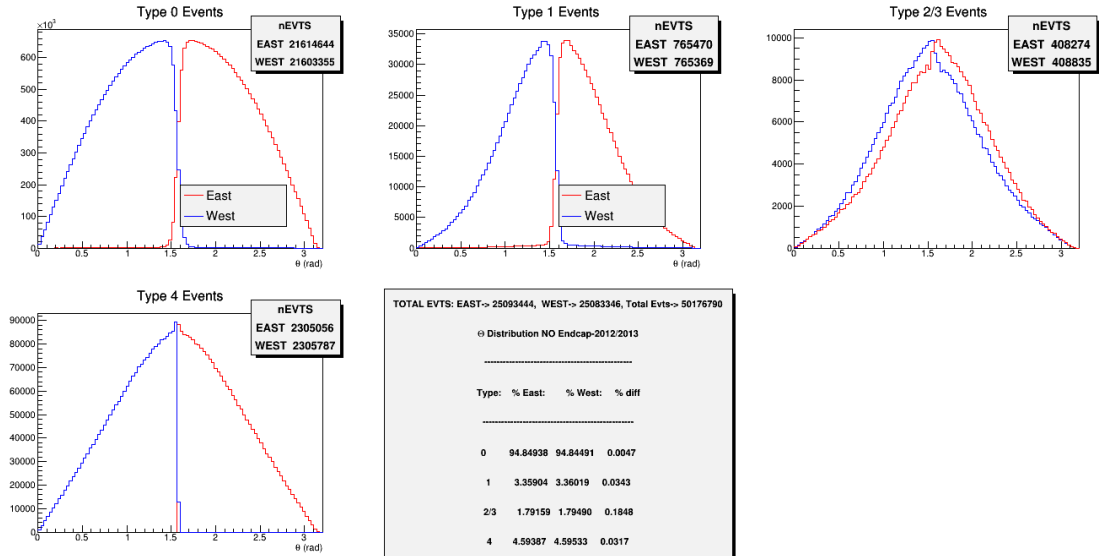


Figure A.32: Angular distribution for the events within the radius cut,  $1.5 < R_0 < 2.0$  cm

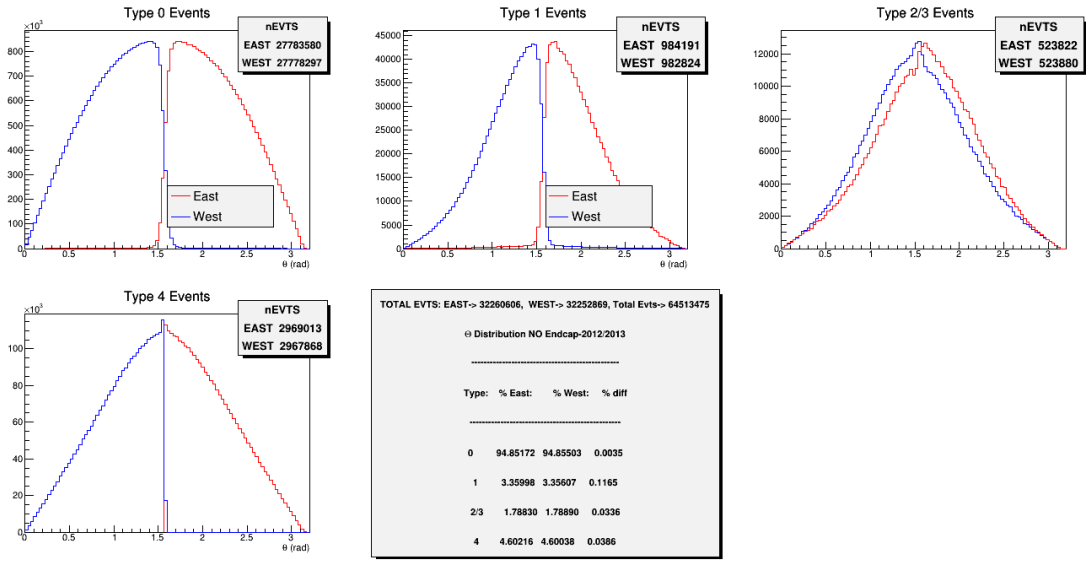


Figure A.33: Angular distribution for the events within the radius cut,  $2.0 < R_0 < 2.5$  cm

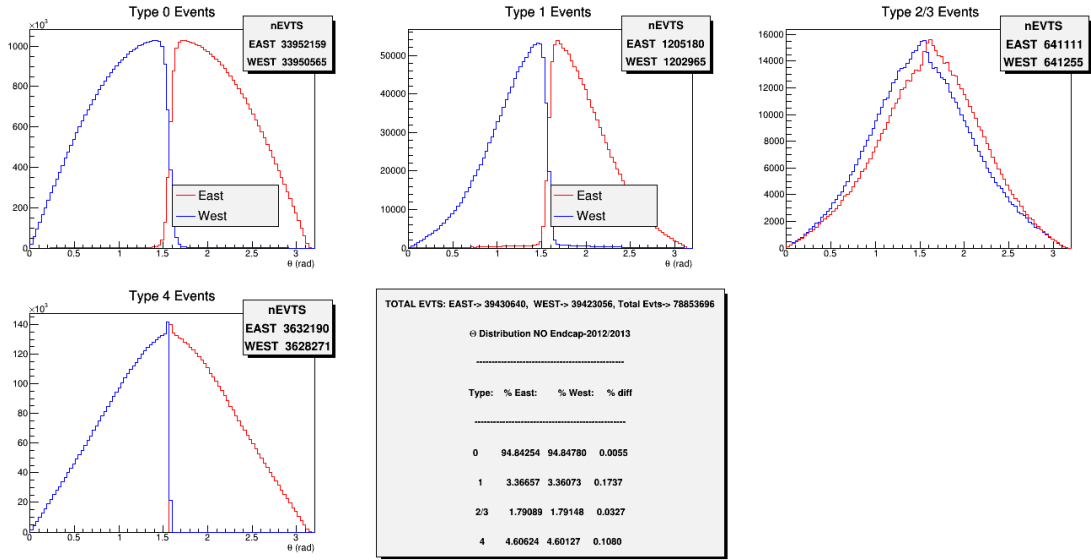


Figure A.34: Angular distribution for the events within the radius cut,  $2.5 < R_0 < 3.0$  cm

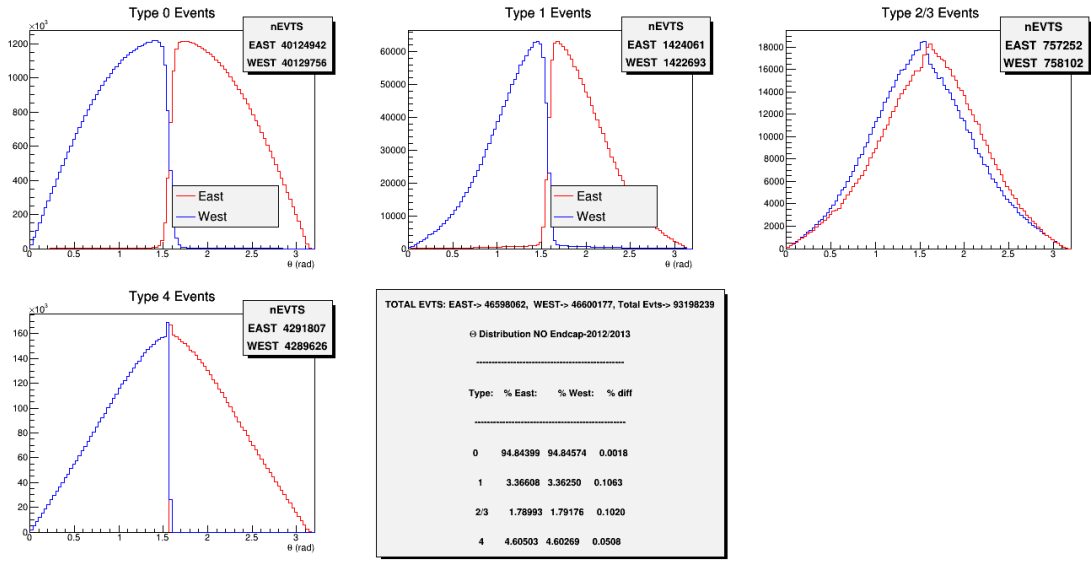


Figure A.35: Angular distribution for the events within the radius cut,  $3.0 < R_0 < 3.5$  cm

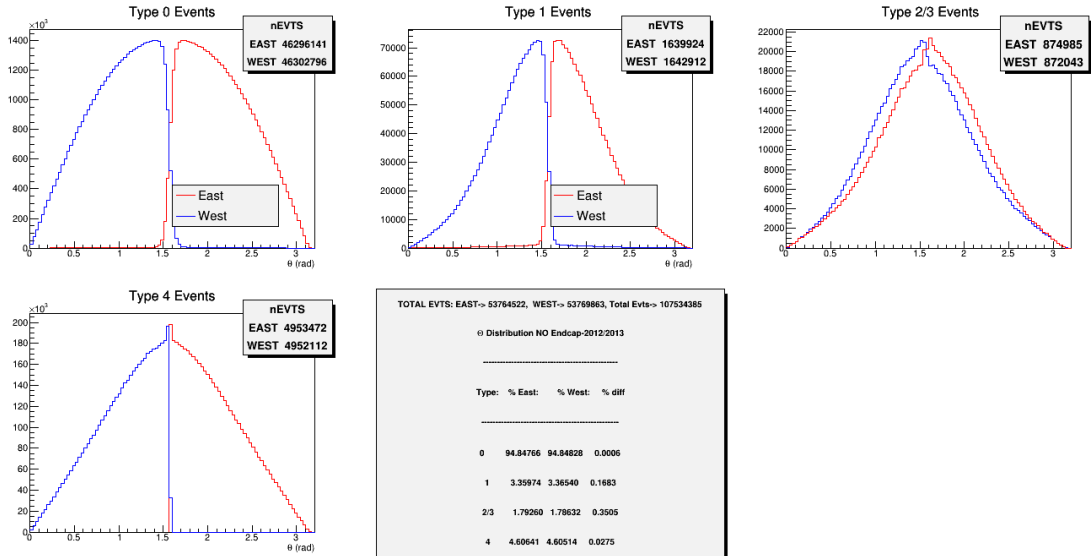


Figure A.36: Angular distribution for the events within the radius cut,  $3.5 < R_0 < 4.0$  cm



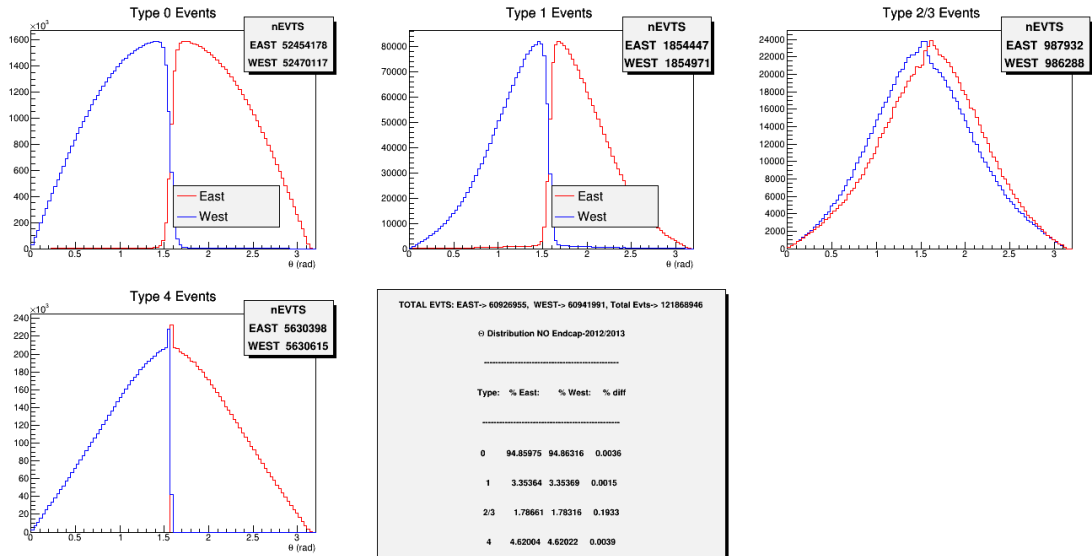


Figure A.37: Angular distribution for the events within the radius cut,  $4.0 < R_0 < 4.5$  cm

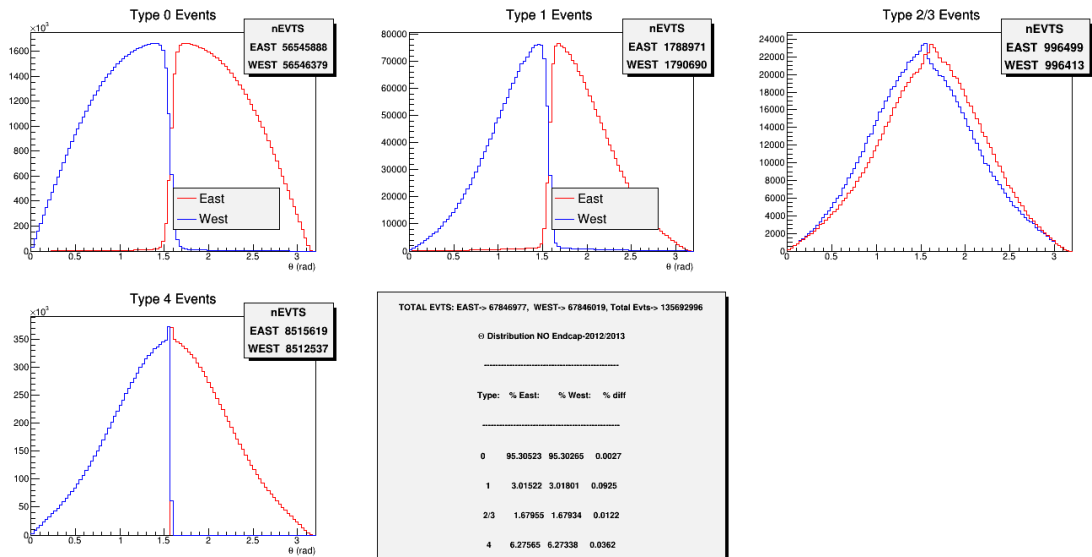


Figure A.38: Angular distribution for the events within the radius cut,  $4.5 < R_0 < 5.0$  cm

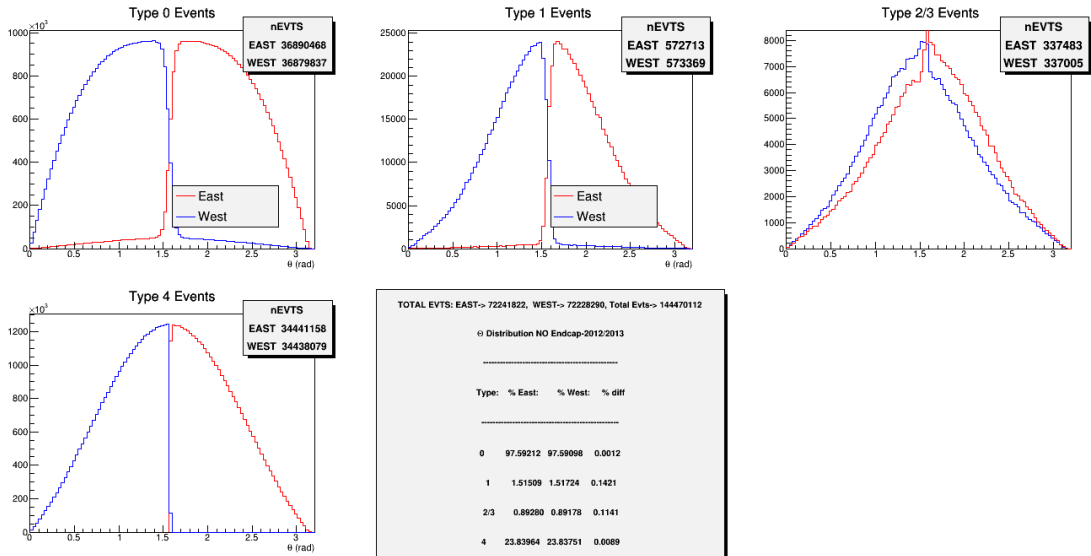


Figure A.39: Angular distribution for the events within the radius cut,  $5.0 < R_0 < 5.5$  cm

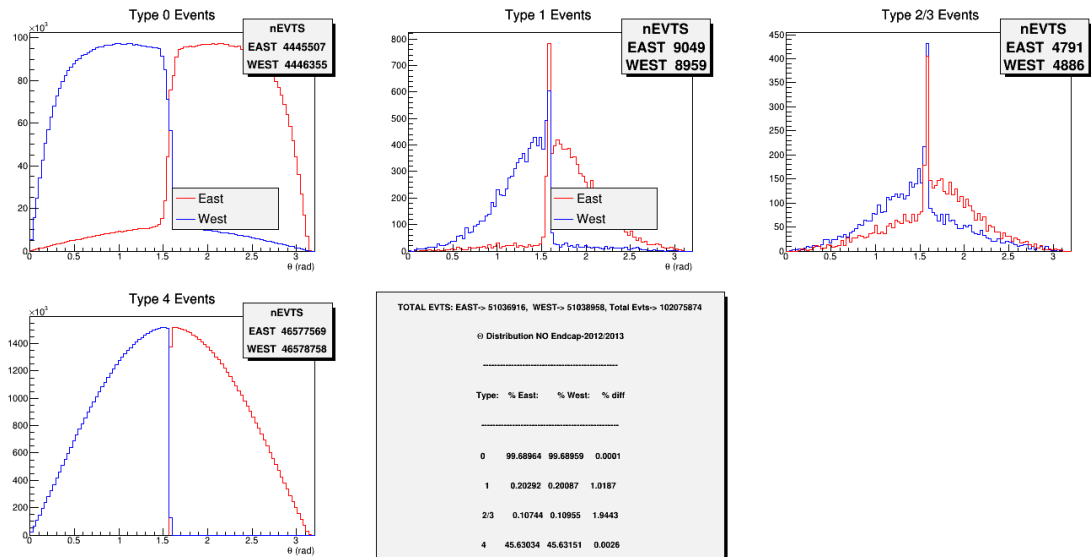


Figure A.40: Angular distribution for the events within the radius cut,  $5.5 < R_0 < 6.0$  cm

# A0 Vs Energy (keV)

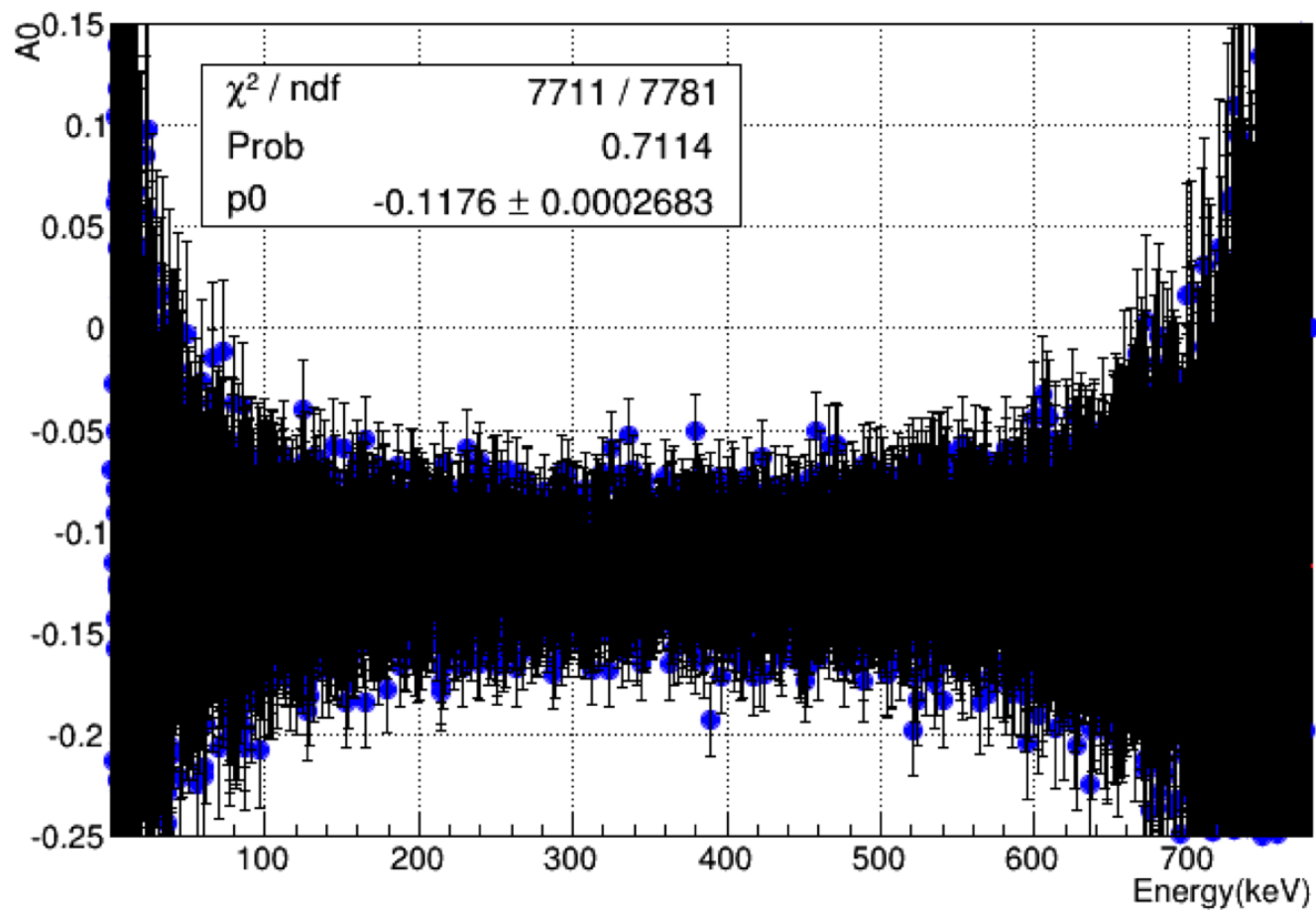


Figure A.41: Electron asymmetry  $A_0$

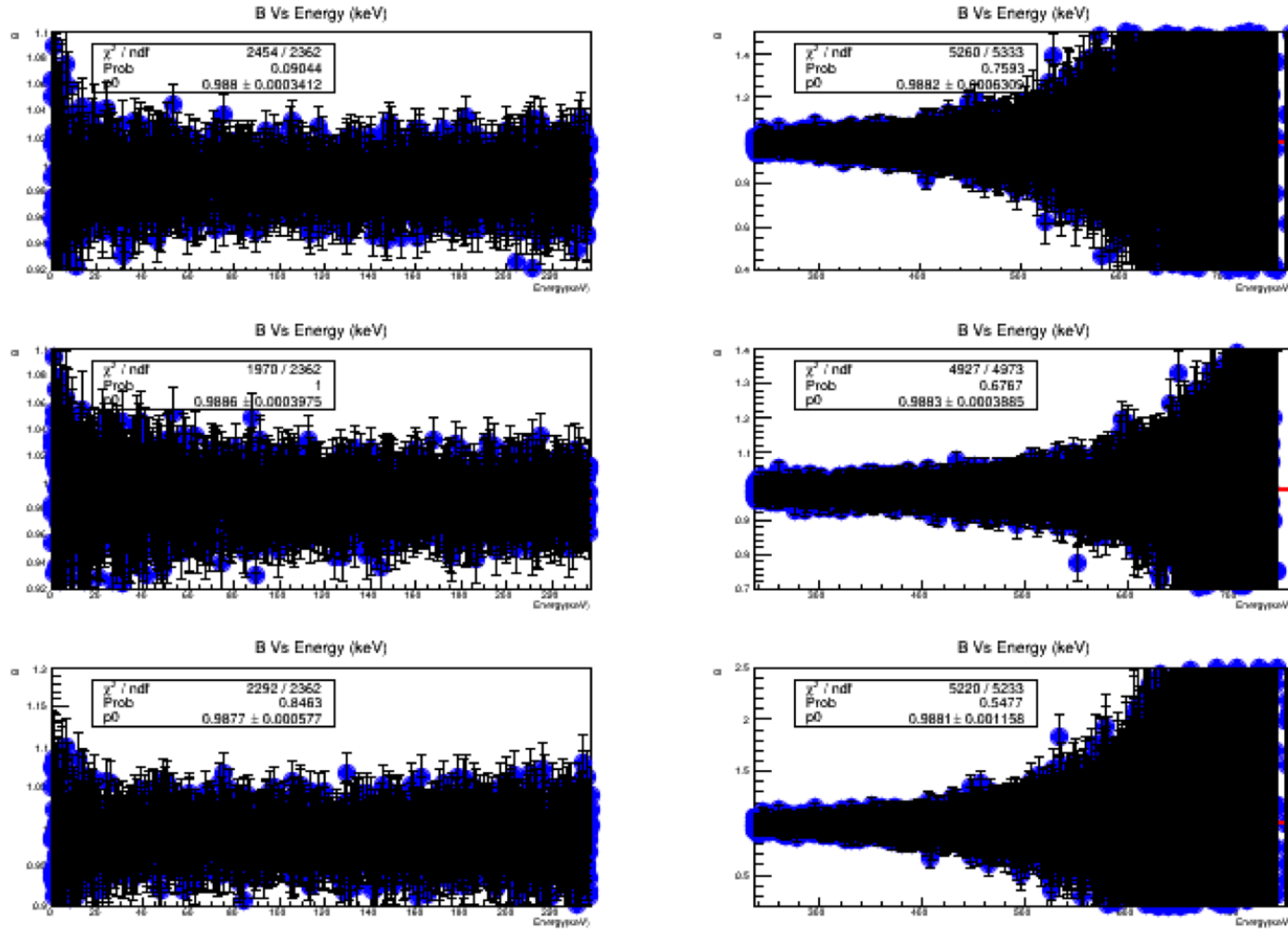


Figure A.42:  $B_0$  obtained from  $\alpha_p$  (first row),  $\alpha_{ep}$  (second row) and  $\tilde{\alpha}_{ep}$  (third row) for  $r < 1$  and  $r > 1$  cases.

### A.6.1 Values for $A_0$ , $B_0$ and $\lambda$

The number of sigma deviations for the quantity  $X$  ( where  $X = A_0$  or  $B_0$ ) is calculated using

$$\sigma_X = \frac{|X_{input} - X_{calculated}|}{\delta X}$$

INPUT PARAMETERS:

$$\lambda = -1.2701$$

$$a_0 = -0.105002$$

$$A_0 = -0.117495$$

$$B_0 = 0.987506$$

Table A.4: Calculations of  $A_0$  and  $\lambda$

Simulation	$A_0$	$\delta A_0$	$\lambda$	$\delta \lambda$	$d\lambda/dA$	$\sigma_A$
1	-0.117636	0.000268337	-1.27048	0.000717429	2.67361	0.5254590
2	-0.117482	0.000268332	-1.27007	0.000717090	2.67240	0.0484474
3	-0.117353	0.000268343	-1.26972	0.000716847	2.67138	0.5291730
4	-0.117347	0.000268340	-1.26970	0.000716827	2.67134	0.5515390
5	-0.117454	0.000268345	-1.26999	0.000717066	2.67218	0.1527880
6	-0.117381	0.000268335	-1.26980	0.000716885	2.67160	0.4248420
7	-0.117585	0.000268340	-1.27034	0.000717329	2.67321	0.3353950
8	-0.117589	0.000268341	-1.27035	0.000717340	2.67324	0.3503010
9	-0.117696	0.000268341	-1.27064	0.000717566	2.67408	0.7490470
10	-0.117298	0.000268344	-1.26957	0.000716734	2.67095	0.7341320

Table A.5: Calculations of  $B_0$  and  $\lambda$  from  $\alpha_p$  for ( $r < 1.0$ )

Simulation	$B_0$	$\delta B_0$	$\lambda$	$d\lambda$	$d\lambda/dB$	$\sigma_B$
1	0.987596	0.000341218	-1.26893	0.00448672	13.1491	0.263761
2	0.987879	0.000341222	-1.26519	0.00451627	13.2356	1.093130
3	0.987977	0.000341182	-1.26390	0.00452624	13.2663	1.380490
4	0.987370	0.000341227	-1.27189	0.00446412	13.0971	0.398562
5	0.987420	0.000341209	-1.27124	0.00446885	13.0971	0.252045
6	0.988332	0.000341213	-1.25917	0.00456598	13.3816	2.420780
7	0.987937	0.000341190	-1.26443	0.00452204	13.2537	1.263230
8	0.988140	0.000341157	-1.26173	0.00454370	13.3185	1.858380
9	0.987997	0.000341157	-1.26363	0.00452807	13.2727	1.439220
10	0.987637	0.000341183	-1.26839	0.00449046	13.1614	0.383958

Table A.6: Calculations of  $B_0$  and  $\lambda$  and from  $\alpha_p$  for ( $r > 1.0$ )

Simulation	$B_0$	$\delta B_0$	$\lambda$	$d\lambda$	$d\lambda/dB$	$\sigma_B$
1	0.988676	0.000630928	-1.25454	0.00851710	13.4993	1.854410
2	0.988584	0.000630880	-1.25578	0.00849621	13.4672	1.708720
3	0.987992	0.000630941	-1.26370	0.00837328	13.2711	0.770278
4	0.988462	0.000630909	-1.25742	0.00847019	13.4254	1.515270
5	0.989343	0.000630897	-1.24546	0.00867242	13.7462	2.911730
6	0.988397	0.000630818	-1.25830	0.00845510	13.4034	1.412450
7	0.987999	0.000630931	-1.26360	0.00837454	13.2733	0.781385
8	0.987933	0.000630950	-1.26448	0.00836165	13.2525	0.676757
9	0.988182	0.000630931	-1.26117	0.00841168	13.3322	1.071430
10	0.988980	0.000630952	-1.25042	0.00858639	13.6086	2.336150

Table A.7: Calculations of  $B_0$  and  $\lambda$  from  $\alpha_{ep}$  for ( $r < 1.0$ )

Simulation	$B_0$	$\delta B_0$	$\lambda$	$d\lambda$	$d\lambda/dB$	$\sigma_B$
1	0.988234	0.000456337	-1.26048	0.00609173	13.3492	1.595310
2	0.987885	0.000456494	-1.26511	0.00604281	13.2374	0.830241
3	0.987887	0.000456316	-1.26509	0.00604074	13.2381	0.834948
4	0.987246	0.000456570	-1.27351	0.00595684	13.0469	0.569464
5	0.987863	0.000456421	-1.26541	0.00603872	13.2306	0.782173
6	0.988356	0.000456334	-1.25884	0.00611014	13.3896	1.862670
7	0.987726	0.000456553	-1.26722	0.00602120	13.1884	0.481872
8	0.988072	0.000456384	-1.26263	0.00606835	13.2966	1.240180
9	0.988397	0.000456312	-1.25830	0.00611613	13.4034	1.952610
10	0.987883	0.000456452	-1.26514	0.00604197	13.2368	0.825936

Table A.8: Calculations of  $B_0$  and  $\lambda$  from  $\alpha_{ep}$  for ( $r > 1.0$ )

Simulation	$B_0$	$\delta B_0$	$\lambda$	$d\lambda$	$d\lambda/dB$	$\sigma_B$
1	0.988153	0.000401987	-1.26156	0.00535556	13.3227	1.6095000
2	0.988192	0.000401962	-1.26104	0.00536033	13.3354	1.7066300
3	0.987715	0.000402189	-1.26736	0.00530288	13.1850	0.5196560
4	0.987520	0.000402121	-1.26993	0.00527844	13.1265	0.0348154
5	0.988890	0.000401723	-1.25165	0.00545368	13.5757	3.4451600
6	0.987703	0.000402061	-1.26752	0.00529972	13.1814	0.4899750
7	0.988542	0.000401822	-1.25635	0.00540560	13.4527	2.5782600
8	0.988494	0.000401889	-1.25699	0.00539989	13.4363	2.4583900
9	0.988124	0.000401945	-1.26194	0.00535123	13.3133	1.5375200
10	0.987806	0.000402068	-1.26616	0.00531250	13.2129	0.7461420

Table A.9: Calculations of  $B_0$  and  $\lambda$  from  $\tilde{\alpha}_{ep}$  for ( $r < 1.0$ )

Simulation	$B_0$	$\delta B_0$	$\lambda$	$d\lambda$	$d\lambda/dB$	$\sigma_B$
1	0.987126	0.000566888	-1.27508	0.00737694	13.0130	0.670326
2	0.987710	0.000566961	-1.26743	0.00747454	13.1835	0.359813
3	0.987839	0.000566899	-1.26572	0.00749618	13.2231	0.587406
4	0.987661	0.000566780	-1.26807	0.00746374	13.1687	0.273475
5	0.987066	0.000566843	-1.27586	0.00736687	12.9963	0.776229
6	0.988253	0.000566959	-1.26022	0.00757198	13.3554	1.317560
7	0.988185	0.000566783	-1.26113	0.00755700	13.3331	1.197990
8	0.988315	0.000566784	-1.25939	0.00758128	13.3760	1.427350
9	0.987686	0.000566810	-1.26774	0.00746842	13.1762	0.317567
10	0.987568	0.000566799	-1.26930	0.00744817	13.1408	0.109386

Table A.10: Calculations of  $B_0$  and  $\lambda$  from  $\tilde{\alpha}_{ep}$  for ( $r > 1.0$ )

Simulation	$B_0$	$\delta B_0$	$\lambda$	$d\lambda$	$d\lambda/dB$	$\sigma_B$
1	0.989055	0.00115800	-1.24940	0.0157910	13.6364	1.337650
2	0.989097	0.00115792	-1.24883	0.0158080	13.6521	1.374020
3	0.988412	0.00115799	-1.25809	0.0155268	13.4084	0.782390
4	0.988632	0.00115807	-1.25514	0.0156153	13.4839	0.972307
5	0.989526	0.00115804	-1.24294	0.0160025	13.8186	1.744330
6	0.988997	0.00115781	-1.25019	0.0157635	13.6149	1.287780
7	0.987052	0.00115807	-1.27604	0.0150461	12.9924	0.392032
8	0.987288	0.00115807	-1.27296	0.0151232	13.0589	0.188244
9	0.988069	0.00115799	-1.26267	0.0153962	13.2956	0.486187
10	0.989925	0.00115808	-1.23739	0.0161949	13.9843	2.088800

A.7  $A_0$  and  $B_0$  calculations with no bremsstrahlung effects

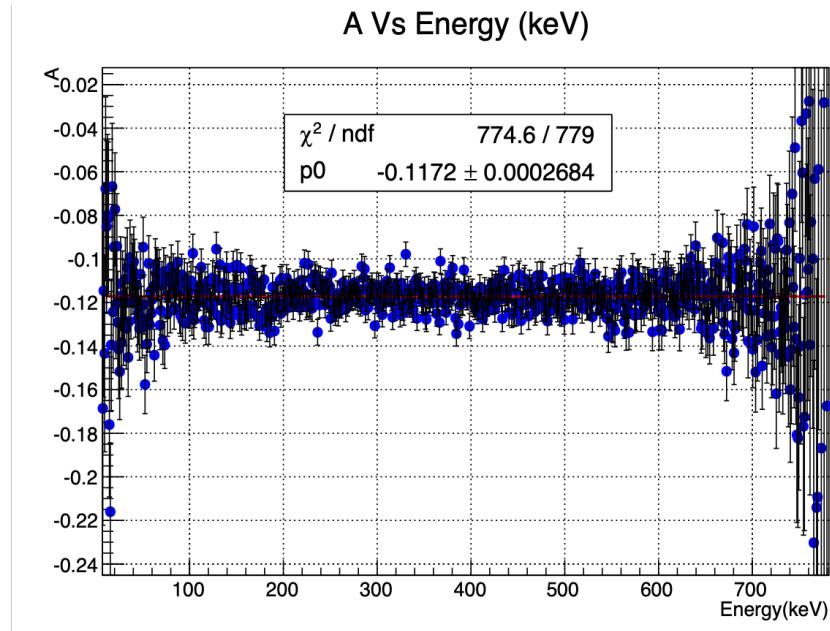


Figure A.43: Electron asymmetry  $A$  as a function of electron energy.



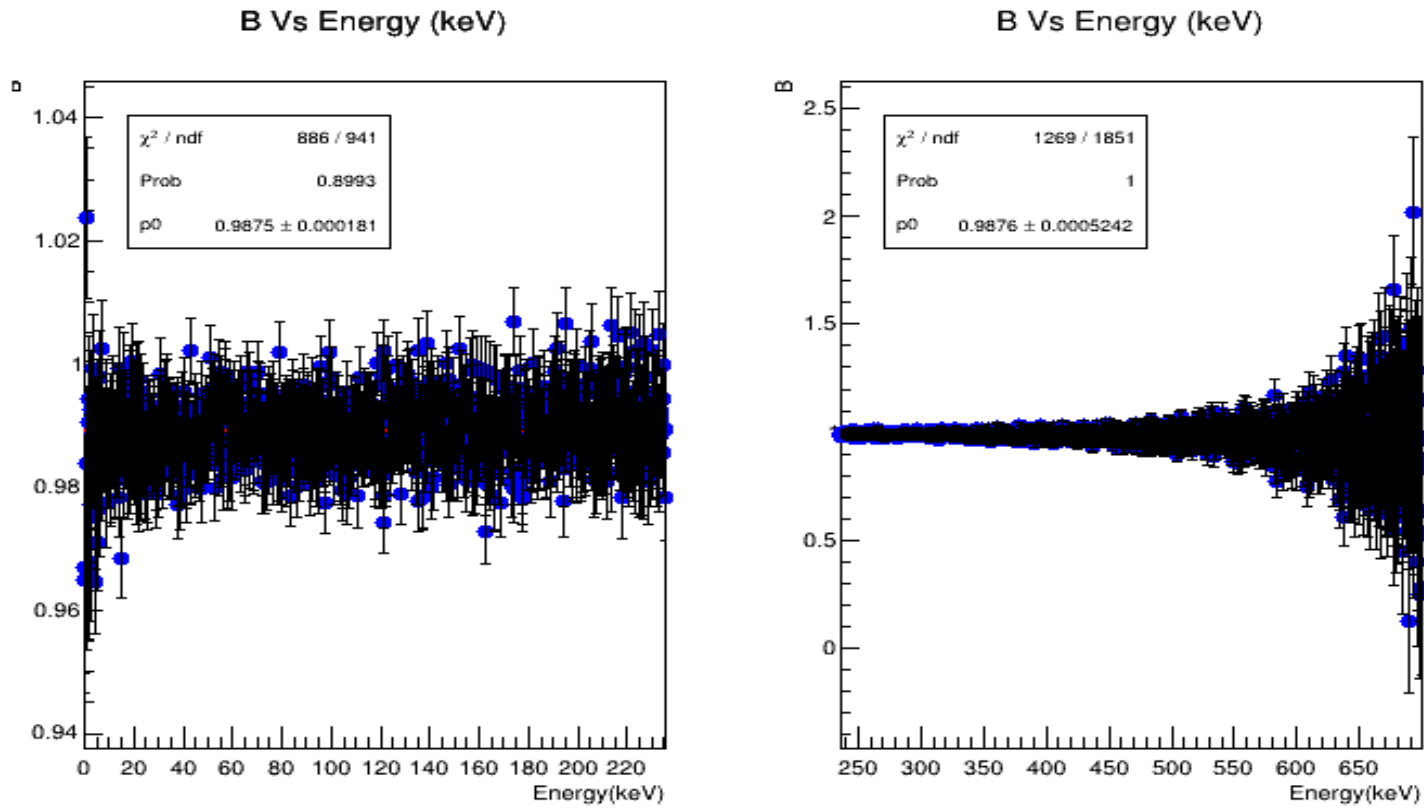


Figure A.44: Neutrino asymmetry  $B$  as a function of electron energy for the regions  $r < 1$  (left) and  $r > 1$  (right) obtained from  $\alpha_p$ .

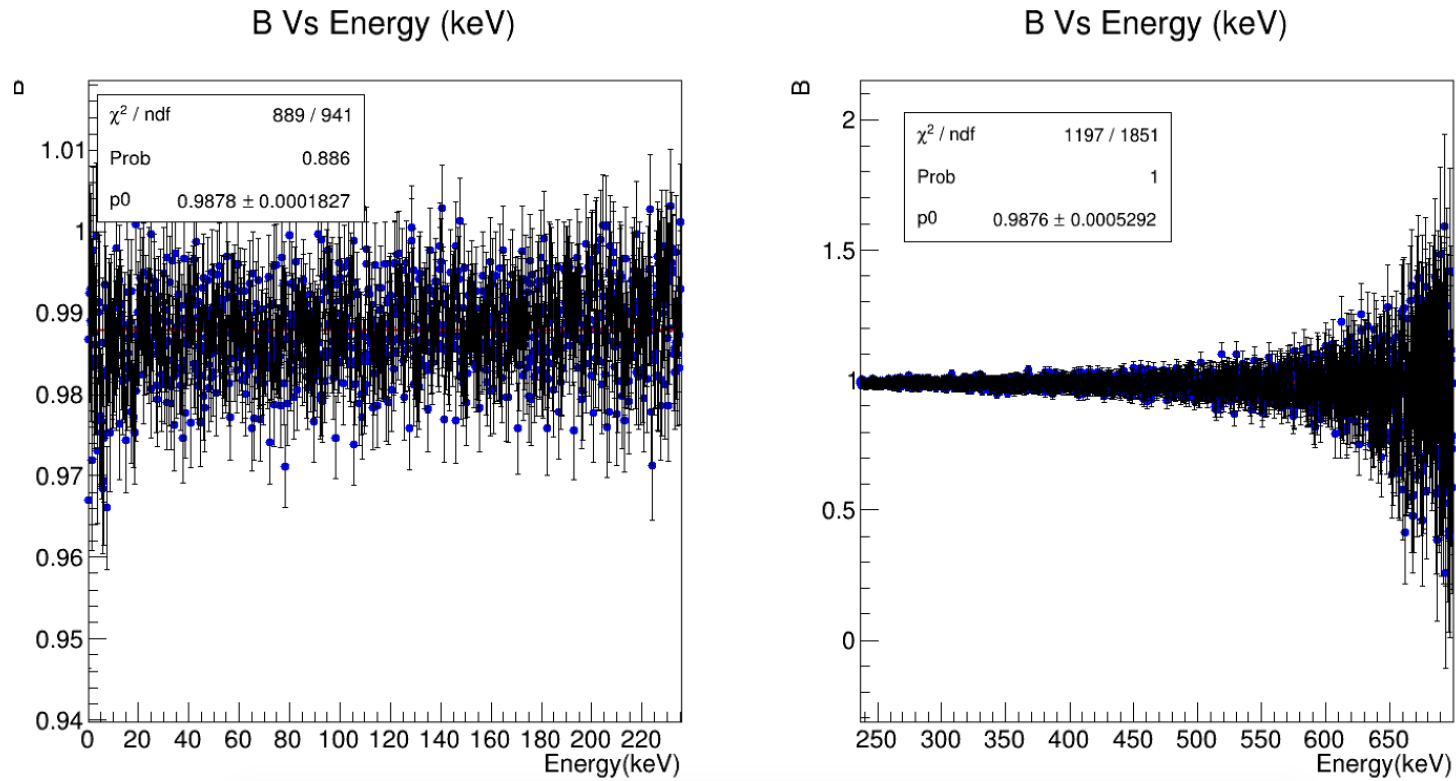


Figure A.45: Neutrino asymmetry  $B$  as a function of electron energy for the regions  $r < 1$  (left) and  $r > 1$  (right) obtained from  $\alpha_{ep}$ .

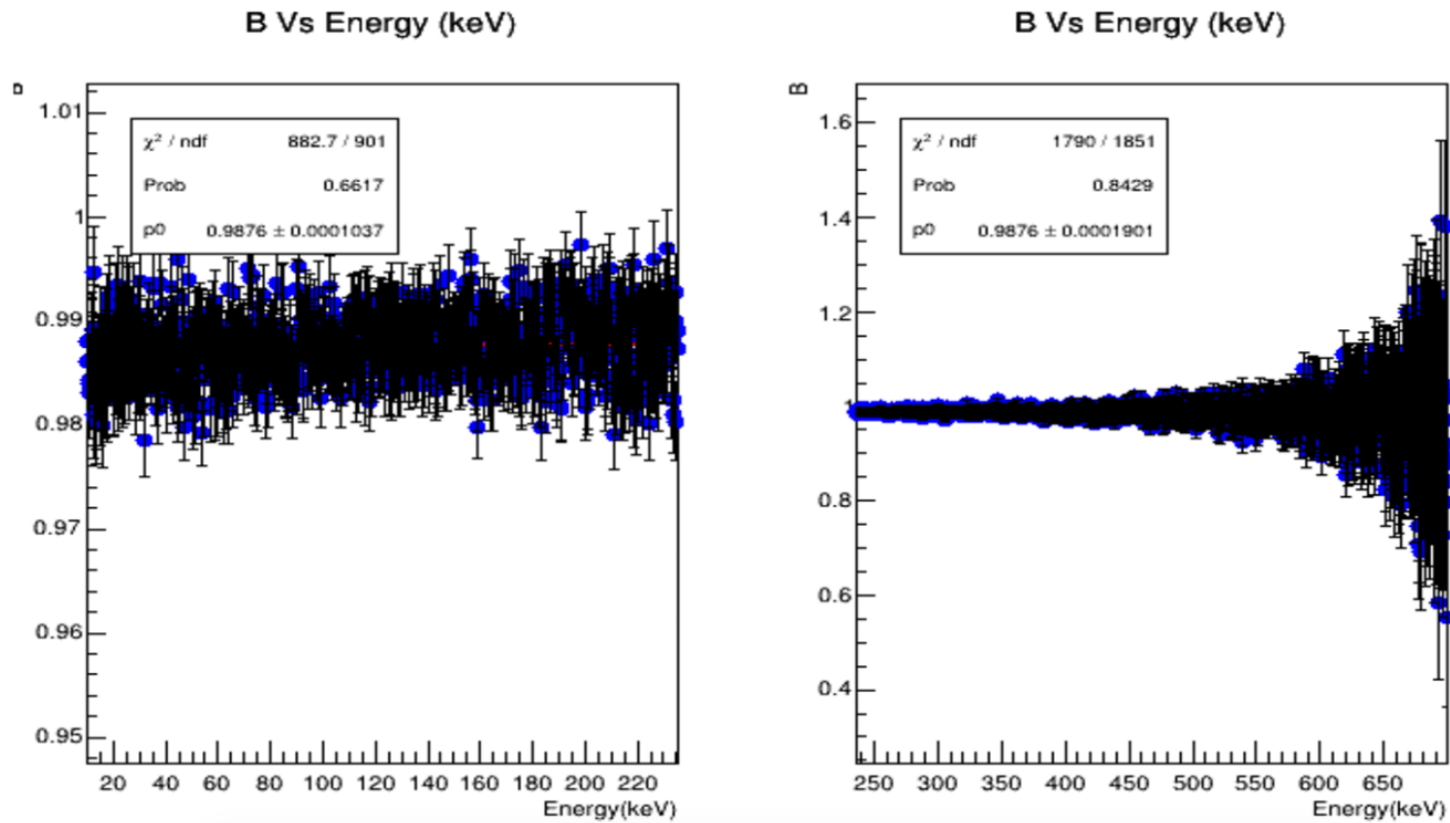


Figure A.46: Neutrino asymmetry  $B$  as a function of electron energy for the regions  $r < 1$  (left) and  $r > 1$  (right) obtained from  $\tilde{\alpha}_{ep}$ .

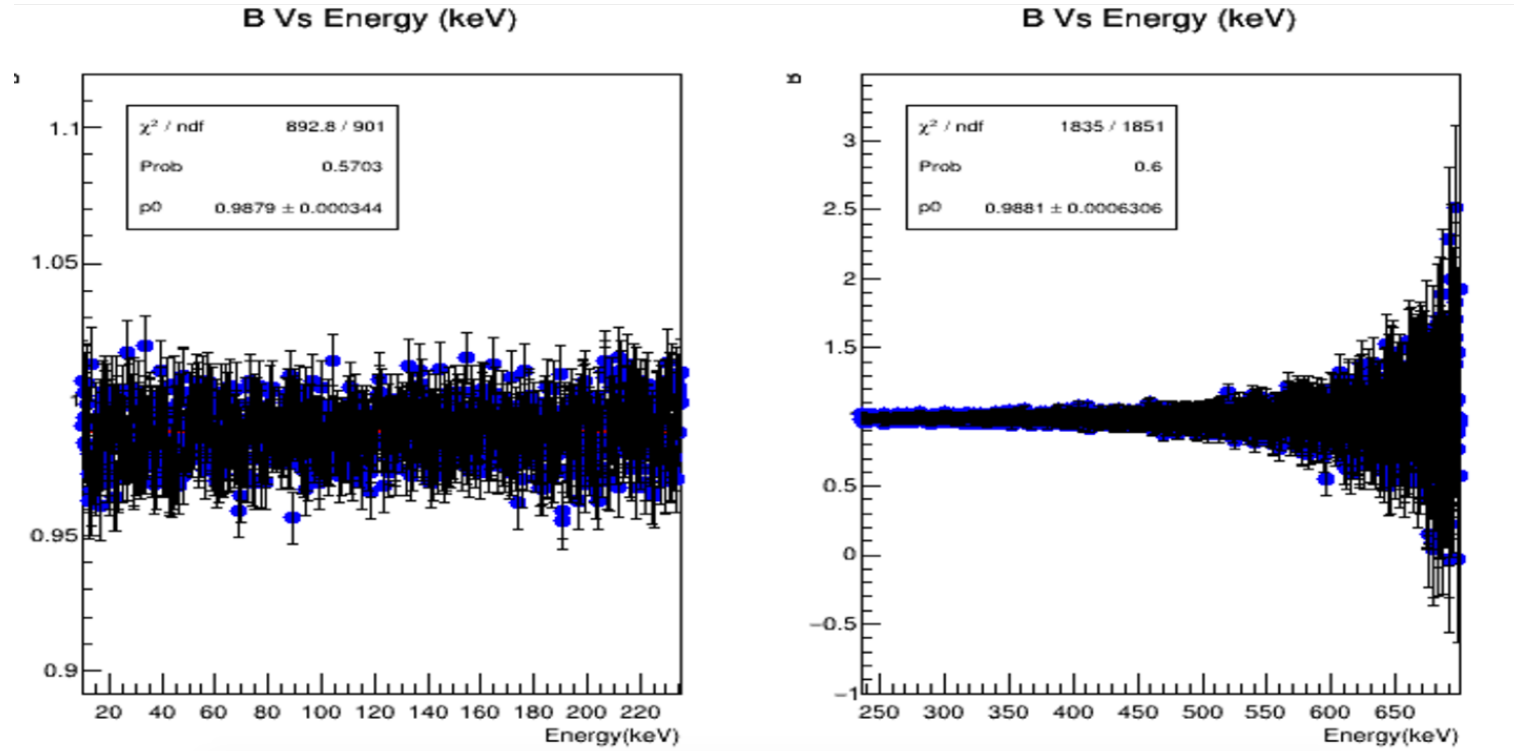


Figure A.47: Neutrino asymmetry  $B$  as a function of electron energy for the regions  $r < 1$  (left) and  $r > 1$  (right) obtained from  $r_{ep}$ .

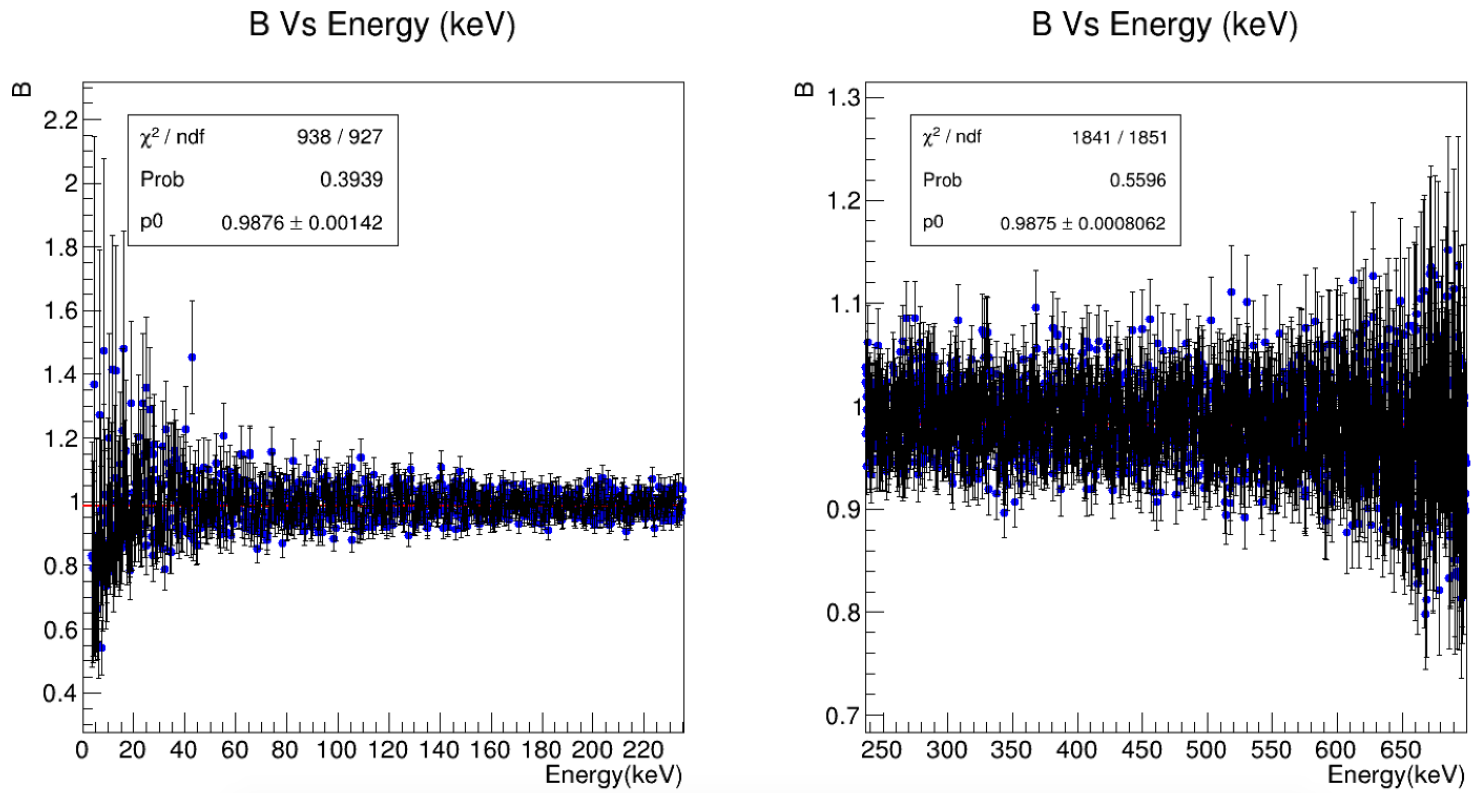


Figure A.48: Neutrino asymmetry  $B$  as a function of electron energy for the regions  $r < 1$  (left) and  $r > 1$  (right) obtained from  $\alpha_x$ .

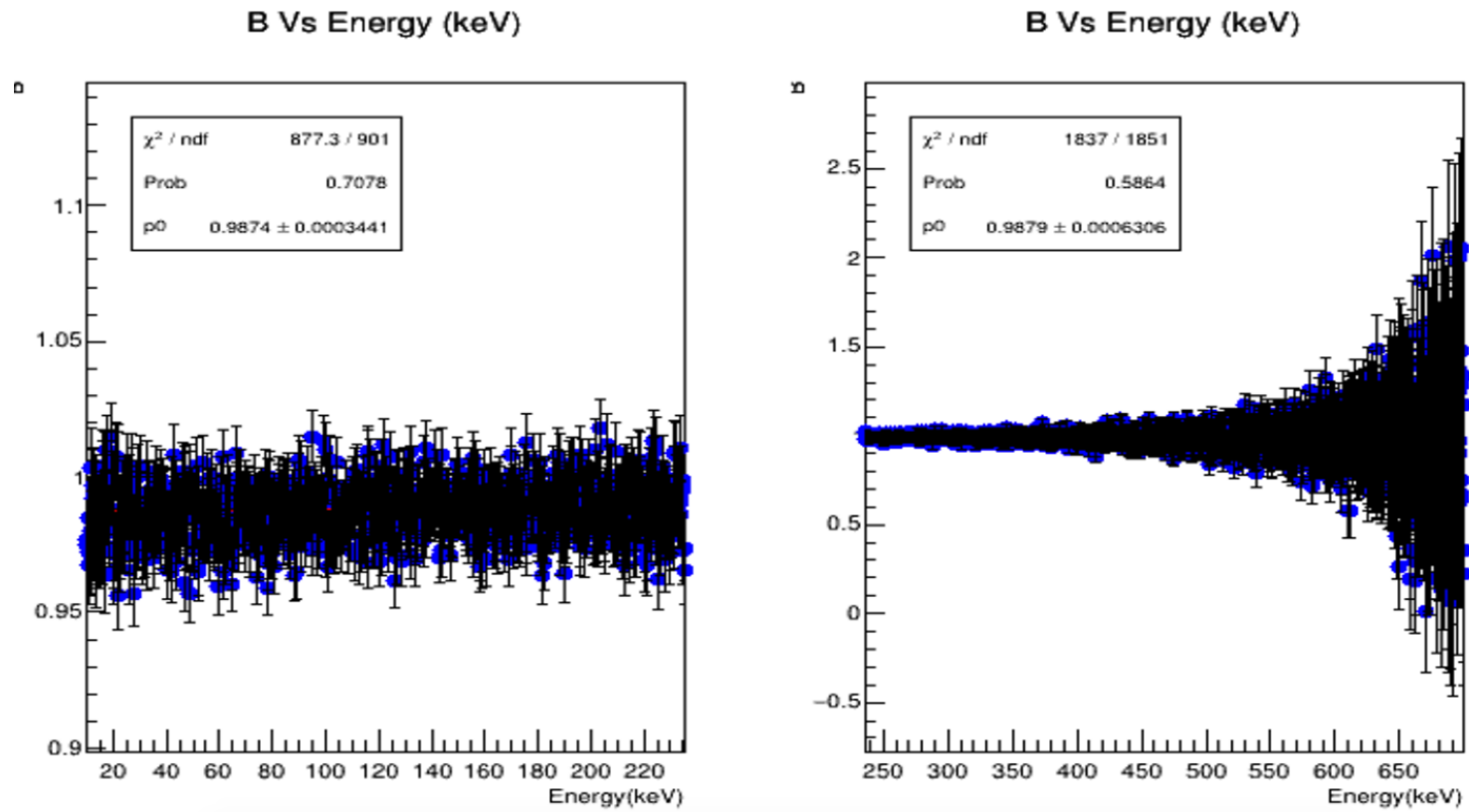


Figure A.49: Neutrino asymmetry  $B$  as a function of electron energy for the regions  $r < 1$  (left) and  $r > 1$  (right) obtained from  $\alpha_R$ .

A.8  $A_0$  and  $B_0$  calculations with bremsstrahlung effects enabled

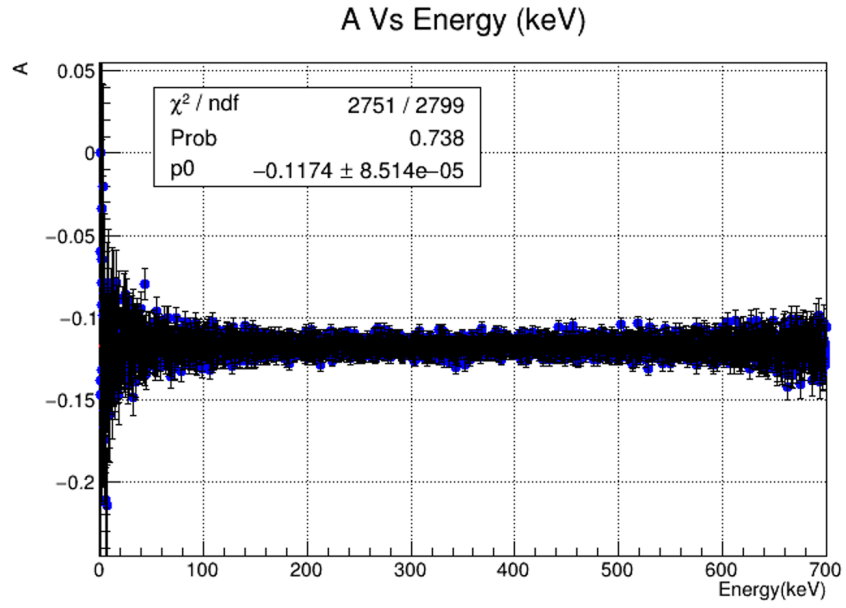


Figure A.50: Electron asymmetry  $A$  as a function of electron energy.

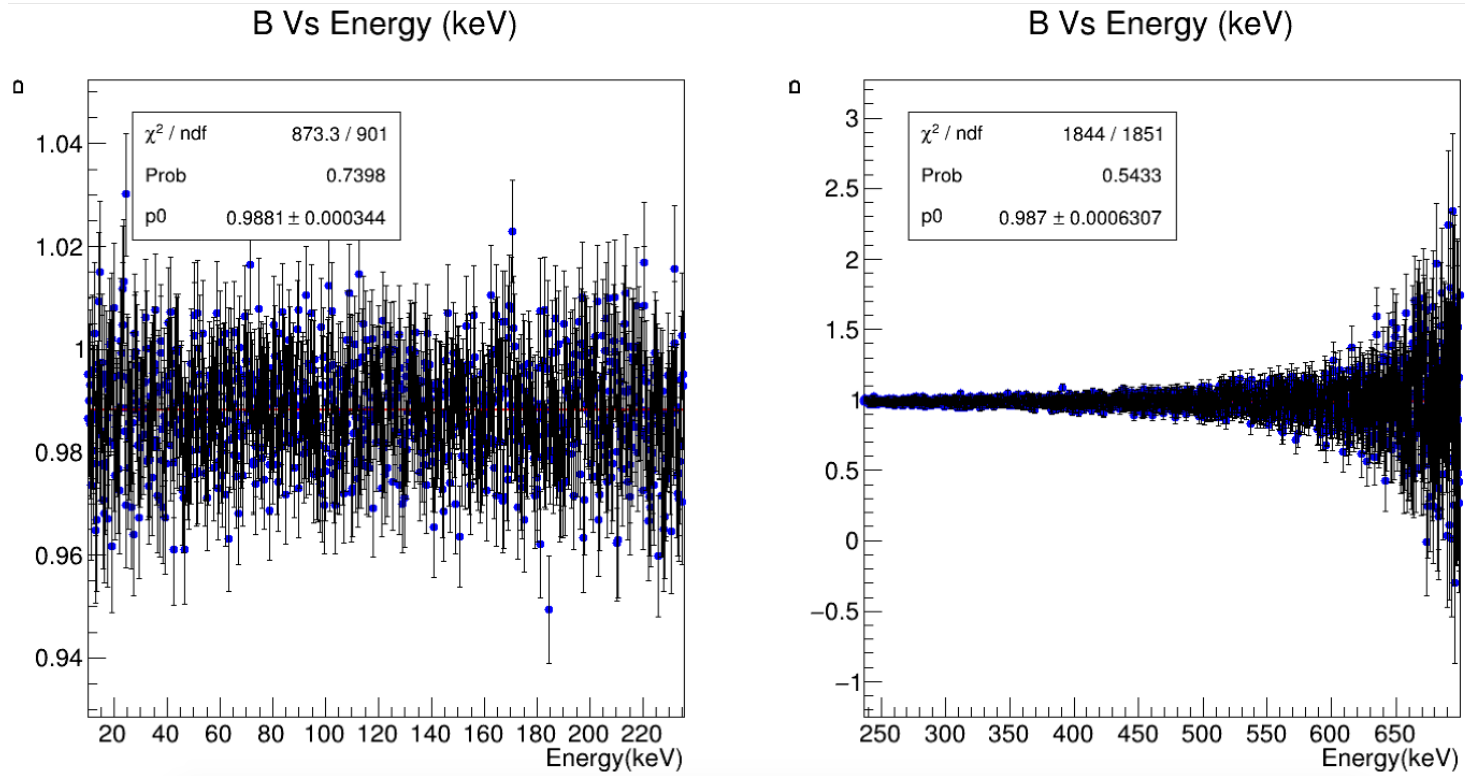


Figure A.51: Neutrino asymmetry  $B$  as a function of electron energy for the regions  $r < 1$  (left) and  $r > 1$  (right) obtained from  $\alpha_p$ .



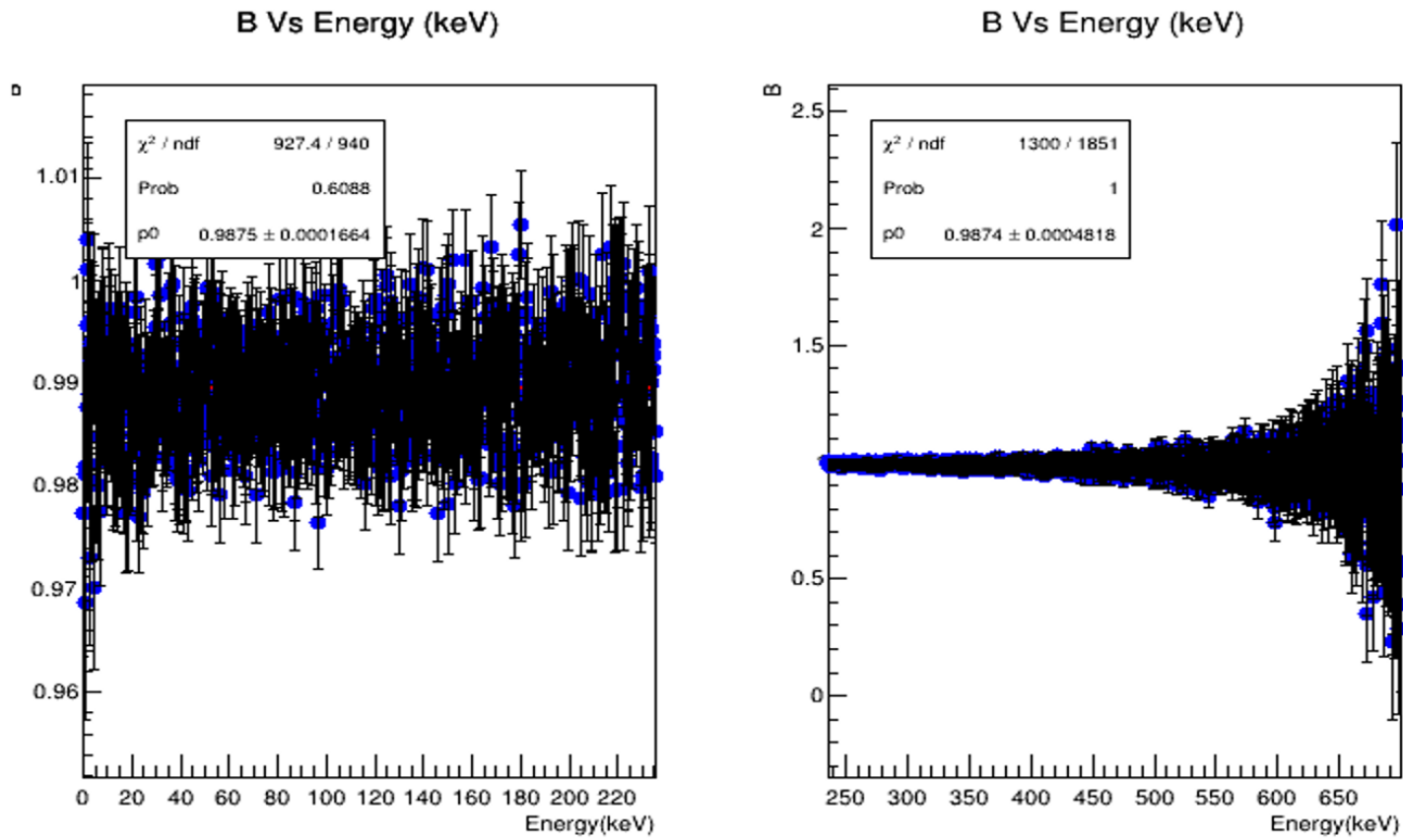


Figure A.52: Neutrino asymmetry  $B$  as a function of electron energy for the regions  $r < 1$  (left) and  $r > 1$  (right) obtained from  $\alpha_{ep}$ .

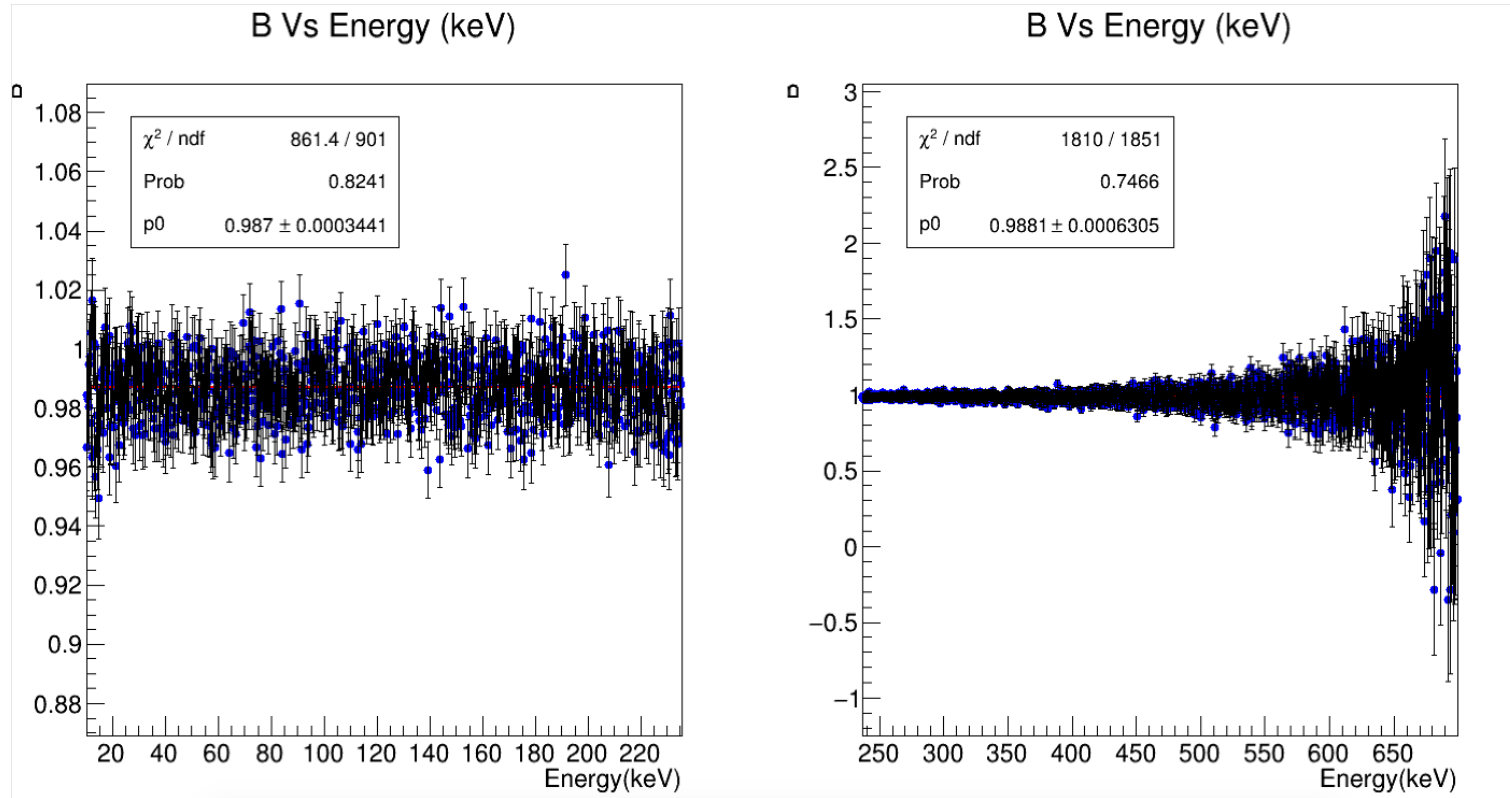


Figure A.53: Neutrino asymmetry  $B$  as a function of electron energy for the regions  $r < 1$  (left) and  $r > 1$  (right) obtained from  $\tilde{\alpha}_{ep}$ .

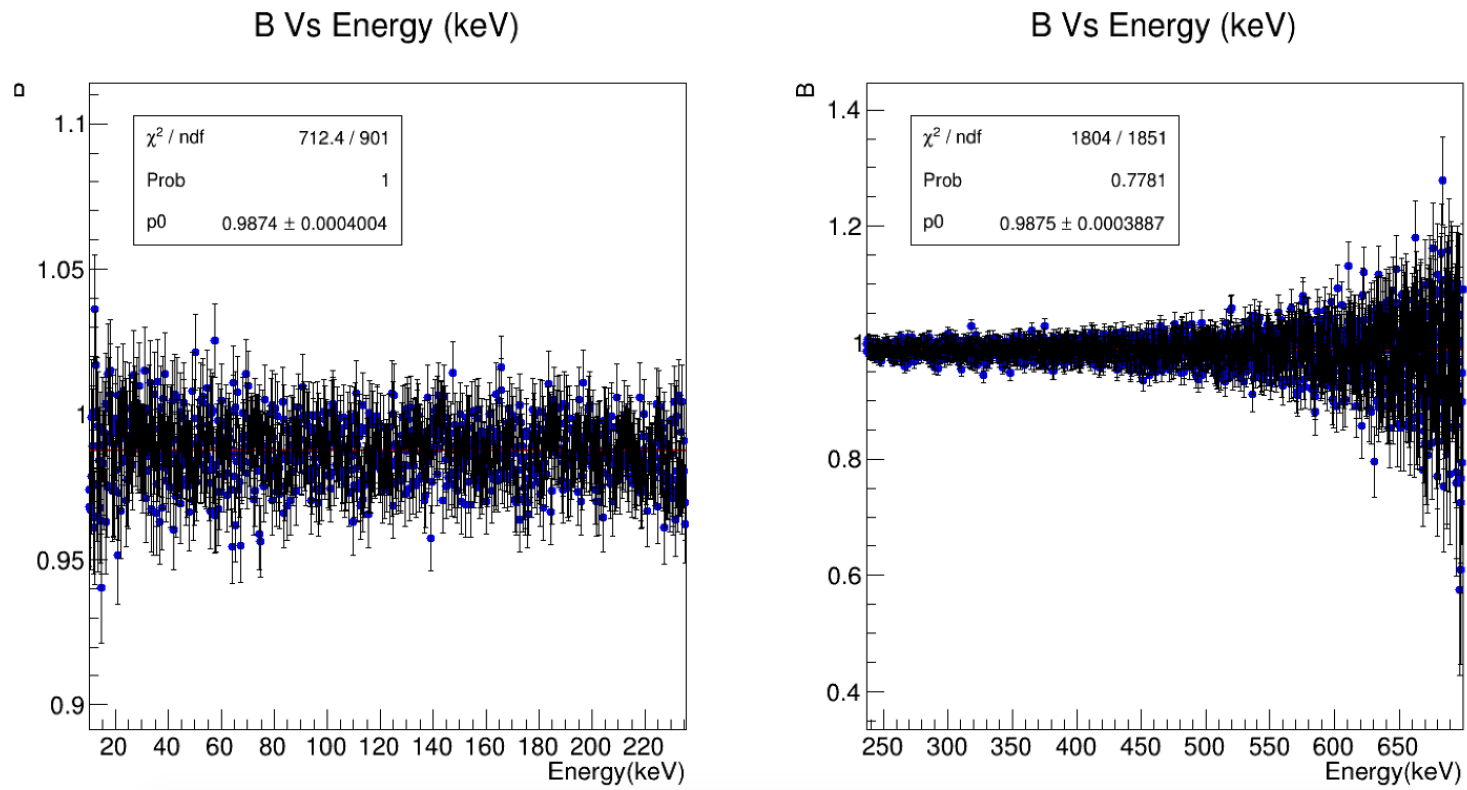


Figure A.54: Neutrino asymmetry  $B$  as a function of electron energy for the regions  $r < 1$  (left) and  $r > 1$  (right) obtained from  $r_{ep}$ .

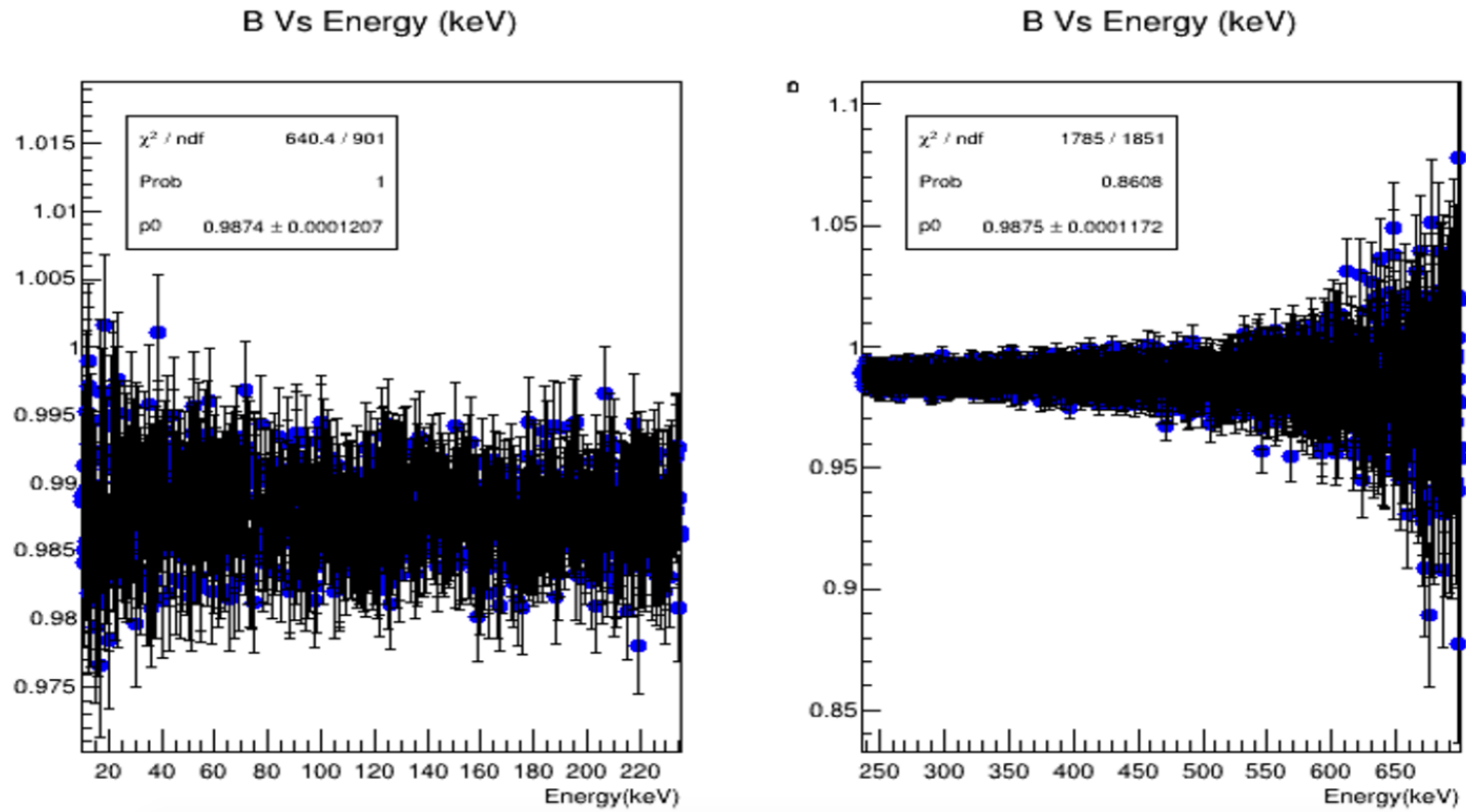


Figure A.55: Neutrino asymmetry  $B$  as a function of electron energy for the regions  $r < 1$  (left) and  $r > 1$  (right) obtained from  $\alpha_x$ .

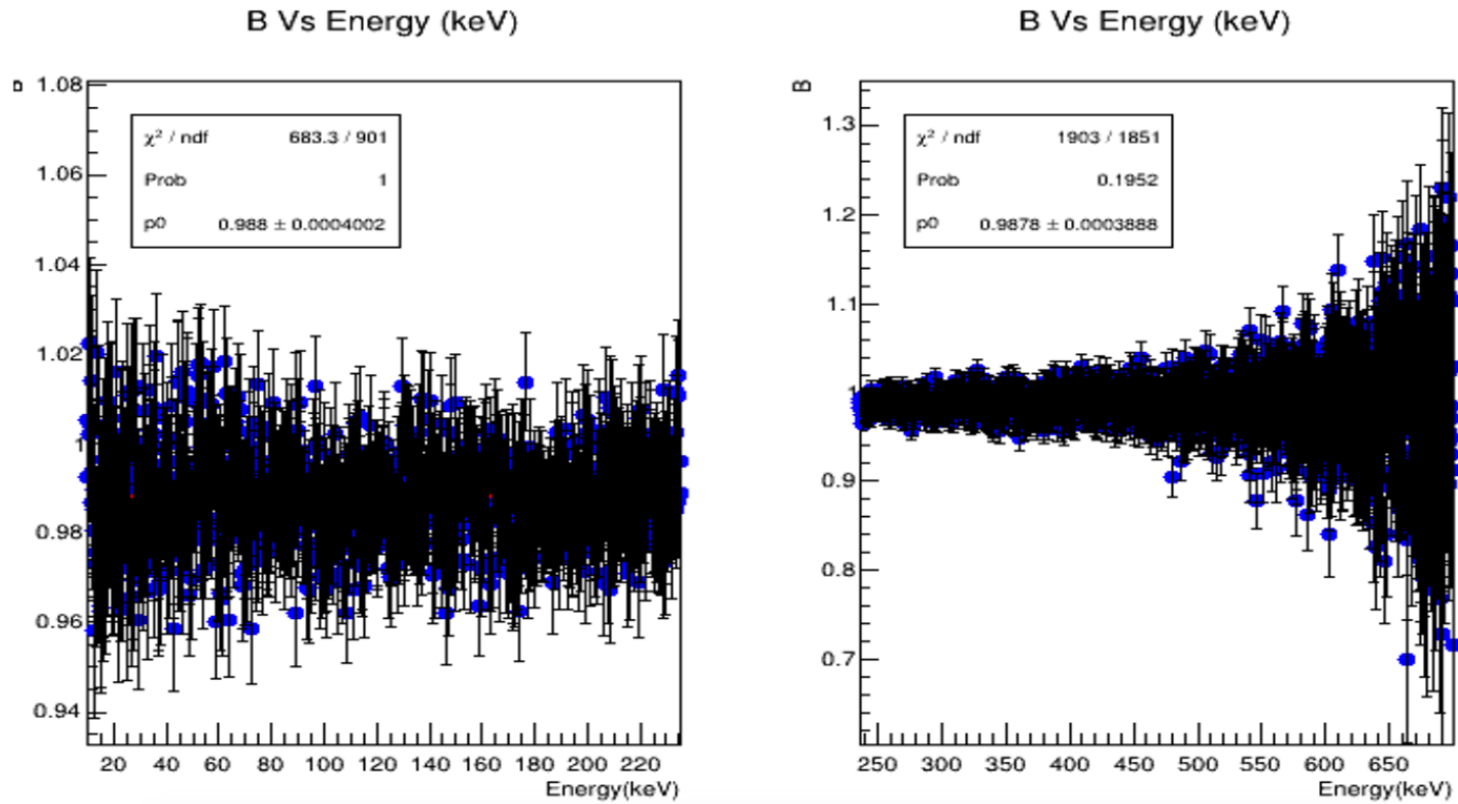


Figure A.56: Neutrino asymmetry  $B$  as a function of electron energy for the regions  $r < 1$  (left) and  $r > 1$  (right) obtained from  $\alpha_R$ .

## A.9 Distortion of electron spectrum

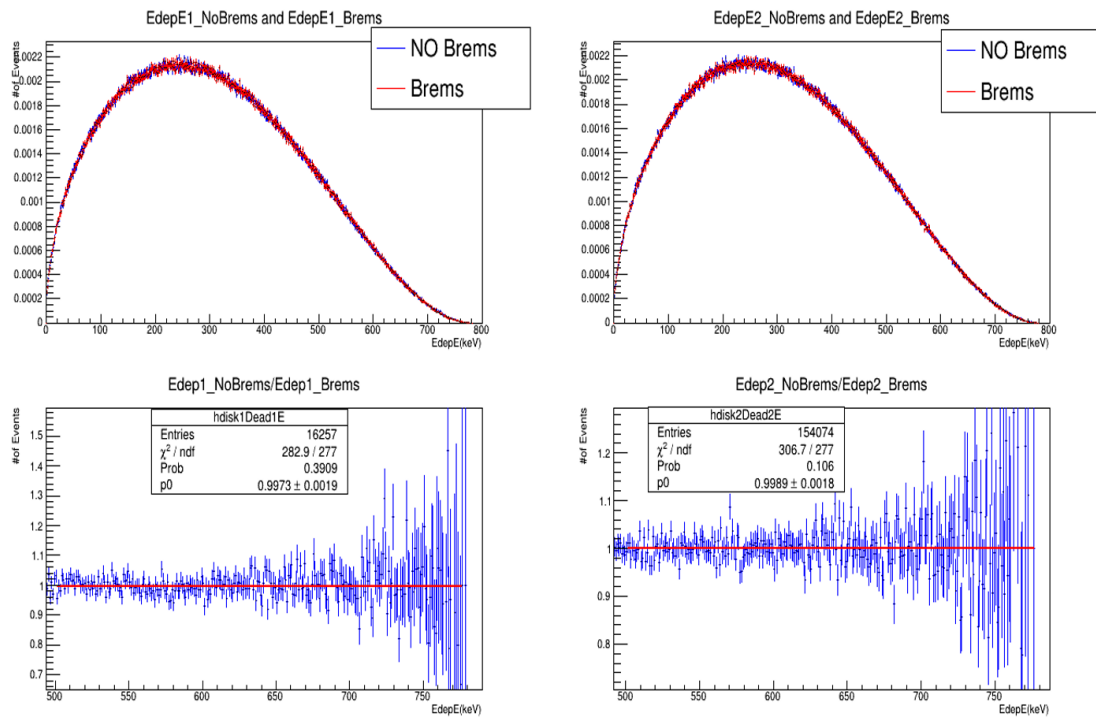


Figure A.57: Distortion in the electron energy spectrum.

## Bibliography

- [1] G. Rajasekaran. Fermi and the theory of weak interactions. *Resonance*, 19(1):18–44, 2014.
- [2] C. S. Wu, E. Ambler, R. W. Hayward, D. D. Hoppes, and R. P. Hudson. Experimental test of parity conservation in beta decay. *Phys. Rev.*, 105:1413–1415, Feb 1957.
- [3] L. J. Broussard et al. Neutron decay correlations in the nab experiment. *Journal of Physics: Conference Series*, 876:012005, jul 2017.
- [4] W. Wilburn, V. Cirigliano, Andi Klein, Mark Makela, P. McGaughey, C. Morris, John Ramsey, A. Salas-Bacci, A. Saunders, L. Broussard, and A. Young. Measurement of the neutrino-spin correlation parameter  $b$  in neutron decay using ultracold neutrons. pages 119–122, 12 2009.
- [5] Michael A.-P. Brown. *Determination of the Neutron Beta-Decay Asymmetry Parameter  $A$  Using Polarized Ultracold Neutrons*. PhD thesis, University of Kentucky, 2018.
- [6] M. Schumann, M. Kreuz, M. Deissenroth, F. Glueck, J. Krempel, B. Maerkisch, D. Mund, A. Petoukhov, T. Soldner, and H. Abele. Measurement of the proton asymmetry parameter  $c$  in neutron beta decay, 2007.
- [7] Guido Altarelli and James Wells. *Gauge Theories and the Standard Model*, pages 1–25. Springer International Publishing, Cham, 2017.
- [8] Thomas Hambye.  $C_p$  violation and the matter and antimatter asymmetry of the universe. *Comptes Rendus Physique*, 13(2):193 – 203, 2012. Flavour physics and CP violation / Physique de la saveur et violation de CP.
- [9] C. Patrignani et al. Review of Particle Physics. *Chin. Phys.*, C40(10):100001, 2016.
- [10] S. M. Bilenky, C. Giunti, and W. Grimus. Neutrino mass spectrum from the results of neutrino oscillation experiments. *The European Physical Journal C*, 1(1):247–253, Mar 1998.
- [11] E. Radermacher. The Experimental Discovery of the Intermediate Vector Bosons  $W^+$ ,  $W^-$  and  $Z^0$  at the CERN  $p\bar{p}$  Collider. *Prog. Part. Nucl. Phys.*, 14:231–328, 1985.
- [12] P. Bagnaia et al. Evidence for  $Z^0 \rightarrow e^+ e^-$  at the CERN anti-p p Collider. *Phys. Lett.*, 129B:130–140, 1983. [,7.69(1983)].

- [13] G. Aad, T. Abajyan, B. Abbott, J. Abdallah, S. Abdel Khalek, and A.A. Abdelalim. Observation of a new particle in the search for the standard model higgs boson with the atlas detector at the lhc. *Physics Letters B*, 716(1):1 – 29, 2012.
- [14] J. Chadwick. Possible Existence of a Neutron. *Nature*, 129:312, 1932.
- [15] Yoann Kermaidic. The nedm experiment at the paul scherrer institute, 2015.
- [16] C. Abel et al. nedm experiment at psi: data-taking strategy and sensitivity of the dataset, 2018.
- [17] C. Abel et al. Measurement of the permanent electric dipole moment of the neutron. *Phys. Rev. Lett.*, 124:081803, Feb 2020.
- [18] Guillaume Pignol. A magic magnetic field to measure the neutron electric dipole moment. *Physics Letters B*, 793:440 – 444, 2019.
- [19] Makoto Kobayashi and Toshihide Maskawa. CP-Violation in the Renormalizable Theory of Weak Interaction. *Progress of Theoretical Physics*, 49(2):652–657, 02 1973.
- [20] A.A. Anselm, V.E. Bunakov, V.P. Gudkov, and N.G. Uraltsev. On the neutron electric dipole moment in the weinberg cp-violation model. *Physics Letters B*, 152(1):116 – 120, 1985.
- [21] M.B. Gavela, A. [Le Yaouanc], L. Oliver, O. PĀšne, J.-C. RaynaL, and T.N. Pham. Cp violation induced by penguin diagrams and the neutron electric dipole moment. *Physics Letters B*, 109(3):215 – 220, 1982.
- [22] John Ellis, Sergio Ferrara, and D.V. Nanopoulos. Cp violation and supersymmetry. *Physics Letters B*, 114(4):231 – 234, 1982.
- [23] Zyla P. A et al. *Prog. Theor. Exp. Phys.*, 083C01(10):100001, 2020.
- [24] J S Nico. Neutron beta decay. *Journal of Physics G: Nuclear and Particle Physics*, 36(10):104001, sep 2009.
- [25] R. P. Feynman and M. Gell-Mann. Theory of the fermi interaction. *Phys. Rev.*, 109:193–198, Jan 1958.
- [26] Fred L. Wilson. Fermi’s Theory of Beta Decay. *American Journal of Physics*, 36(12):1150–1160, Dec 1968.
- [27] Luca Nanni. Fermi theory of beta decay: A first attempt at electroweak unification. *Advanced Studies in Theoretical Physics*, 13:281, 07 2019.
- [28] G. Gamow and E. Teller. Selection rules for the  $\beta$ -disintegration. *Phys. Rev.*, 49:895–899, Jun 1936.



- [29] T. D. Lee and C. N. Yang. Question of parity conservation in weak interactions. *Phys. Rev.*, 104:254–258, Oct 1956.
- [30] Richard L. Garwin, Leon M. Lederman, and Marcel Weinrich. Observations of the failure of conservation of parity and charge conjugation in meson decays: the magnetic moment of the free muon. *Phys. Rev.*, 105:1415–1417, Feb 1957.
- [31] L. D. Landau. On the conservation laws for weak interactions. *Nucl. Phys.*, 3:127–131, 1957.
- [32] Abdus Salam. On parity conservation and neutrino mass. *Nuovo Cim.*, 5:299–301, 1957.
- [33] T. D. Lee and C. N. Yang. Parity nonconservation and a two-component theory of the neutrino. *Phys. Rev.*, 105:1671–1675, Mar 1957.
- [34] Robert Eugene Marshak, M Riazuddin, and Ciaran P Ryan. *Theory of weak interactions in particle physics*. Internat. Sci. Mono. Texts Phys. Astron. Wiley, New York, NY, 1969.
- [35] M. Goldhaber, L. Grodzins, and A. W. Sunyar. Helicity of neutrinos. *Phys. Rev.*, 109:1015–1017, Feb 1958.
- [36] J. Serpe. Remarks on parity conservation and the two-component theory of the neutrino. *Nuclear Physics*, 4:183 – 187, 1957.
- [37] E. C. G. Sudarshan and R. E. Marshak. Chirality invariance and the universal fermi interaction. *Phys. Rev.*, 109:1860–1862, Mar 1958.
- [38] Hideki Yukawa. On the Interaction of Elementary Particles I. *Proc. Phys. Math. Soc. Jap.*, 17:48–57, 1935. [Prog. Theor. Phys. Suppl.1,1(1935)].
- [39] H. Abele, M. Astruc Hoffmann, S. Baeßler, D. Dubbers, F. Glück, U. Müller, V. Nesvizhevsky, J. Reich, and O. Zimmer. Is the unitarity of the quark-mixing ckm matrix violated in neutron  $\beta$ -decay? *Phys. Rev. Lett.*, 88:211801, May 2002.
- [40] Nicola Cabibbo. Unitary symmetry and leptonic decays. *Phys. Rev. Lett.*, 10:531–533, Jun 1963.
- [41] Tanmoy Bhattacharya, Vincenzo Cirigliano, Saul D. Cohen, Rajan Gupta, Huey-Wen Lin, and Boram Yoon. Axial, scalar, and tensor charges of the nucleon from  $2 + 1 + 1$ -flavor lattice qcd. *Phys. Rev. D*, 94:054508, Sep 2016.
- [42] Makoto Kobayashi and Toshihide Maskawa. CP Violation in the Renormalizable Theory of Weak Interaction. *Prog. Theor. Phys.*, 49:652–657, 1973.
- [43] I S Towner and J C Hardy. The evaluation of  $V_{ud}$  and its impact on the unitarity of the cabibbo–kobayashi–maskawa quark-mixing matrix. *Reports on Progress in Physics*, 73(4):046301, mar 2010.

- [44] John Hardy and I. S. Towner.  $|V_{ud}|$  from nuclear  $\beta$  decays. *PoS*, CKM2016:028, 2016.
- [45] M. P. Mendenhall et al. Precision measurement of the neutron  $\beta$ -decay asymmetry. *Phys. Rev. C*, 87:032501, Mar 2013.
- [46] M. A.-P. Brown, E. B. Dees, E. Adamek, B. Allgeier, M. Blatnik, T. J. Bowles, L. J. Broussard, R. Carr, S. Clayton, C. Cude-Woods, S. Currie, X. Ding, B. W. Filippone, A. García, P. Geltenbort, S. Hasan, K. P. Hickerson, J. Hoagland, R. Hong, G. E. Hogan, A. T. Holley, T. M. Ito, A. Knecht, C.-Y. Liu, J. Liu, M. Makela, J. W. Martin, D. Melconian, M. P. Mendenhall, S. D. Moore, C. L. Morris, S. Nepal, N. Nouri, R. W. Pattie, A. Pérez Galván, D. G. Phillips, R. Picker, M. L. Pitt, B. Plaster, J. C. Ramsey, R. Rios, D. J. Salvat, A. Saunders, W. Sondheim, S. J. Seestrom, S. Sjue, S. Slutsky, X. Sun, C. Swank, G. Swift, E. Tatar, R. B. Vogelaar, B. VornDick, Z. Wang, J. Wexler, T. Womack, C. Wrede, A. R. Young, and B. A. Zeck. New result for the neutron  $\beta$ -asymmetry parameter  $A_0$  from ucna. *Phys. Rev. C*, 97:035505, Mar 2018.
- [47] William J. Marciano and Alberto Sirlin. Improved calculation of electroweak radiative corrections and the value of  $V_{ud}$ . *Phys. Rev. Lett.*, 96:032002, Jan 2006.
- [48] Piotr Kielanowski. Two-angle parametrization of the kobayashi-maskawa matrix: A relation between cp violation and the cabibbo-type angles. *Phys. Rev. Lett.*, 63:2189–2191, Nov 1989.
- [49] Ling-Lie Chau and Wai-Yee Keung. Comments on the parametrization of the kobayashi-maskawa matrix. *Phys. Rev. Lett.*, 53:1802–1805, Nov 1984.
- [50] C. Jarlskog. Commutator of the quark mass matrices in the standard electroweak model and a measure of maximal CP nonconservation. *Phys. Rev. Lett.*, 55:1039–1042, Sep 1985.
- [51] Lincoln Wolfenstein. Parametrization of the kobayashi-maskawa matrix. *Phys. Rev. Lett.*, 51:1945–1947, Nov 1983.
- [52] S. Gardner and C. Zhang. Sharpening low-energy, standard-model tests via correlation coefficients in neutron  $\beta$  decay. *Phys. Rev. Lett.*, 86:5666–5669, Jun 2001.
- [53] Murray Gell-Mann. Test of the nature of the vector interaction in  $\beta$  decay. *Phys. Rev.*, 111:362–365, Jul 1958.
- [54] A. W. Thomas. Conserved vector current in particle physics, 1996.
- [55] Susumu Okubo. Second-class currents in weak interactions. *Phys. Rev. Lett.*, 25:1593–1596, Nov 1970.

- [56] B. Plaster et al. Measurement of the neutron  $\beta$ -asymmetry parameter  $A_0$  with ultracold neutrons. *Phys. Rev. C*, 86:055501, Nov 2012.
- [57] J. D. Jackson, S. B. Treiman, and H. W. Wyld. Possible tests of time reversal invariance in beta decay. *Phys. Rev.*, 106:517–521, May 1957.
- [58] M.E. Ebel and G. Feldman. Further remarks on coulomb corrections in allowed beta transitions. *Nuclear Physics*, 4:213 – 214, 1957.
- [59] M. L. Goldberger and S. B. Treiman. Conserved currents in the theory of fermi interactions. *Phys. Rev.*, 110:1478–1479, Jun 1958.
- [60] F. Glück, I. Joó, and J. Last. Measurable parameters of neutron decay. *Nuclear Physics A*, 593(2):125 – 150, 1995.
- [61] Susan Gardner and B. Plaster. Framework for maximum likelihood analysis of neutron decay observables to resolve the limits of the  $v \ll c$  law. *Physical Review C*, 87, 04 2013.
- [62] Tanmoy Bhattacharya, Vincenzo Cirigliano, Saul Cohen, Alberto Filipuzzi, Martín González-Alonso, Michael Graesser, Rajan Gupta, and Huey-Wen Lin. Probing novel scalar and tensor interactions from (ultra)cold neutrons to the lhc. *Phys. Rev. D*, 85, 03 2012.
- [63] R. W. Pattie Jr. et al. Measurement of the neutron lifetime using an asymmetric magneto- gravitational trap and in situ detection, 2017.
- [64] S. Materne, R. Picker, I. Altarev, H. Angerer, B. Franke, E. Gutschiedl, F. J. Hartmann, A. R. Müller, S. Paul, and R. Stoepler. PENeLOPE—on the way towards a new neutron lifetime experiment with magnetic storage of ultra-cold neutrons and proton extraction. *Nuclear Instruments and Methods in Physics Research A*, 611(2-3):176–180, December 2009.
- [65] A. T. Yue, M. S. Dewey, D. M. Gilliam, G. L. Greene, A. B. Laptev, J. S. Nico, W. M. Snow, and F. E. Wietfeldt. Improved determination of the neutron lifetime, 2013.
- [66] D. J. Salvat et al. Storage of ultracold neutrons in the ucn magneto-gravitational trap, 2013.
- [67] Y. Arimoto, N. Higashi, et al. Development of time projection chamber for precise neutron lifetime measurement using pulsed cold neutron beams. *Nuclear Instruments and Methods in Physics Research Section A: Accelerators, Spectrometers, Detectors and Associated Equipment*, 799:187 – 196, 2015.
- [68] J Byrne, P. G Dawber, C. G Habeck, S. J Smidt, J. A Spain, and A. P Williams. A revised value for the neutron lifetime measured using a penning trap. *Europhysics Letters (EPL)*, 33(3):187–192, jan 1996.

- [69] K. K. H. Leung, P. Geltenbort, S. Ivanov, F. Rosenau, and O. Zimmer. Neutron lifetime measurements and effective spectral cleaning with an ultracold neutron trap using a vertical halfbach octupole permanent magnet array. *Phys. Rev. C*, 94:045502, Oct 2016.
- [70] V. F. Ezhov, A. Z. Andreev, G. Ban, B. A. Bazarov, P. Geltenbort, A. G. Glushkov, V. A. Knyazkov, N. A. Kovrizhnykh, G. B. Krygin, O. Naviliat-Cuncic, and V. L. Ryabov. Measurement of the neutron lifetime with ultra-cold neutrons stored in a magneto-gravitational trap, 2014.
- [71] S. Arzumanov, L. Bondarenko, S. Chernyavsky, P. Geltenbort, V. Morozov, V.V. Nesvizhevsky, Yu. Panin, and A. Strepetov. A measurement of the neutron lifetime using the method of storage of ultracold neutrons and detection of inelastically up-scattered neutrons. *Physics Letters B*, 745:79 – 89, 2015.
- [72] A. P. Serebrov, V. E. Varlamov, A. G. Kharitonov, A. K. Fomin, Yu. N. Pokotilovski, P. Geltenbort, I. A. Krasnoschekova, M. S. Lasakov, R. R. Taldaev, A. V. Vassiljev, and O. M. Zhrebtsov. Neutron lifetime measurements using gravitationally trapped ultracold neutrons. *Phys. Rev. C*, 78:035505, Sep 2008.
- [73] A. Serebrov, V. Varlamov, A. Kharitonov, A. Fomin, Yu. Pokotilovski, P. Geltenbort, J. Butterworth, I. Krasnoschekova, M. Lasakov, R. Taldaev, A. Vassiljev, and O. Zhrebtsov. Measurement of the neutron lifetime using a gravitational trap and a low-temperature fomblin coating, 2004.
- [74] H. A. Mook and John B. Hayter. Transmission optical device to produce intense polarized neutron beams. *Applied Physics Letters*, 53(8):648–650, 1988.
- [75] A R Young, S Clayton, B W Filippone, P Geltenbort, T M Ito, C-Y Liu, M Makela, C L Morris, B Plaster, A Saunders, S J Seestrom, and R B Vogelaar. Beta decay measurements with ultracold neutrons: a review of recent measurements and the research program at los alamos national laboratory. *Journal of Physics G: Nuclear and Particle Physics*, 41(11):114007, oct 2014.
- [76] Kevin Peter Hickerson. *The physics of ultracold neutrons and Fierz interference in beta decay*. PhD thesis, Caltech, 2012.
- [77] A Saunders et al. Demonstration of a solid deuterium source of ultra-cold neutrons. *Physics Letters B*, 593(1):55 – 60, 2004.
- [78] T. M. Ito et al. Performance of the upgraded ultracold neutron source at los alamos national laboratory and its implication for a possible neutron electric dipole moment experiment. *Phys. Rev. C*, 97:012501, Jan 2018.
- [79] S. Wlokka, P. Fierlinger, A. Frei, P. Geltenbort, S. Paul, T. Pöschl, F. Schmid, W. Schreyer, and D. Steffen. Consistent description of ucn transport properties, 2017.

- [80] E. Korobkina, R. Golub, J. Butterworth, P. Geltenbort, and S. Arzumanov. Temperature dependence of ultracold neutron loss rates. *Phys. Rev. B*, 70:035409, Jul 2004.
- [81] S. K. Lamoreaux and R. Golub. Calculation of the ultracold neutron upscattering loss probability in fluid walled storage bottles using experimental measurements of the thermomechanical properties of fomblin, 2002.
- [82] C. L. Morris et al. A new method for measuring the neutron lifetime using an in situ neutron detector. *Review of Scientific Instruments*, 88(5):053508, 2017.
- [83] B.G. Erozolimsky, L.N. Bondarenko, Yu.A. Mostovoy, B.A. Obinyakov, V.A. Titov, V.P. Zacharova, and A.I. Frank. Angular correlation between the neutron spin and the antineutrino momentum in the neutron decay. *Physics Letters B*, 33(5):351 – 352, 1970.
- [84] C. J. Christensen, V. E. Krohn, and G. R. Ringo. Measurement of angular correlations in the decay of polarized neutrons. *Phys. Rev. C*, 1:1693–1698, May 1970.
- [85] Rajan Gupta, Yong-Chull Jang, Huey-Wen Lin, Boram Yoon, and Tanmoy Bhattacharya. Axial-vector form factors of the nucleon from lattice qcd. *Phys. Rev. D*, 96:114503, Dec 2017.
- [86] R. W. Pattie et al. First measurement of the neutron  $\beta$  asymmetry with ultracold neutrons. *Phys. Rev. Lett.*, 102:012301, Jan 2009.
- [87] R. W. Pattie Jr. *A Precision Measurement of the Neutron Asymmetry using Ultracold Neutrons*. PhD thesis, North Carolina State University, 2012.
- [88] Yu. A. Mostovoi et al. Experimental value of  $g_a/g_v$  from a measurement of both p-odd correlations in free-neutron decay. *Physics of Atomic Nuclei*, 64:1955–1960, Jul 2001.
- [89] D.E. Groom et al. Review of particle physics. *The European Physical Journal*, C15:1+, 2000.
- [90] M. Kreuz et al. A measurement of the antineutrino asymmetry  $b$  in free neutron decay. *Phys. Lett.*, B619:263–270, 2005.
- [91] I. A. Kuznetsov, A. P. Serebrov, I. V. Stepanenko, A. V. Alduschenkov, M. S. Lasakov, A. A. Kokin, Yu. A. Mostovoi, B. G. Yerozolimsky, and M. S. Dewey. Measurements of the antineutrino spin asymmetry in beta decay of the neutron and restrictions on the mass of a right-handed gauge boson. *Phys. Rev. Lett.*, 75:794–797, Jul 1995.
- [92] X. Sun et al. Improved limits on Fierz interference using asymmetry measurements from the Ultracold Neutron Asymmetry (UCNA) experiment. *Phys. Rev. C*, 101:035503, Mar 2020.

- [93] S Baekler, J D Bowman, S Penttilä, and D Počanić. New precision measurements of free neutron beta decay with cold neutrons. *Journal of Physics G: Nuclear and Particle Physics*, 41(11):114003, oct 2014.
- [94] M. Morita and I. Tanihata. Asymmetry of beta-ray angular distribution in polarized nuclei and  $g$ -parity nonconservation. *Phys. Rev. Lett.*, 35:26–29, Jul 1975.
- [95] Jameel-Un Nabi, Mavra Ishfaq, Ovidiu Nişescu, Mihail Mirea, and Sabin Stoica.  $\beta$ -decay half-lives of even-even nuclei using the recently introduced phase space recipe. *Universe*, 6(1), 2019.
- [96] Ferenc Glück. Measurable distributions of unpolarized neutron decay. *Physical review D: Particles and fields*, 47:2840–2848, 05 1993.
- [97] D.H. Wilkinson. Analysis of neutron  $\beta$ -decay. *Nuclear Physics A*, 377(2):474 – 504, 1982.
- [98] S. Agostinelli et al. GEANT4: A Simulation toolkit. *Nucl. Instrum. Meth.*, A506:250–303, 2003.
- [99] Fry, J. et al. The nab experiment: A precision measurement of unpolarized neutron beta decay. *EPJ Web Conf.*, 219:04002, 2019.
- [100] M. Schumann, M. Kreuz, M. Deissenroth, F. Glück, J. Krempel, B. Märkisch, D. Mund, A. Petoukhov, T. Soldner, and H. Abele. Measurement of the proton asymmetry parameter in neutron beta decay. *Phys. Rev. Lett.*, 100:151801, Apr 2008.
- [101] John David Jackson. *Classical electrodynamics*. 1999.
- [102] Dirk Dubbers. Characterization of electron detectors by time-of-flight in neutron  $\eta$  decay experiments, 2016.
- [103] C. Roick, D. Dubbers, B. Märkisch, H. Saul, and U. Schmidt. Electron time-of-flight: A new tool in  $\beta$ -decay spectroscopy. *Phys. Rev. C*, 97:035502, Mar 2018.
- [104] B.L. Wall and other. Dead layer on silicon p-n diode charged-particle detectors. *Nuclear Instruments and Methods in Physics Research Section A: Accelerators, Spectrometers, Detectors and Associated Equipment*, 744:73 – 79, 2014.
- [105] Zine-El-Abidine Chaoui and Pascal Renschler. Dead layer effect in silicon detectors: energy deposited. *Surface and Interface Analysis*, 42(6&7):1093–1095, 2010.
- [106] Leah Broussard. UCNB: The neutrino asymmetry in polarized ultracold neutron decay. *AIP Conf. Proc.*, 1560(1):149–151, 2013.

- [107] A. T. Holley, L. J. Broussard, J. L. Davis, K. Hickerson, T. M. Ito, C.-Y. Liu, J. T. M. Lyles, M. Makela, R. R. Mammei, M. P. Mendenhall, C. L. Morris, R. Mortensen, R. W. Pattie, R. Rios, A. Saunders, and A. R. Young. A high-field adiabatic fast passage ultracold neutron spin flipper for the ucna experiment. *Review of Scientific Instruments*, 83(7):073505, 2012.
- [108] S. Chauvie, S. Guatelli, V. Ivanchenko, F. Longo, A. Mantero, B. Mascialino, P. Nieminen, L. Pandola, S. Parlati, L. Peralta, M. G. Pia, M. Piergentili, P. Rodrigues, S. Saliceti, and A. Tndade. Geant4 low energy electromagnetic physics. In *IEEE Symposium Conference Record Nuclear Science 2004.*, volume 3, pages 1881–1885 Vol. 3, Oct 2004.
- [109] John Allison. Facilities and methods: Geant4 â a simulation toolkit. *Nuclear Physics News*, 17(2):20–24, 2007.
- [110] Junhua Yuan. *Progress towards a high precision measurement of the neutron spin–electron angular correlation in polarized neutron beta de- cay with ultra- cold neutrons*. PhD thesis, California Institute of Technology, 2006.
- [111] X. Sun et al. Search for dark matter decay of the free neutron from the UCNA experiment:  $n \rightarrow \chi + e^+e^-$ . *Phys. Rev. C*, 97(5):052501, 2018.
- [112] X. Sun et al. Search for neutron dark decay:  $n \rightarrow \chi + e^+e^-$ . *EPJ Web Conf.*, 219:05008, 2019.
- [113] B. Plaster et al. Final results for the neutron  $\beta$ -asymmetry parameter  $A_0$  from the UCNA experiment. *EPJ Web Conf.*, 219:04004, 2019.
- [114] F. James. MINUIT Function Minimization and Error Analysis: Reference Manual Version 94.1. 1994.
- [115] D.H. Wilkinson. Evaluation of beta-decay. pt. 1. the traditional phase space factors. in: Nuclear instruments and methods in physics research section a: Accelerators, spectrometers, detectors and associated equipment. *Nucl. Instrum. Methods Phys. Res.*, 275(2):378–386, Feb 1989.

## Vita

### Personal Information

Name: Subash Chandra Nepal  
Place of Birth: Tsirang, Bhutan

### Educational Institutions

M.S. Physics  
University of Kentucky, Lexington, KY  
May 2017

M.S. Physics  
North Carolina Central University, Durham, NC  
August 2014

M.S. Physics  
Tribhuvan University, Kathmandu, Nepal  
October 2005

B.S. Physics(Major), Mathematics and Chemistry  
North Bengal University, Siliguri, (West Bengal) India  
August 2001

### Professional Positions

Graduate Research Assistant  
University of Kentucky, Lexington, KY  
Department of Physics and Astronomy  
August 2017 - July 2020

Graduate Teaching Assistant  
University of Kentucky, Lexington, KY  
Department of Physics and Astronomy  
August 2014 - August 2017

Graduate Teaching Assistant  
North Carolina Central University, Durham, NC  
Department of Physics  
August 2012 - August 2014



## Publications

X. Sun et al. "Improved limits on Fierz interference using asymmetry measurements from the Ultracold Neutron Asymmetry (UCNA) experiment." *Phys. Rev.C*, 101:035503, Mar 2020.

B. Plaster et al. "Final results for the neutron  $\beta$ -asymmetry parameter  $A_0$  from the UCNA experiment." *EPJ Web Conf.*, 219:04004, 2019.

X. Sun et al. "Search for neutron dark decay:  $n \rightarrow +e + e^-$ ." *EPJ Web Conf.*, 219:05008, 2019.

Brown, M. A.-P., et al. "New result for the neutron  $\beta$ -asymmetry parameter  $A_0$  from UCNA." *Physical Review C* 97 (2018): 035505.

X. Sun et al. " Search for dark matter decay of the free neutron from the UCNA experiment:  $n \rightarrow +e + e^-$ ." *Phys. Rev. C*, 97(5):052501, 2018.